EVALUATION OF BATCH PROCESSES FOR CONTINUOUS FLOW SYNTHESIS OF METAL & METAL OXIDE NANOMATERIALS

THESIS

Submitted To The

UNIVERSITY OF PUNE

For The Degree Of

DOCTOR OF PHILOSOPHY
In
CHEMISTRY

By

VENKATA RAVI KUMAR. DARBHA

Research Guide

Dr. B. L. V. PRASAD

Research Co-Guide

Dr. AMOL A. KULKARNI

DIVISION OF PHYSICAL AND MATERIAL CHEMISTRY
NATIONAL CHEMICAL LABORATORY, PUNE – 411008

March 2013

राष्ट्रीय रासायनिक प्रयोगशाला
(वैज्ञानिक तथा औद्योगिक अनुसंधान परिषद)
डॉ. होमी भाभा मार्ग पुणे - 411 008. भारत
NATIONAL CHEMICAL LABORATORY
(Council of Scientific & Industrial Research)
Dr. Homi Bhabha Road, Pune - 411 008. India.

CERTIFICATE

This is to certify that the work incorporated in the thesis entitled: "**Evaluation of batch processes for continuous flow synthesis of metal & metal oxide nanomaterials**", submitted by Mr. Venkata Ravi Kumar. Darbha, for the degree of Doctor of Philosophy in Chemistry to the University of Pune, has been carried out by him under my supervision at Physical and Material Chemistry Division, National Chemical Laboratory, Pune - 411008, India. All the materials from other sources have been duly acknowledged in this thesis. To the best of my knowledge, the present work or any part of thereof has not been submitted to any other university for the award of any degree or diploma.

Date: 22-March-2013

Place: PUNE

B. L. V. Prasad
(Research Guide)

Communication Channels
+91-20-2590 2000
+91-20-2590 (DID)
FAX
+91-20-2590 2601(DIR)
+91-20-2590 2660 (COA)
WEBSITE
www.ncl-india.org

सीएसआयआर–राष्ट्रीय रासायनिक प्रयोगशाला
(वैज्ञानिक तथा औद्योगिक अनुसंधान परिषद)
डॉ. होमी भाभा मार्ग, पुणे – 411 008. भारत
CSIR-NATIONAL CHEMICAL LABORATORY
(Council of Scientific & Industrial Research)
Dr. Homi Bhabha Road, Pune - 411008. India

CERTIFICATE

This is to certify that the work incorporated in the thesis entitled: "**Evaluation of batch processes for continuous flow synthesis of metal & metal oxide nanomaterials**", submitted by Mr. Venkata Ravi Kumar. Darbha, for the degree of Doctor of Philosophy in Chemistry to the University of Pune, has been carried out by him under my joint supervision at Chemical Engineering and Process Development Division, National Chemical Laboratory, Pune-411008, India. All the materials from other sources have been duly acknowledged in this thesis. To the best of my knowledge, the present work or any part of thereof has not been submitted to any other university for the award of any degree or diploma.

Date: March 22, 2013
Place: PUNE

Dr. Amol A. Kulkarni
(Research Co-Guide)

Communication Channels
NCL Level DID : 2590
NCL Board No. : +91-20-25902000
EPABX : +91-20-25893300
: +91-20-25893400
FAX
Director's Office : +91-20-25902601
COA's Office : +91-20-25902660
COS&P's Office : +91-20-25902664
WEBSITE
www.ncl-india.org

Declaration

I, hereby declare that all the experiments embodies in this thesis entitled **"Evaluation of batch processes for continuous flow synthesis of metal & metal oxide nanomaterials"** submitted for the degree of Doctor of Philosophy in Chemistry, to the University of Pune has been carried out by me at Physical and Material Chemistry Division and Chemical Engineering and Process Development Divisions, National Chemical Laboratory, Pune, India, under the guidance of Dr. B. L. V. Prasad and co-guidance of Dr. Amol A. Kulkarni. Such material as has been obtained by other sources fully acknowledged in this thesis. The work is original and has not been submitted in part or full by me, for any degree or diploma to this or to any other University.

Date 22nd March 2013

Place: PUNE

Venkata Ravi Kumar. Darbha

Acknowledgements

I would like to take this opportunity to express my gratitude to some of the people to whom I met at NCL, without their help and contribution this work would be highly impossible. First of all, I express my sincere thanks to Dr. B. L.V. Prasad and Dr. Amol A. Kulkarni for their guidance, encouragement, valuable discussions and patience. I can not imagine the fate of this thesis without their contribution. They gave me enough freedom to express my views whether they are right or wrong. I am grateful to Amol sir for his encouragement and enthusiastic discussions. I am very much thankful to Prasad sir for bearing me and for his patience to correct my poor written English.

I am thankful to Ex- Director of NCL, Dr. S. Sivaram, present Director Dr. Sourav Pal, Head of Physical Chemistry division Dr. Anil Kumar, Head of CEPD division Dr. V. V. Ranade for giving me an opportunity to work with NCL. I like to thank Dr. B.D. Kulkarni for attending my seminars with patience and for giving valuable suggestions. I am thankful to Council of Scientific and Industrial Research (CSIR, New Delhi) for financial assistance.

My special thanks to all of the past and present members of both the Amol sir group and Prasad groups for their help and contribution during my work. I like to thank Mr. Sunil Jadhav, D. M. Solutions for providing us microreactors and Mr. Wanjale, workshop – CEPD division for his valuable help. I am thankful to all the technicians of CMC for their contribution to get good quality data. I am thankful to other scientists of NCL for allowing us to use some of their characterization facilities. I am thankful to all of my NCL and Telugu friends, without their company it is not possible to stay at NCL for long time. My sincere thanks to each and every one who helped me, during my visit to France, especially Dr. Malvi, Amol sir were bearing all of my stupid questions and they helped me with patience. I am thankful Department of Science and Technology (DST, New Delhi) and NCL for providing me financial help. Finally I thank each and every one who helped me a lot.

RAVI KUMAR

Abstract

Nanomaterials have several applications in various areas and from last few decades they are proved to be potential candidates to bring drastic changes in technologically fast growing research areas like drug delivery, biological imaging, polymer composites, solar cells, Li batteries, catalysis etc., The increasing technological application of the nanomaterials demand their synthesis at large scale. The properties of nanomaterials and hence their applications mainly depend upon their size and shape. Several synthetic methods exist to prepare the nanomaterials like physical, biological, and chemical methods and among these chemical methods proved to be efficient methods to get control over the size and shape of the materials. Many of these synthetic methods (chemical methods) are successful to prepare small amount of nanomaterials (like few mg or few mL dispersions). When these bench top protocols are extended to large scale synthesis they suffer from several limitations like inhomogeneous mass and heat transfers and affect the final selectivity in terms of size and shape of the particles.

Microreactors are one of the alternatives to overcome the limitations of batch processes. In general the microreactors are operated under laminar flow conditions (Re < 2000). Although mixing is through diffusion under these conditions, at small length scales mixing becomes faster. Because of the high surface to volume ratios the heat transfer is also faster. Above all fluid flow, reagent addition, mixing can be effectively controlled in microreactors by adjusting the flow rates and other parameters. Especially microreactors very useful to handle hazardous chemicals, to carry out chemical reaction with faster kinetics and they are easy to handle. In organic synthesis microreactors are proved to be efficient in terms of decreasing the reaction time, improving the product quality (decreasing the byproducts). Advantages of microreactors make them researchers first choice to synthesize various nanomaterials with fine control on size distribution. As the microreactors are operated in continuous flow methods, nanomaterials can be obtained at large

scale without altering the properties of the nanomaterials and in fact more control can be attained over the size and shape of the particles.

Many of the literature reports on continuous flow nanomaterials syntheses describe the process development from batch to continuous flow without proper validation of batch process. Quantum dots, metal nanoparticles and some precipitation methods to synthesize metal oxide nanoparticles are described in literature. However, synthesis of anisotropic nanoparticles, process developments to very rapid reactions, solid formation reactions are not addressed in the literature. In this view the main objectives of this thesis work are:

1. Continuous flow synthesis of metal nanoparticles.
    a. Introduction to our previous efforts to synthesize Ag nanoparticles using sophorolipid and initial continuous flow methods.
    b. Understanding the role of channel geometry on particle size distribution.
    c. Understanding the combination of segmented flow and secondary flows (which are generated because of channel geometry) on particle size distribution.
    d. Understanding the role of other hydrodynamic parameters on the particle size distribution.
2. Developing continuous flow method to synthesize anisotropic Au nanoparticles by taking triangle as case study.
    a. Understanding and validation of batch process.
    b. Continuous flow synthesis of triangular gold nanoplates and the role of different parameters.
3. Developing continuous flow methods for rapid and solid formation reactions: synthesis of nanocrystalline MgO using sol gel process as a case study.

a. Designing Jet micromixer and continuous flow synthesis of nanocrystalline MgO

b. Understanding the role of different parameters which effect the surface are of the MgO.

The thesis has been divided into five chapters.

Chapter 1: Introduction

This chapter briefly discuss about the (i) increasing applications of nanomaterials in various areas, (ii) the requirement to synthesize them in large scale quantities and limitations of batch process to synthesize the nanomaterials at large scale, (iii) introduction to microreactors and their advantages when compared to bench top batch preparative methods, (iv) review of literature which discuss about the synthesis of nanomaterials in microreactors followed by objective of this work.

Chapter 2:

Chapter 2 has been divided into two parts.

Part A: Continuous flow synthesis of functionalized Ag nanoparticles in spiral micro reactor.

Batch process conditions to synthesize Ag nanoparticles were optimized in terms of selecting suitable reducing and capping agent, reaction temperature and reaction time. The optimized reaction conditions were used to synthesize them in continuous flow method. When microreactors operated in laminar flow regime (Re <2000) velocity profiles are parabolic and this situation leads to broad size distribution. To avoid this Khan et al suggested segmented flow methods by using an inert phase like air, but it decreases the effective volume of the reactor. So we came up with a spiral reactor where the velocity profiles are skewed and because of curved geometries secondary flow are generated and these secondary flow continuously change with the radius of curvature and expected to get narrow size distribution.

We synthesized Ag nanoparticles in spiral microreactor using $AgNO_3$ and stearic acid sophorolipid in spiral microreactor. We studied the effect of several hydrodynamic parameters like flow rates, channel width, secondary flows on particle size distribution.

Part B: Segmented flow synthesis of Ag nanoparticles in spiral microreactor

Segmented flow methods in straight channels are known to give narrow size distributions of nanoparticles. To understand the effect of segmentation in curved channels and to understand effect of discontinuity in secondary flows on particles size distribution we carried out the segmented flow synthesis of Ag nanoparticles using kerosene and air as inert phases to generated liquid - liquid and gas - liquid segmented flows. We studied the effect of slug sizes, stagnant zones on particle size distribution. Moreover we tried to understand the effect of segmented flow hydrodynamics on particle size distribution. We carried out the segmented flow synthesis using two microreactors made up of PMMA and SS 316 using kerosene as inert phase and because of the wettability differences in one case reactant phase acts as continuous phase and in other case reactant phase acts as dispersed phase. In curved channel segmented flow generates two wall films with different thicknesses and in spiral thickness of these films continuously changes and we observed that this situation effects the particle size distribution considerably.

Chapter 3:

Chapter 3 has been divided into two parts.

Part A: Surfactant directed synthesis of triangular gold nanoplates: Understanding and optimizing reaction parameters.

Anisotropic noble metal nanoparticles can be synthesized by using seed mediated, polyol method, biological processes etc. These well known synthetic methods suffer from limitations like, using low reactant volumes, nature and quality of seeds, batch to batch reproducibility etc. One of the relatively fast method to synthesize Au nanoplates is using surfactant methods. Surfactant directed methods to synthesize

Au triangular nanoplates are known to give high percentage yield of triangles within short time. This process involves reducing $HAuCl_4$ using trisodium citrate under thermal conditions in presence of surfactant like CTAB. Haung et al reported that the edgelength of the triangles is sensitive to volume of the reactant used. Formation of these two dimensional triangular nanoplates is kinetically controlled process so we believe that temperature and heat transfer can affect the yield and edge length of the triangles considerably in these methods. To understand this we carried out the synthesis of triangular gold nanoplates in flat bottom jacketed batch reactor by varying the temperature at which the nucleation starts. We observed that yield and edge length of the triangles gets affected by the initial nucleation temperature and time span to reach final reaction temperature. Our observation reveal that, to get the maximum yield of kinetically controlled Au nanoplates initial nucleation rates should be low enough and the system has to be maintained for enough time at low nucleation rates.

Concentration of CTAB is another parameter which can control the yield of the triangles. So reaction was carried out at different CTAB to $HAuCl_4$ molar ratios. When this ratio is beyond 24, we did not observe any nanostructure formation. Depending upon the micellar charge stabilization, when CTAB is used above CMC it releases Br^- ions and these can change the nature of the complex, finally decreasing the rate of reaction. To understand this we replaced CTAB with HBr and carried out the same procedure and we observed that Br^- acts as shape directing agent.

Part B: Continuous flow synthesis of triangular gold nanoplates

The optimized batch process parameters used to synthesize triangular nanoplates was extended to synthesize the triangles in continuous flow methods. PTFE helical coil was used as microreactor. Temperature profiles calculated at different reaction temperatures showed that, temperature reached to maximum value within 1-2 sec. From the batch process results it is known that this situation is unfavourable to get maximum yield of the triangles. This limitation can be overcome by maintaining a temperature gradient along the length of the reactor or by decreasing the feed of the citrate. Decreasing the flow rate ratios of citrate to Au-CTAB solution from 1.5 to 1,

helped to improve the yield of the triangles and further decreasing the rate to 0.5, we observed lot of reaction intermediates indicating that the reaction is uncomplete.

Chapter 4: Continuous flow synthesis of nanocrystalline MgO using Jet micromixer

Nanocrystalline MgO (NC-MgO) is very good catalyst and destructive adsorbent for poisonous gases. NC- MgO with high surface area can be synthesized using sol gel process. This process involves the hydrolysis of metal alkoxide in presence of its parent alcohol. Hydrolysis of $Mg(OCH_3)_2$ is very rapid and forms a rigid gel within seconds. In these kind of reactions mixing should be faster than the rate of reaction and solid gel formation should not block the channel. Jet micromixer, where the two jets come and meet outside of the micromixer satisfy the above condition and it is used to synthesize NC- MgO.

We studied the effect of angle between the two jets and effect of flow rate on the surface area of the material. High speed camera was used to calculate the thickness and area available for mixing zone and to understand its effect on the surface area of the final material.

Chapter 5: Conclusions and future directions:

This chapter presents an overall summary of the work described in the previous chapters in terms of achievements to develop continuous flow methods for materials processing. Further directions about the opportunities and challenges in this area to synthesize much complex and functional materials by continuous flow methods have been presented.

Table of Contents

List of Figures

List of Tables

Chapter 1

Introduction

1.1 Introduction:

The buzz word "NANO" does not need any introduction even to the common man of 21st century. Nanomaterials (any one of the length dimension is 1-100 nm) which behave differently from their bulk counterparts, have several applications in various areas. The properties and hence the applications of nanomaterials are sensitive to their size and shape.[1] Figure 1.1 displays some of the property changes observed due to nanosizing and their applications.

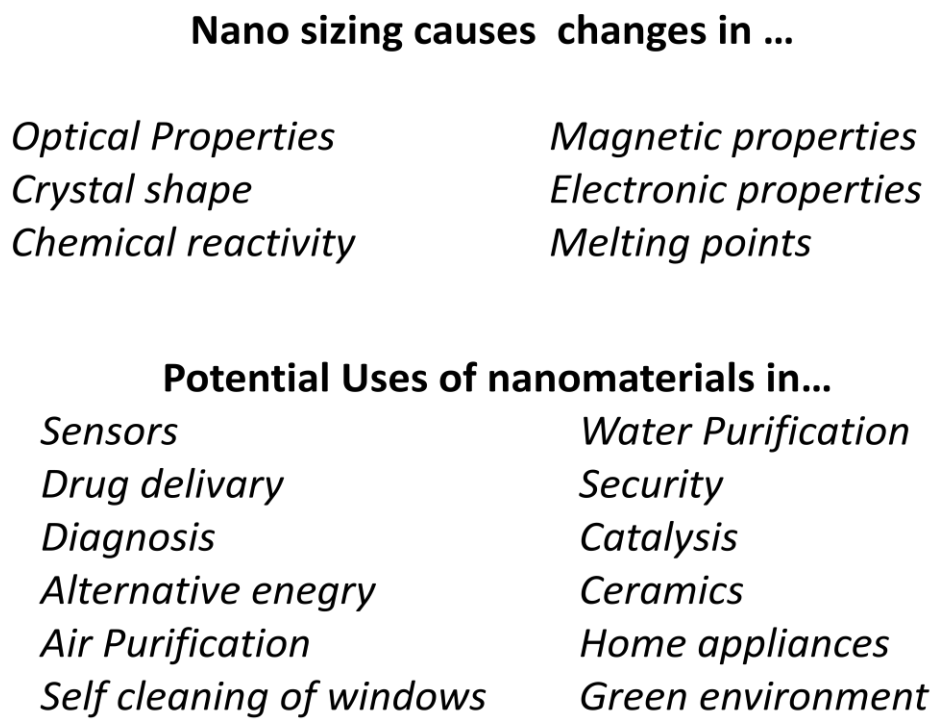

Figure 1. 1: Properties and applications of nanomaterials (taken from Ref.1).

One can notice that, they are widely used in home appliances, consumer products, construction industry, health care, green environment, alternative energy production etc.,[2-4] Nanotechnology based products hold multibillion US $ market and expected to reach trillion US $ market by 2015.[5] Table 1.1 shows some of the widely used nanomaterials, their applications and companies.

Table 1. 1: Commercially available Nanoproducts

Product	Applications	Manufacture company
Gold nanoparticles, nanorods and wires	R&D, Drug delivery, Catalysis	Sigma- Aldrich, USA; Nanopartz, Metal nanopowders Ltd.,Nanotecture Ltd,UK.,
Silver nanoparticles	Anti microbial applications, home appliances	Sigma-Aldrich,USA., Metal nanopowders Ltd,Nanotecture Ltd, UK
TiO_2	Photocatalysis, R&D, Sunscreens, lotions and coatings	Sigma-Aldrich, Nanoamor, Degussa
MgO	Catalysis	Sigma- Aldrich; Nanoscale Corporation, USA
Fe_3O_4	Data storage devices	Sigma- Aldrich,Nanoamor Inc.,
Carbon nanomaterials	Super capacitors, Electrochemistry	Sigma- Aldrich; Nanoshel, USA
Platinum nanoparticles	Fuel cells, Catalysis	Sigma -Aldrich
Quantum Dots	LEDs	Invitrogen, Nanotechnologies Ltd. UK

Figure 1. 2: Some of the nanomaterial based consumer products (www.nanotechproject.org/inventories/consumer/browse/products).

For many of the above stated applications, nanomaterials have to be produced in large quantities and highlighting the importance of their bulk synthesis. Among the several methods of nanomaterial syntheses, wet chemical methods or liquid phase syntheses are promising methods for the size/ shape controlled synthesis of nanomaterials.[6]

1.2 Wet chemical synthesis of nanomaterials:

Wet chemical synthetic methods which are generally referred as bottom – up methods, have great control in the shape and size selectivity of nanomaterials than the other methods of nanomaterials production like top down (physical methods) or biological syntheses routes. Reductions, precipitations, sol gel processes, hydrothermal/solvothermal methods, microemulsion based methods, thermal decompositions, template assisted routes are some of the widely used methods for the synthesis of inorganic nanomaterials.[7] [8]

Metal nanoparticles are generally synthesized by the reduction of metal precursors in presence of surfactants/ligands. Formation of metal nanoparticles generally occurs through nucleation and growth processes. Separation nucleation and growth processes by successful manipulation of relative rates of nucleation and growth, controlling the equilibrium shape of the nuclei and by using surfactants provide great control on the size and shape of the metal nanostructures.[9] Sol gel process involves the hydrolysis of metal alkoxide precursors in presence of its parent alcohol. This process is well known for the synthesis of metal oxides. Here also the formation of nanostructures occurs through two processes, hydrolysis and condensation followed by controlled drying and thermal treatment.[10] Successful manipulation of gelation kinetics can be achieved by varying the solvents, pH, temperature, catalysts, chelating agents and this helps to tune size and properties of nanostructures. These laboratory based wet chemical methods are successful to synthesize various nanomaterials with high size and shape control, but they have serious limitations when they are extended to the large scale synthesis using conventional batch reactors.

1.3 Limitations of batch processes:

In general, chemists carryout the reactions in standardized glassware called as batch reactors. The same procedure has been practiced from the ancient times and novel process intensification methods are not implemented till recent years. Scale up methods, using batch processes involve the usage of reactors with large volumes and which are associated with their own drawbacks. For the scale up of any reaction, mixing plays an important role in deciding the conversions, yields and quality of the products. In batch reactors the mixing can be carried out by mechanical agitation by the use of impellers. Hence the quality of mixing depends on the shape and size of the impeller used, which varies from size of the batch reactor and the stirring rate. Moreover, uniform mixing can not be expected throughout the large scale batch reactor and this variation increases with increase in reactor size.[11] This situation is unwanted for the large scale production, especially in case of nanoparticle synthesis where the reproducibility and the uniform size distributions are highly desired. Figure 1.3 shows the mixing of a fluorescent dye (rhodamine G) in 20 L capacity batch reactor under laminar flow conditions, after few minutes of the mixing, the segregated regions clearly demonstrating the limitations of mixing in batch reactor.[12] Nature of addition of reagents, geometry of the reactor used for the scale up, reaction workup, managing the wastes are some of the associated problems with scale up synthesis in batch reactors. Large scale batch reactors require huge space for the plant operation and it is difficult to replace the reactor with new design. Reactions which occur at high temperatures (thermal decompositions) are widely used in the syntheses procedures. The reaction kinetics and nucleation rate highly depends upon the local temperature and heat transfer rates.

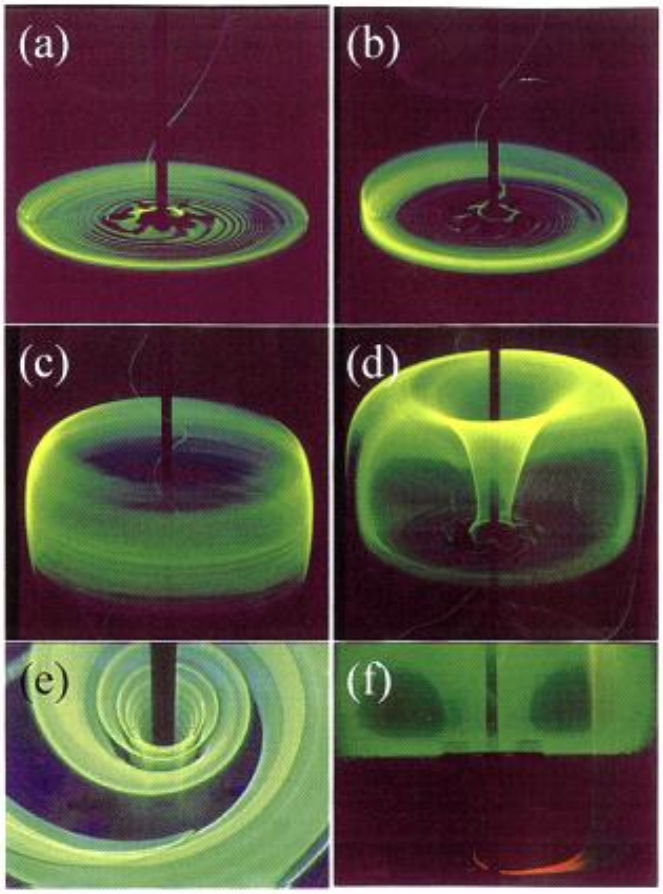

Figure 1. 3: Pictures of fluorescent dye dispersions in stirred tank after (a) 3 (b) 5 (c) 10 and (d) 30 sec of mixing (e) helical ribbons observed after 3 minutes of mixing and (f) shows the segregation of dye in upper part of the tank (taken from Ref.12).

In typical synthesis of nanoparticles by reduction, the nucleation becomes homogeneous at higher temperatures. Similar to mixing, here also the heterogeneity in temperature exists in batch reactors and it is difficult to quantify the effect. This heterogeneity finally may result in broad size distribution of particles. Similarly, in exothermic processes, it is difficult to maintain the batch reactor system in nearly isothermal condition and this drives the situation to unsafe conditions. Safety is another major limitation of scale up of batch processes. As it involve the addition of larger volumes/quantities of the reactants at different time scales, the unstable and explosive reactants and reactant intermediates may cause safety issues regarding the scale up. In this scenario, new process intensification methods like continuous flow process methods using microreactors attracted the attention of process chemists in recent years. Microreactors, often require very less space than the batch counter parts and can be easily replaced by the reactor of our interest. Continuous flow operations of microreactors always allow great control over the mixing, flow rates and temperature. Reactant volumes, energy can be efficiently used, reactions can be optimized by using very low volumes of reactants, and the production of waste can be minimized effectively. Hence it can be realized that, continuous flow methods offer great advantages and successfully overcome the limitations of batch reactors mentioned above.

1.4 Microreactors:

1.4.1 What are microreactors:

Microreactors, in general can be defined as miniature reactors with channel dimension varying from few hundreds of microns to few millimeters and with volume capacity of few μL to mL. Unlike conventional batch reactors, microreactors can be operated in continuous manner. Reaction progress occurs along the length of the microreactor in contrast to time scale progression in conventional batch reactors. Because of its dimensions, microreactor contain high surface to volume ratio. In general, if we compare the surface to volume ratio of the 250 mL round bottom flask and microreactor with channel 0.4 mm × 0.4 mm channel, the value is nearly 100

times higher. Figure 1.4 compares the microreactor used for the flow synthesis and simple glass vial with magnetic stirrer bar which can be used as batch reactor.[13]

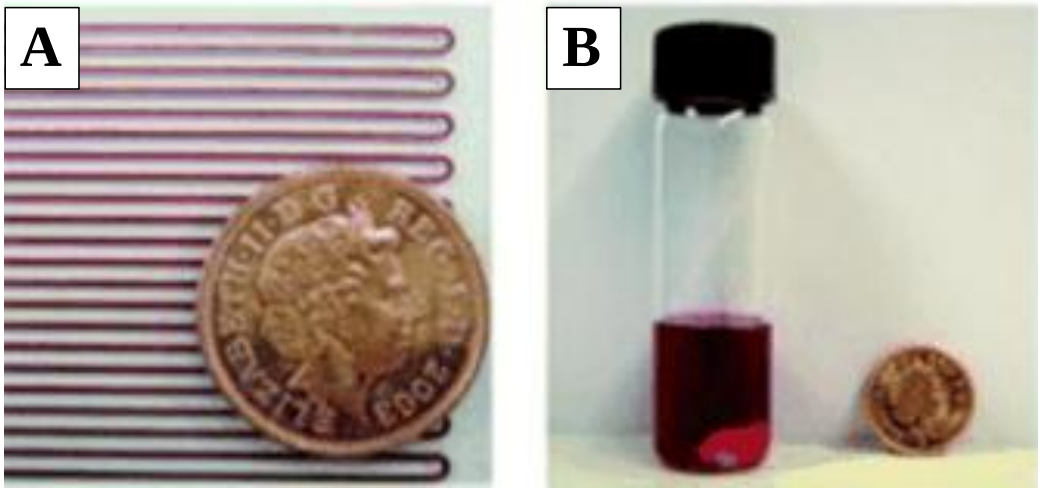

Figure 1. 4: (A) Microreactor and (B) Sample vial with magnetic stirrer bar which is a batch reactor (taken from Ref.13).

In general microreactors are operated at flow rates such that the flow regime is laminar (Reynolds Number Re<2000). Here the viscous forces are prominent in than the inertial forces and mixing is dominated by diffusion. In a channel of few micron dimensions, diffusion dominated mixing is prominent and takes very few seconds along the width of the channel. As mentioned earlier because of their high surface and volume ratios, heat transfer in micro channel is very fast and hence the reactions which involve thermal reductions can be carried with better yields. Moreover, in exothermic reactions, the heat generated during the reaction can be taken care of easily and more safety can be assured.

1.4.2 Fabrication:

Depending upon the (i) requirement of the reaction, (ii) compatibility of the reactants with reactor material and (iii) the experimental condition at which the reaction has to be operated to get better yields, materials to fabricate microreactors have to be chosen. In addition to this, simple tubular reactors of different materials

like SS 316, PTFE and silicone can also be used as microreactors for wide range of reactions. Fabrication technique generally depends upon the reactor materials. Wet chemical etching is one of the widely used and cost effective microfabrication technique, which is generally used for silicon and glass.[14] Glass microreactors, which are widely used for their optical transparency can be fabricated by using HF as chemical etchant.[15] In addition to this, photolithographic techniques, reactive ion etching, plasma etching, laser lithographic techniques can also be used for the glass and silicone microreactor fabrication.[15] Wet chemical etching method cannot be employed for wide range of metals, so micro machining is the widely used techniques for the fabrication of microreactors using metals and alloys.[16] Mechanical micromachining can also be used to fabricate ceramic microreactors in addition to the conventional moulding techniques.[17, 18]Fabrication of microreactors from ceramic materials mandates that the grain size should be atleast one order of magnitude less than the smallest dimensions of the device. This helps in avoiding the reduction in channel dimension that may during the sintering.[15, 19] It is very easy to fabricate the microstructures using polymeric materials. Micromachining, laser ablation, soft lithography are some of the widely used techniques for the microfabrication using polymer materials. PDMS is one of such polymeric materials which can be widely used for microreactors and because of its elastomeric nature micro patterns can be easily designed on PDMS using soft lithographic techniques.[20] Like glass microreactors, the optical transparent nature of the most of the polymeric materials is well suited for the wide range of applications. Since the polymers undergo deformation at high temperatures and pressures, it is not advisable to use them for such reactions.

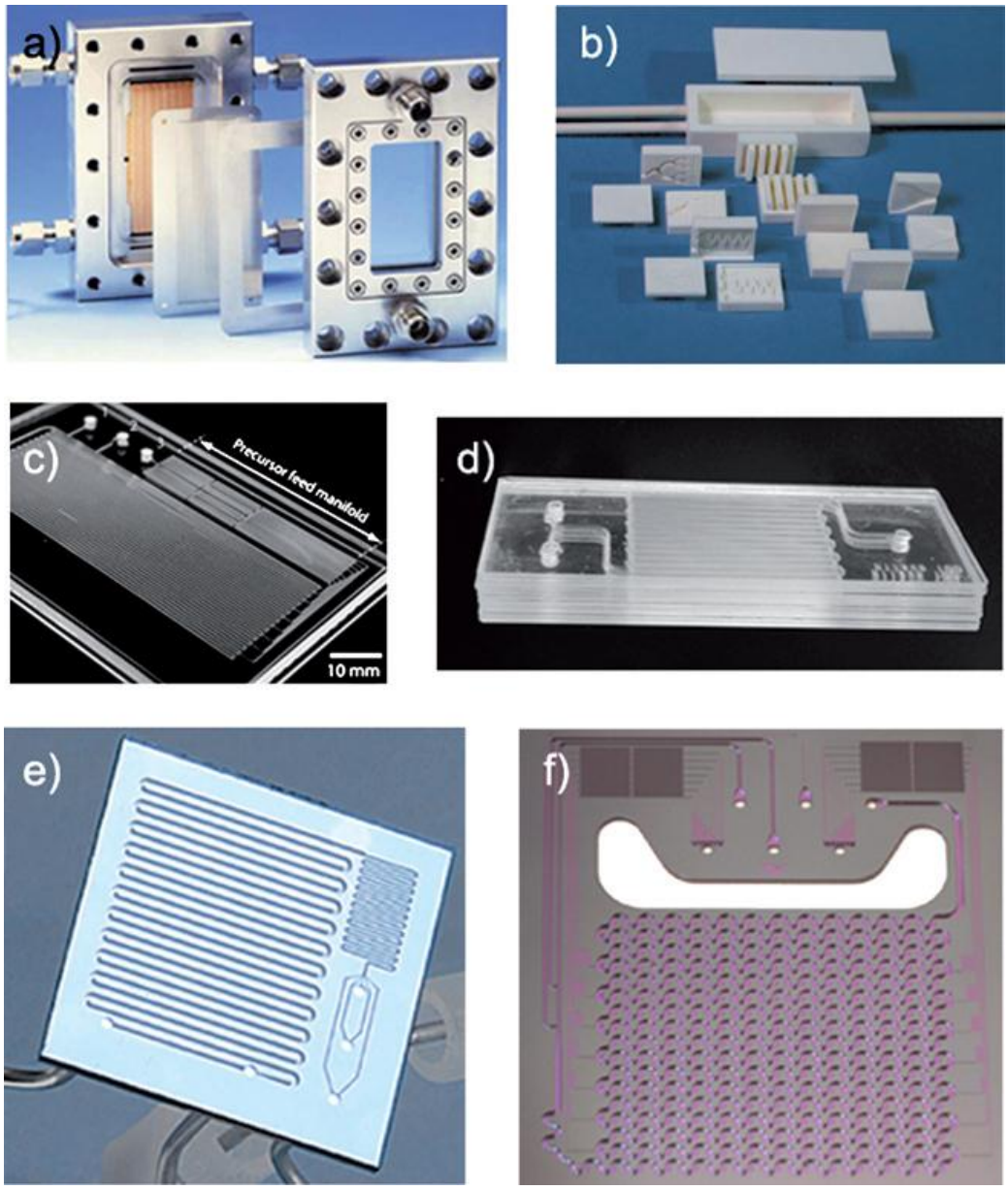

Figure 1. 5: Photographs of the microreactors fabricated in different materials (a) metal (b) ceramic (c) glass (d) PDMS and (e,f) silicon (taken from Ref. 16).

1.4.3 Continuous Flow Operation:

Microreactors, unlike in batch process, can be operated in continuous flow conditions. In addition to microreactors, several components are required for the continuous flow operation.[15] Figure 1.6 shows the schematic of a continuous flow

synthesis. Here, the reactant fluid can be manipulated through the micro channels with the help of pumps and valves. Syringe pumps, peristaltic pumps and gear pumps are some of the widely used pumps depending upon the flow rate required. In addition to this, fluid flow in micro channel can be controlled by electro osmatic, electro chemical, electro hydrodynamic, acoustic, magneto hydrodynamic micro pumps.[21] Microreactors are connected to other components of the continuous flow system (like pumps, in line analysis, sample collection) using standard fittings and tubing.[22] Micromixers are the other important components of the flow system which can be generally categorized as active and passive micromixers. Simple Y-micromixers, T-micromixers are called as passive micromixers. They do not require any additional force other than pumping. Active micromixer involves the usage of external force. Acoustic, piezoelectric, ultrasonic, magnetic and electric fields can be applied to get the enhanced mixing.[22] In addition to the above described components, flow system generally requires the integration of temperature sensors like thermocouples, optical/ electrochemical sensors, inline spectrometers for monitoring the reaction progress, detection and analysis of the compounds. It should be noted that, very broad picture of general components of the continuous flow system are described here. Depending upon the requirements, system and reaction the flow system may require more components to develop efficient process chemistry.

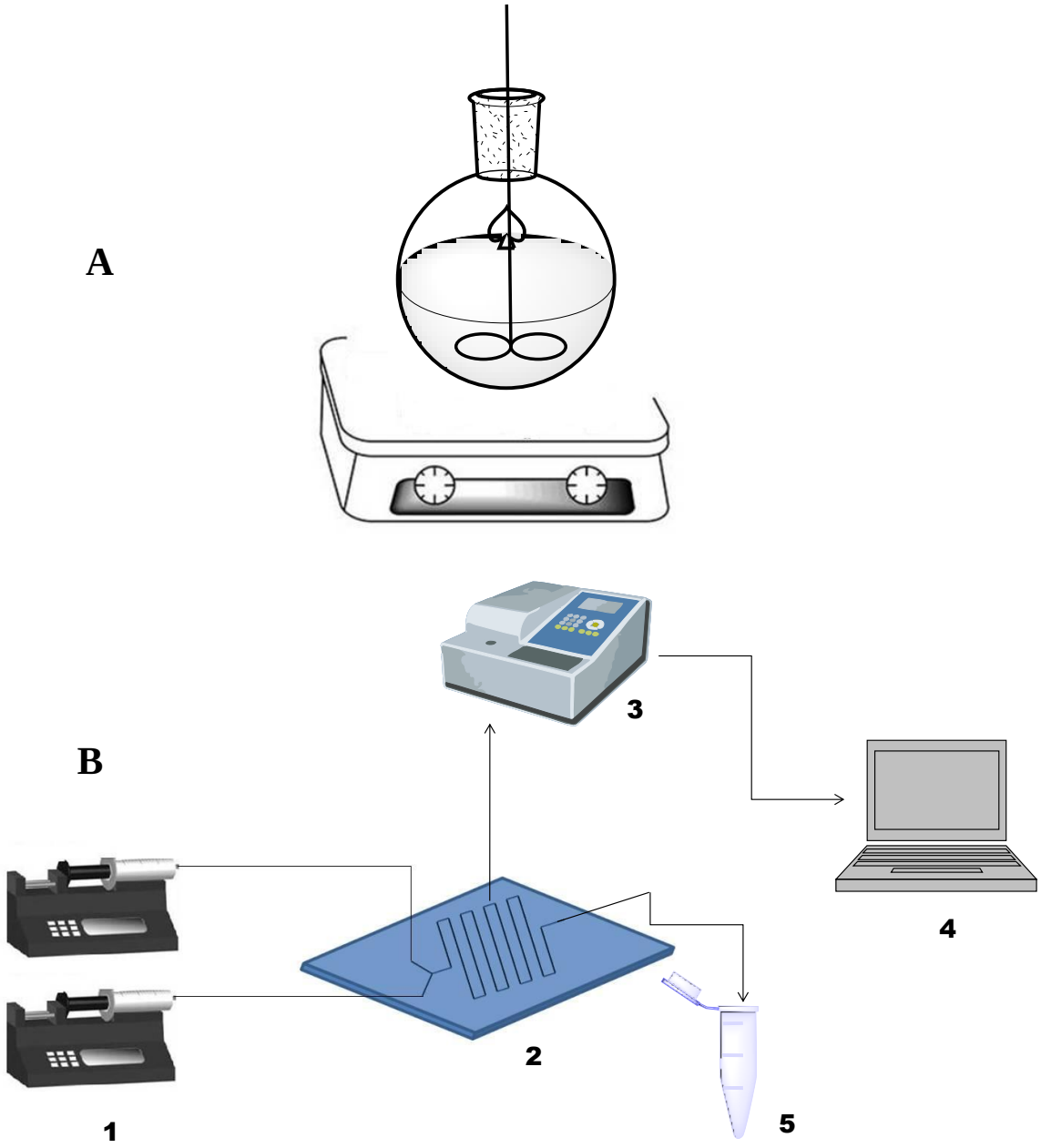

Figure 1. 6: Schematic of (A) batch and (B) continuous flow processes with different components like (1) syringe pumps (2) microreactor (3) inline analyzing system (4) data collection and (5) sample collection.

1.4.4 Impact of microreactors on organic process industry:

Any process intensification methods of a reaction should take care about the (i) efficient mixing of reactants (ii) dissipation of heat generated during the reaction (iii) minimization of waste etc. In this scenario, microreactors can improve the efficiency of many industrially important organic reactions.[23, 24] In addition to the process efficiency, combinatorial synthesis, atom efficiency which are important in terms of pharma industry perspective[25] can also be practiced and improved by micro reactors. In this premise it is not surprising to see that, most of the well known organic reactions such as Aldol,[26] Wittig,[27] Dies- Alder,[28] Coupling reactions,[27] additions,[29, 30] eliminations,[31] aliphatic substitution reactions, cyclo additions[28] are now being carried out in microreactors by process engineers/ chemists with improved yield and enantio/ regio selectivities than the batch reactors.[27, 32]

For example, diazotizations of aromatic amines which are industrially important reactions, are difficult to handle because of the explosive nature of diazonium salts.[33] Similarly, nitrations of organic compounds[34] involving the usage of corrosive nitration mixture (mixture of con. H_2SO_4 and HNO_3) can be easily handled by the flow methods assuring more safety and sustainability even at the scaled up conditions. Due to the high exothermic nature of the reaction, nitration reactions in batch are operated at very low temperatures around -20 °C. Enhanced heat transfer rates in microreactors are allow the same reactions to be carried out at room temperature with improved selectivity.[35] Microreactors are very much suitable for the multi phase reactions because of the large interfacial areas available. In general the interfacial areas in micro channel reactor are very high (any where from 10,000 m^2/m^3 to 50, 000 m^2/m^3)[36] than the conventional batch interfacial areas; typically ~100 m^2/m^3. Higher interfacial areas facilitate the mass transfer of the two reactions at interface and hence improved reaction efficiency can be expected. For example, Koyabashi et al., designed and used multiphase microreactor for hydrogenation of various organic compounds over the Pd catalyst surface.[37] The reaction happens at the gas (Hydrogen), liquid (organic reactants) and solid (catalyst) interface and almost pure products were collected at the outlet continuously. Direct fluorination reactions of aromatic compounds and their scale up

which is unsolved problem in batch process have been successfully made continuous using micro channel reactors.[38] Jahnisch et al., carried out the direct fluorination of toluene in micro bubble column reactor and falling film microreactors with reasonably good conversion and selectivity yields than the batch processes.[36]

1.5 Synthesis of nanomaterials in microreactors:

1.5.1 Continuous flow synthesis:

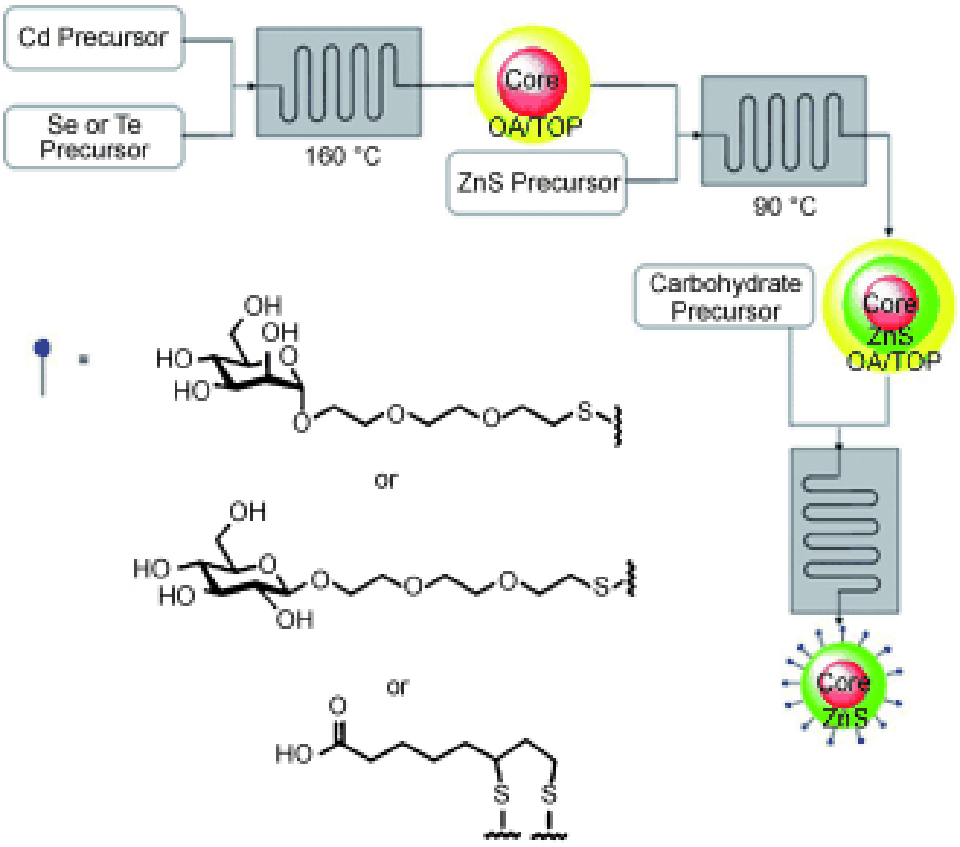

Figure 1. 7: Schematic of the continuous flow synthesis of functionalized quantum dots (taken from Ref.48).

As the potentiality of the microreactors in the organic process industry being recognized, the usage of microreactors for the nanoparticle synthesis started around 2002.[39] Significant variations in the quality of the nanomaterials (in terms of size and shape distributions, which affect the properties of those materials) from batch to batch demand the "intelligent routes" to synthesize the nanomaterials[40] with more quality assurance. As a part of understanding the efficiency of microreactors, few research groups compared the synthesis of nanoparticles by batch and continuous flow methods and the size distributions of the nanoparticles obtained.[41, 42]

deMello and coworkers prepared the CdS nanoparticles using $Cd(NO_3)_2$ and Na_2S as cadmium and sulphide precursors by microfluidic methods.[39] Properties of quantum dots are ultrasensitive to their size variations and their synthetic procedures generally involve high temperature conditions. Advantages of microreactors in maintaining the uniformity in temperature resulting in rapid homogeneous nucleation leading to narrow size distributions (which is very crucial in case of quantum dots) attracted the attention of several research groups.[43-47]. Ligands/ surfactants are widely used in nanochemistry to give enough stability and improved shelf life of the synthesized nanoparticles. Seeberger and coworkers developed the continuous flow synthesis of quantum dots by their in - situ functionalization by variety of sugar molecules.[48] The functionalized quantum dots could then be readily used for the biological applications (figure 1.7).

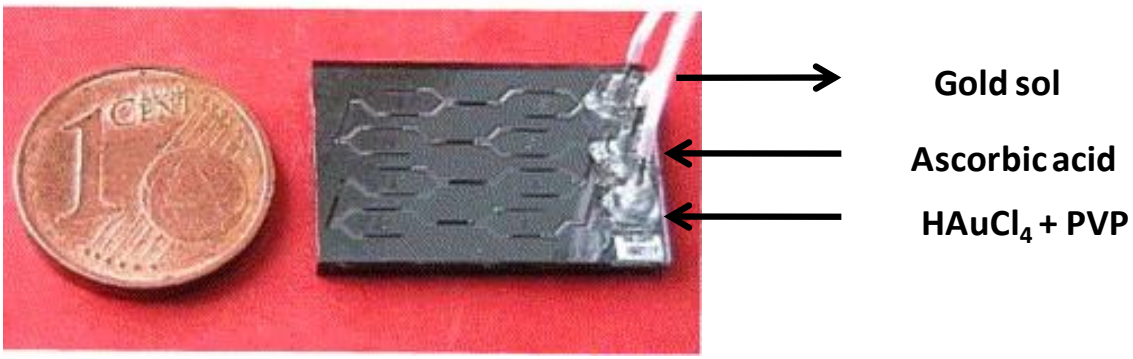

Figure 1. 8: Microfluidic chip used for the flow synthesis of gold sol (taken from Ref.50).

Lin et al., reported the continuous flow synthesis of Ag nanoparticles using thermal decomposition of Ag precursor.[49] Similarly Au nanoparticles were synthesized by continuous flow method by Wagner et al., by reducing $HAuCl_4$ with ascorbic acid and PVP. [50, 51]

Later on continuous flow synthesis noble metal nanoparticles was reported by several groups and most of the methods involve the synthesis of nanoparticles by the reduction of metal ions.[52-58] Superior control on the manipulation and additions of the reagents by microfluidic methods offer great advantages to get control over the particle sizes. Using this advantage, Sugano et al., synthesized the Au nanoparticles of several sizes by using pulsed microfluidic system.[59] In very recent years, by usage of microfluidic systems reached advance level and stable metal nano clusters were successfully produced by continuous flow methods.[60, 61]

Further, the continuous flow methods using microreactors were extended to synthesize variety of materials like transition metal nanoparticles,[62, 63] Zeolites,[64] metal oxides,[65, 66] silica,[41, 66] core shell structures,[56] polymers[67] and so on. Here, in table 1.2 we summarize the some of the important reports on the continuous flow synthesis of nanoparticles using microreactors. Although there are several inorganic and polymeric materials reported by continuous flow methods, we restrict ourselves to inorganic nanomaterials.

Table 1. 2: Summary of the literature reports on the continuous flow synthesis of nanomaterials.

Author & Year	**System Studied**	**Microreactor details Channel width (W), Length (L)**	**Conditions Flow rate ~ (Q µL/min) Temperature ~ (T)**	**Observations Particle size (d_P)**
Kawa et al., 2003[46]	CdSe	SS tube 4.2 mm i.d.	Q ~ of TOPO is 42.4 mL/min; Cd/Se stock solution 17.6 mL/min	d_P < 10 nm
Yen et al., 2003	CdSe	W = 0.25 mm	T ~ 180 - 320 ^{0}C Residence time 1-15 min	d_P ~ 1.52 - 2.7 nm
Wagner et al., 2005[51]	Au	No details on the channel width	Q ~ 10 - 50 µL/min	d_P ~ 11.8-23.7 nm
Lin et al.,2004[49]	Silver	L (immersed in oil bath) = 20 cm, i.d = 0.84 mm	Q ~ 0.08 - 0.7 mL/min T ~ 110-140 ^{0}C	d_P ~ 8.7-5.6 nm
Khan et al.,2004[41]	Colloidal Silica	L = 40 mm W = 0.05 mm	Q ~ 2 - 20µL/min	d_P ~ 10nm-1µm
Wagner et al., 2004[54]	Gold	W = 0.178-0.7 mm	Q ~ 0.5 - 8 mL/min	d_P ~ 5-50nm
Shalom et al., 2007[68]	Thiol capped Gold	W = 0.15 mm	Q ~ 0.4-0.8 mL/min	d_P ~ 2.9-4.9 nm
Song et al ., 2006[63]	Co	Polymeric microfluidic reactor W ~ 150-400µm	Q ~ 0.08, 0.9 mL/min,	Different phases of Co NPs were synthesized by varying the flow rate and quenching time
Kohler et al., 2007[56]	Au-Ag	Glass channels W = 0.5-0.3 mm L = 10 mm	Q ~ 20& 50 µL/min	Results star like core shell type Au/Ag nanoparticles , d_P ~ 80 - 120 nm
Kohler et al., 2008[55]	Au-Ag	W ~ 0.2 -0.7 mm	Q ~ 5µL/min - 5 mL/min	Metal nano particles of various composition

He et al., 2008[52]	Ag	PTFE capillary tube L = 200 cms and 0.3 mm i.d.	Q ~ 70.7, 28.2, 14.2 mL/min	d_P ~ 4.8 - 8.1 nm
Huang et al., 2008[53]	Ag	Microreactors of three different i.d 5, 3, 0.5 mm	Q ~ 0.5 - 1 mL/min T ~ 90 ^{0}C	d_P ~ 10.5 - 23.3 nm
Tsunoyama et al.,2008[69]	Au clusters	Micromixer made of Hastealloy	Q- 200 mL/h	PVP capped Gold nanoclusters of size< 2nm were synthesized.
Wen-Ben Lee et al., 2009[70]	Iron Oxide	PDMS micromixer of Two different channels (inner&outer) of W ~ 974 & 724 µm	Q ~ 300 - 640 µL/min	d_P ~ 4.83-5.24 nm
Song et al., 2010[71]	Fe	Simple Y-micromixer	Q- 80µL/min	d_p ~ 4-6 nm
Gomez-dePadro et al., 2010[72]	Au	Ceramic micro reactor. 120 × 150 µm	Q of $NaBH_4$ 1 µL/sec; Q of $HAuCl_4$ 2.5 µL/sec	d_P ~ 2 - 6 nm
Gutierrez et al.,2011[42]	Silica	Slit interdigital micromixer followed by reaction tubing	-	d_P ~ from 50 nm -150 nm
Hossain et al., 2011[73]	Pt	Channel width 50 µm and depth 150 µm	Q – 200 mL/h	d_p ~ 1-6 nm
Jun et al., 2012[74]	Au	Three different micromixers were compared	Q ~ very high(20mL/min) and low flow rates(100 µL/min) were used to synthesize the particles	d_P ~ 20 - 5 nm
Ftouni et.al., 2012[75]	Au	Fused silica capillary of i.d 0.2 mm and length 1.5m	60 – 80 µL/min	d_P ~ 1-4 nm
Biswas et al.,	Cu	Channel width 2	At different	Ultra small

2012[61]	nanoclusters	mm, depth 125 μm and length 14 cm	flow rates varying from 6.81 mL/h to 51.4 mL/h	Cu clusters of Size < 2 nm
Shovel et al., 2012[76]	$Cu_2Zn\ SnS_4$	Bronze tube of length 1m and i.d 3 mm	Q-1-5 mL/min	d_p ~10 nm

1.5.2 Segmented/droplet flow synthesis:

In general, microreactors operate under continuous flow conditions in laminar flow regime, in which the velocity profiles are parabolic (figure 1.9) and mixing is dominated by diffusion.[77] Hence, the velocity of the fluid in the middle of the channel is high and it becomes zero at the channel walls. In chemical reactions, which involve particle formation (like nanoparticle synthesis) this situation allows the particles to grow at the walls and leads to broadening in size distributions.[41, 78] In addition to this, continuous operation of the reactor often leads to fouling.[54] The above limitations can be successfully overcome by switching the flow patterns to segmented flow or droplet flow.[79, 80] To generate segmented/ droplet flow an inert, immiscible fluid can be used in the flow direction of reactant fluid.[81] Depending upon the contact angle of the inert fluid and reactant fluids with the channel, one fluid acts as continuous phase and another fluid acts as dispersed phase.[82] Differences in physical properties of both the reactant phase and dispersed phases, flow rates,[83] channel width and geometry[84] and mechanism of droplet formation[85, 86] play major role in controlling the size of the segment or droplet of the reactant phase.[87] Figure 1.10 shows the schematic of the segmented and droplet flows.

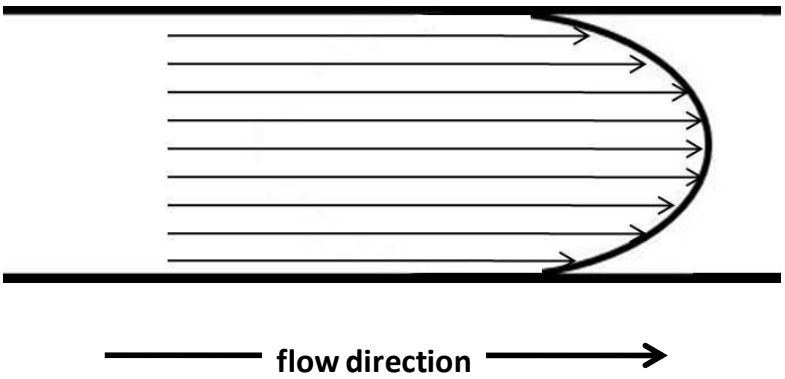

Figure 1. 9: Schematic of parabolic velocity profile in the micro channel.

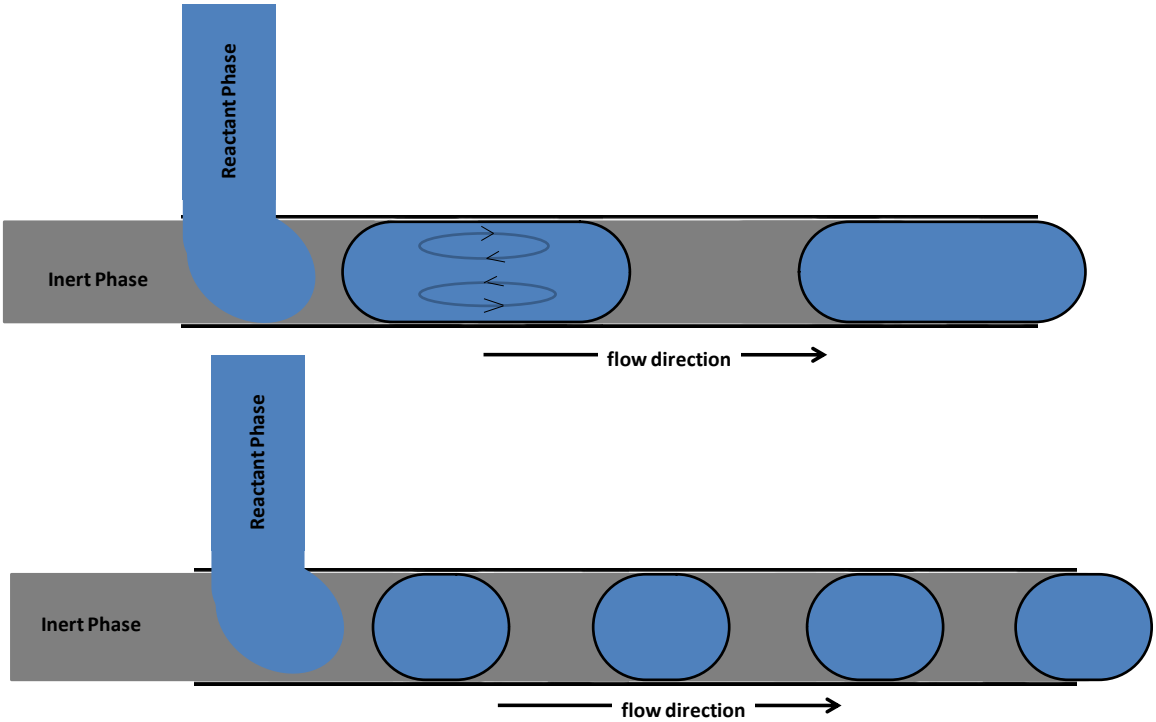

Figure 1. 10: Schematic representation of segment and droplet flow in micro channel.

Unlike in homogeneous continuous flow, in segmented flow mixing occurs by convection and the problem of axial dispersion can be completely eliminated. Synthesis of nanoparticles through segmented flow methods offers great control on the particles size and facilitates the analysis/characterization of single segment/ droplet while the reaction is in progress.[88, 89] This offers way to understand/establish the mechanism of nucleation and growth of nanoparticles. Synthesis of nanoparticles by segmented flow methods initially reported by Yen et al.,[78](CdSe) and Khan et al.,[41] (silica) with very narrow size distributions. Very recently, deMello and coworkers[90] demonstrated the efficiency of droplet reactors for the large scale production of nanomaterials. The concept of scaling out with microreactors was successfully adopted by splitting the highly concentrated metal precursor into several PTFE tubes with the combination of inert phase. The continuous operation of droplet reactor led to the production of ~55 g of CdTe without any fouling even after operating the reactor for 9 hours (figure 1.11).

In addition to this variety of nanoparticles were synthesized in segmented flow methods[91] and the significant reports are summarized in table 1.3.

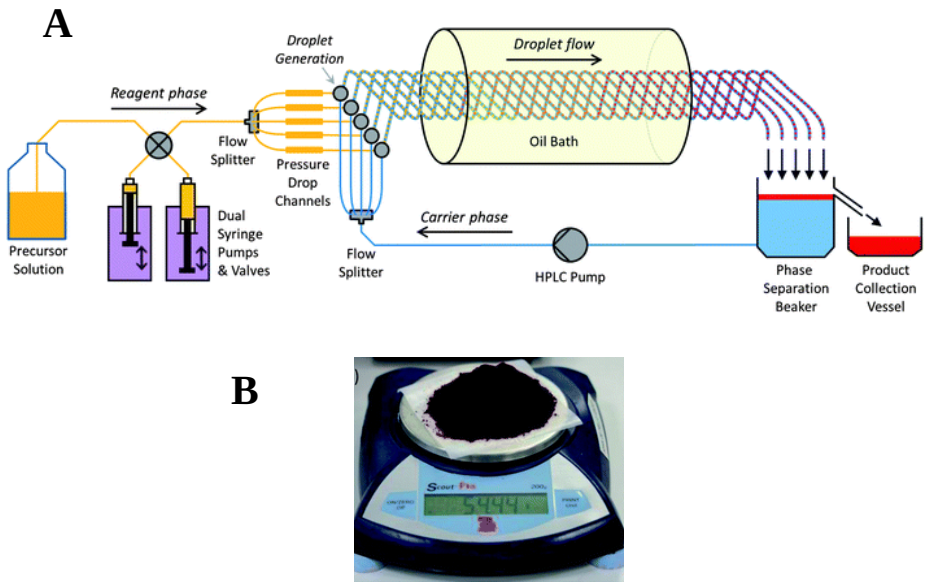

Figure 1. 11: (A) Schematic of droplet reactor for the large scale synthesis of CdTe nanoparticles. (B) Dry powder of CdSe obtained after continuous operation of droplet reactor for 9 hours (taken from Ref. 90).

Table 1. 3: Summary of the literature reports on the segmented/ droplet flow synthesis of nanomaterials.

Author & Year	System	Microreactor specifications$	Flow rates (μL/min)#	Observations
Li et al.,[92] 2008	$BaSO_4$ nano-particles	T-junction micro channel device of PMMA square cross section main channel 1000 μm size and dispersed channel of W = D = 200μm	1) Q_C = 50, Q_d = 5 2) Qc = 60, Q_d =10 3) Qc = 60, Q_d = 20 4) Qc = 40, Q_d = 30 5) Qc = 50, Q_d = 20 All the above flow rates were with butyl alcohol as carrier fluid	Aliphatic alcohols with different sulfuric acid concentrations used as carrier phase and $BaCl_2$ solution is dispersed phase.
Khan et al., 2007[93]	Titania shell on colloidal silica	PDMS main reaction channel W = 300μm D = 250μm, L = 2.1m and manifold channels are of W= 40μm D = 250μm and L~ 0.1-0.2m	Q_d = 6 Qc1= Qsilica= 5 Qc2= titania precursor 2.5-5	N_2 used to create segments and reactant form continuous phase.
Khan et al, 2004[41]	Colloidal Silica	Different designs of microreactors were used W-400μm D-150μm L-0.975 and in other design	Q-4-30 Here Q is total flow rate of both gas and liquid phases and flow	Air is used create gas-liquid segmented flow.

		micromixing unit has W-50μm, L-0.056m followed by channels of W-300μm D-200μm and L-2.3m	rates were adjusted such that the ratio is 1:1 and 1:2	
Fernz et al.,2008[94]	Iron Oxide nanoparticles	D = 25μm in PDMS	Qc = 6.6 – 13.2 Qd1 = 0.9 – 9.1 Qd2 = 0.5 – 1.66 Qd1 and Qd2 are the flow rates of aqueous phase reactants which forms dispersed phase	Perfluoro carbon oil with surfactant used as continuous phase
Chokkalingam et al.,[95] 2010	Silica by sol-gel process	D- 120μm W- 160μm L- 0.027m	Qc = 16.2 Qd1 = 19.2 Qd2 = 11.4 Qd1 and Qd2 are the flow rates of aqueous phase reactants which forms dispersed phase	Perfluoro decalin used as continuous phase
Li et al., 2009[96]	ZnO nanoparticles	Combination of T-micromixer and knot micromixers were used	Total flow rates 200,5000	-
Pan et al.,	Zeolite A	Inner tube of stainless steel of	Q_d 133	Paraffin is used as a carrier

2009[64]	crystals	i.d 600 μm Outer tubes(PTFE) of i.d 3000,1500,1000 μm	Q_c 333	fluid.
Hartlieb et al., 2010[97]	Ag nanoparticles	Two different narrow channels of length 2.69 m, 30.48 m and i.d 1590 μm	Flow rates of liquids were maintained from Qc-5000-50000 and H_2 flow rate Qd-5000	Silver nanoparticles were synthesized by reducing Ag ions with H_2 gas using gas-liquid segmented flow method
Cottam et al.,2007[98]	Titania nanostructures	D-60 μm W-100 μm L-0.4m	Qorganic~ 1.2, Qaqueous 0.6	Reaction is between both the phase and Titania nanostructures were obtained.
Yen et al., 2005[78]	CdSe quantum dots	Channels were fabricated on silicon	At different gas to liquid flow rates by keeping flow rates kept constant 2, and at various gas flow rate at constant liquid flow rate of 20	Cd and Se precursors are continuous phase and gas is dispersed phase
Gross et al.,2007[99]	Polymer and nanoparticle doped polymer rods	PTFE tubing of L-2m and i.d between 250μm to 1000 μm	-	Perfluorinated aliphatic solvents
Kohler et al., 2008[100]	Metal nanoparticles with varied	PTFE tubing with T-micromixer	flow rates between 5-4000	Tetra decane used as carried fluid

	composition			
Chan et al., 2005[101]	CdSe quantum dots were synthesized in liquid-liquid segmented flow.	A cross shaped nanojet generator used for drop let formation followed by W-200 μm serpentine channels and L-0.107m of reaction channel.	Two different flow ratios of ODE (dispersed phase)to PFPE(carrier fluid) i.e 0.1:2 & 1:2	Perfluorinated polyether used as carrier liquid
Hung et al., 2006[102]	CdS nanoparticles	Droplet are generated at pitch junctions of different widths (30,40, 50μm) followed by exiting junction and outlet channel.	At different water flow rates silicon oil flow rates varied from 1 - 6	Silicon oil used as carrier fluid

1.5.3 Other functional nanomaterials:

Other than spherical nanoparticles, microfluidc syntheses of other functional nanostructures like anisotropic nanostructures and core - shell particles are very few. The concept of continuous flow synthesis of anisotropic nanostructures like Au and Ag nanorods was first proved by Boleininger et al.,[103] Duraiswamy et al., reported the droplet based synthesis anisotropic Au nanostructures by seed mediated method.[104] Highly viscous silicone oil was used as inert phase. In another report, seedless approach to synthesize gold nanorods was adopted and demonstrated by continuous flow.[105] Lysine, an amino acid was used as shape directing agent for the continuous flow synthesis of biocompatible gold nanorods.[106] Other than rod shaped particles continuous flow syntheses of noble metal nanotriangles were also reported. A mixture of gold precursor, PVP and citrate was pumped through the quartz coil under the illumination of UV light resulted the gold nanospheres and triangles.[107] Ag nanoparticles with decahedron and triangular shapes were synthesized by photochemical methods using PTFE microreactor.[108] Seed mediated, micro segmented flow method was employed for room temperature synthesis of Ag triangular prisms.[109, 110]

Batch processes to synthesis of core-shell nanostructures often result multi core-single shell structures and they are not always reproducible. Microfluidic continuous flow methods, which are highly promising candidates for reproducibility were successfully utilized to synthesize titania shell on silica core,[111] $Au@SiO_2$,[112] $Fe_2O_3@SiO_2$[113] core shell nanostructures.

1.5.4 Other novel flow techniques:

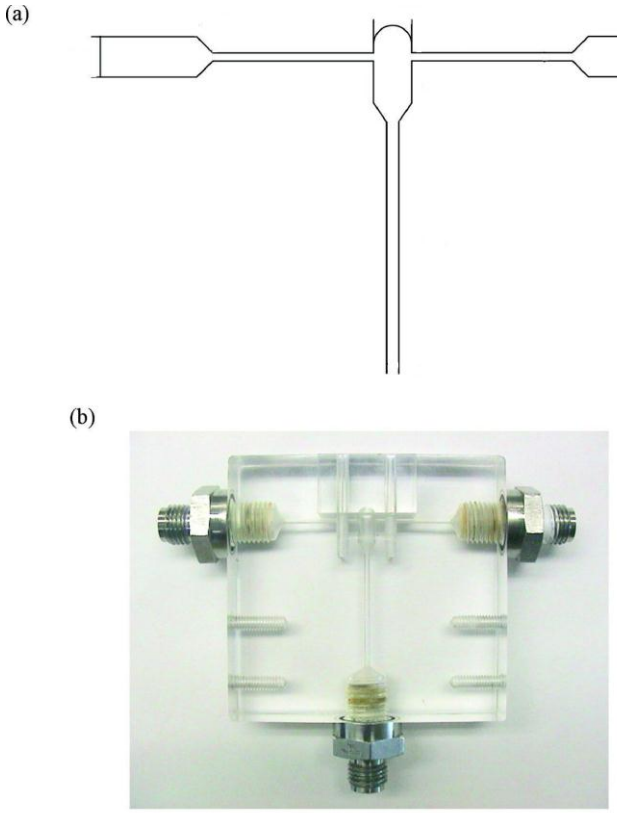

Figure 1. 12: Schematic representation of CIJ and its photograph (taken from Ref. 116).

Precipitation reactions are the one of the widely used procedures for the synthesis of nanoparticles. They often involve the nucleation and growth from super saturated solutions. Hence mixing is very important in these reactions and it has to be faster than the reaction. Like batch reactors, simple micromixers/microreactors can not be

used for this purpose. In order to achieve the rapid mixing which is comparable to time scales of nucleation and growth, confined impinging jet micromixers[114, 115] (CIJs) were successfully employed for the nanoparticle synthesis using fast precipitation reactions. In CIJs two reactant fluid jets come in opposite directions and collide with each other. This rapid collision in shorter residence times, with high velocities and low volume of the reactor lead to great control over the mixing of vary fast reactions.[116] Several nanoparticles like $CaCO_3$,[117] $BaSO_4$,[118] Fe_3O_4[119] which are prepared by precipitation reaction were successfully synthesized using CIJs. Figure1.12 shows the schematic representation of the CIJ.

1.6 Objective and Outline of the thesis:

In the view of increasing in demand for the large scale synthesis of nanomaterials, in this thesis work we aimed the continuous flow synthesis of some commercially important inorganic nanomaterials. This involves the process transformation from the batch to continuous systems and addressing the associated problems. Prior to this, we give paramount importance to the understanding and optimization of the batch process parameters.

Chapter 2 is divided in two parts. In Part A, we study the continuous flow synthesis of functionalized Ag nanoparticles using a biosurfactant, sophorolipid. We used a spiral microreactor for this purpose. Because of the curved geometry of the channel, secondary flows minimize the time variation spent by the particles at the wall region and in the middle of the channel. We studied effect of flow rates, secondary flows, channel cross section geometry and width of the channel on particle size distribution. In Part B, we discuss the segmented flow synthesis of Ag nanoparticles in spiral microreactor using liquid – liquid and gas – liquid segmented flows using kerosene and air respectively. Segmentation of the reactant phase using inert phase leads to the discontinuity in secondary flows and could affect the size distributions considerably. In addition to this, we discuss the role of reactant phase as continuous phase and dispersed phase. Dependence of particle size on film thickness and the problem of diffusion of reactants to the inert liquid phase are also addressed.

Chapter 3 is also divided into two parts. In this chapter we aimed at the flow synthesis of anisotropic noble metal nanoparticles by taking triangular gold nanoplates as an example. In Part A we study the effect of temperature and heat transfer on the edge length and yield of the triangles. In addition to this we study the role of bromide ions as shape directing agents and we establish CTAB less synthesis of triangular gold nanoplates using HBr. In Part B, we demonstrate the flow synthesis of triangular gold nanoplates with and without CTAB. We discuss the role of heat transfer and other process parameters to synthesis the triangular plates in good yield.

In Chapter 4, instead of opting for reduction to synthesize nanoparticles, we chose sol gel process to synthesis commercially important nanocrystalline MgO. Synthesis of MgO through sol gel process involves very rapid gel formation and therefore it is difficult to establish continuous flow routes using simple microreactros. We solve this problem by choosing "wall free" jet micromixer. We study the effect of angle between the jets and Reynolds number (Re) on area and thickness of the mixing zone and finally the BET surface area of the material.

Chapter 5 summarizes the salient features and outcome of thesis work. We also present the possible directions for the future work.

1.7 References:

1. Klabunde, K. J., *Nanoscale materials in chemistry*. Wiley Interscience: New York, 2001.

2. Lee, J.; Mahendra, S.; Alvarez, P. J. J., *ACS Nano* **2010,** *4*, 3580-3590.

3. Salata, O., *J.Nanobitechnology* **2004,** *2*, 3.

4. Lohse, S. E.; Murphy, C. J., *J. Am. Chem. Soc.* **2012**.

5. Aitken, R.; Chaudhry, M.; Boxall, A.; Hull, M., *Occup. Med* **2006,** *56*, 300-306.

6. Cushing, B. L.; Kolesnichenko, V. L.; O'Connor, C. J., *Chem.Rev* **2004,** *104*, 3893-3946.

7. Cushing, B. L.; Kolesnichenko, V. L.; O'Connor, C. J., *Chem. Rev.* **2004,** *104*, 3893-3946.

8. Rao, C.; Matte, H. R.; Voggu, R.; Govindaraj, A., *Dalton Trans.* **2012,** *41*, 5089-5120.

9. Park, J.; Joo, J.; Kwon, S. G.; Jang, Y.; Hyeon, T., *Angew. Chem., Int. Ed.* **2007,** *46*, 4630-4660.

10. Burda, C.; Chen, X.; Narayanan, R.; El-Sayed, M. A., *Chem.Rev* **2005,** *105*, 1025-1102.

11. Hartman, R. L.; McMullen, J. P.; Jensen, K. F., *Angew. Chem., Int. Ed.* **2011,** *50*, 7502-7519.

12. Alvarez, M. M.; Zalc, J. M.; Shinbrot, T.; Arratia, P. E.; Muzzio, F. J., *AIChE J.* **2002,** *48*, 2135-2148.

13. Valera, F. E.; Quaranta, M.; Moran, A.; Blacker, J.; Armstrong, A.; Cabral, J. T.; Blackmond, D. G., *Angew. Chem., Int. Ed.* **2010,** *49*, 2478-2485.

14. Madou, M. J., *Fundamentals of microfabrication: the science of miniaturization*. CRC: 2002.

15. Geschke, O.; Klank, H.; Tellemann, P.; Wiley, J., *Microsystem Engineering of Lab-on-a-chip Devices*. Wiley Online Library: 2004; Vol. 258.

16. Marre, S.; Jensen, K. F., *Chem. Soc. Rev.* **2010,** *39*, 1183-1202.

17. Christian; Mitchell, M.; Kim, D. P.; Kenis, P. J. A., *J. Catal.* **2006,** *241*, 235-242.

18. Knitter, R.; Göhring, D.; Risthaus, P.; Haußelt, J., *Microsyst. Technol* **2001,** *7*, 85-90.

19. Hessel, V.; Renken, A.; Schouten, J. C.; Yoshida, J.-i., *Micro process engineering: a comprehensive handbook*. Wiley-VCH: 2009; Vol. 1.

20. McDonald, J. C.; Duffy, D. C.; Anderson, J. R.; Chiu, D. T.; Wu, H.; Schueller, O. J. A.; Whitesides, G. M., *Electrophoresis* **2000,** *21*, 27-40.

21. Nge, P. N.; Rogers, C. I.; Woolley, A. T., *Chem. Rev.* **2013**.

22. Hartman, R. L.; Jensen, K. F., *Lab Chip* **2009,** *9*, 2495-2507.

23. Mason, B. P.; Price, K. E.; Steinbacher, J. L.; Bogdan, A. R.; McQuade, D. T., *Chem. Rev.* **2007,** *107*, 2300-2318.

24. Jähnisch, K.; Hessel, V.; Löwe, H.; Baerns, M., *Angew. Chem., Int. Ed.* **2004,** *43*, 406-446.

25. Malet-Sanz, L.; Susanne, F., *J. Med. Chem.* **2012,** *55*, 4062.

26. Wiles, C.; Watts, P.; Haswell, S. J.; Pombo-Villar, E., *Lab Chip* **2001,** *1*, 100-101.

27. Fletcher, P. D. I.; Haswell, S. J.; Pombo-Villar, E.; Warrington, B. H.; Watts, P.; Wong, S. Y. F.; Zhang, X., *Tetrahedron* **2002,** *58*, 4735-4757.

28. Fernandez-Suarez, M.; Wong, S. Y. F.; Warrington, B. H., *Lab Chip* **2002,** *2*, 170-174.

29. Kestenbaum, H.; Lange de Oliveira, A.; Schmidt, W.; Schüth, F.; Ehrfeld, W.; Gebauer, K.; Löwe, H.; Richter, T.; Lebiedz, D.; Untiedt, I.; Züchner, H., *Ind. Eng. Chem. Res.* **2002,** *41*, 710-719.

30. Wiles, C.; Watts, P.; Haswell, S. J.; Pombo-Villar, E., *Lab Chip* **2002,** *2*, 62-64.

31. Rouge, A.; Spoetzl, B.; Gebauer, K.; Schenk, R.; Renken, A., *Chem. Eng. Sci.* **2001,** *56*, 1419-1427.

32. Watts, P.; Wiles, C.; Haswell, S. J.; Pombo-Villar, E., *Tetrahedron* **2002,** *58*, 5427-5439.

33. Watts, P.; Haswell, S. J., *Chem. Soc. Rev.* **2005,** *34*, 235-246.

34. Kulkarni, A. A.; Kalyani, V. S.; Joshi, R. A.; Joshi, R. R., *Org. Process Res. Dev.* **2009,** *13*, 999-1002.

35. Pelleter, J.; Renaud, F., *Org. Process Res. Dev.* **2009,** *13*, 698-705.

36. Jähnisch, K.; Baerns, M.; Hessel, V.; Ehrfeld, W.; Haverkamp, V.; Löwe, H.; Wille, C.; Guber, A., *J. Fluorine Chem.* **2000,** *105*, 117-128.

37. Kobayashi, J.; Mori, Y.; Okamoto, K.; Akiyama, R.; Ueno, M.; Kitamori, T.; Kobayashi, S., *Science* **2004,** *304*, 1305-1308.

38. Pennemann, H.; Watts, P.; Haswell, S. J.; Hessel, V.; Löwe, H., *Org. Process Res. Dev.* **2004,** *8*, 422-439.

39. Edel, J. B.; Fortt, R., *Chem. Commun.* **2002**, 1136-1137.

40. Krishnadasan, S.; Brown, R., *Lab Chip* **2007,** *7*, 1434-1441.

41. Khan, S. A.; Gunther, A.; Schmidt, M. A.; Jensen, K. F., *Langmuir* **2004,** *20*, 8604-8611.

42. Gutierrez, L.; Gomez, L.; Irusta, S.; Arruebo, M.; Santamaria, J., *Chem. Eng. J.* **2011,** *171*, 674-683.

43. Chan, E. M.; Mathies, R. A.; Alivisatos, A. P., *Nano Lett.* **2003,** *3*, 199-201.

44. Gómez, S.; Martinez, C.; Puyol, M., *Lab Chip* **2012**.

45. Gómez-de Pedro, S.; Puyol, M.; Izquierdo, D.; Salinas, I.; de La Fuente, J.; Alonso-Chamarro, J., *Nanoscale* **2012,** *4*, 1328-1335.

46. Kawa, M.; Morii, H.; Ioku, A.; Saita, S.; Okuyama, K., *J.Nanopart.Res* **2003,** *5*, 81-85.

47. Toyota, A.; Nakamura, H.; Ozono, H.; Yamashita, K.; Uehara, M.; Maeda, H., *J. Phys. Chem. C* **2010,** *114*, 7527-7534.

48. Kikkeri, R.; Laurino, P.; Odedra, A.; Seeberger, P. H., *Angew. Chem., Int. Ed.* **2010,** *49*, 2054-2057.

49. Lin, X. Z.; Terepka, A. D.; Yang, H., *Nano Lett.* **2004,** *4*, 2227-2232.

50. Wagner, J.; Kirner, T.; Mayer, G.; Albert, J.; Kohler, J. M., *Chem. Eng. J.* **2004,** *101*, 251-260.

51. Wagner, J.; Kohler, J. M., *Nano Lett.* **2005,** *5*, 685-691.

52. He, S. T.; Liu, Y. L.; Maeda, H., *J.Nanopart.Res* **2008,** *10*, 209-215.

53. Huang, J. L.; Lin, L. Q.; Li, Q. B.; Sun, D. H.; Wang, Y. P.; Lu, Y. H.; He, N.; Yang, K.; Yang, X.; Wang, H. X.; Wang, W. T.; Lin, W. S., *Ind. Eng. Chem. Res.* **2008,** *47*, 6081-6090.

54. J. Wagner , T. K., G. Mayer, J. Albert , J.M. Köhler *Chem. Eng. J.* **2004,** *101*, 251-260.

55. J.M. Köhler, L. A., J.Wagner, J. Albert, G. Mayer, *Chem. Eng. Sci.* **2008,** *63*, 5048-5055.

56. J.Michael Kohler, H. Romanus, U. H¨ ubner, and J.Wagner, *J. Nanomater* **2007,** *2007(2007)*, 1-7.

57. Wagner, J.; Tshikhudo, T. R.; Koehler, J. M., *Chem. Eng. J.* **2008,** *135*, S104-S109.

58. Weng, C. H.; Huang, C. C.; Yeh, C. S.; Lei, H. Y.; Lee, G. B., *J.Micromech.Microeng.* **2008,** *18*, 035019.

59. Sugano, K.; Uchida, Y.; Ichihashi, O.; Yamada, H.; Tsuchiya, T.; Tabata, O., *Microfluid.Nanofluid* **2010,** *9*, 1165-1174.

60. Tsunoyama, H.; Ichikuni, N.; Tsukuda, T., *Langmuir* **2008,** *24*, 11327-11330.

61. Biswas, S.; Miller, J. T.; Li, Y.; Nandakumar, K.; Kumar, C. S., *Small* **2012**.

62. Song, Y. J.; Doomes, E. E.; Prindle, J.; Tittsworth, R.; Hormes, J.; Kumar, C. S. S. R., *J. Phys. Chem. B* **2005,** *109*, 9330-9338.

63. Song, Y. J.; Modrow, H.; Henry, L. L.; Saw, C. K.; Doomes, E. E.; Palshin, V.; Hormes, J.; Kumar, C. S. S. R., *Chem. Mater.* **2006,** *18*, 2817-2827.

64. Pan, Y. C.; Yao, J. F.; Zhang, L. X.; Xu, N. P., *Ind. Eng. Chem. Res.* **2009,** *48*, 8471-8477.

65. A.A Hassan, O. S., V. Cabuila and Patrick Tabelingb, *Chem.Commun* **2008**, 1783-1785.

66. Li, S.; Meierott, S.; Kohler, J. M., *Chem. Eng. J.* **2010,** *165*, 958-965.

67. Park, J. I.; Saffari, A.; Kumar, S.; Günther, A.; Kumacheva, E., *Annu. Rev. Mater. Res.* **2010,** *40*, 415-443.

68. Shalom, D.; Wootton, R. C. R.; Winkle, R. F.; Cottam, B. F.; Vilar, R.; deMello, A. J.; Wilde, C. P., *Mater. Lett.* **2007,** *61*, 1146-1150.

69. Tsunoyama, H.; Ichikuni, N.; Tsukuda, T., *Langmuir* **2008,** *24*, 11327-11330.

70. Lee, W. B.; Weng, C. H.; Cheng, F. Y.; Yeh, C. S.; Lei, H. Y.; Lee, G. B., *Biomed. Microdevices* **2009,** *11*, 161-171.

71. Song, Y.; Jin, P.; Zhang, T., *Mater. Lett.* **2010,** *64*, 1789-1792.

72. Gómez-de Pedro, S.; Puyol, M.; Alonso-Chamarro, J., *Nanotechnology* **2010,** *21*, 415603.

73. Hossain, M. J.; Tsunoyama, H.; Yamauchi, M.; Ichikuni, N.; Tsukuda, T., *Catal. Today* **2011**.

74. Jun, H.; Fabienne, T.; Florent, M.; Coulon, P. E.; Nicolas, M.; Olivier, S., *Langmuir* **2012,** *28*, 15966-15974.

75. Ftouni, J.; Penhoat, M.; Addad, A.; Payen, E.; Rolando, C.; Girardon, J. S., *Nanoscale* **2012,** *4*, 4450-4454.

76. Shovel, A.; Cadavid, D.; Ibanez, M.; Carrete, A.; Cabot, A., *J. Am. Chem. Soc.* **2012,** *134*, 1438-1441.

77. Squires, T. M.; Quake, S. R., *Rev.Mod.Phys* **2005,** *77*, 977.

78. Yen, B. K. H.; Gunther, A.; Schmidt, M. A.; Jensen, K. F.; Bawendi, M. G., *Angew. Chem.-Int. Edit.* **2005,** *44*, 5447-5451.

79. Huebner, A.; Sharma, S.; Srisa-Art, M.; Hollfelder, F.; Edel, J. B., *Lab Chip* **2008,** *8*, 1244-1254.

80. Teh, S.-Y.; Lin, R.; Hung, L.-H.; Lee, A. P., *Lab Chip* **2008,** *8*, 198-220.

81. Christopher, G. F.; Anna, S. L., *J.Phys.D:Appl.Phys* **2007,** *40*, R319-R336.

82. Kumar, D. V. R.; Prasad, B. L. V.; Kulkarni, A. A., *Chem. Eng. J.* **2012,** *192*, 357-368.

83. Kulkarni, A. A.; Kalyani, V. S., *Ind. Eng. Chem. Res.* **2009,** *48*, 8193-8204.

84. Abate, A. R.; Poitzsch, A.; Hwang, Y.; Lee, J.; Czerwinska, J.; Weitz, D. A., *Phys.Rev.E* **2009,** *80*.

85. Garstecki, P.; Fuerstman, M. J.; Stone, H. A.; Whitesides, G. M., *Lab Chip* **2006,** *6*, 437-446.

86. De Menech, M.; Garstecki, P.; Jousse, F.; Stone, H., *J. Fluid Mech.* **2008,** *595*, 141-161.

87. Ghaini, A.; Mescher, A.; Agar, D. W., *Chem. Eng. Sci.* **2011,** *66*, 1168-1178.

88. Knauer, A.; Csaki, A.; Moeller, F.; Huehn, C.; Fritzsche, W.; Koehler, J. M., *J. Phys. Chem. C* **2012,** *116*, 9251-9258.

89. Knauer, A.; Thete, A.; Li, S.; Romanus, H.; Csaki, A.; Fritzsche, W.; Kohler, J. M., *Chem. Eng. J.* **2011,** *166*, 1164-1169.

90. Nightingale, A. M.; Bannock, J. H.; Krishnadasan, S. H.; O'Mahony, F. T. F.; Haque, S. A.; Sloan, J.; Drury, C.; McIntyre, R.; deMello, J. C., *J.Mater.Chem.A* **2013**.

91. Nightingale, A. M.; Demello, J. C., *Adv Mater* **2012**.

92. Li, S. W.; Xu, H. H.; Wang, Y. J.; Luo, G. S., *Langmuir* **2008,** *24*, 4194-4199.

93. Khan, S. A.; Jensen, K. F., *Adv. Mater. (Weinheim, Ger.)* **2007,** *19*, 2556-+.

94. Frenz, L.; El Harrak, A.; Pauly, M.; Begin-Colin, S.; Griffiths, A. D.; Baret, J. C., *Angew. Chem., Int. Ed.* **2008,** *47*, 6817-6820.

95. Chokkalingam, V.; Weidenhof, B.; Kramer, M.; Maier, W. F.; Herminghaus, S.; Seemann, R., *Lab Chip* **2010,** *10*, 1700-1705.

96. Li, S. N.; Gunther, P. M.; Kohler, J. M., *J. Chem. Eng. Jpn.* **2009,** *42*, 338-345.

97. Hartlieb, K. J.; Saunders, M.; Jachuck, R. J. J.; Raston, C. L., *Green Chem.* **2010,** *12*, 1012-1017.

98. Cottam, B. F.; Krishnadasan, S.; deMello, A. J.; deMello, J. C.; Shaffer, M. S. P., *Lab Chip* **2007,** *7*, 167-169.

99. Gross, G. A.; Hamann, C.; Gunther, M.; Kohler, J. M., *Chem. Eng. Technol.* **2007,** *30*, 341-346.

100. Kohler, J. M.; Abahmane, L.; Wagner, J.; Albert, J.; Mayer, G., *Chem. Eng. Sci.* **2008,** *63*, 5048-5055.

101. Chan, E. M.; Alivisatos, A. P.; Mathies, R. A., *J. Am. Chem. Soc.* **2005,** *127*, 13854-13861.

102. Hung, L. H.; Choi, K. M.; Tseng, W. Y.; Tan, Y. C.; Shea, K. J.; Lee, A. P., *Lab Chip* **2006,** *6*, 174-178.

103. Boleininger, J.; Kurz, A.; Reuss, V.; Sonnichsen, C., *Phys. Chem. Chem. Phys.* **2006,** *8*, 3824-3827.

104. Duraiswamy, S.; Khan, S. A., *Small* **2009,** *5*, 2828-2834.

105. Bullen, C.; Latter, M. J.; D'Alonzo, N. J.; Willis, G. J.; Raston, C. L., *Chem. Commun.* **2011,** *47*, 4123-4125.

106. Sebastian, V.; Lee, S.-K.; Zhou, C.; Kraus, M. F.; Fujimoto, J. G.; Jensen, K. F., *Chem. Commun.* **2012,** *48*, 6654-6656.

107. Yang, S.; Zhang, T.; Zhang, L.; Wang, S.; Yang, Z.; Ding, B., *Colloids Surf., A* **2007,** *296*, 37-44.

108. Silvestrini, S.; Carofiglio, T.; Maggini, M., *Chem. Commun.* **2013,** *49*, 84-86.

109. Knauer, A.; Csáki, A.; Möller, F.; Hühn, C.; Fritzsche, W.; Köhler, J. M., *J. Phys. Chem. C* **2012,** *116*, 9251-9258.

110. Knauer, A.; Csáki, A.; Fritzsche, W.; Serra, C. A.; Leclerc, N.; Michael Köhler, J., *Chem. Eng. J.* **2012**.

111. Khan, S. A.; Jensen, K. F., *Adv. Mater. (Weinheim, Ger.)* **2007,** *19*, 2556-2560.

112. Gomez, L.; Arruebo, M.; Sebastian, V.; Gutierrez, L.; Santamaria, J., *J. Mater. Chem.* **2012,** *22*, 21420-21425.

113. Abou-Hassan, A.; Bazzi, R.; Cabuil, V., *Angew. Chem., Int. Ed.* **2009,** *48*, 7180-7183.

114. Gavi, E.; Marchisio, D. L.; Barresi, A. A., *Chem. Eng. Sci.* **2007,** *62*, 2228-2241.

115. Johnson, B. K.; Prud'homme, R. K., *AIChE J.* **2003,** *49*, 2264-2282.

116. Siddiqui, S. W.; Zhao, Y.; Kukukova, A.; Kresta, S. M., *Ind. Eng. Chem. Res.* **2009,** *48*, 7945-7958.

117. Casanova, H.; Higuita, L. P., *Chem. Eng. J.* **2011,** *175*, 569-578.

118. Marchisio, D. L.; Rivautella, L.; Barresi, A. A., *AIChE J.* **2006,** *52*, 1877-1887.

119. Siddiqui, S. W.; Unwin, P. J.; Xu, Z.; Kresta, S. M., *Colloids Surf., A* **2009,** *350*, 38-50

Chapter 2

Part A: Continuous flow homogeneous phase synthesis of Ag NPs in spiral microreactor

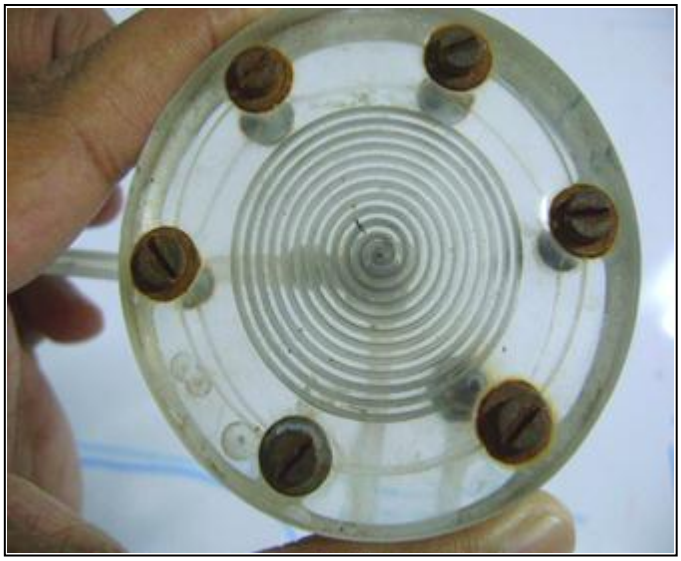

2A.1 Introduction:

The first chapter of this thesis clearly lays a foundation for the necessity of nanoparticle synthesis in large scale. In this scenario, continuous flow methods[1-4] to synthesize nanoparticles have been attracting great attention. Because of their applications as anti-bacterial, antifungal agent[5] and SERS[6] activity, one of the nanoscale materials to have wide market potential is silver nanoparticles. Therefore, we wanted to develop a continuous flow method for the synthesis of Ag nanoparticles.

Before venturing to work in the area of continuous flow synthesis of Ag nanoparticles we identified few reaction parameters as important features. (i) The reaction should proceed to completion rapidly and yield high quantities of nanoparticles and (ii) as far as possible we need to reduce the number of steps and reagents used. Generally, the synthesis of noble metal nanoparticles[7-11] involves two reagents, namely, reducing and capping agents.[12-18] As the number of reagents involved in any reaction increases it becomes more difficult for the same to be extended to continuous flow. Hence we were looking for the methods/procedures that would involve fewer reagents and yet lead to formation of silver nanoparticles in rapid time scales and good quantities.

In this premise in recent years nanoparticle synthesis by molecules/systems that act as dual (both reducing and capping) agents have gained much attention.[19] Prasad and coworkers[20-22] developed a simple one step protocol to synthesize Ag nanoparticles using a lipid molecule called sophorolipid,[23-26] as reducing and capping agent. They have also optimized the reaction conditions and showed that if stearic acid sophorolipid is used, the reaction goes to completion within 5 minutes. We reckoned that this would be an ideal system to extend into a continuous flow synthesis.

In general, tubular reactors are widely used as microreactors for the continuous flow synthesis of nanoparticles. Parabolic velocity profiles cause axial dispersion (Taylor dispersion) in tubular reactors leading to particle deposition at the walls of channel.[27] Figure 2A.1 shows the schematic representation of Taylor

dispersion of a tracer.[28] Here t is the time, D is the molecular diffusivity, w is the radius of the channel and U_0 is velocity of the tracer. It can be seen that, thin tracer strip when t=0 (part a of the figure), gets convectively stretched to parabolic shape under pressure driven conditions (part b). The width of the parabola (ΔW) varies linearly with time. After characteristic time scales the parabola gets smoothened (part c of the figure) into a plug of width $W_{TD} = U_0 w^2/D$. The plug can be broken into many thin stripes and each stripe goes through the same process (a to c in the figure). After N steps, initial thin stripe evolves into a Gaussian with width $N^{1/2}W_{TD}$ (part d in the figure).

Segmented flow methods can be employed to overcome the problem of axial dispersion,[27, 29] but it decreases the effective volume of the reactor. To overcome this problem, we used a microreactor of spiral geometry where secondary flows are prevalent because of the curved nature of the channel.[30, 31] Dean forces and lift forces act on the particles in curved channels and by manipulating these forces, successful size separation can also be done.[30-34] Because of the skewed velocity profiles in curved channels, the variation in time spent by particle at different locations of the channel decreases and this can be used to overcome the axial dispersion during the nanoparticle synthesis.

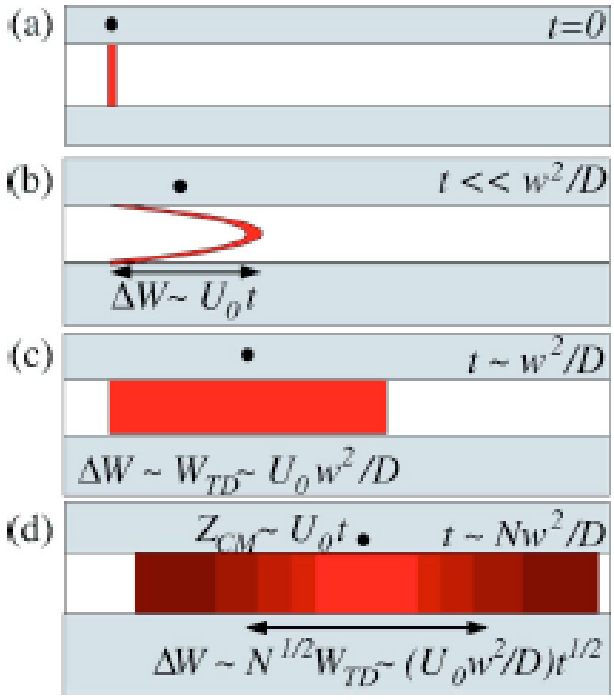

Figure 2A. 1: Schematic representation of Taylor dispersion of tracer in tubular micro channel (taken from Ref.28).

By combining the above two concepts (one step synthesis of Ag nanoparticles and spiral geometry) in this chapter, we discuss the continuous flow synthesis of Ag nanoparticles in spiral microreactor. We also study the effect of residence time, channel cross section and role of secondary flows on the particle size distribution.

Initially, the reaction conditions were optimized in the batch process by using different sophorolipids and at different temperatures. These optimized parameters are extended for the continuous process.

2A.2 Synthesis of Ag nanoparticles using sophorolipid:

One step synthesis of very stable, aqueous dispersed Ag nanoparticles was established by Prasad and coworkers.[20, 22] Before discussing the continuous flow method of synthesis, synthesis of sophorolipid (SL) and batch synthesis of Ag nanoparticles are briefly reviewed here.

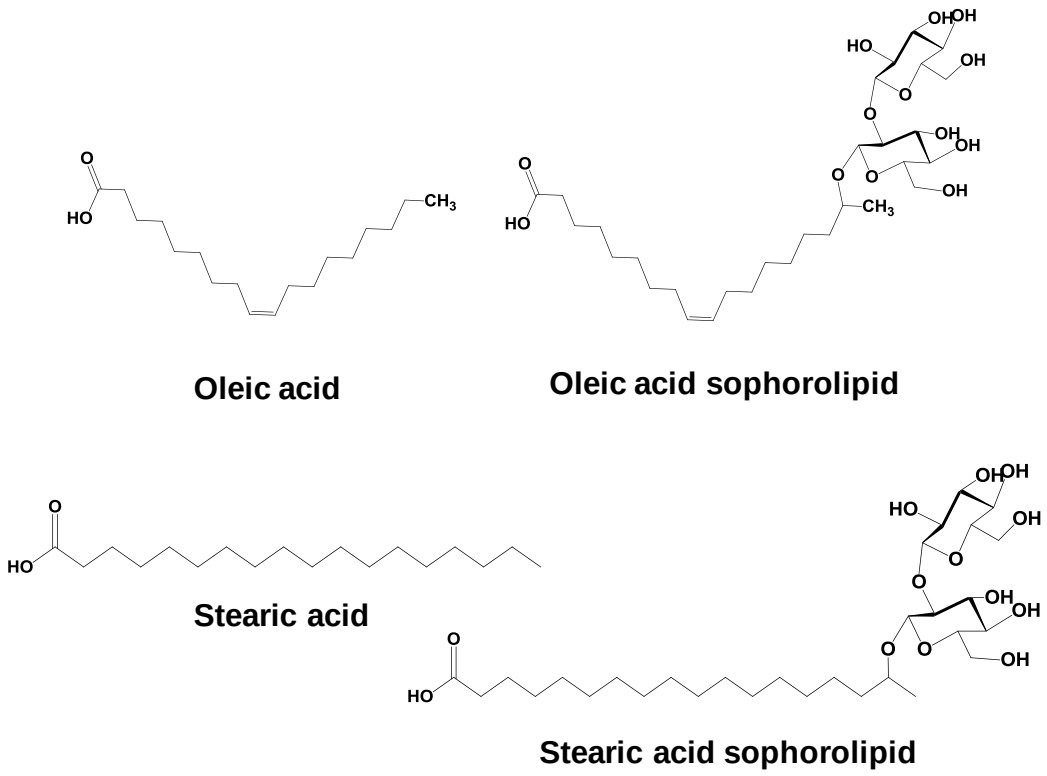

Figure 2A. 2: Structures of oleic, stearic acids and corresponding sophorolipids.

Sophorolipid is a class of glycolipid molecule, in which a sophorose, a dimeric glucose is attached to the ω or ω-1 carbon of fatty acids.[23] One of the attractive features of these molecules is that they can be accessed by biochemical transformations. For example, oliec acid sophorolipid (OASL) can be synthesized by using yeast candida bombicola. Initially, candida bombicola was grown in MGYP medium under shaking conditions. To the biomass obtained by centrifugation 2 ml of oleic acid and 100 ml of 10% glucose solutions were added and incubated at 30 °C for 96 hours. The viscous solution obtained was separated and purified to yield acidic form of sophorolipid.[21, 35] This method can be used to synthesize other sophorolipids by taking different fatty acids instead of oleic acid. Stearic acid sophorolipid (SASL) can be obtained by subjecting the oleic acid sophorolipid to hydrogenation (figure 2A.2).

Ag nanoparticles were first synthesized in batch method using earlier reported methods to optimize the reaction conditions and to select the suitable sophorolipid for the fast and efficient synthesis.[20] In brief, 10 mL of 10^{-3}M $AgNO_3$ and sophorolipd aqueous solution mixture was heated at 90 °C and to this, 1 mL of KOH solution (~0.005 M) was added. The solution turns to yellow colour indicating the formation of Ag nanoparticles. The method was repeated for different sophorolipids and at different temperatures. From the experimental results, it was concluded that, stearic acid sophorolipid (SASL) was more suitable for the synthesis of Ag nanoparticles. At 90 °C, SASL took only 5 minutes to completely reduce the Ag ions to Ag nanoparticles. Hence this optimized method was used for the continuous flow synthesis of Ag nanoparticles in spiral microreactor.

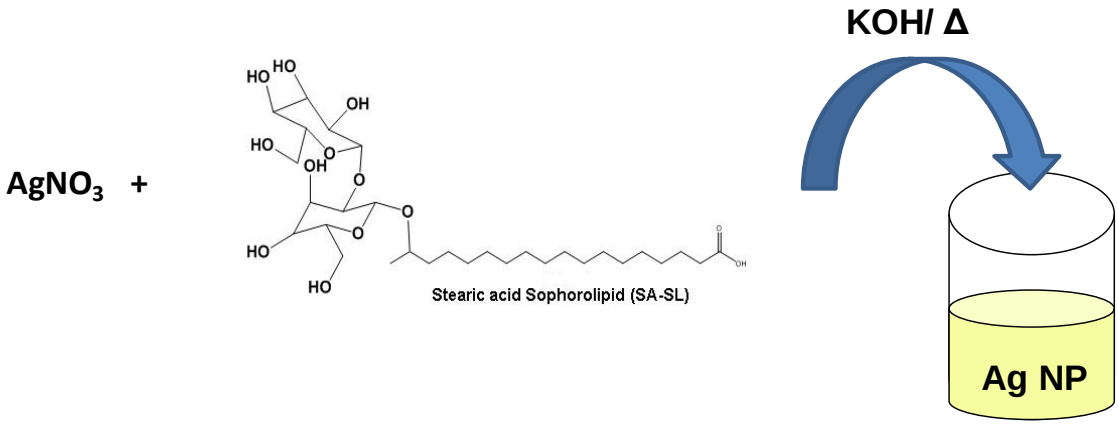

Figure 2A. 3: Schematic of synthesis of Ag nanoparticles using stearic acid sophorolipid.

2A.3 Continuous flow synthesis of Ag nanoparticles (Ag NPs) in spiral microreactor:

2A.3.1 Fabrication of microreactor:

A microchannel reactor of spiral geometry was fabricated on PMMA plate by micromachining (Computer numerical control – CNC micromachining). The microchannel has a square cross section with dimensions of 0.5 mm width and depth, and a length of 0.7 m (with 12 spiral rounds). In addition to this, two microreactors of same spiral geometry with different channel dimensions (width and depth of 1 mm and length of ~ 50 cms; width 1.5 mm, depth 1 mm and length 57 cm) were also fabricated by using same technique. Photograph of the actual spiral microreactor are shown in figure 2A.4.

2A.3.2 Synthesis of Ag nanoparticles in 0.5 mm spiral microreactor - Effect of residence time:

From the batch process results, stearic acid sophorolipid (SASL) was chosen as the capping and reducing agent for the continuous flow experiments.[36] 10^{-3} M $AgNO_3$-SASL mixture and KOH (~0.005 M) solutions were taken in 20 mL and 2 mL glass syringes respectively. The outlets of the syringes were connected to a simple T-mixture (1.38 mm i.d.) using in-house designed and fabricated glass to metal connectors. The fluids mixed in the T-mixer subsequently entered the spiral microreactor through center of the spiral which acts as inlet. The whole experimental setup (micromixer and spiral microreactor) was completely immersed in thermostat (Julabo, Germany) which was maintained at 90 °C. Ag NPs were synthesized at different residence times (10.5 sec, 105 sec, 300 sec) by adjusting flow rates of the syringe pump. Experimental setup is shown in figure 2A.4.

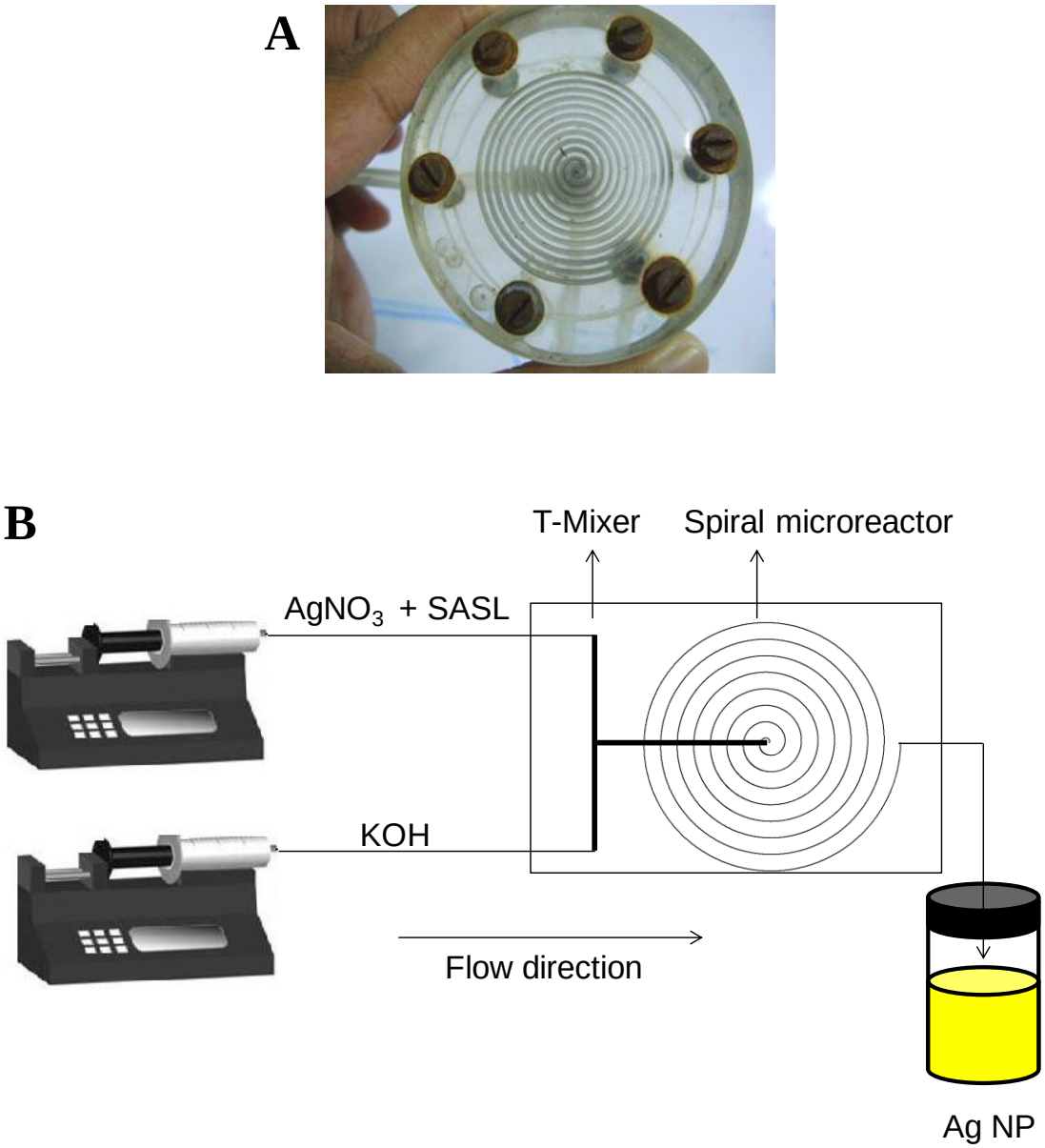

Figure 2A. 2 : (A) Photograph of spiral microreactor (B) Schematic of experimental setup.

2A.3.2.a UV-Vis, DLS and XRD analysis:

Ag nanoparticles synthesized in 0.5 mm i.d spiral microreactor at different residence times (different flow rates) were characterized with UV-Vis and dynamic light scattering (DLS). For particles synthesized at flow rate of 1 mL/min, we observed SPR peak of Ag NPs at ~418 nm with full width at half maximum (FWHM) of 134 nm. When the flow rate decreased from 1 mL/min to 0.035 mL/min (residence time increases from 10.5 sec to 5 minutes) SPR peak position is shifted to ~ 411 nm and FWHM decreased from 134 nm to 87 nm (figure 2A.5). These observations clearly indicate that, as the residence time increases particle size decreased and the size distribution became narrow. The particle size distributions obtained from dynamic light scattering (DLS) support the above observations.

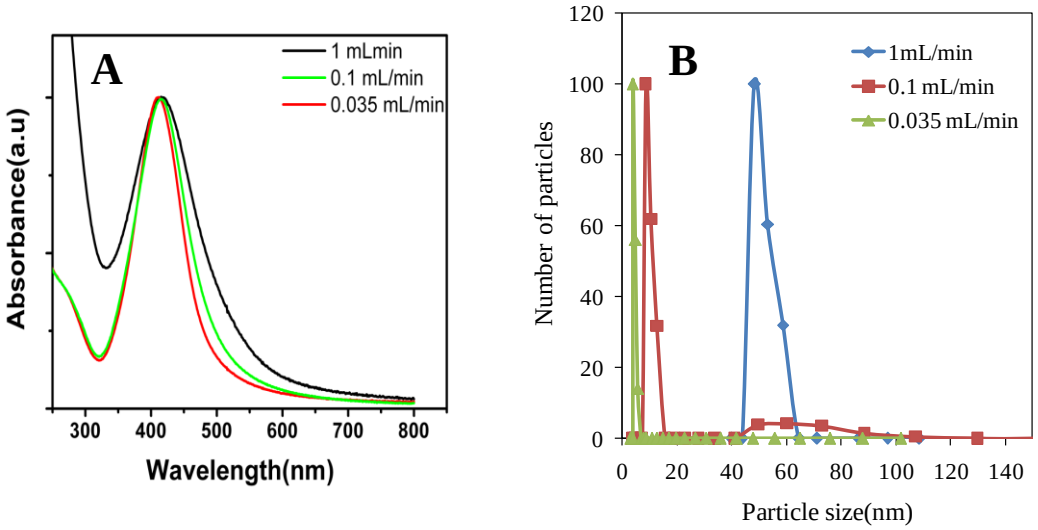

Figure 2A. 3: (A) UV-Vis spectra and (B) DLS particle size distribution of Ag nanoparticles synthesized at different flow rates (residence times).

Crystalline nature of the Ag nanoparticles synthesized at 0.035 mL/min was confirmed by characterizing the sample with PXRD (figure 2A.6) and the pattern matched with the JCPDS PDF no- 04-0783.

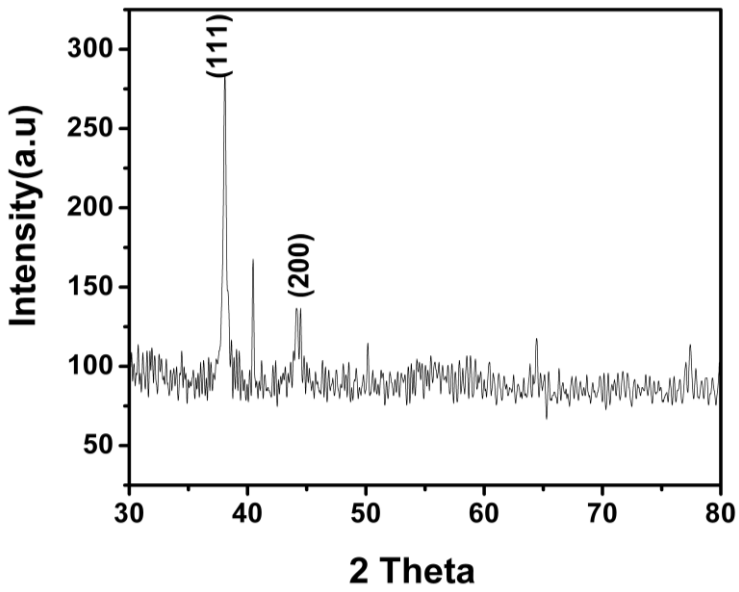

Figure 2A. 4: PXRD of Ag nanoparticles synthesized at flow rate of 0.035 mL/min.

2A.3.2.b TEM analysis:

Ag NPs synthesized at different flow rates were characterized with TEM. Corroborating UV-Visible and DLS results the particle size decreased with decrease in flow rate from 1 mL/min to 0.035mL/min (figure 2A.7 to 2A.9).

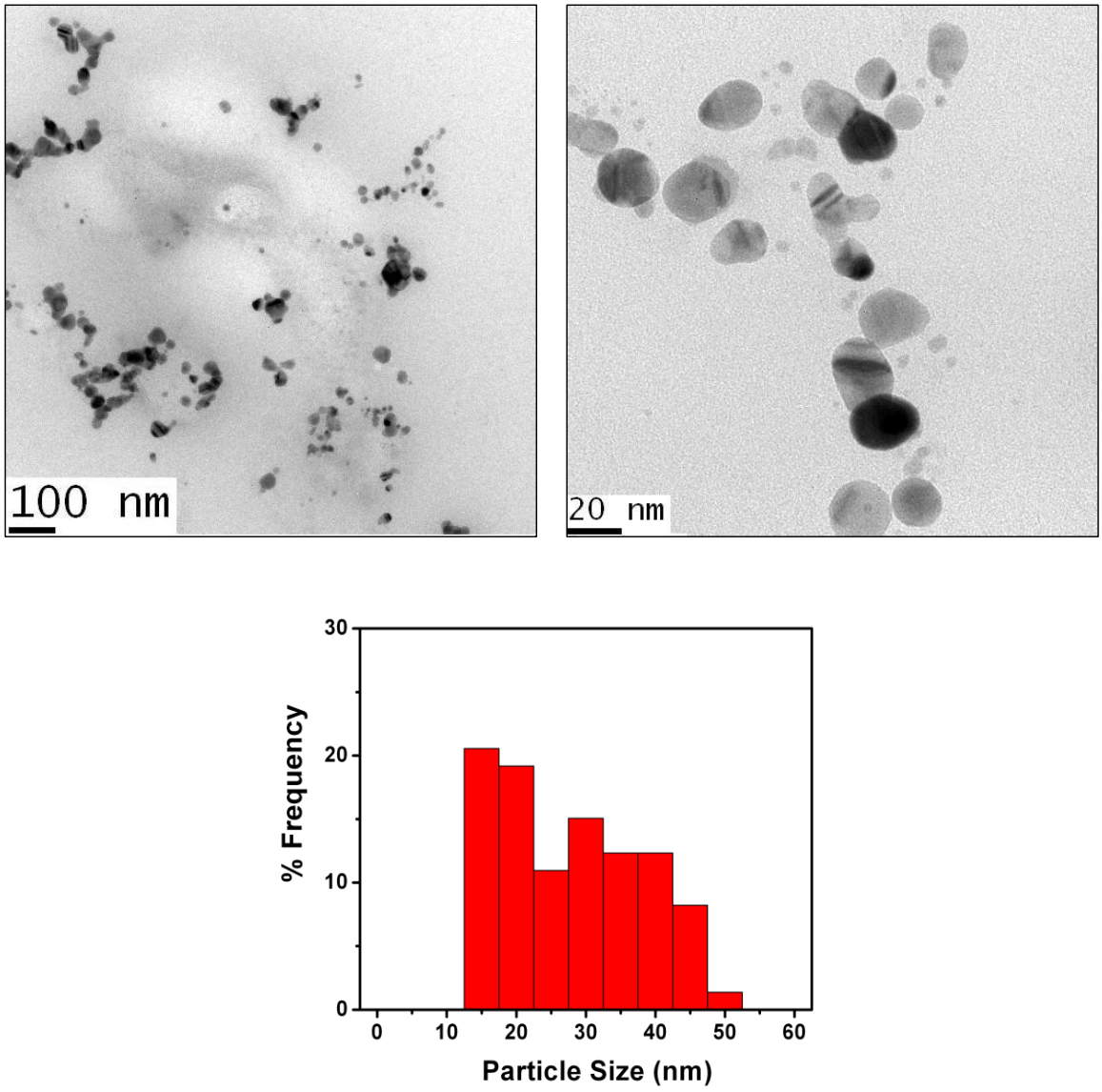

Figure 2A. 5: TEM images of the Ag nanoparticles synthesized at flow rate of 1 mL/min and the corresponding particle size distribution.

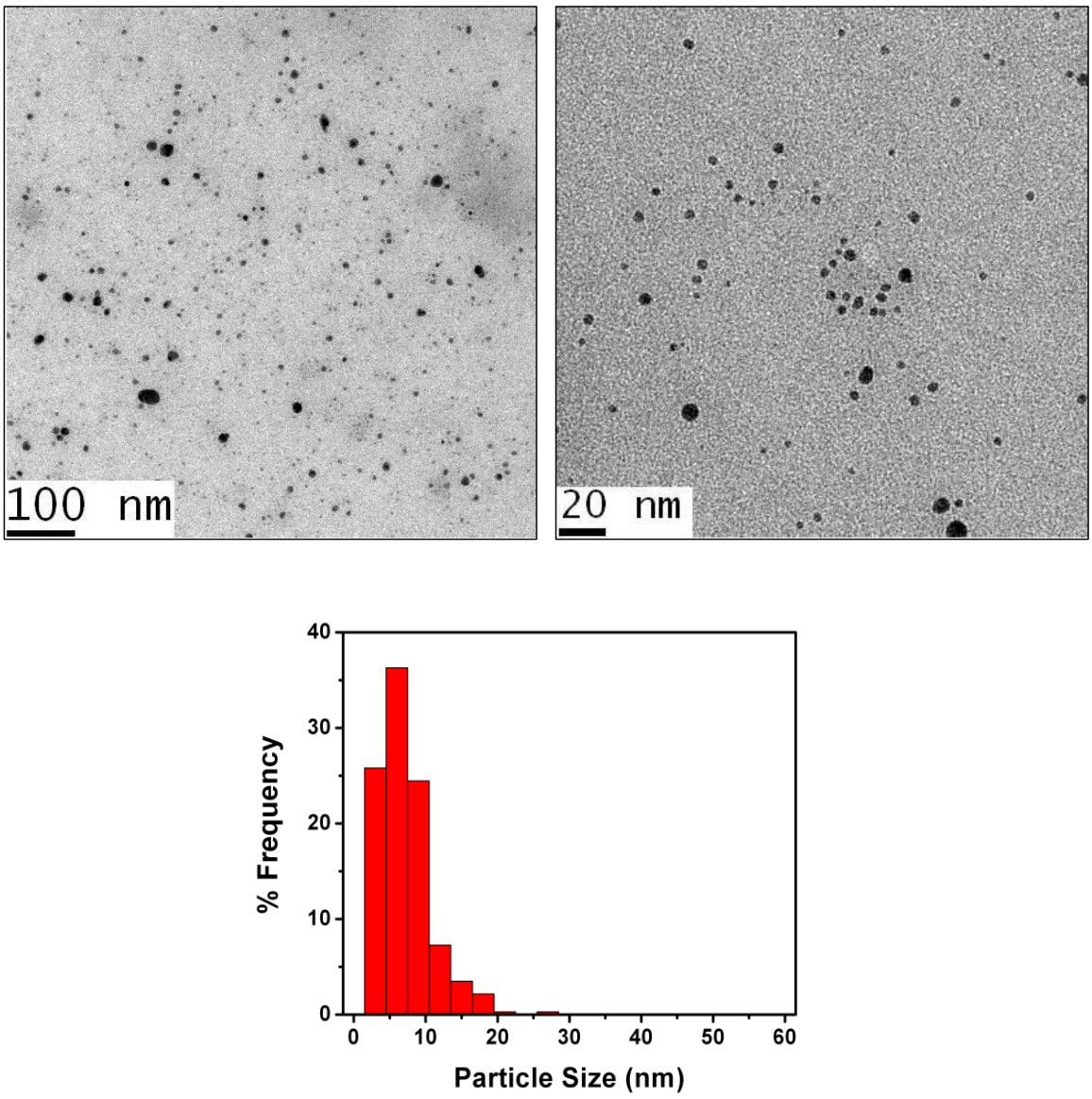

Figure 2A. 6: TEM images and corresponding particle size distribution of Ag nanoparticles synthesized at flow rate of 0.1 mL/min in spiral microreactor.

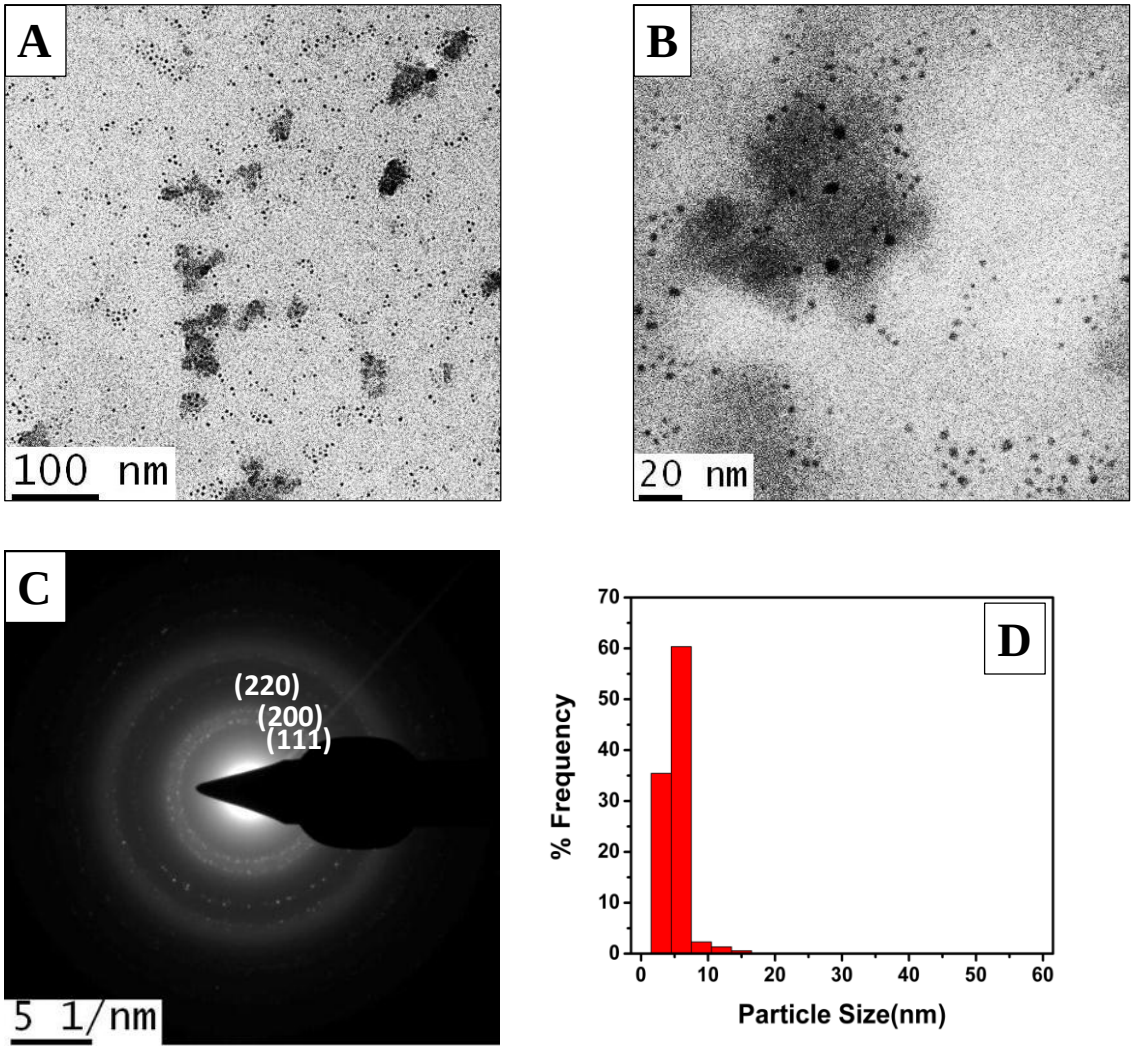

Figure 2A. 7: (A-B) TEM images (C) selective area electron diffraction and (D) corresponding particle size distribution of Ag nanoparticles synthesized in spiral microreactor at flow rate of 0.035 mL/min.

2A.3.3 Effect of channel width:

To understand the role of microchannel cross section and channel width on particle size distribution, synthesis of Ag nanoparticles was repeated in spiral microreactors of channel widths 0.5 mm, 1 mm and 1.5 mm respectively. In case of 0.5 mm and 1 mm channels, the channel cross section is square and in 1.5 mm spiral, the channel has rectangular cross section with depth of 1 mm and width of 1.5 mm. As the volume of these three reactors is different, Ag NPs were synthesized at different flow rates by keeping residence time (5 min) constant in each case. Samples were characterized using UV-Vis and TEM techniques.

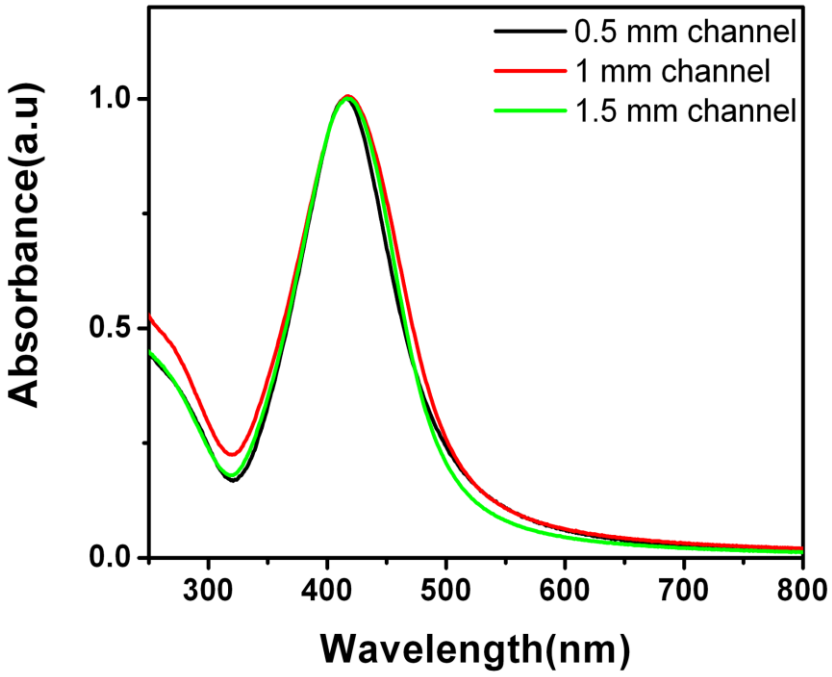

Figure 2A. 8: UV-Visible spectra of Ag nanoparticles synthesized in spiral microreactonrs of different channel widths.

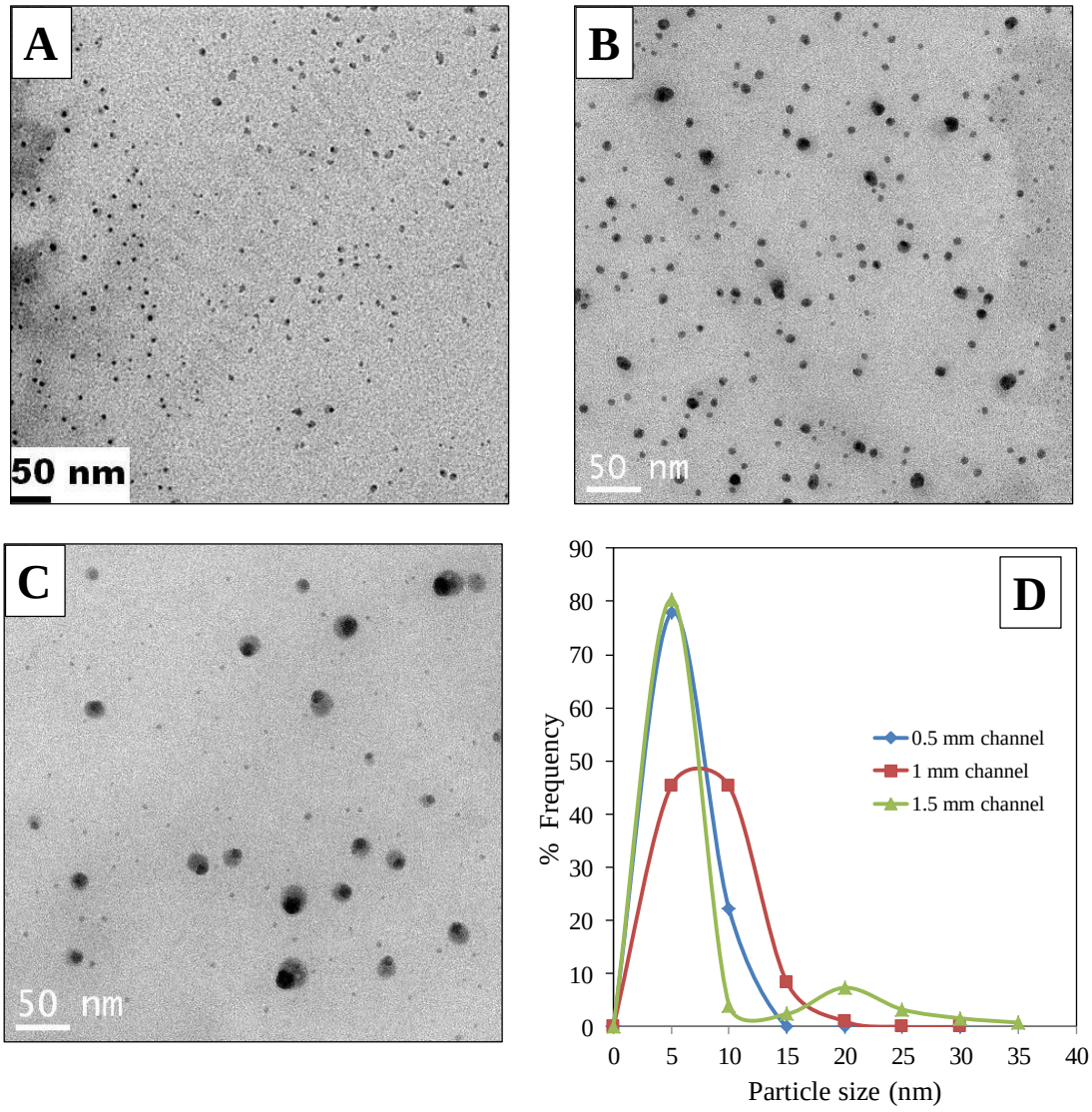

Figure 2A. 9: TEM images of Ag nanoparticles synthesized in spiral microreactors of channel widths (A) 0.5 mm, (B) 1 mm and (C) 1.5 mm for a residence time of 300 seconds. Particle size distributions of the samples are shown in the (D).

We did not observe considerable change in the UV-Vis spectra of the Ag nanoparticles (figure 2A.10). From the TEM images of Ag NPs, it can be easily realized that the average particle size increased and the size distribution became broader when the channel width changed from 0.5 mm to 1 mm (figure 2A.11). On further increasing the channel size width from 1 mm to 1.5 mm, nearly bimodal size distribution was observed.

2A.3.4 Effect of secondary flows:

In a microreactor of spiral geometry, Dean number (De) and hence the extent of secondary flows decreases as the radius of curvature increases.[30] This affects the initial mixing, which is expected to be strong at the center. Hence we carried out the continuous flow synthesis of Ag NPs in 0.5 mm spiral microreactor using (i) center of spiral as inlet and (ii) center of spiral as outlet. In both the cases synthesis was carried out by maintaining residence time constant. Figure 2A.12 shows the schematic representation of experiments.

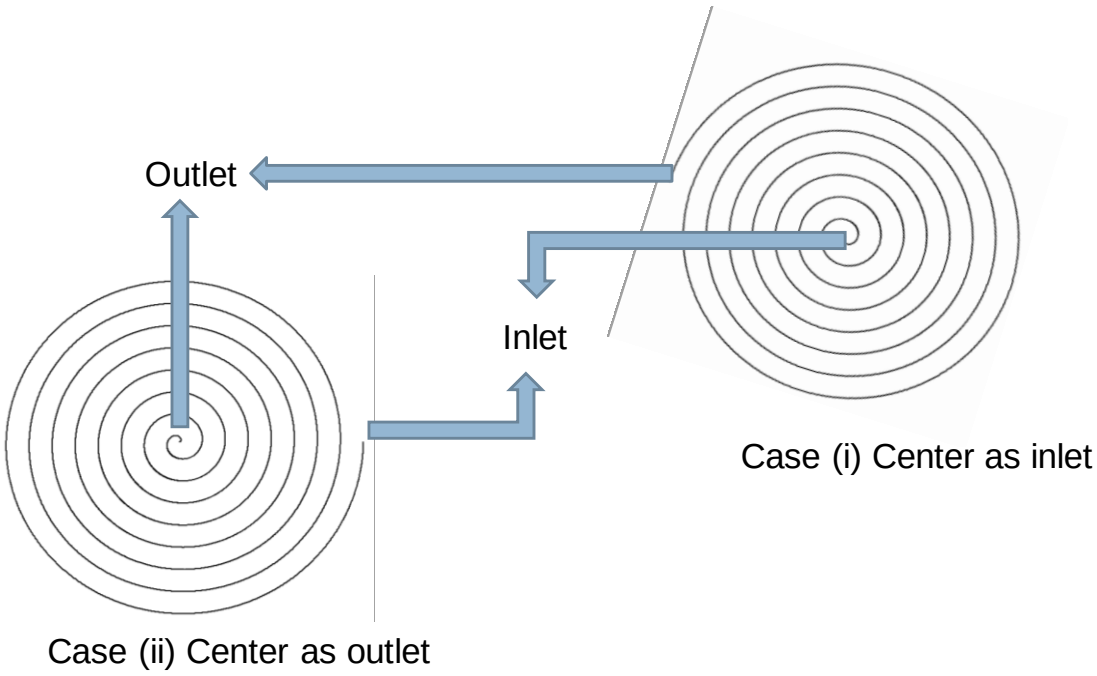

Figure 2A. 10: Schematic of spiral microreactor used for the nanoparticle synthesis. Case (i) center of spiral used as inlet and Case (ii) Center of spiral used as outlet for the nanoparticle synthesis.

2A.3.4.a UV-Vis, DLS and TEM analysis:

The Ag nanoparticles synthesized in both the cases (center of spiral used as inlet and center of spiral used as outlets) were characterized by several techniques. Increase in UV-Vis absorbance intensity was seen when the center of spiral reactor was used as outlet while there was no significant change in the average particle size from DLS results. The Ag nanoparticles were further characterized with TEM and the results are in good agreement with the DLS results (figure 2A.13).

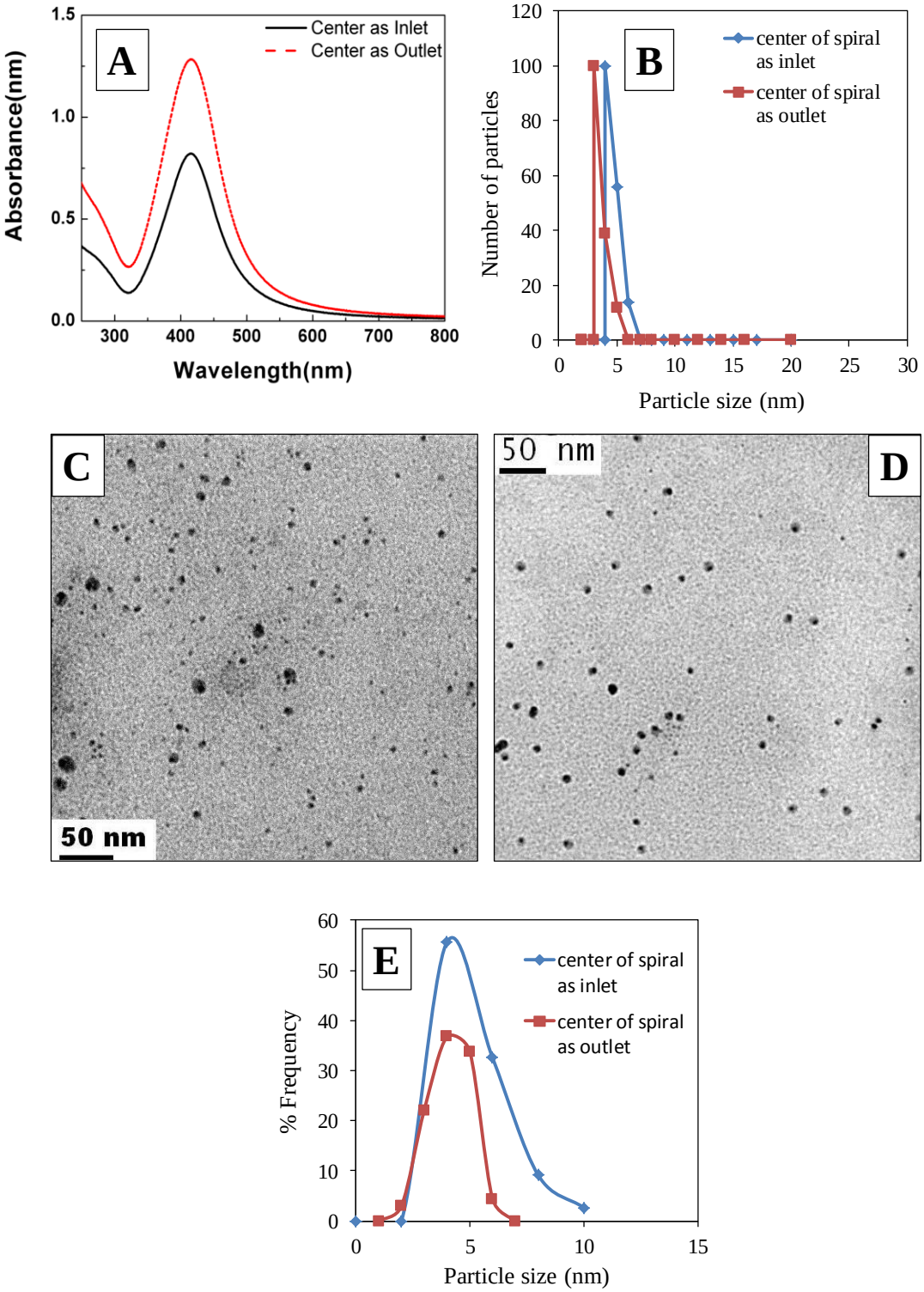

Figure 2A. 11: (A) UV-Visible (B) DLS of the Ag nanoparticles synthesized using center of spiral as inlet and outlet. TEM images of Ag nanoparticles synthesized in (C) center of spiral as inlet, (D) center of spiral as out let and (E) is corresponding particle size distribution.

2A.4 Discussion:

It is reported in the literature that the size distribution of the nanoparticles in continuous flow gets affected by the velocity profile in the channel.[27] In a microchannel, since the flows are laminar (Reynolds number, Re< 2000), the velocity profile is parabolic, where in the absence of significant radial dispersion, the particles in the center of the channel spend relatively less time in the channel than those in the near wall region. This results in the formation of polydispersed particles and the segmented flow method is one of the ways to overcome this limitation as demonstrated by Khan et al and Yen et al.[8,27] However, segmented flow decreases the active volume of the channel and thus reduces the throughput. In view of this, we thought to use a channel geometry where in addition to the convective flow, the fluid also has a secondary circulating flow which helps to reduce the variation in the time spent by the particles at any location. This can be achieved by using spiral evolving channel where the centrifugal force varies continuously and thus induces a secondary flow in the channel.

2A.4.1 Effect of residence time:

Initially the experiments were carried out in spiral microreactor fabricated on PMMA plates of channel width 0.5 mm, depth 0.5 mm and length ~70 cm at different flow rates (i.e. residence times). TEM image of the particles which were synthesized at 1 mL/min clearly shows the particles are polydispersed, not well separated. On the other hand, the particles which were synthesized at lower flow rates are nearly monodisperse with smaller sizes. Batch experimental results conclude that the reaction takes 5 minutes for completion. At higher flow rates 1 mL/min and 0.1 mL/min the residence times are 10.5 and 105 seconds respectively. These values are much below than the required reaction time (5 minutes) and not enough to complete the reaction. In case of 1 mL/min flow rate the residence time 10.5 seconds is just sufficient to initiate the nucleation.

As the flow rate decreased from 1 mL/min to 0.1 mL/min, although the reaction mixture gets sufficient time to yield smaller particles, still the residence time is less than the required reaction time. Hence the synthesis of Ag nanoparticles was carried out by changing the flow rate from 0.1 mL/min to 0.035 mL/min and the

reaction mixture gets the enough residence time (300 sec) to complete the reaction. At sufficiently low flow rate (0.035 mL/min), reaction mixture gets rapidly heated to the reaction temperature (90 °C) and results in rapid and homogeneous nucleation. Hence large quantity of initial reaction mixture will be consumed in the nucleation step and results smaller particles with narrow size distributions are ensued. The results are summarized in the table 2A.1.

Table 2A. 1: Summary of the experimental results of Ag nanoparticle synthesis carried out at different residence times in spiral microreactor.

S.No	Flow rate(mL/min)	Residence time(sec)	Reynolds Number (Re)	Average particle size(nm) from TEM
1	1	10.5	~33	30±20
2	0.1	105	~3	12±9
3	0.035	300	~1	6±3

2A.4.2 Effect of channel dimensions:

Syntheses of Ag nanoparticles were carried out in three different spiral microreactors of i.ds 0.5 mm, 1 mm and 1.5 mm by maintaining the same residence time (5 min). In case of 0.5 mm and 1 mm spiral microreactors the cross section of the channel is square and in 1.5 mm spiral cross section is rectangular. The figure 2A.14 shows the schematic of the channel geometries for the different microreactors.

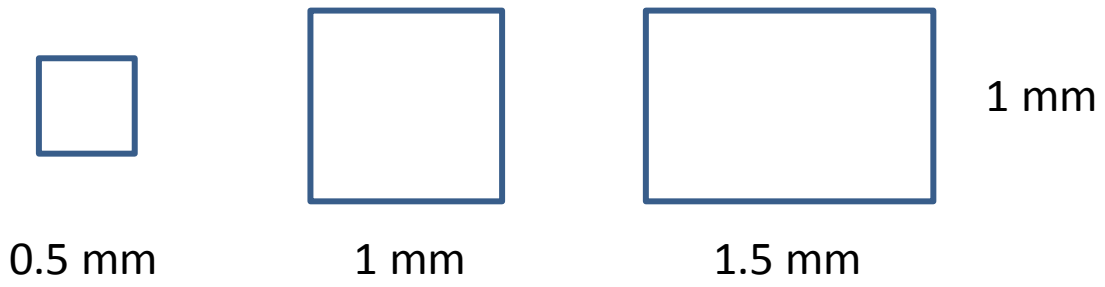

Figure 2A. 12; Schematic of the microchannel cross section of spiral microreactors with different channel widths.

As the aspect ratio (depth/width= d/h) channel changes, hydraulic diameter and the velocity profile of the channel also changes. In spiral microreactor, when the width of the channel increases, velocity profile becomes flat.[30] In case of 0.5 mm and 1 mm square cross sectional channels, the average particle size increased with increase in size distribution. Similar results were obtained when the helical coils used as microreactors.[17, 37] The changes in velocity profiles considerably affected the particle size distribution as the channel cross section changes from square (1×1) to rectangle (1.5×1). Such changes generally lead to broad size distributions. However in the present case, we observed both smaller (~ 5 nm) and larger particles (~15 nm) with nearly bimodal size distribution when the channel dimension was 1.5×1. Summary of the results is shown in the table 2A.2.

Table 2A. 2: Summary of the experiment results of synthesis of Ag nanoparticles in spiral microreactors of different channel widths.

Channel dimensions [width(w), depth(d)	Residence time(sec)	Reynolds number (Re)	Average particle size(nm)
w-0.5, d-0.5	300	1.16	~ 5
w-1, d-1	300	1.63	~5-10
w-1.5, d-1	300	2.57	~5,~20

2A.4.3 Effect of secondary flows:

Secondary flows or Dean flows are function of radius of curvature of a curved channel. The dimensional less Dean number (De) can be expressed as

$$D_e = R_e \sqrt{\frac{D}{2R_C}}$$

Where D is diameter of the channel (m)

R_C is radius of curvature (m)

Re is Reynolds Number $R_e = \frac{\rho V D_h}{\mu}$

ρ is density of the fluid(kg/m^3)

V is velocity (m/sec)

D_h is hydraulic diameter (m)

μ is viscosity of the fluid (kg/m-sec)

From the above expression, it can be realized that Dean number and hence the secondary flows decreases with increase in radius of curvature at constant velocity of the fluid. For spiral geometry, the secondary flows are stronger at the center of the spiral and the extent of secondary flows continuously decrease with increase in radius of curvature Rc, (in helical coil, Rc is constant, so Dean flows do not vary with the length of the channel). For a 0.5 mm spiral microreactor, figure 2A.15 shows the variation in Dean number with radius of curvature.

As we explained previously, to quantify the role of secondary flows on particle size distribution, Ag NPs synthesized in 0.5 mm spiral microreactor (i) using center of spiral as inlet (ii) center of spiral as outlet. Although, the variation in secondary flows could not bring any considerable change in the particle size distribution, high UV-Vis absorbance was seen for the particle synthesized by using center of spiral as outlet. When the center of the spiral used as outlet, the secondary flows which are stronger at the center would be useful to washout particles synthesized. In the other case (center of the spiral used as inlet) as the outlet is situated far away from the center, the secondary flows become relatively weak and may not be sufficient to washout the particles effectively from the channel. This could be reason for different results obtained (table 2A.3).

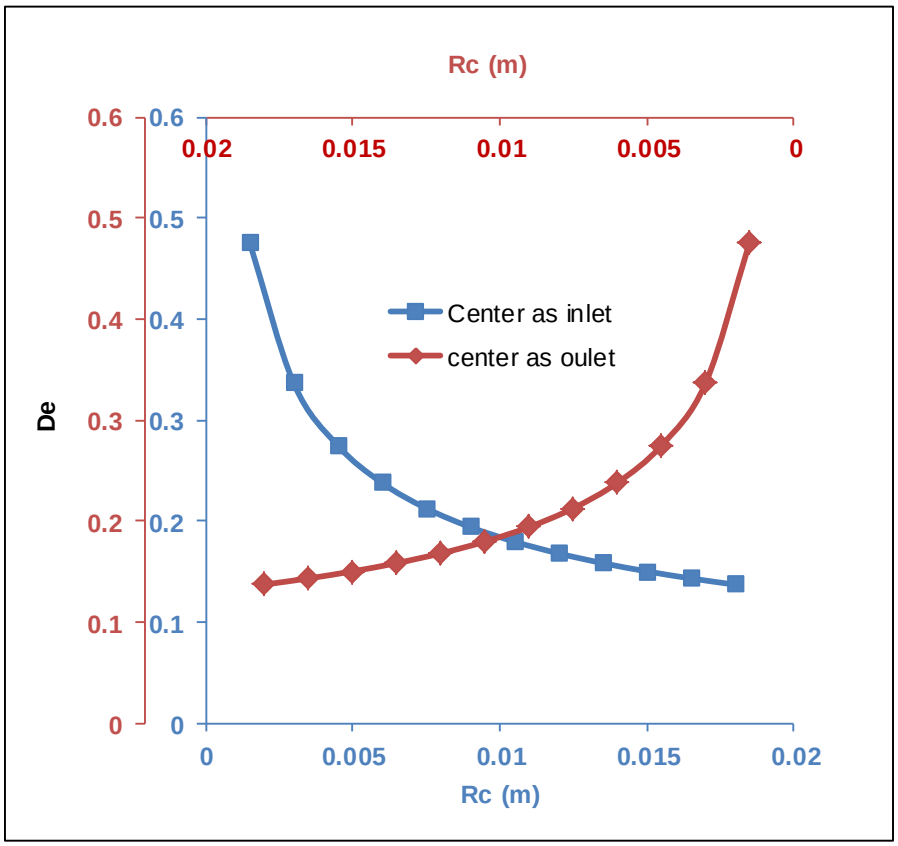

Figure 2A. 13: Change in Dean number with radius of curvature when (■) center of spiral used as inlet and (♦) center of spiral used as outlet for the nanoparticle synthesis.

Table 2A. 3: Summary of the experimental results of Ag nanoparticle synthesis in spiral microreactor using center of spiral as inlet and outlet

Experimental condition	Residence time(sec)	Average particle size(nm)
1. Center of the spiral used as inlet	300	4-8
2. Center of spiral used as outlet	300	3-7

2A.5 Conclusions:

A simple, one step protocol to synthesize highly stable and well dispersed Ag NPs was successfully transformed to continuous flow method. To overcome the limitation of parabolic velocity profiles under laminar flows, instead of electing segmented flow, spiral geometry was used to synthesize the particles. Curved channels in the spiral geometry induce secondary flows, which helps to eliminate the time variation spent by the synthesized particles at any location and to get narrow size distributions. Moreover, effect of several fluid dynamic parameters on particle size distribution was also studied.

2A.6 References:

1. Abou Hassan, A.; Sandre, O.; Cabuil, V., *Angew. Chem., Int. Ed.* **2010,** *49*, 6268-6286.

2. Zhao, C. X.; He, L.; Qiao, S. Z.; Middelberg, A. P. J., *Chem. Eng. Sci.* **2011,** *66*, 1463-1479.

3. Song, Y. J.; Hormes, J.; Kumar, C. S. S. R., *Small* **2008,** *4*, 698-711.

4. Wiles, C.; Watts, P., *Eur. J. Org. Chem.* **2008**, 1655-1671.

5. Kumar, A.; Vemula, P. K.; Ajayan, P. M.; John, G., *Nat. Mater.* **2008,** *7*, 236-241.

6. Emory, S. R.; Nie, S. M., *Anal. Chem.* **1997,** *69*, 2631-2635.

7. Wagner, J.; Kohler, J. M., *Nano Lett.* **2005,** *5*, 685-691.

8. Kohler, J. M.; Abahmane, L.; Wagner, J.; Albert, J.; Mayer, G., *Chem. Eng. Sci.* **2008,** *63*, 5048-5055.

9. Wagner, J.; Tshikhudo, T. R.; Koehler, J. M., *Chem. Eng. J.* **2008,** *135*, S104-S109.

10. Weng, C. H.; Huang, C. C.; Yeh, C. S.; Lei, H. Y.; Lee, G. B., *J.Micromech.Microeng.* **2008,** *18*, 035019.

11. Wojnicki, M.; Paclawski, K.; Jaworski, W.; Luty-Blocho, M.; Streszewski, B.; Szacilowski, K.; Fitzner, K., *Rudy Met. Niezelaz.* **2011,** *56*, 745-752.

12. Xue, Z. L.; Terepka, A. D.; Hong, Y., *Nano Lett.* **2004,** *4*, 2227-2232.

13. Gottesman, R.; Tangy, A.; Oussadon, I.; Zitoun, D., *New J. Chem.* **2012,** *36*, 2456-2459.

14. Hartlieb, K. J.; Saunders, M.; Jachuck, R. J. J.; Raston, C. L., *Green Chem.* **2010,** *12*, 1012-1017.

15. He, S. T.; Liu, Y. L.; Maeda, H., *J.Nanopart.Res* **2008,** *10*, 209-215.

16. Lazarus, L. L.; Riche, C. T.; Marin, B. C.; Gupta, M.; Malmstadt, N.; Brutchey, R. L., *ACS Appl. Mater. Interfaces* **2012,** *4*, 3077-3083.

17. Lin, X. Z.; Terepka, A. D.; Yang, H., *Nano Lett.* **2004,** *4*, 2227-2232.

18. Patil, G. A.; Bari, M. L.; Bhanvase, B. A.; Ganvir, V.; Mishra, S.; Sonawane, S. H., *Chem. Eng. Process.* **2012,** *62*, 69-77.

19. Dumur, F.; Guerlin, A.; Dumas, E.; Bertin, D.; Gigmes, D.; Mayer, C. R., *Gold Bull.* **2011,** *44*, 119-137.

20. Kasture, M. B.; Patel, P.; Prabhune, A. A.; Ramana, C. V.; Kulkarni, A. A.; Prasad, B. L. V., *J. Chem. Sci.* **2008,** *120*, 515-520.

21. Singh, S.; Patel, P.; Jaiswal, S.; Prabhune, A.; Ramana, C.; Prasad, B., *New J. Chem.* **2009,** *33*, 646-652.

22. Singh, S.; D'Britto, V.; Prabhune, A. A.; Ramana, C. V.; Dhawan, A.; Prasad, B. L. V., *New J. Chem.* **2009,** *34*, 294-301.

23. Van Bogaert, I. N. A.; Saerens, K.; De Muynck, C.; Develter, D.; Soetaert, W.; Vandamme, E. J., *Appl. Microbiol. Biotechnol.* **2007,** *76*, 23-34.

24. Van Bogaert, I.; Soetaert, W., *Biosurfactants* **2011,** *20*, 179-210.

25. Baccile, N.; Noiville, R.; Stievano, L.; Van Bogaert, I., *Phys. Chem. Chem. Phys.* **2013,** *15*, 1606-1620.

26. Kasture, M.; Singh, S.; Patel, P.; Joy, P.; Prabhune, A.; Ramana, C.; Prasad, B., *Langmuir* **2007,** *23*, 11409-11412.

27. Yen, B. H. K.; Günther, A.; Schmidt, M. A.; Jensen, K. F.; Bawendi, M. G., *Angew. Chem., Int. Ed.* **2005,** *44*, 5447-5451.

28. Squires, T. M.; Quake, S. R., *Rev.Mod.Phys.* **2005,** *77*, 977.

29. Khan, S. A.; Gunther, A.; Schmidt, M. A.; Jensen, K. F., *Langmuir* **2004,** *20*, 8604-8611.

30. Martel, J. M.; Toner, M., *Phys. Fluids* **2012,** *24*, 032001.

31. Bhagat;, A. A. S.; Kuntaegowdanahalli, S. S.; Papautsky, I., *Lab Chip* **2008,** *8*, 1906-1914.

32. Dutz, S.; Hayden, M. E.; Schaap, A.; Stoeber, B.; Häfeli, U. O., *J. Magn. Magn. Mater.* **2012**.

33. Kuntaegowdanahalli, S. S.; Bhagat, A. A. S.; Kumar, G.; Papautsky, I., *Lab Chip* **2009,** *9*, 2973-2980.

34. Di Carlo, D., *Lab Chip* **2009,** *9*, 3038-3046.

35. Shah, S.; Prabhune, A., *Biotechnol. Lett.* **2007,** *29*, 267-272.

36. Kumar, D. V. R.; Kasture, M.; Prabhune, A. A.; Ramana, C. V.; Prasad, B. L. V.; Kulkarni, A. A., *Green Chem.* **2010,** *12*, 609-615.

37. Huang, J. L.; Lin, L. Q.; Li, Q. B.; Sun, D. H.; Wang, Y. P.; Lu, Y. H.; He, N.; Yang, K.; Yang, X.; Wang, H. X.; Wang, W. T.; Lin, W. S., *Ind. Eng. Chem. Res.* **2008,** *47*, 6081-6090.

Part B: Segmented flow synthesis of Ag nanoparticles in spiral microreactor

2B.1 Introduction:

The continuous flow synthesis of nanoparticles in microchannel reactors is known to overcome the limitations of traditional batch preparative methods in terms of reproducibility, narrow size distribution and easy scale up. This approach to synthesize nanostructured materials has been employed for variety of systems like metal nanostructures, quantum dots, metal oxides and core shell structures etc.[1] Although the homogeneous phase continuous flow synthesis methods are very good in getting a relatively narrow particle size distribution (as compared to conventional batch methods), they are still affected by the diffusive mixing and axial dispersion due to the parabolic velocity profile and yields a significant non uniformity in the particle sizes.[2] Furthermore, longer time operations of reactors by these methods end up with deposition of materials at channel walls along the length of the microchannel.[3] Among few of the approaches that help to overcome these limitations, the prominent ones are (i) use of segmented flow to reduce the axial dispersion[4] (ii) droplet based flow focusing[5] and (iii) inducing secondary flows by gradual variation in the channel configuration.[6] Among these segmented flow syntheses of variety of nanoparticles systems like anisotropic structures,[7] metals,[8, 9] metal oxides,[10-13] metal salts,[14] quantum dots,[2, 15, 16] zeolite,[17] silica[4, 18] and polymer[19] have been reported in the literature.

As the flow pattern changes from single phase to segmented or droplet flow the mixing is dominated by convection and recirculation.[20] In general the inert phase that leads to the formation of segments can be a gas or liquid which gives gas-liquid and liquid-liquid segmented flows respectively. The nature of the flow in such cases depends on physicochemical properties of the fluids, (i.e. density, viscosity, interfacial tension etc.), microchannel wettability, surface roughness and flow rates of the continuous and dispersed phase fluids. The nature of the flow is quantified in terms of dimensionless numbers viz. Reynolds number $Re = \rho D_h U/\mu$, Capillary number $Ca = \mu U/\gamma$ and Weber numbers $We = \rho U^2 d/\gamma$, where U is superficial velocity, D_h is hydraulic diameter, d is slug diameter, ρ is the fluid density, γ is interfacial tension and μ is the dynamic viscosity.[21] The hydrodynamics of segmented flow (slug sizes, pressure drop, specific interfacial area for mass transfer

etc.) in different microreactors have been studied extensively.[22-25] Effect of channel cross section[24], inlet configuration[26] and channel geometry[27, 28] on the two phase flow are also reported. The gas-liquid and liquid-liquid segmented flows in a microchannel show distinct hydrodynamic behavior. Thus depending upon the nature of system where one phase is inert (mainly to achieve segmented flow), the hydrodynamics affect the performance of the microreactor. In view of this, here we have studied the effect of segmentation on the particle size distribution.

In spiral microreactor, because of the curved nature of the microchannels secondary flows exist and they are prevalent in the absence of segmentation. Stearic acid sophorolipd (SASL) reduced/capped silver nanoparticles (Ag NPs) in aqueous phase was used as a model system and in a spiral poly methyl methacrylate (PMMA) microreactor (0.5 mm channel size with square cross-section and 0.7 m length) liquid-liquid and gas-liquid segmented flows were achieved using kerosene and air as inert phase respectively. In all the experiments, centre of the spiral was used as the inlet of the reactor. According to the mechanism of generation of segmented flow, the slugs are generated by the squeezing-in of the dispersed phase in the micromixer[29] and the force balance at the detachment point governs the slug properties. For example, when the i.d. of the micromixers is bigger than the width of the microchannel, very long slugs (having L/D > 20) were observed than the normal segmented flow. For the gas-liquid system, liquid, which is the reacting phase, is the continuous phase and gas (air) forms dispersed slugs. On the other hand in liquid-liquid system, kerosene has a lower contact angle with PMMA and hence forms the continuous phase while the aqueous mixture forms dispersed slugs. Kerosene was selected as inert phase to generate liquid – liquid segmented flow since it is very compatible with PMMA surface (PMMA is very sensitive to most of the organic solvents). We studied the synthesis of the nanoparticles for both the segmented flow systems at different residence times 10.5 s, 105 s, 300s of the reactant phase (for the total flow rates of 1 mL/min, 0.1 mL/min and 0.035 mL/min respectively). As reported previously[6], when the stearic acid sophorolipid molecule acts as reducing and capping agent the synthesis is complete in 300 s at 90 °C. The effect of flow rate ratio (inert phase to reactant phase at constant total flow rate), role of inert phase as

continuous and dispersed phases and the inlet diameter (where the segmentation takes place) on the slug size and hence on the particle size distribution has also been studied.

2B.2 Slug size measurements:

Like in chapter 2A, a spiral PMMA microreactor with channel dimensions of 0.5 mm width and depth, and a length of the total channel is about 0.7 m with 12 spiral rounds (figure 2B.1) was used here. A 4-way connector/micromixer (of two different micromixers of different i.d., i.e. 1.38 mm i.d. in SS 316 and 0.5 mm in PEEK-Polyether ether ketone; were used) was connected at the center of the spiral (inlet). Pumping of fluids was achieved by using syringe pumps (Longer Syringe Pumps, China). The slug sizes were measured using high speed camera (100 frames per second) and high resolution Sony digital camera (in case of 0.5 mm PEEK micromixer) at different total flow rates of inert and the reactant phases. At a given flow rate, experiments were carried out at different flow ratios 1:1, 1:2 and 1:0.5 of inert to aqueous phase fluid. Methylene Blue dye was used to distinguish the aqueous slugs from inert phase slugs. The image analysis was carried out using Image Pro Plus® software. The slug size measurements were carried out at the room temperature (mainly because the steam from hot water used to get condensed on the camera lens or the reflector) and the relevant data is given in section 2B.4.

2B.3 Segmented flow synthesis of Ag nanoparticles:

The method of synthesis of Ag NPs using sophorolipids was explained previously[30, 31] and the same method was used here for segmented flow synthesis. In brief, 1×10^{-3} M equimolar solutions of $AgNO_3$ and SASL and 0.005 M of KOH solution were prepared and both of these solutions act as reactant phase. The fluids ($AgNO_3$-SASL mixture, KOH and inert phase) were taken in three different leak proof syringes and were driven by syringe pumps (Longer syringe pumps, China). The three fluids namely (i) the inert phase (air or kerosene), (ii) a mixture of aqueous silver nitrate and sophorolipid solution and (iii) base, come in contact through the 4-way micromixer. The whole microreactor was immersed in thermostat (JULABO,

Germany) maintained at 90°C (figure 2B.1). The details of the different experimental conditions used are documented below(table 2B.1).

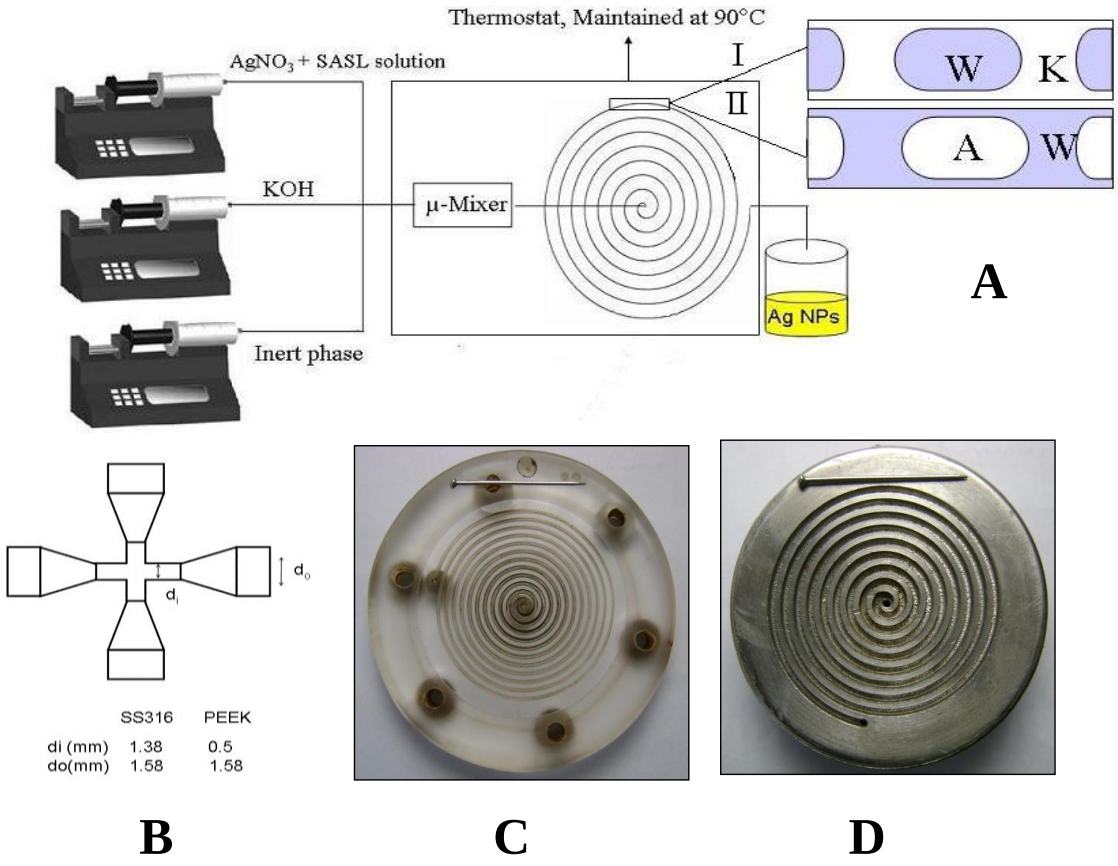

Figure 2B. 1: (A) Experimental setup for the segmented flow synthesis of Ag nanoparticles, (B) Schematic of the micromixer (C) PMMA spiral microreactor (i.d 0.5 mm) and (D) SS316 spiral microreactor (i.d 1mm).

Reactant phase : $AgNO_3$-SASL solution and KOH solutions

Inert phase : Air in case of gas-liquid segmented flow and kerosene in case of liquid-liquid segmented flow.

Micromixing units : (1) SS micromixing unit of i.d 1.38 mm

(2) PEEK micromixing unit of i.d 0.5 mm

Table 2B. 1: Summary of the experiments carried out for the segmented flow synthesis of Ag nanoparticles

Inert phase flow rates Q_I (mL/min)	Reactant phase flow rate Q_R (mL/min)	Q_I / Q_R	Total flow rate $Q_I + Q_R$ (mL/min)	Micromixer used
Summary of experiments carried out in PMMA microreactor (0.5 mm channel size)				
0.5	0.5	1	1	SS
0.33	0.66	1:2	1	SS
0.66	0.33	1:0.5	1	SS
0.050	0.050	1	0.1	SS
0.0333	0.0666	1:2	0.1	SS
0.0666	0.0333	1:0.5	0.1	SS
0.0175	0.0175	1	0.035	SS
0.01166	0.02333	1:2	0.035	SS
0.02333	0.01166	1:0.5	0.035	SS
0.0175	0.0175	1	0.035	PEEK
Summary of experiments carried out in PMMA microreactor (1 mm channel size)				
0.049	0.049	1	0.098	SS
Summary of experiments carried out in SSmicroreactor (1 mm channel size)				
0.049	0.049	1	0.098	SS

A 0.1 m long tube was used to collect the samples from outlet. The samples were kept in ice bath (to quench the reaction) and were subjected to further analysis. A list of all the experiments is given in the table 2B.1 and the details of the experiments are given in the corresponding sections. Schematic of the experimental set-up, micromixer, photographs of the PMMA and SS 316 spiral reactor are given in figure 2B.1.

2B.3.1 Using SS 316 (i.d 1.38 mm) micromixer:

As mentioned previously, we used kerosene (density-ρ_k = 810 kg/m^3, viscosity-μ_k = 0.0014 kg/m s,) and air (ρ_{Air} = 1.17kg/m^3, μ_{Air} = 0.000017894 kg/m s) as the inert phases that would help to achieve a liquid - liquid and gas - liquid segmented flow in the microreactor. The surface tension between air and reactant phase and the interfacial tension between the aqueous reactant and kerosene were measured at room temperature using Tensiometer (K100 model, KRÜSS GmbH) and the values are 0.052 N/m and 0.03688 N/m respectively. In the kerosene - reactant aqueous phase case, kerosene acted as continuous phase because of its lower contact angle with PMMA (8^0) while the reacting aqueous phase formed discontinuous slugs (water - PMMA contact angle is 77^0).[32] On the other hand, with air as the inert phase, the reacting aqueous phase was continuous and the air was present in the form of discontinuous slugs(dispersed phase). Hence even at identical flow rates, the expected flow behavior for two cases will be different due to the difference in the relative viscosity, density of the two phases, interfacial tension of inert phase with reactant phase and phase behavior of the inert phase (depending upon whether it is acting as continuous phase or dispersed phase).

2B.3.1.a Liquid (kerosene) – liquid (reactant phase) segmented flow:

For the case of kerosene as inert phase, in order to see the effect of flow ratio on the dynamics of particle formation, three different volumetric flow rate ratios between kerosene and the reactant phase were maintained (1:0.5, 1:1 and 1:2) by adjusting the flow rates of these two phases, the experiments were conducted at three different residence times (10.5 s, 105 s and 300 s) at every flow ratio. As indicated

before, in this case, kerosene becomes the continuous phase and the reaction takes place in the dispersed aqueous reactant phase.

2B.3.1.a.1 UV – Visible spectra and DLS analysis:

The UV-Visible spectra of Ag NPs synthesized at different flow rates are shown in figure 2B.2. While the absorbance intensity of the Ag NPs should increase with increase in residence time (as the time required for the completion of the reaction is 300 seconds)[6], in reality, the absorbance intensity was seen to decrease with increase in residence time from 105 sec (flow rate 0.1mL/min) to 300 sec (flow rate 0.035 mL/min). At all the flow rates it was observed that in the UV-Visible spectra of Ag NPs, absorption intensity is maximum when the kerosene to water (K/W) flow ratio was 1:2. The particle size distribution measured using the dynamic light scattering obtained at different residence times showed trends similar to the homogeneous flow synthesis (figure 2B.2). With increase in the residence time, the average particle size as well as the standard deviation in the particle sizes decreased significantly.

.

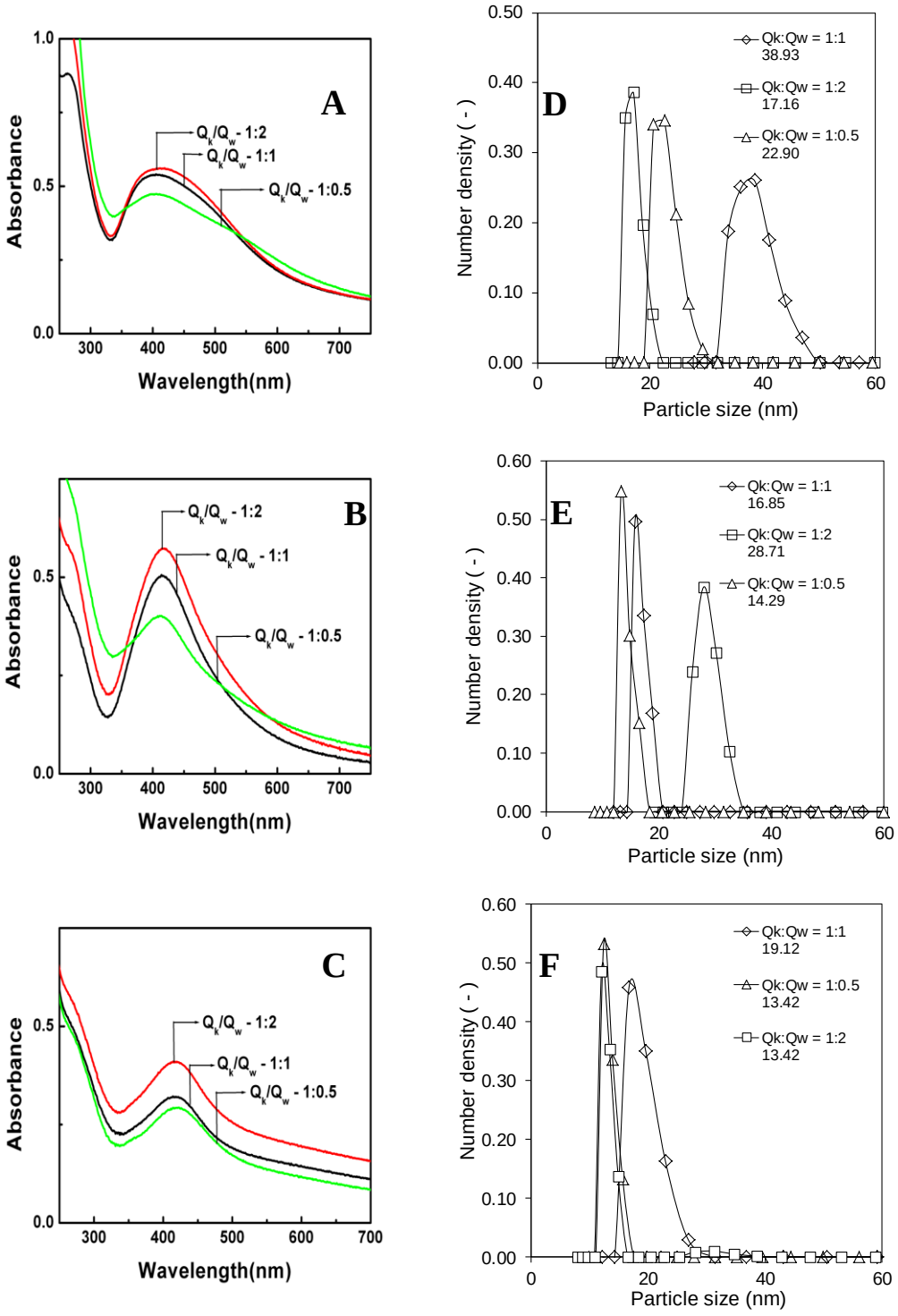

Figure 2B. 2: UV-Visible spectra and Particle size distribution (from DLS) of Ag NPs synthesized in kerosene- water system at different kerosene to reactant phase (aqueous solution) flow ratios at a total flow rate of [A and D: 1 mL/min (residence time 10.5 sec), (B and E) 0.1 mL/min (residence time 105 sec), (C and F) 0.035 mL/min (residence time 300 sec]. The legends in the particle size distribution plots indicate the flow ratio of two phases (Kerosene: Water) and the corresponding value of weight averaged particle size in nm.

2B.3.1.a.2 TEM analysis:

TEM images of Ag NPs synthesized in kerosene-water segmented flow at different volumetric flow ratios of kerosene to water and at a total flow rate of 0.035 mL/min are shown in figure 2B.3. Along with a large number of small particles, a few bigger particles were also seen in the images. The fraction of bigger particles decreased with decrease in the reactant aqueous phase slug size. The particle size observed in light scattering measurements was bigger than the actual TEM images. In addition to this, many of the small particles could not be detected by DLS. This is obvious because, in light scattering measurements hydrodynamic size of the particles is measured and the scattering from bigger particles overwhelm that of the small particles.

2B.3.1.b Gas – liquid segmented flow:

Like in kerosene water segmented flow here also the particles were synthesized at different flow ratios of inert to reactant phase 1:1, 1:2 and 1:0.5 by adjusting the flow rates by syringe pumps.

2B.3.1.b.1 UV – Visible and DLS analysis:

The UV-Visible spectra of silver nanoparticles synthesized at different residence times shows that the absorbance intensity of Ag NPs increase with increase in residence time (figure 2B.4, A-C). This trend was similar to that of the homogeneous flow (unlike in kerosene – water segmented flow). The DLS analysis of the samples is shown in figure 2B.4 (D-F). Since the reaction time is 300 s, it is quite evident that, as the residence time increases the reaction goes to completion and results small particles sizes. However, while the average particle size decreased from the flow rate ratio (Qg/Qw) of 1:2 to 1:1 in all the cases, the particle size did not change much as the flow ratios were changed from 1:1 to 1:0.5.

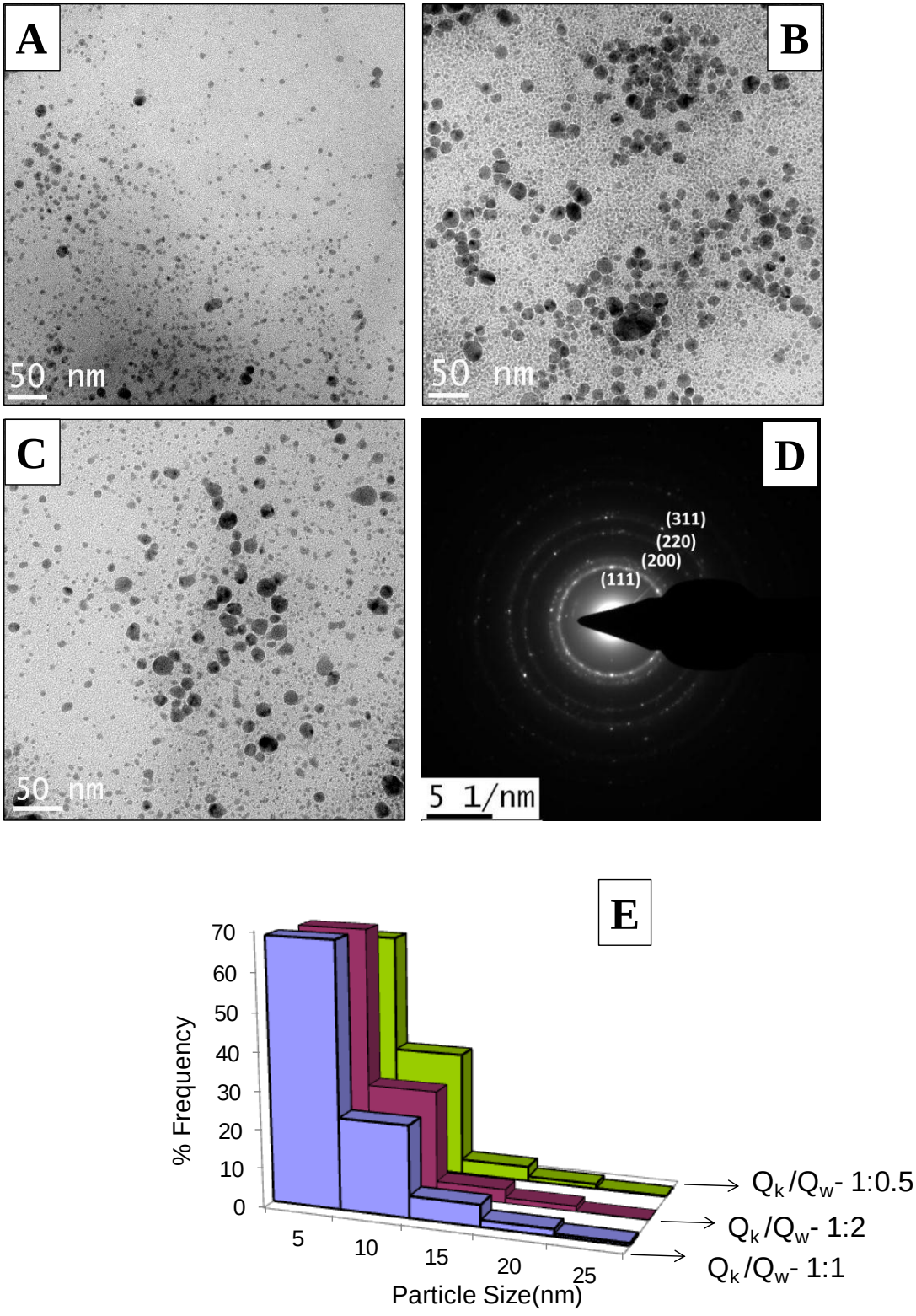

Figure 2B. 3: TEM images of Ag NPs synthesized in kerosene - water segmented flow at a total flow rate of 0.035 mL/min (A) Q_k/Q_w = 1:0.5, (B) Q_k/Q_w = 1:1, (C) Q_k/Q_w = 1:2, (D) Selective area electron diffraction of the particles shown in (B) and (E)shows particle size distribution from corresponding TEM images.

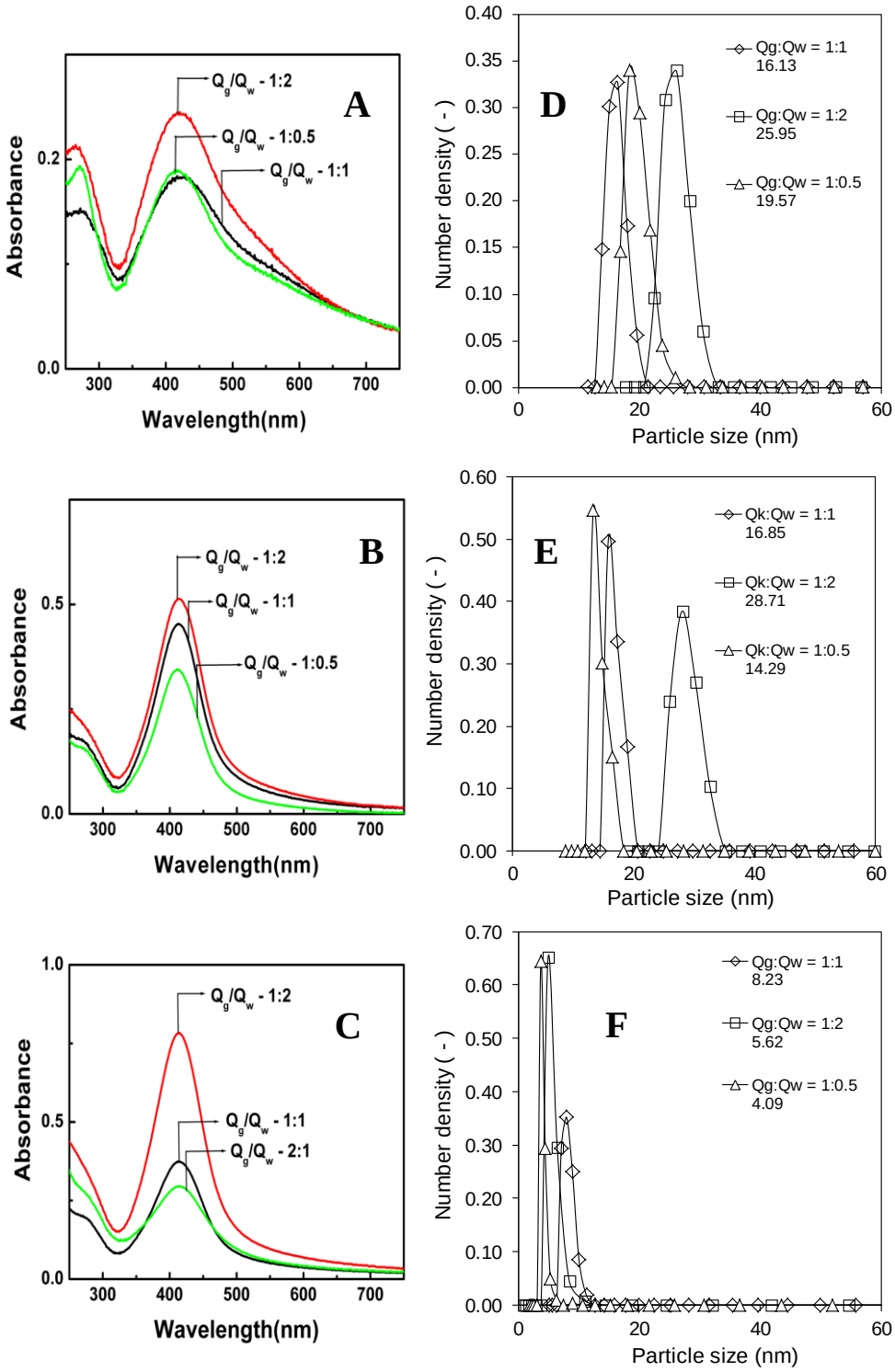

Figure 2B. 4: UV-Visible spectra and Particle size distribution (from DLS) of Ag NPs synthesized in gas (air) - water system at different gas (air) to reactant phase (aqueous solution) flow ratios at a total flow rate of (A) 1 mL/min (residence time 10.5 sec), (B) 0.1 mL/min (residence time 105 sec), (C) 0.035 mL/min (residence time 300 sec). (D, E, F) are the corresponding particle size distribution from DLS. The legends in the particle size distribution plots indicate the flow ratio of two phases (Air: Water) and the corresponding value of weight averaged particle size in nm.

2B.3.1.b.2 TEM analysis:

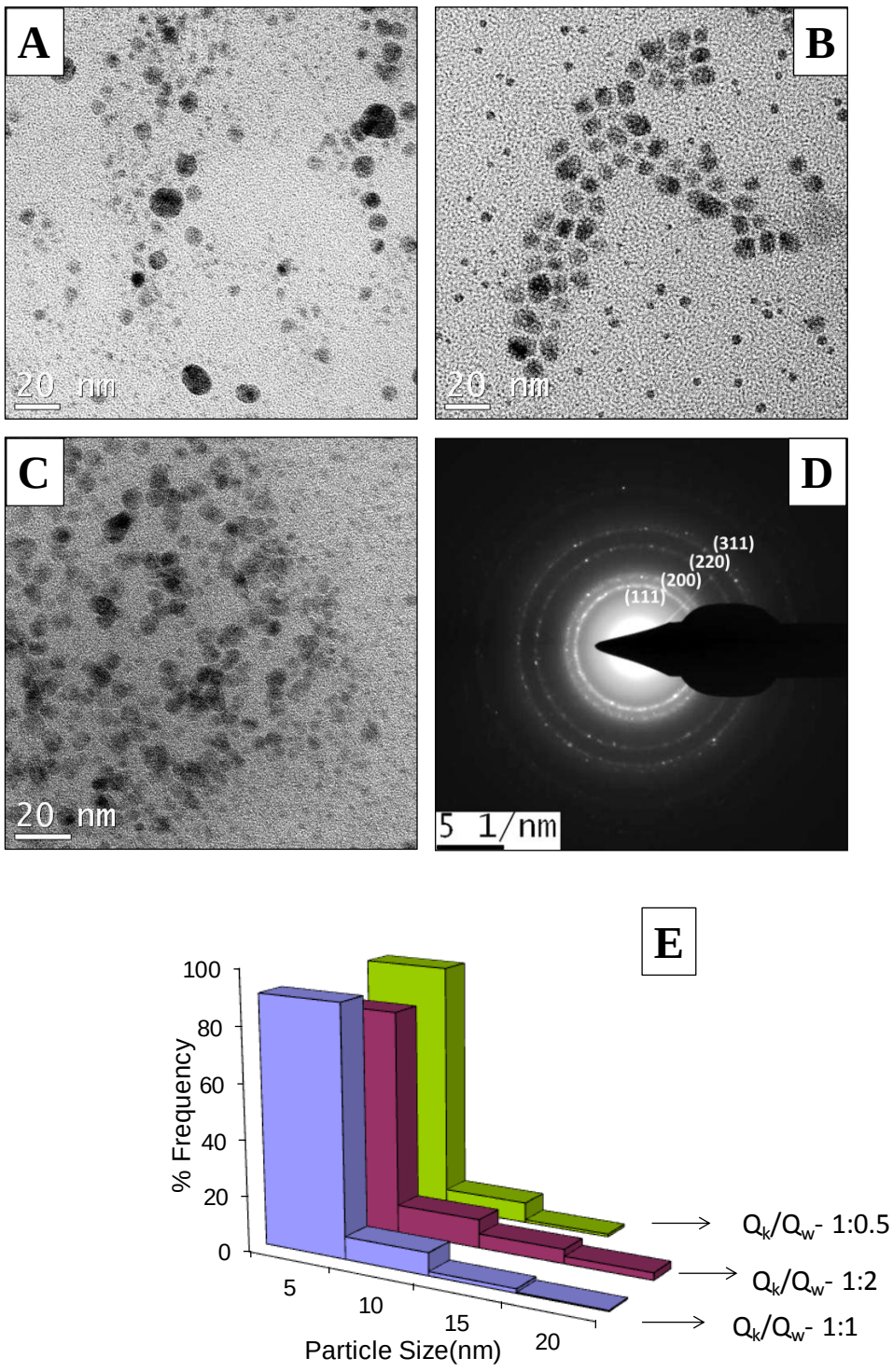

Figure 2B. 5: TEM images of Ag NPs synthesized in gas(air) - liquid segmented flow at a total flow rate of 0.035 mL/min (A) Q_G/Q_w = 1:0.5, (B) Q_G/Q_w = 1:1, (C) Q_G/Q_w = 1:2 and (D) is the SAED pattern of the particles shown in (B) and corresponding particle size distributions are given in (E).

TEM images of Ag NPs synthesized at a total flow rate of 0.035 mL/min in air–water segmented flow at different volumetric flow ratios of air and water are shown in figure 2B.5. The particle size distribution was seen to get narrow with decrease in phase fraction of the reacting aqueous liquid.

2B.3.1.b.3 XRD analysis:

The PXRD of the Ag nanoparticles synthesized in kerosene – water and air – water segmented flows at total flow rate of 0.035mL/min are shown in the figure 2B.6. The data was compared with the standard JCPDS file no - 04-0783 and XRD patterns confirm the crystalline nature of the sample.

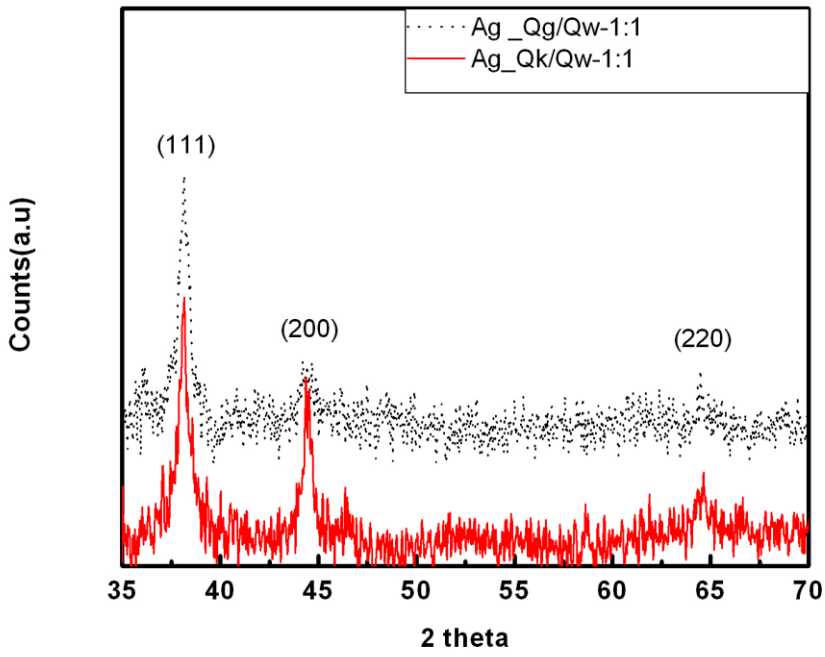

Figure 2B. 6: PXRD of the Ag nanoparticles synthesized in kerosene-water and air –water segmented flows with a flow rate of 0.035 mL/min and flow ratio of inert to aqueous reactant phase1:1.

2B.3.2 Segmented flow synthesis of Ag NPs in 1 mm SS 316 and 1 mm PMMA microreactors:

From the previous results, it can be easily realized that, there is a significant variation in the observed particle size distribution for the case where reaction phase is the continuous phase or dispersed phase that is achieved by varying the nature of inert phase. To further understand the role of hydrodynamics in the continuous phase and the dispersed phase on the particle sizes, the experiments were carried out in 1 mm spiral microchannel made in SS316 and also in PMMA. In the former case, the reacting aqueous phase is the continuous phase while in the latter case, it is in dispersed state, because of wettability differences. Thus, with identical inert phase material, the particle size distribution at the outlet will entirely be because of the mode in which aqueous phase is used. Especially two different situations arise here. One where a inter-slug mass transfer is possible and another where it is completely avoided.

TEM images of the corresponding Ag NPs are shown in figure 2B.7. Interestingly, for the case of SS spiral microreactor, the particles were seen to be scattered over the entire TEM grid with less extent of polydispersity. For the case of PMMA microchannel reactor, the particle size distribution was almost bimodal with by increased number of large size particles. The smaller size particles were almost of identical size range for both the cases, while the larger particle sizes were relatively high for PMMA microchannel.

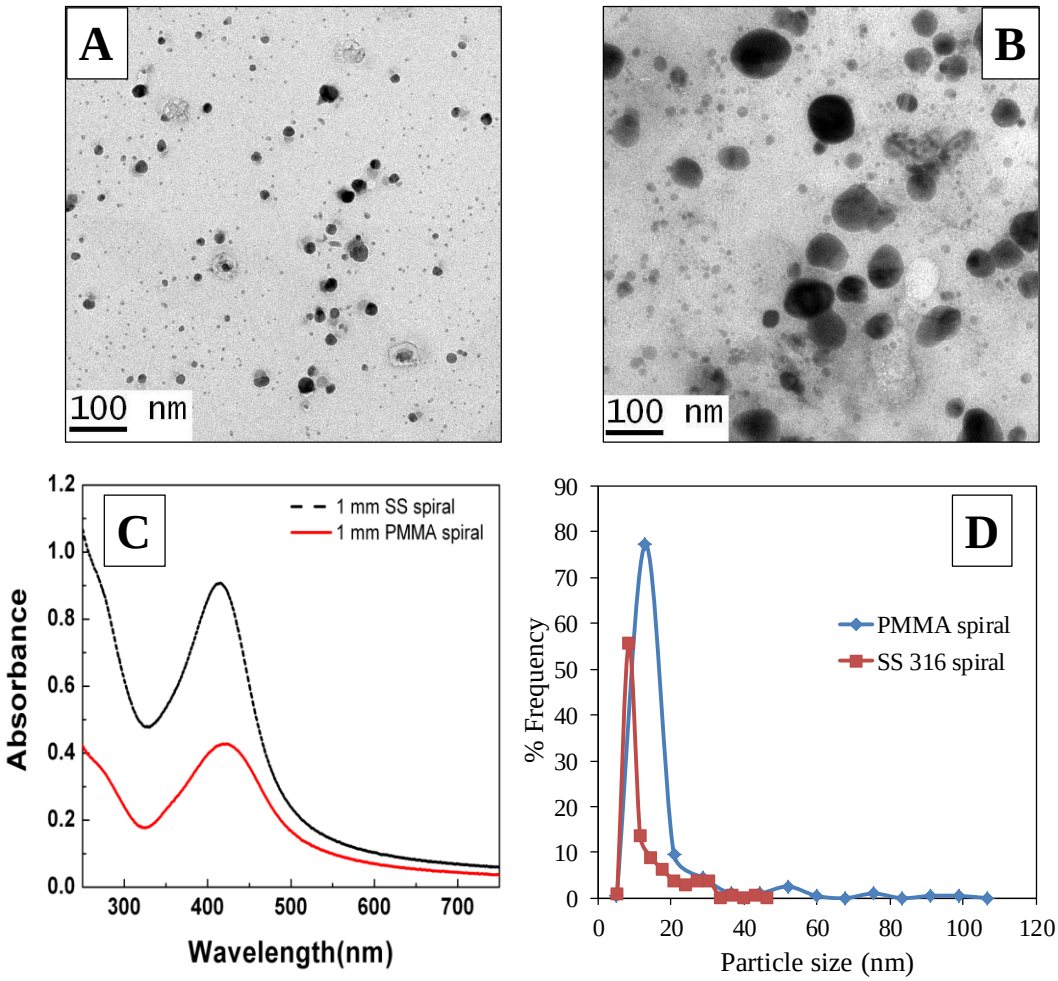

Figure 2B. 7: TEM images of the Ag NPs synthesized in kerosene-water segmented flow in 1mm spiral microchannel made of (A) SS 316, (B) PMMA and (C) UV-Vis spectra of the Ag NPs and (D) is the particle size distribution from TEM images.

2B.3.3 Small nozzle (0.5 mm PEEK) for segmentation:

Further to the analysis of particle sizes in PMMA microchannel with 1.38 mm i.d. SS316 contact section, experiments were carried out using a PEEK 4-way connector having 0.5 mm i.d. All other experimental conditions were maintained identical. The UV-Visible and DLS results of Ag NPs synthesized in gas-water and kerosene-water in PMMA spiral microreactor with 0.5 mm PEEK fitting are shown in the figure 2B.8. The observations were similar to those obtained using a larger contact device (1.38 mm i.d SS micromixing unit). Here also, we observed the absorbance intensity for Ag NPs synthesized in kerosene – aqueous reactant segmented flow to be more than that obtained for air – aqueous reactant segmented flow. The average slug size of reactant phase is nearly same in both the cases (kerosene-water and gas-water) and there was not much difference in particle size distribution from DLS in both the cases, however for both the segmented flows, the mean particle sizes were different.

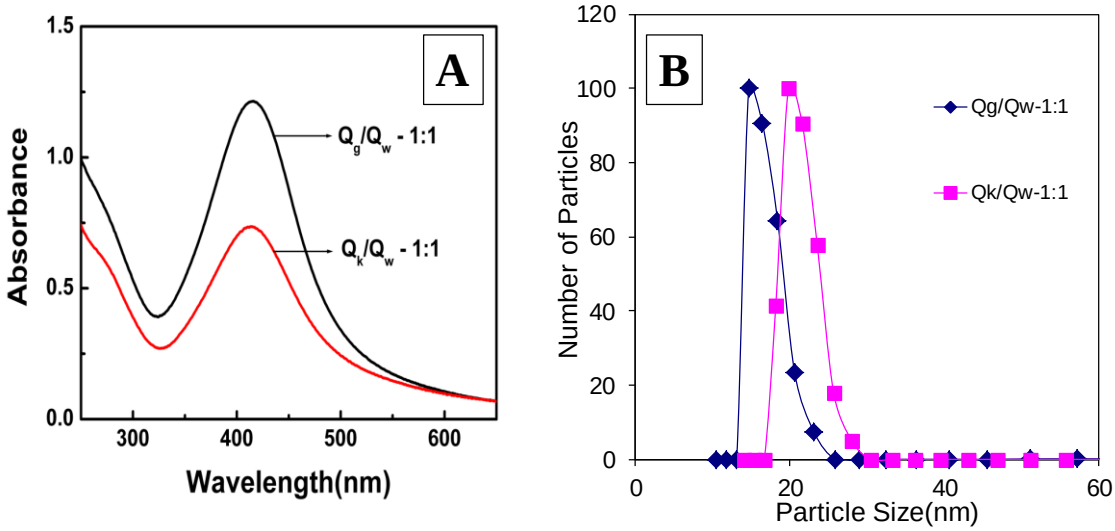

Figure 2B. 8: (A) UV-Visible spectra and (B) DLS particle size distribution of Ag nanoparticles synthesized in segmented flow in 0.5 mm spiral with 0.5 mm PEEK micromixer.

The TEM images of the particles synthesized in kerosene – water and gas – water segmented flows shown in the figures 2B.9 and 2B.10 respectively. Smaller particles with narrow size distributions were observed in both cases as compared to the particles synthesized using 1.38 mm i.d SS 316 as micromixer.

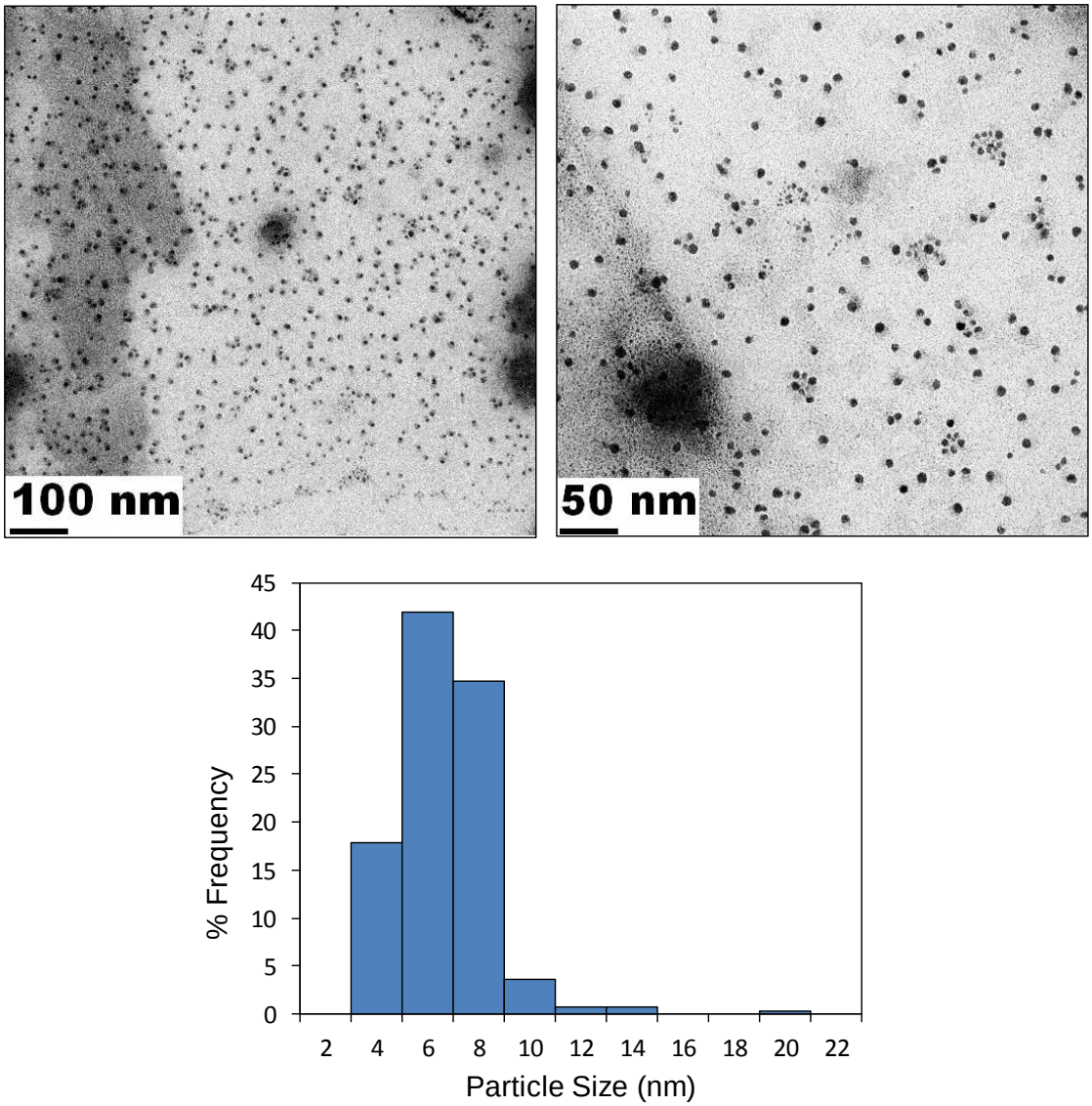

Figure 2B. 9: TEM images and particle size distribution of Ag nanoparticles synthesized in kerosene – water segmented flow in 0.5 mm spiral with 0.5 mm i.d PEEK micromixer.

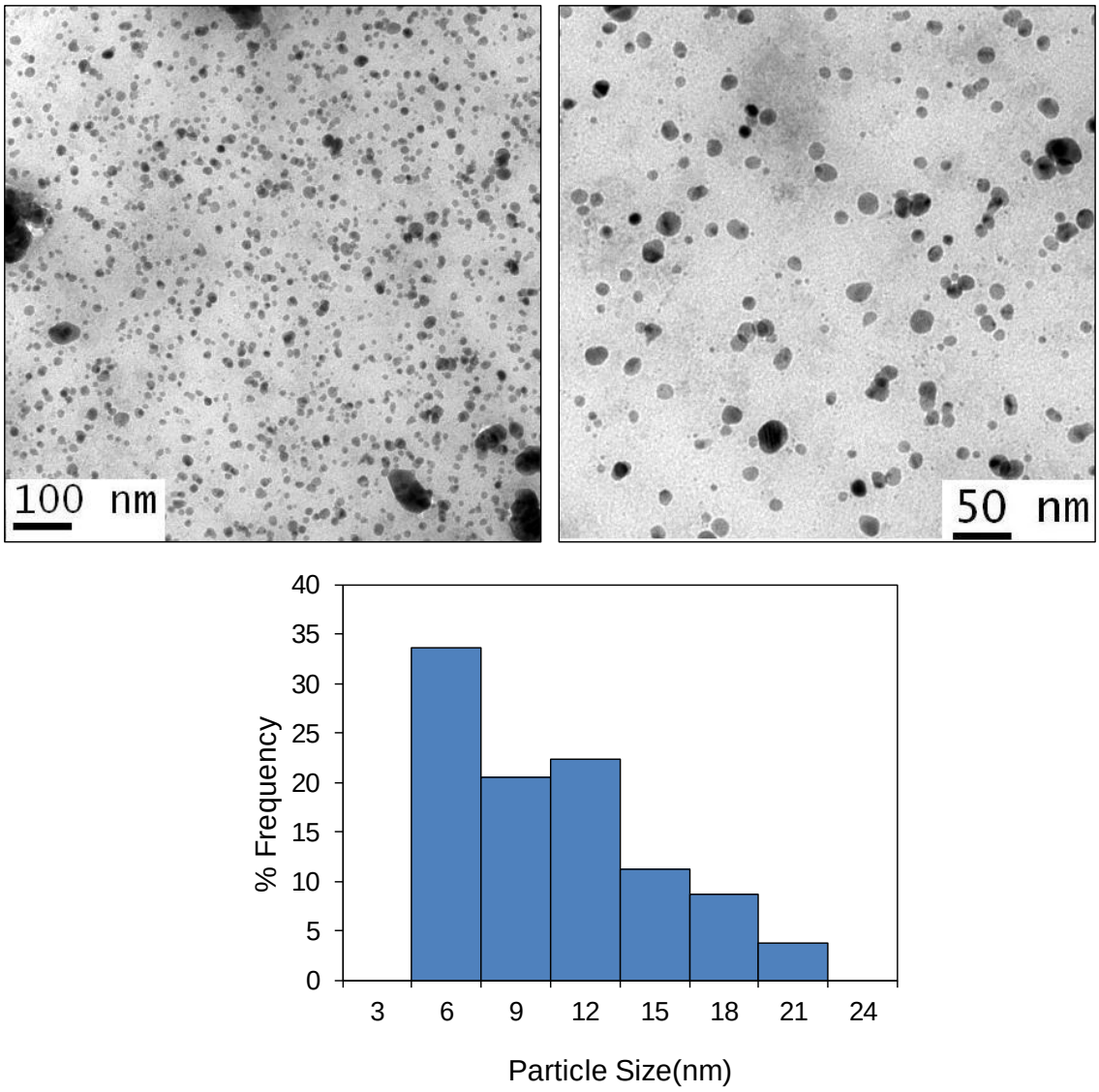

Figure 2B. 10: TEM images and particle size distribution of Ag nanoparticles synthesized in air – water segmented flow in 0.5 mm spiral with 0.5 mm i.d PEEK micromixer.

2B.4 Discussion:

2B.4.1 Using SS 316 (i.d 1.38 mm) micromixer

2B.4.1.a Liquid - liquid segmented flow:

In the UV- Visible spectra of Ag nanoparticles synthesized in liquid - liquid segmented flow (using kerosene), unexpectedly, the absorbance intensity of nanoparticles decreased with increase in residence time (figure 2B.2). From this observation (decrease in intensity of optical spectra) we realized that, the sophorolipid could have some solubility in kerosene[33, 34] leading to a loss of available reducing agent in the aqueous phase.

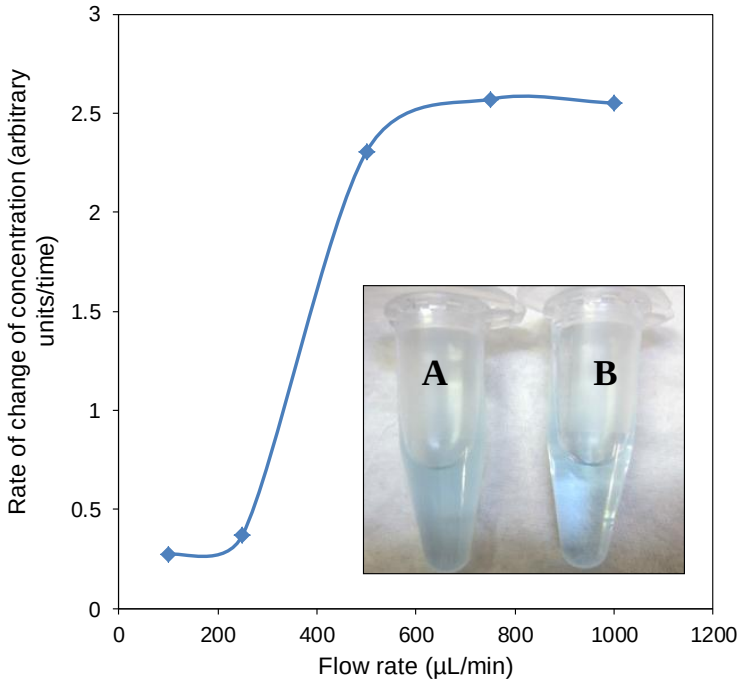

Figure 2B. 11: Rate of change in the sophorolipid concentration in kerosene with flow rate. Inset- Photographs of the kerosene phase (A) with sophorolipid and (B) pure kerosene.

The rate of diffusion of sophorolipid into kerosene would increase with increase in the flow rate, which helps to enhance the interfacial mass transfer. Therefore, the amount of lipid which was diffusing into the kerosene phase at different flow rates was measured and the data is given in figure 2B.11. However at lower flow rates, although the interfacial mass transfer rates are relatively low, the reactants and the inert phase are in contact for longer time, which makes relatively larger amount of the reactant diffuse in the inert phase. This feature is more prominent at higher temperature corroborating the observation of decreased absorbance with increase in residence time.

At all the flow rates it was observed that the absorbance intensity is maximum when the kerosene to water (Qk/Qw) flow ratio was 1:2. As mentioned earlier, the slugs were relatively longer and would have relatively lower shear rate (~3.1 s^{-1} at total flow rate of 0.035 mL/min). Smaller values of shear rate would induce relatively poor internal circulation finally leading to poor mixing of reactants in the dispersed phase. At identical flow rate, varying the flow rate ratio of the inert phase and the aqueous reactants also showed that in 1:2 case there is higher phase hold-up of the reactants resulting in more number of particles. Importantly, longer slugs will have more quantity of reactants to be mixed by internal recirculation (although the internal recirculation is weak in these slugs) and hence would yield higher absorbance in UV-Visible spectra with wider particle size distribution. On the other hand, smaller slugs (at high shear rate) induce better internal circulation and vice versa. However the role of internal circulation in governing the particle size distribution strongly depends on the relative rates of reaction and the relative rate of internal circulation. Since in this case, the reaction is relatively slow (reaction time ~ 300 s) the poor internal circulation can yield a bimodal distribution as observed or even a broader particle size distribution.

The TEM images indicate the particles to be spherical in shape (figure 2B.3). The particles sizes as well as the number of particles were seen to be more with increase in the phase fraction of the reacting phase. Since in the laminar slug flows, the particles would follow specific streamlines inside the slugs (figure 2B.12), the

internal recirculation rates would have a wider variation from slip velocity to almost stagnancy. This variation in the internal circulation rates would yield different particle sizes, largely a bimodal distribution due to stagnant regions inside the circulating regions in slugs due to directionally opposite velocities. The bimodal nature in particle size distribution was also reflected in optical spectra of Ag NPs.[35]

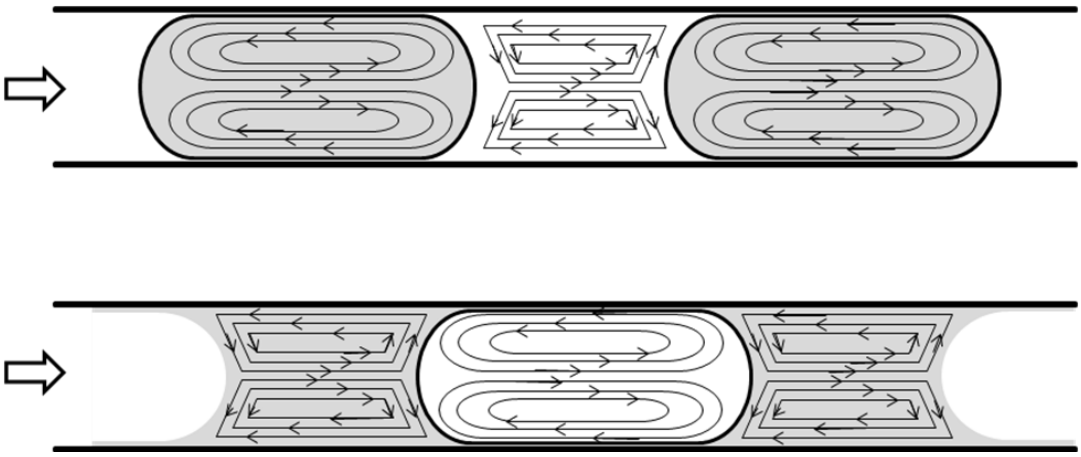

Figure 2B. 12: Schematic representation of mixing in aqueous phase reactant slugs in: (Top) kerosene-water segmented flow and (Bottom) air-water segmented flow. The bulk flow direction is from left to right (shown by block arrow). Gray color indicates the aqueous reacting phase. Typical streamlines in both the phases are shown with arrows pointing the local flow direction. This is a two dimensional depiction of actually three dimensional cylindrical segmented flow reactor.

2B.4.1.b Gas – liquid segmented flow:

To generate gas liquid segmented flow, air was used as inert phase. Unlike in case of kerosene - water segmented flow, here there is no possibility of sophorolipid diffusion to inert phase, and hence as expected the intensity of peak corresponding to Ag NPs increased with increase in residence time. As shown in figure 2B.12, in segmented flow (with finite film thickness), two circulation cells exist in every slug of the dispersed phase as well as in the continuous phase. The extent of circulation or the circulation velocities depend upon the viscosity of the two fluids as well as the relative velocities. Thus, at identical flow rate, although the shear rate would decrease with decrease in the volume fraction of reacting phase the relative values of viscosity and interfacial tension will govern the extent of internal circulation. This would clearly yield different magnitudes of internal circulation for gas-liquid and liquid-liquid segmented flows.

It is necessary to realize that, in this case, the aqueous reacting phase is always the continuous phase and the inter-slug transfer of reactant phase can not be ruled out.[36, 37] However, with increasing gas phase fraction, the film thickness (which is function of Capillary number, *Ca*) will continue to decrease and the extent of inter-slug mass transfer will also reduce. This will help to reduce the particle size as well as the size distribution. This observation is seen to hold when the reaction is allowed to complete (i.e. residence time of 300 s). For short residence times, reverse was seen to hold as the flow regimes are different. The average particle size was larger for the case of kerosene - water (aqueous phase) system when compared to air - water (aqueous phase) segmented flow. This is mainly because of the different hydrodynamic roles of aqueous phase in these two cases. Having the reacting phase in a dispersed condition helps to eliminate the slug to slug mass transfer and also reduce the axial dispersion significantly which helps the particle growth. This is unlikely to happen in the case where the presence of film helps the particles to cross between the slugs thereby leading to back-mixing causing variation in the local concentrations that reduce particle growth rate. At given fluid flow rates, larger the difference in the viscosity, density and surface tension of the two fluids, smaller will

be the dispersed phase drop size. Thus, for the case of air-water flow, always smaller slugs will form than the kerosene-water case at identical flow rates.

The particle size distribution became narrow with decrease in phase fraction of the reacting aqueous liquid. This clearly indicates that the size of gas slug has significant effect on the overall flow. Since the aqueous phase is wetting the reactor wall, the film helps to connect two liquid slugs and the presence of gas phase reduces the axial dispersion. The trend was similar in case of both kerosene-water and air-water segmented flows. As the reactant slug size decreases, the numbers of bigger particles were also decreased. These observations are consistent with the observations based on DLS data.

The large bubbles or slugs in a curved channel is surrounded by the film of continuous phase[27]and depending upon the radius of curvature, the inner and outer film thicknesses vary. A schematic is shown in figure 2B.13 A. As shown by Muradoglu and Stone,[28] in curved microchannels, the curvature helps breaking the symmetry of the thin films on either side of the dispersed phase with the inner film thickness being smaller than the outer film thickness. Thus, the film thickness on either side is a strong function of the *Ca* as well as the radius of curvature. The formulae for the estimation of the various dimensionless numbers are tabulated (table 2B.2) as follows.

Table 2B. 2: Formulae to calculate various dimension less numbers

Parameter	Inner film	Outer film
Radius of curvature	R_i	R_O
Ca	$Ca_i = \frac{\mu U_{b_i}}{\sigma} = \frac{2}{2+\beta} Ca$	$Ca_o = \mu \frac{U_{b_o}}{\sigma} = \frac{2+2\beta}{2+\beta} Ca$
Re	$R_{\text{eff}_i} = \frac{w R_i}{2R_i + w} = \frac{1}{2+\beta} w$	$R_{\text{eff}_o} = \frac{w R_o}{2R_o - w} = \frac{1+\beta}{2+\beta} w$
Film thickness (h)	$h_{i\infty} = 1.3375 R_{\text{eff}_i} Ca_i^{2/3}$	$h_{o\infty} = 1.3375 R_{\text{eff}_o} Ca_o^{2/3}$

In the above equations β is another dimensionless quantity and can be expressed $\beta = w/R_i$ (with w as the channel width and R_i is the radius of curvature). Using above equation inner and outer film thickness was calculated and plotted along the length of the spiral microreactor (figure 2B.13, B).

This variation in film thickness affects the slug velocity and velocity gradient inside the dispersed phase as well as continuous phase slug in the direction of flow as well as in the direction perpendicular to the flow. The change in slug velocity with the radius of curvature affects the internal circulation in the slug.

Thus, although the segmentation of flow would prohibit the secondary flows in spiral geometry significantly, the gradual variation in the film thickness would lead to a transient flow promoting (i) a spatially varying inter-slug mass transfer between the continuous flow slugs through the film and (ii) spatially varying mixing pattern inside the dispersed slug. These two features will have a prominent effect on the resulting particle size distribution.

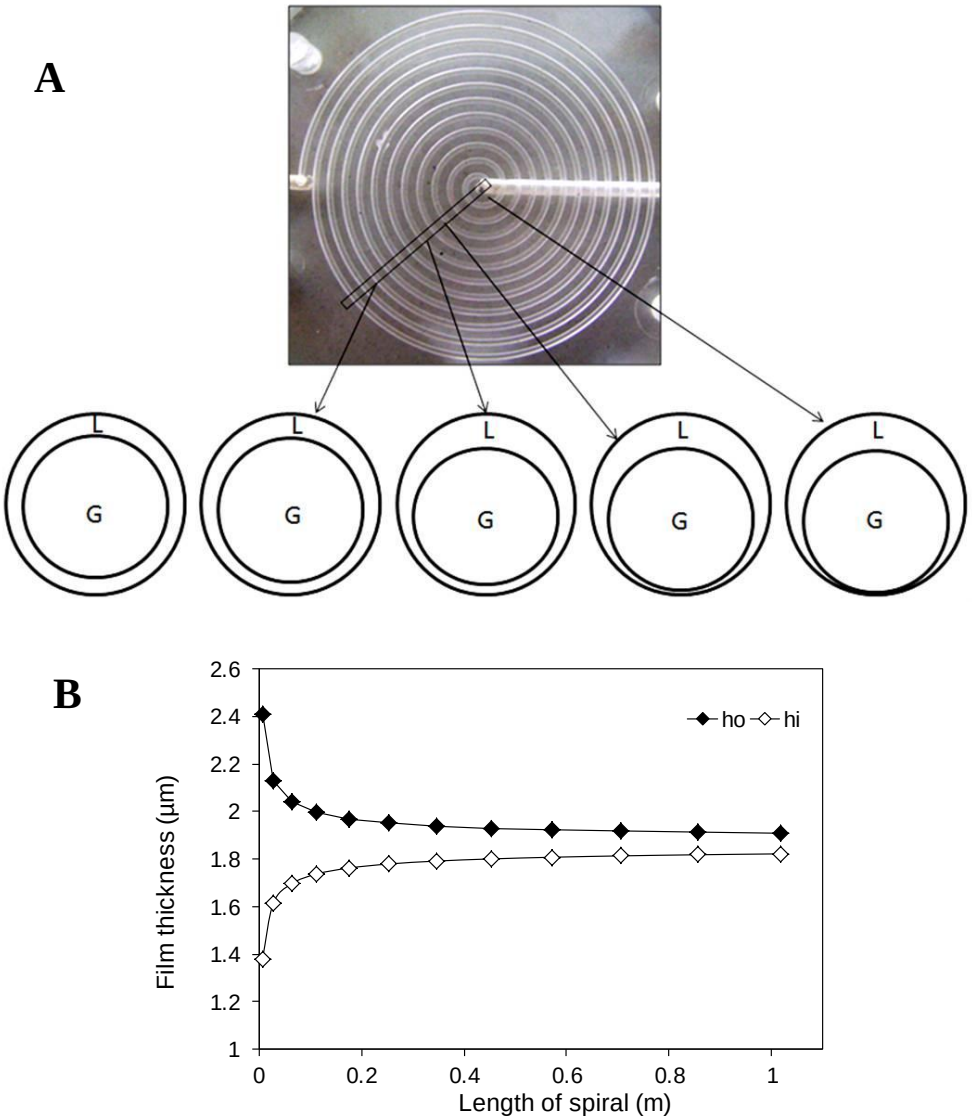

Figure 2B. 13: (A) Schematic of the cross-sections of the slug flow in expanding spiral microchannel. Close to the centre of the spiral, the inner film thickness (towards the bottom of cross-section) would be very small (the right most cross-section) as compared to the outer film thickness. The value of the inner film thickness increases and the outer film thickness decreases along the length of expanding spiral (due to increasing radius of curvature) finally reaching a typical slug flow with concentric slug at the infinitely large radius of curvature leading to a straight microchannel (the left most cross-section). (B) The variation in the film thickness (at inner and outer boundaries) with the radius of curvature of microchannel at a given inlet velocity. The calculations for the film thickness for inner and outer side are based on ref Muradoglu et al., *J. Fluid Mech.*, 2007, 570,455-466.

2B.4.2 Segmented flow synthesis of Ag NPs in 1mm SS 316 and 1 mm PMMA microreactors:

In a SS microreactor, the reacting phase was the continuous phase where the slugs were connected through a film, and it which yields inter-slug mass transfer that actually reduces the extent of variation in dispersion. On the other hand, for the PMMA microractor, the reacting slugs are dispersed and hence the internal circulation velocity and the slip between the two phases decide the particle sizes. The UV-Vis spectra from these experiments are shown in figure 2B.7 and the large number fraction of smaller particles yielded higher absorbance in case of particles synthesized in SS 316. While the possibility of diffusion of lipid into kerosene exists in both the cases, this might be more for the case of PMMA channel, probably due to smaller slugs that result into net higher flux across the interface.

2B.4.3 Small nozzle for segmentation:

Ag nanoparticles were synthesized in the 0.5 mm i.d spiral microreactor with PEEK micromixer of i.d 0.5 mm also. Here also, Ag nanoparticles synthesized in kerosene – water segmented flow were probably less in number (as indicated by lower optical spectral intensities) than those synthesized in air – water segmented flow. Aqueous phase slug sizes are measured in spiral microreacor in both kerosene-water segmented flow and air-water segmented flow with two different micromixers viz. 1.38 mm i.d SS micromixer and 0.5 mm i.d PPEK micromixer (figure 2B.14 and 2B.15). In case of slug formation due to squeezing mechanism, its size highly depends upon inlet conditions like inner diameter. Obviously using 0.5 mm micromixer, smaller slugs were observed, in both the segmented flows. The average slug size of reactant phase is nearly same in both the cases (kerosene-water and gas-water with 0.5 mm PEEK micromixer, figure 2B.15) and there was not much difference in particle size distribution as discerned by DLS measurements. However, for both the segmented flows, the mean particle sizes were different. Because of the generation of relatively smaller slugs of aqueous reactant phase, the slip velocity values are higher than the larger slugs. Higher slip velocity helps in enhancing internal circulation in slugs. From the TEM images it can be realized that, the number of bigger particles was less when compared to the Ag NPs synthesized using

SS 316 micromixer both in kerosene-water and air-water segmented flow at similar flow ratios. We implicate higher internal circulation in the smaller slug sizes as responsible for these observations.

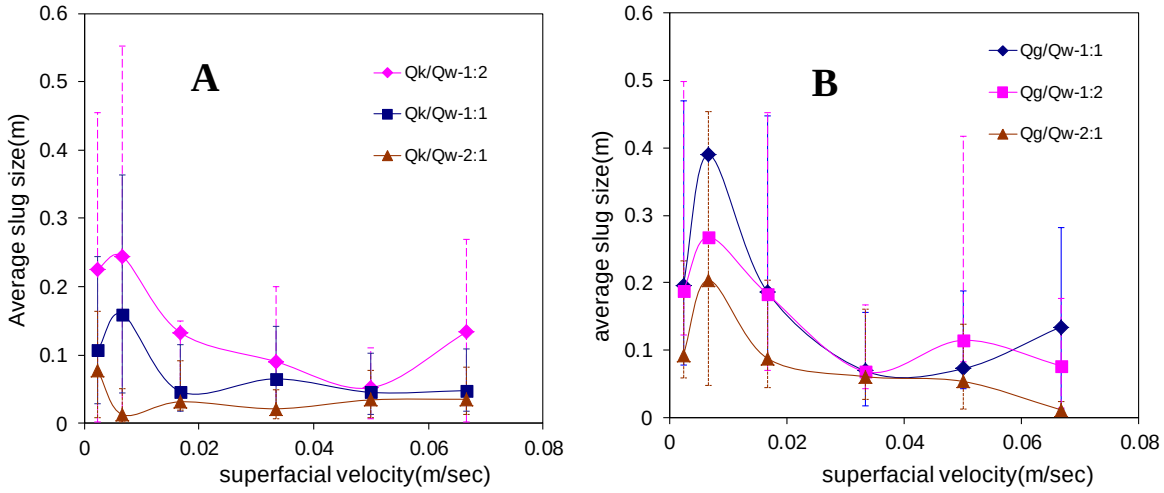

Figure 2B. 14: Average slug sizes of aqueous reactant phase with superficial velocity (A) kerosene –water and (B) air –water segmented flows with 0.5 mm spiral microreactor with 1.38 mm SS 316 micromixer.

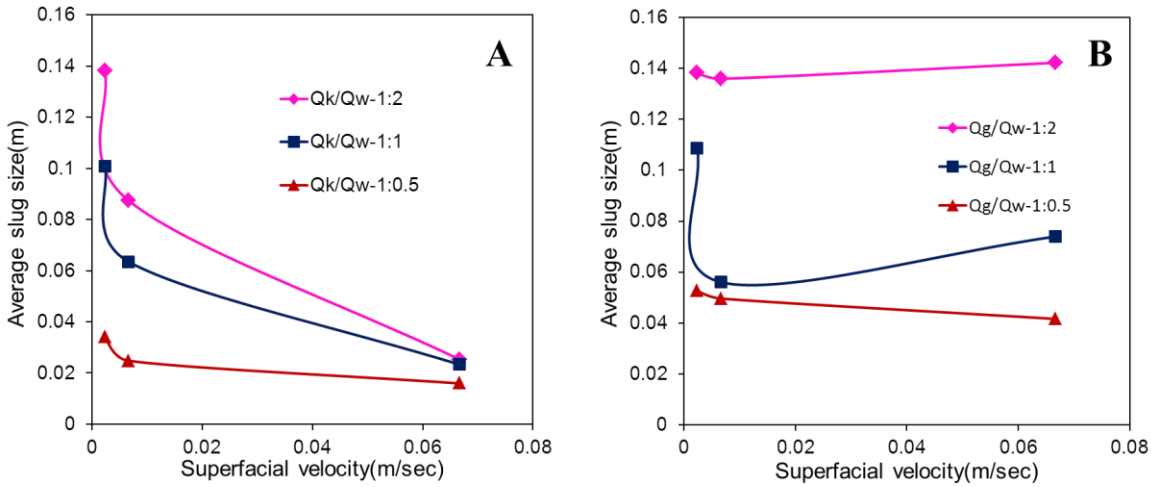

Figure 2B. 15: Average slug sizes of aqueous reactant phase with superficial velocity (A) kerosene –water and (B) air –water segmented flows in 0.5 mm spiral reactor with 0.5mm PEEK micromixer.

2B.5 Conclusions:

Segmented flow synthesis of Ag NPs in spiral microreactor was studied in both, liquid-liquid and gas-liquid segmented flows using kerosene and air as inert phases respectively. The nature of segmentation (slug sizes and inert to reactant flow ratios) on the Ag nanoparticles size was studied. The slug size affects the nature of internal mixing in the reactant phase and hence also affects the nanoparticle size distribution. This observation was consistent for both the cases. In general, the particle sizes were seen to be much smaller for gas-liquid flow rather than for liquid-liquid flow.

2B.6 References:

1. Abou-Hassan, A.; Sandre, O.; Cabuil, V., *Angew. Chem., Int. Ed.* **2010,** *49*, 6268-6286.

2. Yen, B. K. H.; Gunther, A.; Schmidt, M. A.; Jensen, K. F.; Bawendi, M. G., *Angew. Chem., Int. Ed.* **2005,** *44*, 5447-5451.

3. Wagner, J.; Kirner, T.; Mayer, G.; Albert, J.; Kohler, J. M., *Chem. Eng. J.* **2004,** *101*, 251-260.

4. Khan, S. A.; Gunther, A.; Schmidt, M. A.; Jensen, K. F., *Langmuir* **2004,** *20*, 8604-8611.

5. Wang, J. T.; Wang, J.; Han, J. J., *Small* **2011,** *7*, 1728-1754.

6. Kumar, D. V. R.; Kasture, M.; Prabhune, A. A.; Ramana, C. V.; Prasad, B. L. V.; Kulkarni, A. A., *Green Chem.* **2010,** *12*, 609-615.

7. Duraiswamy, S.; Khan, S. A., *Small* **2009,** *5*, 2828-2834.

8. Hartlieb, K. J.; Saunders, M.; Jachuck, R. J. J.; Raston, C. L., *Green Chem.* **2010,** *12*, 1012-1017.

9. Knauer, A.; Thete, A.; Li, S.; Romanus, H.; Csaki, A.; Fritzsche, W.; Kohler, J. M., *Chem. Eng. J.* **2011,** *166*, 1164-1169.

10. Cottam, B. F.; Krishnadasan, S.; deMello, A. J.; deMello, J. C.; Shaffer, M. S. P., *Lab Chip* **2007,** *7*, 167-169.

11. Li, S. N.; Gunther, P. M.; Kohler, J. M., *J. Chem. Eng. Jpn.* **2009,** *42*, 338-345.

12. Khan, S. A.; Jensen, K. F., *Adv. Mater. (Weinheim, Ger.)* **2007,** *19*, 2556-2560.

13. Frenz, L.; El Harrak, A.; Pauly, M.; Begin-Colin, S.; Griffiths, A. D.; Baret, J. C., *Angew. Chem., Int. Ed.* **2008,** *47*, 6817-6820.

14. Li, S. W.; Xu, H. H.; Wang, Y. J.; Luo, G. S., *Langmuir* **2008,** *24*, 4194-4199.

15. Hung, L. H.; Choi, K. M.; Tseng, W. Y.; Tan, Y. C.; Shea, K. J.; Lee, A. P., *Lab Chip* **2006,** *6*, 174-178.

16. Chan, E. M.; Alivisatos, A. P.; Mathies, R. A., *J. Am. Chem. Soc.* **2005,** *127*, 13854-13861.

17. Pan, Y. C.; Yao, J. F.; Zhang, L. X.; Xu, N. P., *Ind. Eng. Chem. Res.* **2009,** *48*, 8471-8477.

18. Chokkalingam, V.; Weidenhof, B.; Kramer, M.; Maier, W. F.; Herminghaus, S.; Seemann, R., *Lab Chip* **2010,** *10*, 1700-1705.

19. Groß, G. A.; Hamann, C.; Günther, P.; Köhler, J., *Chem. Eng. Technol.* **2007,** *30*, 341-346.

20. Tice, J. D.; Song, H.; Lyon, A. D.; Ismagilov, R. F., *Langmuir* **2003,** *19*, 9127-9133.

21. Shui, L.; Eijkel, J. C. T.; van den Berg, A., *Adv. Colloid Interface Sci.* **2007,** *133*, 35-49.

22. Kashid, M. N.; Agar, D. W., *Chem. Eng. J.* **2007,** *131*, 1-13.

23. Kreutzer, M. T.; Kapteijn, F.; Moulijn, J. A.; Heiszwolf, J. J., *Chem. Eng. Sci.* **2005,** *60*, 5895-5916.

24. Kulkarni, A. A.; Kalyani, V. S., *Ind. Eng. Chem. Res.* **2009,** *48*, 8193-8204.

25. Niu, H. N.; Pan, L. W.; Su, H. J.; Wang, S. D., *Ind. Eng. Chem. Res.* **2009,** *48*, 1621-1628.

26. Abate, A. R.; Poitzsch, A.; Hwang, Y.; Lee, J.; Czerwinska, J.; Weitz, D. A., *Phys.Rev.E* **2009,** *80*.

27. Kumar, V.; Vashisth, S.; Hoarau, Y.; Nigam, K. D. P., *Chem. Eng. Sci.* **2007,** *62*, 7494-7504.

28. Muradoglu, M.; Stone, H. A., *J. Fluid Mech.* **2007,** *570*, 455-466.

29. Christopher, G. F.; Anna, S. L., *J. Phys. D: Appl. Phys.* **2007,** *40*, R319-R336.

30. Kasture, M. B.; Patel, P.; Prabhune, A. A.; Ramana, C. V.; Kulkarni, A. A.; Prasad, B. L. V., *J. Chem. Sci.* **2008,** *120*, 515-520.

31. Singh, S.; Patel, P.; Jaiswal, S.; Prabhune, A. A.; Ramana, C. V.; Prasad, B. L. V., *New J. Chem.* **2009,** *33*, 646-652.

32. Cherlo, S. K. R.; Kariveti, S.; Pushpavanam, S., *Ind. Eng. Chem. Res.* **2010,** *49*, 893-899.

33. Andheria, A. P.; Bhagwat, S. S., *J. Colloid Interface Sci.* **1995,** *171*, 211-217.

34. Calvo, B.; Cepeda, E. A., *J. Chem. Eng. Data* **2008,** *53*, 628-633.

35. Inasawa, S.; Sugiyama, M.; Yamaguchi, Y., *J. Phys. Chem. B* **2005,** *109*, 9404-9410.

36. Thulasidas, T. C.; Abraham, M. A.; Cerro, R. L., *Chem. Eng. Sci.* **1995,** *50*, 183-199.

37. Thiers, R. E.; Reed, A. H.; Delander, K., *Clin.Chem* **1971,** *17*, 42-48.

Chapter 3

Part A: Surfactant assisted synthesis of triangular gold nanoplates - Understanding and optimization of reaction parameters

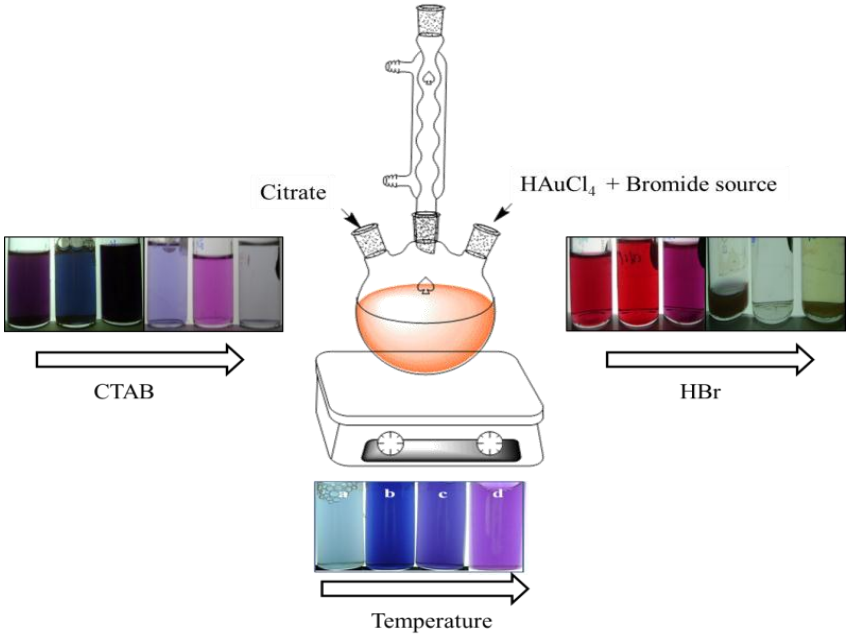

3A.1 Introduction:

So far, majority of efforts in the area of continuous flow synthesis of nanomaterials were focused on the size selective/controlled synthesis of spherical nanoparticles using microreactors. In our earlier chapters, we too focused on the size selective synthesis of spherical Ag nanoparticles using continuous flow methods. When it comes to the anisotropic nanoparticles, although they find several applications in various areas, efforts to synthesize them in large scale are very few. Several batch preparative methods are reported in literature to synthesize anisotropic nanostructures.[1, 2] Since most of these methods are sensitive to several reaction parameters and conditions, it is a big challenge to extend these processes for large scale production. Similar to the case of spherical nanoparticles, flow methods need to be extended to the anisotropic nanostructures in using micro reactors.[3]

However, there exist very few methods in the literature which discuss flow synthesis anisotropic nanostructures. Among the several anisotropic noble metal structures, only gold nanorod[4-6] and silver nanotriangle[7] syntheses were attempted by flow methods using seed mediated procedures. But these flow methods also involved few material processing batch steps (synthesis of seed particles, growth of nanorods etc.,) which were carried out of the channel[8] thus making the process not truly a continuous flow method. We believed that, developing a flow process method to synthesize anisotropic nanostructures requires the complete understanding of reaction parameters in the batch process to determine the shape evolution of a nanocrystal. Therefore, taking gold nanotriangles as model system, we address this problem in the first part of this chapter. In second part using the understanding generated in the batch process, the development of continuous flow method for these materials is presented.

Like other anisotropic structures, several methods exist to synthesize triangular nanoplates, viz. photochemical methods,[9] polyol method,[10, 11] seed mediated synthesis,[12] biological processes[13, 14] etc., and all of these synthetic methods are very sensitive to the quality and size of seed particles,[15] presence of halide ions,[16-21] surfactant purity,[22-24] methods of addition and mixing.[25] To get control over

the different parameters and to improve the yield of nanostructures it is necessary to understand and quantify the role of different reaction parameters/conditions in controlling the shape of the nanostructures.

Many reports implicate surfactant as the main shape directing agent in the synthesis of anisotropic nanostructures. It was hypothesized that these surfactants or shape directing agents (mainly CTAB[12] and PVP[11]) have specific binding ability to some of the facets of noble metals and hinder the growth in that direction. Although recent electrochemical studies support this contention,[26-28] in addition to surfactants, twinning or twinned defects also play a major role in determining the shape anisotropy.[29] Similarly stacking faults play major role in obtaining the two dimensional nanostructures (i.e. triangular/hexagonal plates).[30] The high energy nanoplate formation is favorable under kinetically controlled conditions i.e. at slow reduction conditions.[11] Hence by tuning the reaction parameters (pH, temperature etc.,) the nanoplates can be obtained without using any surfactant.[31] Ravishankar and coworkers proposed morphology diagrams to predict the formation of noble metal nanoplates by altering the free energy of reaction by tuning the reaction parameters.[31-33]

Other than photochemical methods, majority of the methods to produce triangular/hexagonal nanoplates occur under thermal conditions. Since the formation of nanoplates is kinetically controlled process,[34, 35] temperature must be playing an important role in controlling the shape and yield of the anisotropic nanostructures. The existing studies on effect of temperature on nanoplate formation (in presence of PVP or CTAB) are limited to a set of observations rather than to quantify its influence on triangular/ hexagonal plate formation. Besides this, formation of nanoplate formation is very sensitive to halide ions.[16, 17, 20] Trace amounts of halide ion existing as impurity in surfactant considerably affect the shape and yield of the nanoplates. In case of triangular nanoplates, the effect of halide ions on the shape of nanostructures was different for different methods of syntheses.[17, 36] Thus, the above discussion clearly lays the foundation for the importance of understanding the factors affecting the shape control, effect of

operational conditions, effect of halide ions on anisotropic nanoparticle formation, and to find the optimal reaction parameters to expand the scope of shape selective synthetic methods from laboratory to pilot plant to industrial scale.

Among the several anisotropic nanostructures and their methods of syntheses, we chose surfactant assisted thermal methods to synthesize triangular gold nanoplates as model system to study the effect of various reaction parameters discussed above. One such method to produce triangular gold nanoplates was reported by Huang et al.[37, 38] This approach gives relatively good yields of triangular nanoplates in a shorter reaction time which are optimal to scale up. However, the edge length of triangles by this method was reported to be very sensitive to volume of the reaction. Thus, if this method is to be adapted for the large scale synthesis of triangular nanoplates, a clear mapping between the different reaction parameters and the yield and edge-length of triangles is mandatory. In view of the above discussion, in the first part of this chapter (part A) we discuss the effect of parameters viz. temperature, the rate of heat transfer on the nucleation and growth processes, and influence of Br^- ion on the reaction progress and the properties of triangular gold nanoplates. These parameters play an important role in adjusting the edge length and thereby tune the optical properties of the triangular nanoplates.

3A.2 Synthesis of triangular gold nanoplates using surfactant assisted thermal methods:

Synthesis of triangular nanoplates was carried out by modifying the reported methods.[38] In brief, 7.5 mL of 1.7 mM sodium citrate solution, 5 mL of 1.25 mM $HAuCl_4$ solutions were prepared using Milli Q water. To the $HAuCl_4$ solution 16 mg of CTAB was added, which turned the yellow coloured $HAuCl_4$ solution to orange red indicating the formation of $HAuCl_4$-CTAB complex. A two neck, jacketed glass reactor was used as batch reactor (figure 3A.1) and above prepared solutions were poured into this, which was maintained at 90 °C. After 5-10 minutes of the reaction, the colour of the solution turned to bluish brown indicating the formation of triangular plates and the reaction was allowed to proceed for 1 hour to ensure

completion. As described in introduction, effect of several parameters on the number yield and edgelength of triangular nanoplates were studied.

3A.2.1 Effect of temperature/heat transfer:

The following experiments were performed to understand the effect of temperature on the edgelength and yield of the triangular nanoplates.

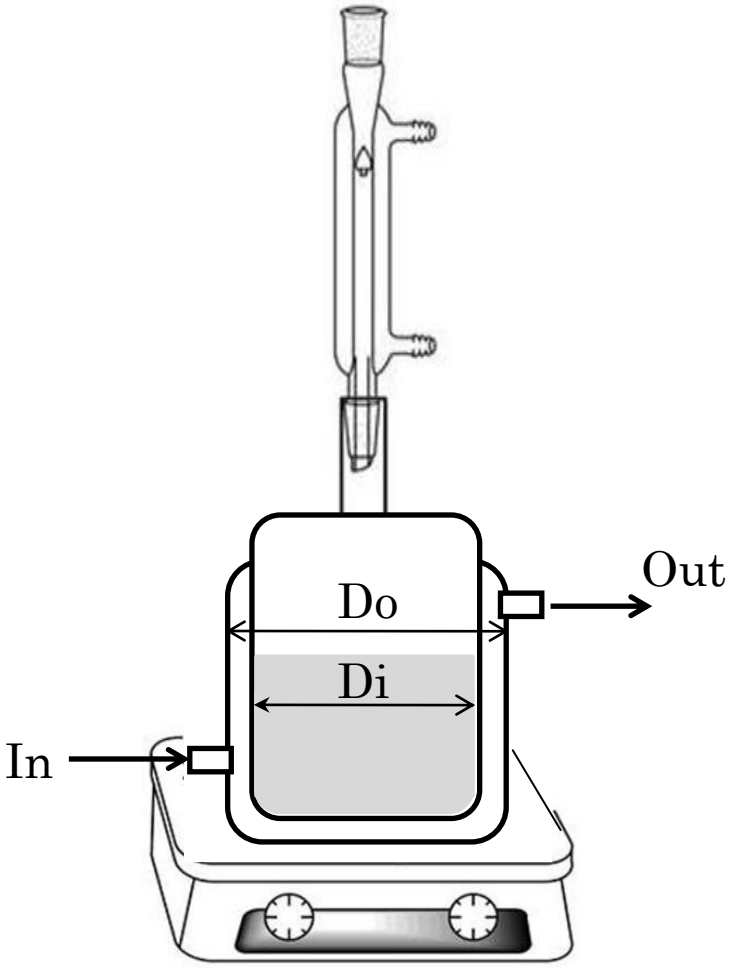

Figure 3A. 1: Schematic of the experimental set up, used as batch reactor to study the effect of different reaction parameters on synthesis of triangular nanoplates.

Experiment (a): To the glass reactor which was maintained at 90 °C, both 7.5 mL of sodium citrate and 5 mL of $HAuCl_4$ - CTAB solutions (which were maintained at room temperature 27 °C) were added simultaneously.

Experiment (b): To the glass reactor containing 7.5 mL of trisodium citrate solution (which was preheated to 90 °C), 5 mL of $HAuCl_4$-CTAB solution preheated to 27 °C was added.

Experiment (c): To the glass reactor containing 7.5 mL of trisodium citrate solution (which was preheated to 90 °C) 5 mL of $HAuCl_4$-CTAB solution preheated to 50 °C was added.

Experiment (d): To the glass reactor containing 7.5 mL of trisodium citrate solution (which was preheated to 90 °C) 5mL of $HAuCl_4$-CTAB solution preheated to 70 °C was added.

In Experiment (a) mixing of the precursors resulted in a colourless solution in less than a minute and after about 2 minutes the solution turned to light bluish brown. The intensity of the solution colour increased with time and saturated after 5 minutes. In Experiments (b), (c) and (d) once $HAuCl_4$-CTAB solution was added to tri sodium citrate solution at 90 °C, the orange red color of the $HAuCl_4$-CTAB solution vanished very fast. Depending upon the temperature to which the $HAuCl_4$-CTAB solutions were heated the colourless solution turned to pink colour initially and then to blue or purple. Aliquots from the reaction mixture were collected from time to time and were subjected to further characterizations.

3A.2.1.a UV-Vis-NIR and PXRD analysis:

Aliquots from the different experiments are taken at intervals of 5, 10, 15, 20, 25 and 30 minutes. Figure 3A.2 shows the time dependent UV-Vis-NIR spectra of triangular gold nanoplates, synthesized at different reaction conditions that are referred to as experiment (a) – (d) and the corresponding photographs of the samples. The distinguishable features in the optical spectra of triangular nanoplates synthesized in experiment (a) are located at 533 and 660 nm (panel (a), figure 3A.2). These could arise from the anisotropic shapes of the nanoparticles and are ascribed

to the quadrupole (533 nm) and dipole (~ 660) surface plasmon resonances (SPRs) of the triangular nanoplates.

One can easily notice that position of the SPR band at ~535 nm is not altered much with the reaction time but the peak at 660 nm, which is a sign of anisotropy, shifted to 680 nm after 10 minutes of the reaction time. No further shift in the position of this band is observed till the completion of reaction. This observation indicates that the edge length (in a more prominent way, aspect ratio) of the triangular nanoplates does not increase after 10 minutes of the reaction and the increase in peak intensity is due to the increase in population of triangles. Except in experiment (a), in all the remaining experiments the spectral features corresponding to anisotropy are observed only after 10 minutes of the reaction and before 10 minutes of reaction only one peak (λ_{max} = 530-550 nm) is observed. Interesting morphological features are observed in the electron microscopic images of some of these aliquots, which are discussed in detail later on. Like in case of experiment (a), we observed two peaks in experiment (b) (panel b, figure 3A.2) and these two peaks are positioned at ~555 nm and ~ 590 nm after 15 minutes of the reaction. As in case of experiment (a), the ~555 nm peak position remained unchanged and the ~590 nm peak is shifted to 600 nm as the reaction time progressed. In experiment (c) also the peak at ~555 nm is retained, but the second peak is blue shifted to ~583 nm and very little shift in the position of this peak (583 nm to 587 nm) is observed as time proceeds (panel c, figure 3A.2). In experiment (d) instead of two distinct peaks, a broad peak is observed (panel d, figure 3A.2) and no time dependent changes were observed in its position. Figure 3A.3 compares the optical spectra of triangular nanoplates synthesized from experiments (a), (b), (c) and (d) after 60 minutes of the reaction. It can be easily noticed that the optical spectra of samples obtained from different experiments display distinct features. The SPR peak observed at ~680 nm in experiment (a) is shifted to 600 nm and 587 nm in experiments (b) and (c) respectively while in (d) the second peak is not distinguishable. This clearly indicates the change in edge length of the triangular nanoplates.

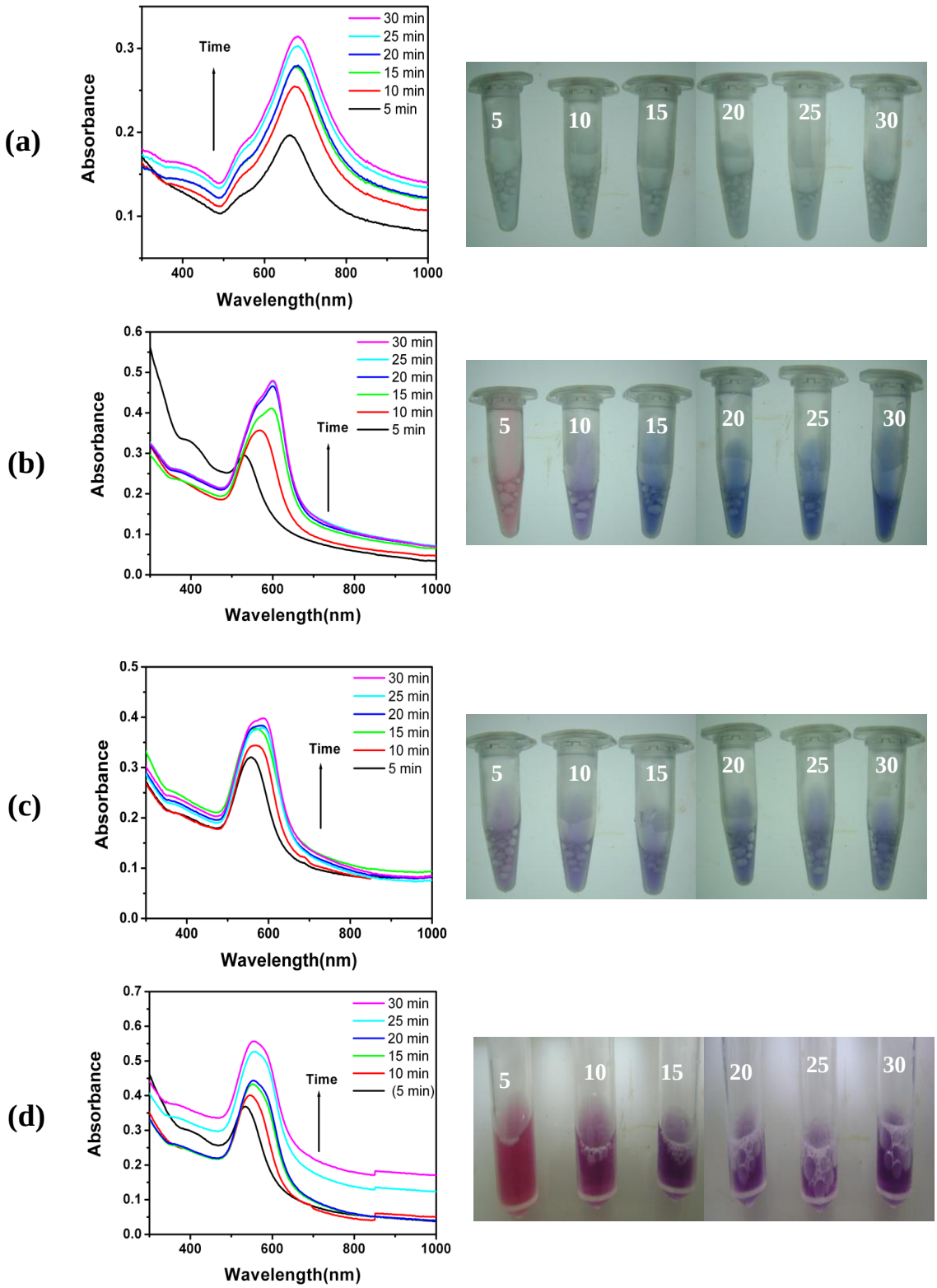

Figure 3A.2: UV-Vis-NIR spectra of Au nanostructures synthesized in different experimental conditions from (a) to (d) and corresponding photographs of the sample aliquots from different experiments are given beside the each spectra.

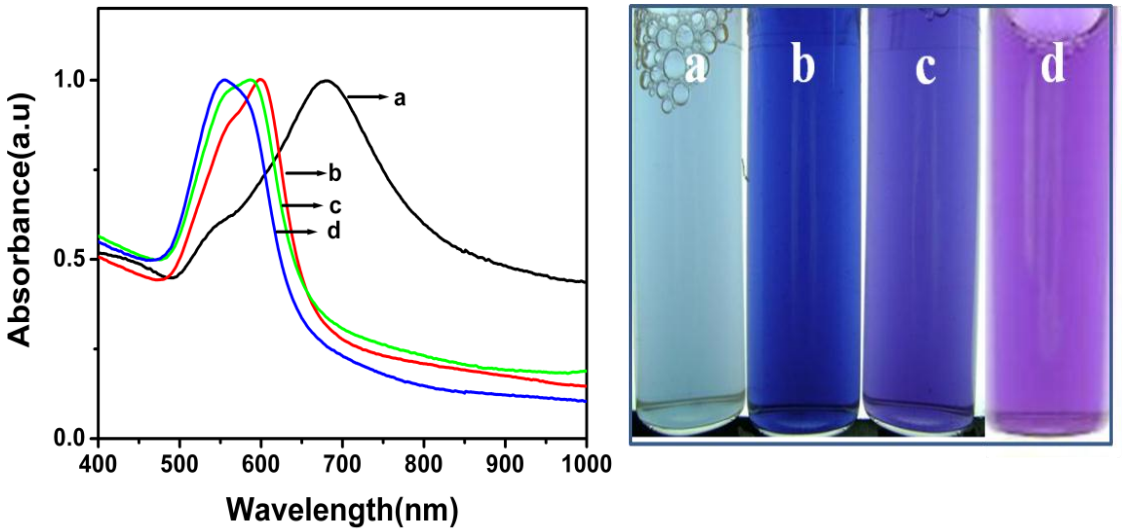

Figure 3A. 3: UV-Vis-NIR spectra of the samples collected after 60 min of the reaction from experiments (a) to (d) and corresponding photograph of the samples.

The powder X-ray diffraction (PXRD) was recorded for the samples collected after 60 minutes. The XRD data showed (figure 3A.4) that all the samples are predominantly oriented along (111) plane although very weak intensity peaks corresponding to (200) are also observed in samples collected form experiments (c) and (d).

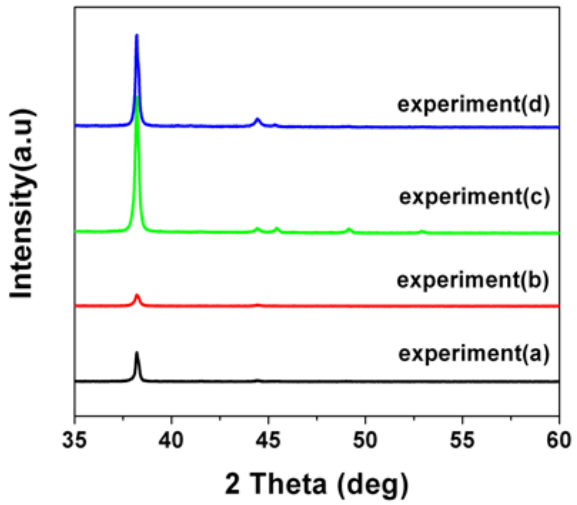

Figure 3A. 4: PXRD of triangular Au nanoplates synthesized under different experimental conditions (a) to (d).

3A.2.1.b TEM analysis:

TEM images of sample aliquots collected after 5 minutes and 60 minutes of the reaction from experiments (a) to (d) are shown in the figure 3A.5 to 3A.8. Samples which were collected after 5 minutes of the reaction were coated directly on TEM grid without any centrifugation. These images helped to identify the actual intermediate nanostructures which led to final triangular shape. In experiment (a), even after 5 minutes, triangular nanoplates can be seen with some spherical particles while after 60 minutes all the particles are featured with very sharp edged triangular nanoplates with some polyhedral structures (figure 3A.5). Results of experiment (b) are in complete contrast to this. Here, for the sample collected after 5 minutes, dendritic intermediate structures can be seen (figure 3A.6). Huang et al[38] described that such dendritic structures originate from central core which is similar to our case. At the edge of a branch of these dendrites, aggregated small triangular shaped particles are observed which get disintegrated and grow to triangular nanoplates with temperature and time. In experiments (c) and (d) no dendritic structures are seen in the samples collected after 5 minutes (figure 3A.7 and 3A.8). Since in both in experiments (c) and (d) precursors are pre-heated before mixing and the initial reaction rates were much higher than the experiments (a) and (b), the dendrimeric structures would have possibly formed in less than 5 minutes and hence we are unable to see them. From the TEM images of the samples collected after 60 minutes of the reaction, it is very clear that the edge-length and yield of the triangles have decreased from experiments (a) to (d). In case of exp (a) the edge length of the triangular plates is in the range of 150 – 350 nm which decreases to 50-125 nm, 40-70 nm, 30-60 nm in experiments (b), (c), (d) respectively (see the images D of the figures 3A.5, 3A.6, 3A.7, & 3A.8). This observation is also reflected in the optical properties of the corresponding nanostructures.

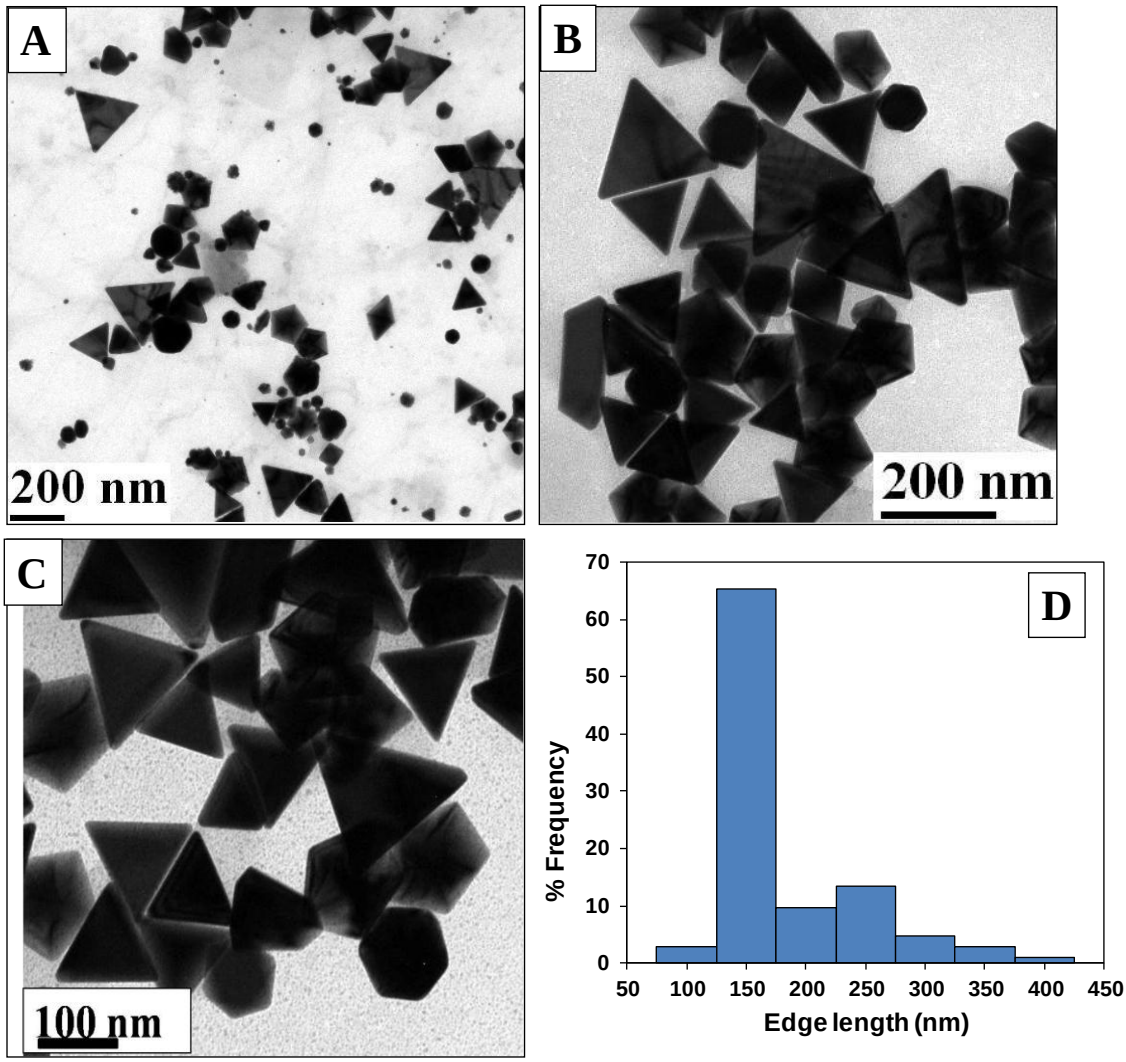

Figure 3A. 5: TEM images of triangular gold nanoplates synthesized in experiment (a) after 5 minutes (images A), 60 minutes of the reaction (images B &C) and D shows the representative edge length distribution of triangular nanoplates.

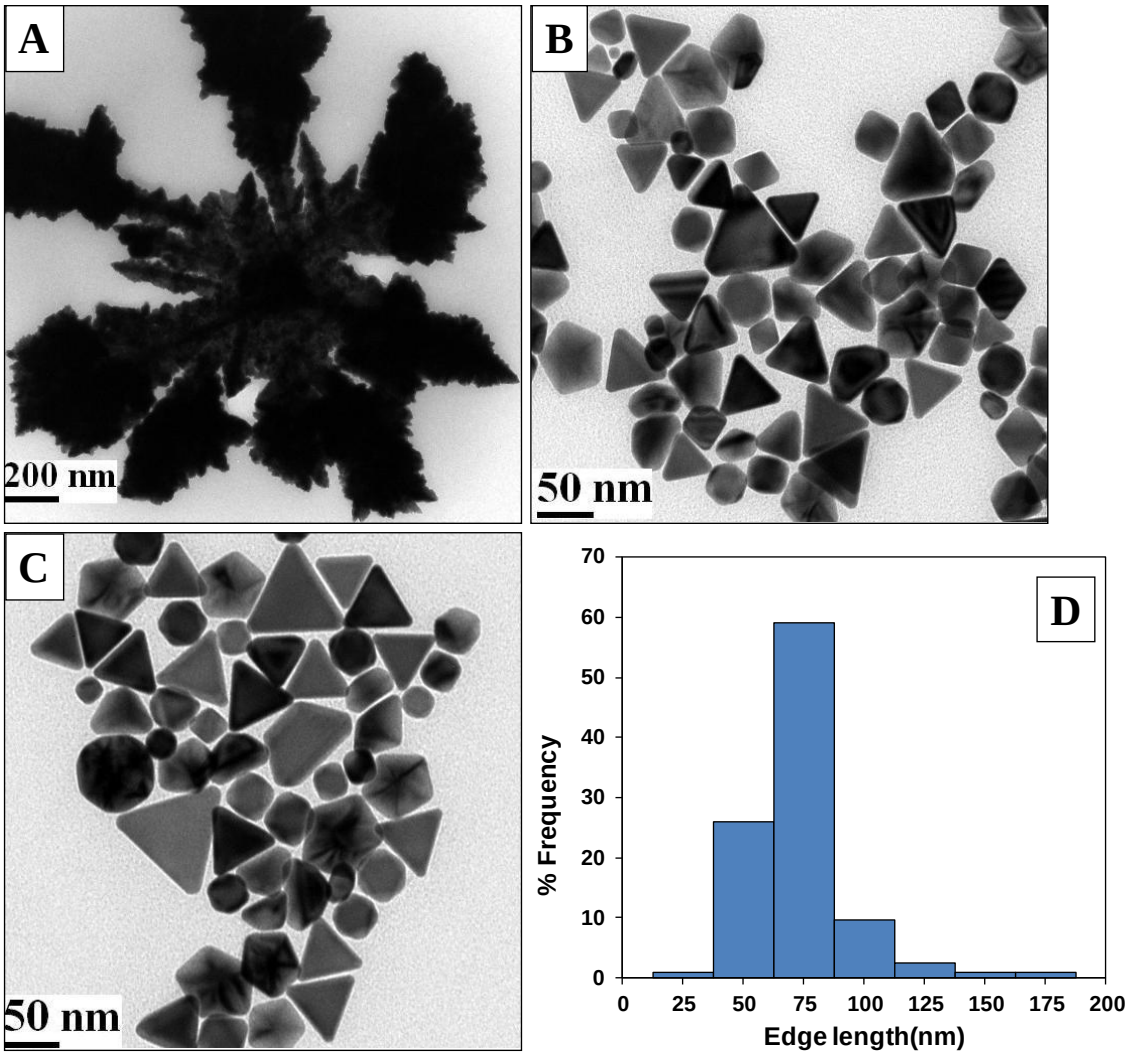

Figure 3A. 6: TEM images of nanostructures synthesized in experiment (b). Image A shows the dendritic intermediate nanostructures obtained after 5 minutes of the reaction, (B & C) represents the triangular nanoplates obtained after 60 minutes of the reaction and D shows the representative edge length of the triangles.

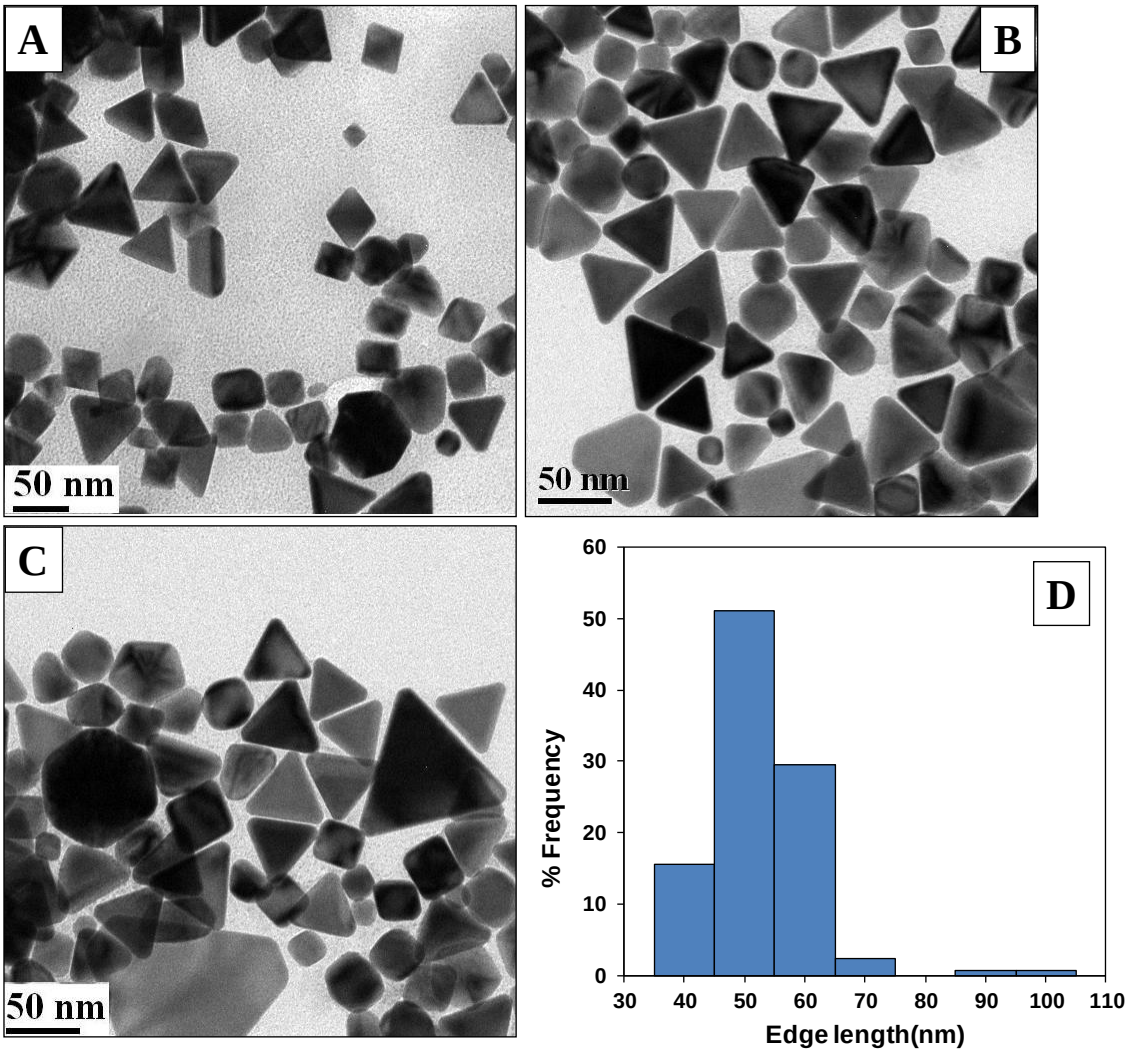

Figure 3A. 7: TEM images of triangular gold nanoplates synthesized in experiment (c) after 5 minutes (images A), 60 minutes of the reaction (images B &C) and D shows the representative edge length distribution of triangular nanoplates.

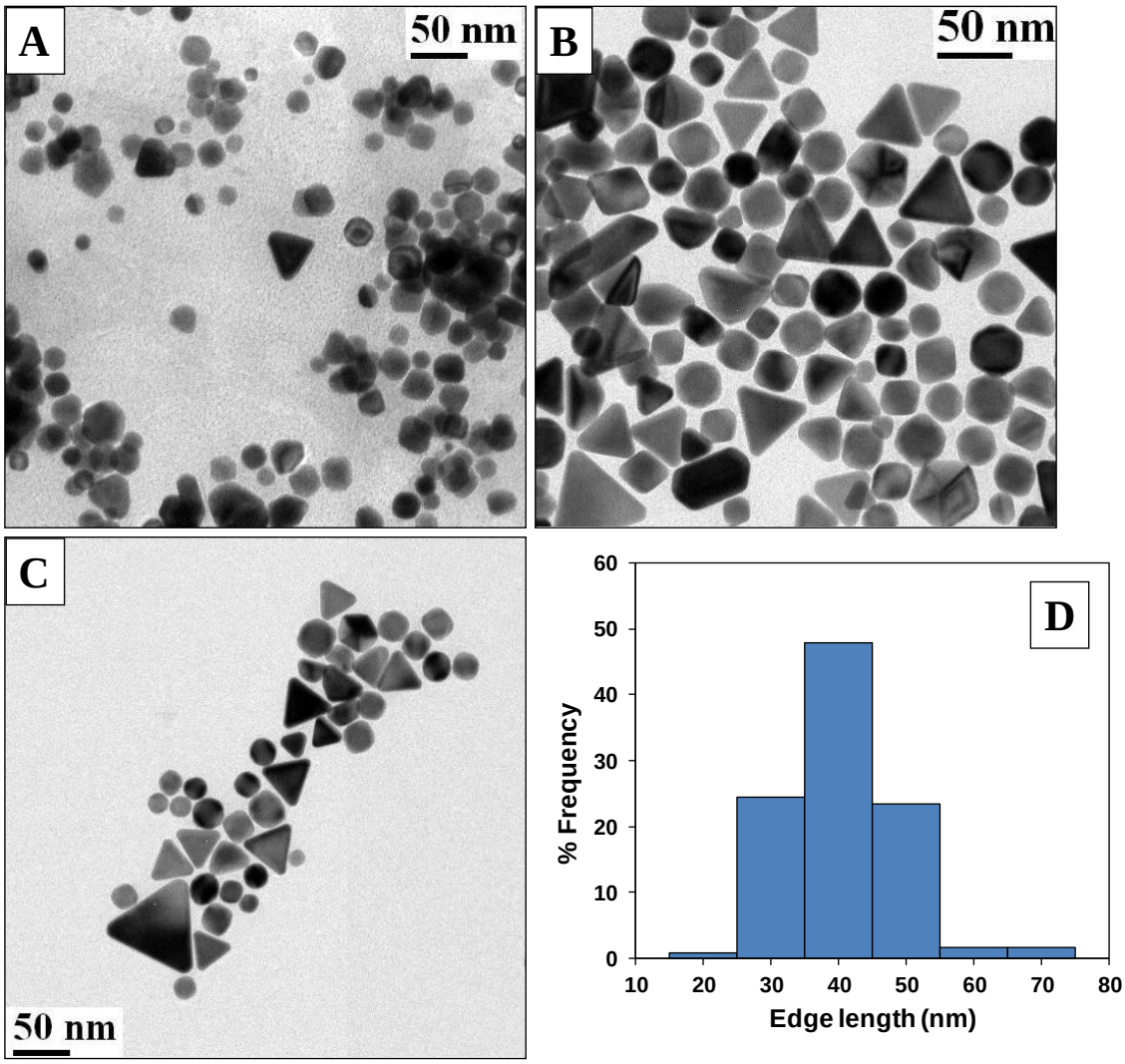

Figure 3A. 8: TEM images of triangular gold nanoplates synthesized in experiment (d) after 5 minutes (images A), 60 minutes of the reaction (images B &C) and D shows the representative edge length distribution of triangular nanoplates.

3A.2.2 Effect of CTAB:

CTAB which is extensively used as shape directing agent, undoubtedly plays an important role in determining the yield of the triangles. To understand the role of CTAB on the synthesis of triangular nanoplates, their synthesis was carried out at different CTAB to $HAuCl_4$ molar ratios of 1, 6, 12, 18, 24 and 36. In all the cases, concentrations of sodium citrate and $HAuCl_4$ solutions were kept unaltered.

3A.2.2.a UV-Vis-NIR and XRD analysis:

In all the experiments (except [CTAB]/[$HAuCl_4$] = 1) the orange red coloured CTAB – $HAuCl_4$ complex turned to colourless Au(I) intermediate (within 1-2 minutes) and then to coloured Au nanostructures which intensified after 15-20 minutes of the reaction. When the [CTAB]/[$HAuCl_4$] increased from 18 to 24, colourless Au(I) to Au(0) reduction was very slow and when the ratio increased further from 24 to 36, the reaction mixture remained almost in colourless Au (I) state, even if the reaction was continued for 1 hour. Hence we did not increase the [CTAB]/[$HAuCl_4$]ratio beyond 36. In the case of [CTAB]/[$HAuCl_4$] - 1 the reduction occurred without any colourless transition. These observations are corroborated by the UV-Vis-NIR spectra of these nanostructures (figure 3A.9) and it shows distinct features for each case indicating that the amount of CTAB significantly affects the morphology of gold nanostructures. PXRD performed on the samples coated on glass slides shows (figure 3A.10) high intense (111) peaks in all the cases indicating the anisotropic nature of the samples which were highly oriented along <111> direction.

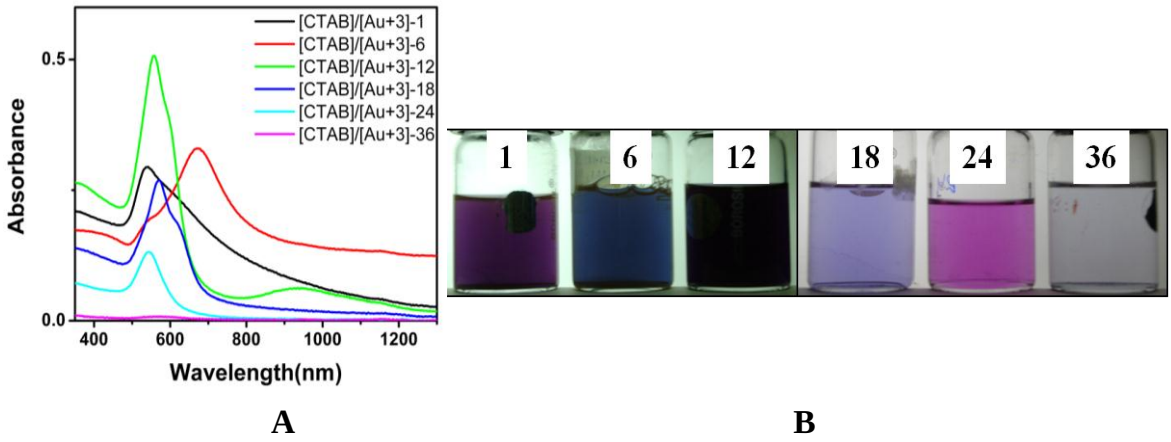

Figure 3A.9: (A) UV-Vis-NIR spectra and (B) photograph of the corresponding samples synthesized at different molar ratios of CTAB to $HAuCl_4$.

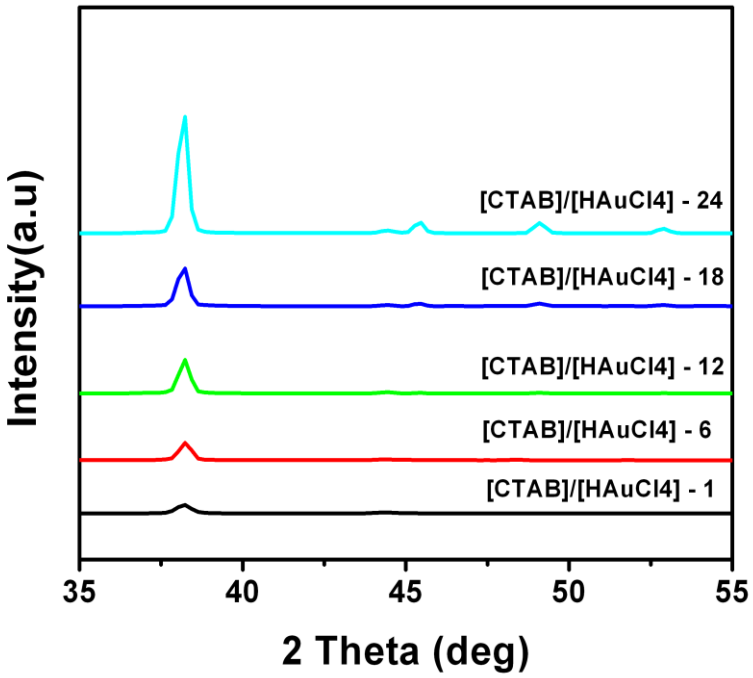

Figure 3A. 10: PXRD of Au nanostructures synthesized at different molar ratios of CTAB to $HAuCl_4$.

3A.2.2.b TEM analysis:

The nanostructures synthesized with [CTAB]/ [$HAuCl_4$] = 1 have nearly spherical morphology (figure 3A.11) and maximum yield of triangular plates was observed when the ratio increased to 6 (figure 3A.12). This indicates that a minimum amount CTAB is required to get reasonably good yields of triangular nanoplates.

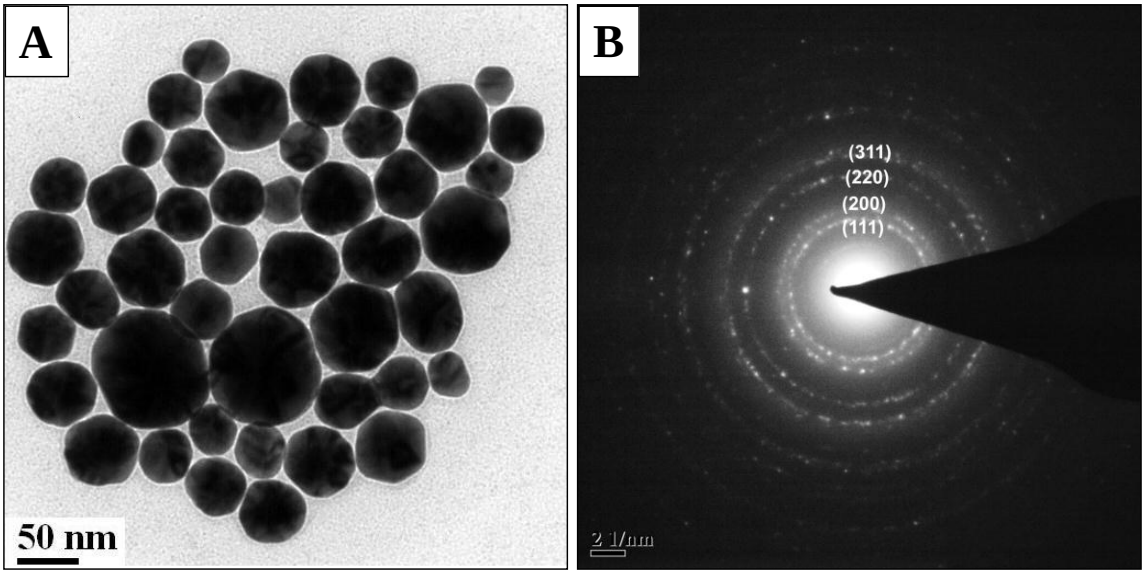

Figure 3A.11: TEM image and corresponding indexed electron diffraction of the quasi nanocrystals synthesized at [CTAB]/[$HAuCl_4$] – 1.

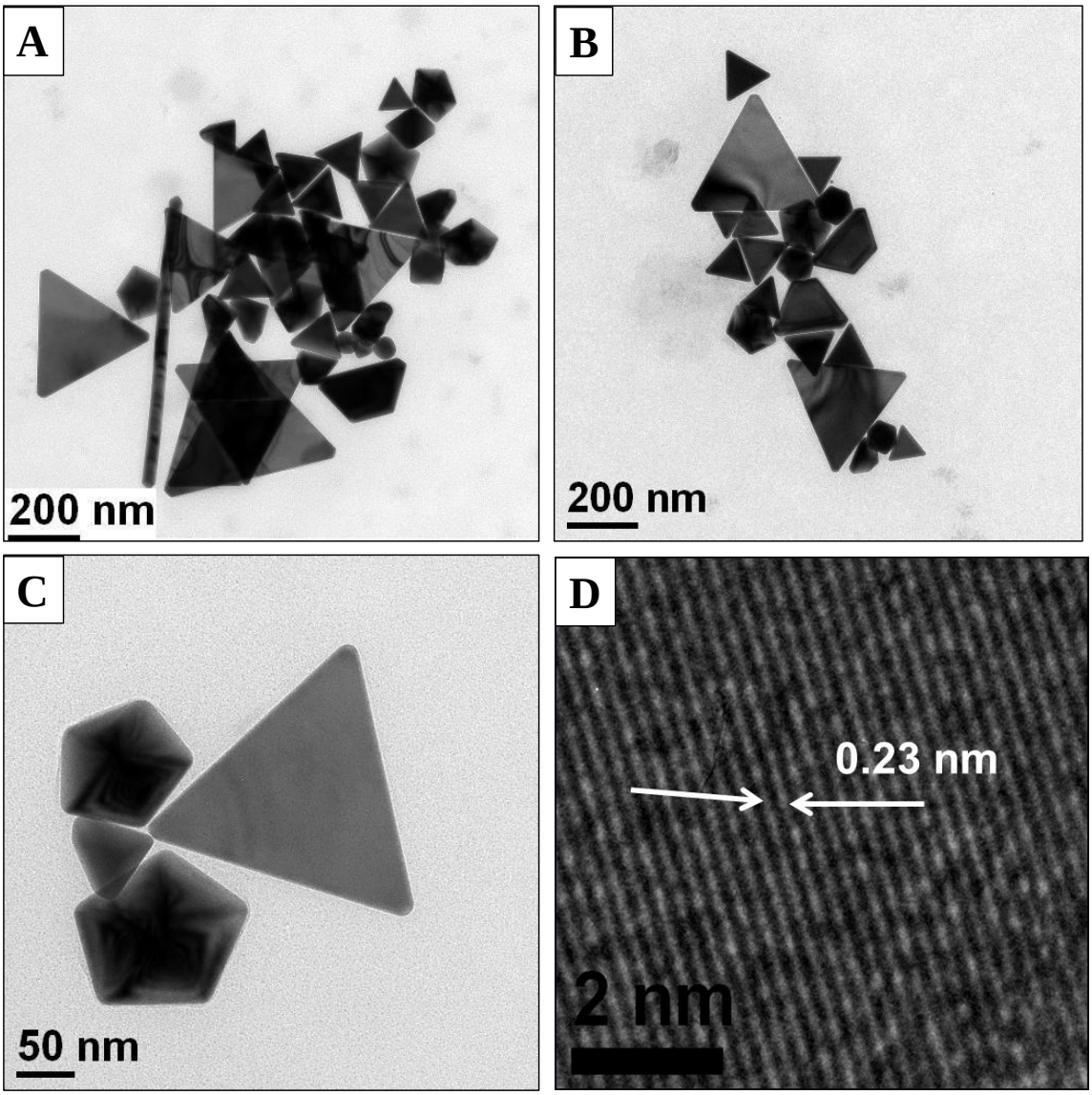

Figure 3A. 12: (A-C) show the TEM images of the gold triangular nanoplates synthesized at [CTAB}/[$HAuCl_4$] – 6 and image D represents the HRTEM of triangular plate shown in image C.

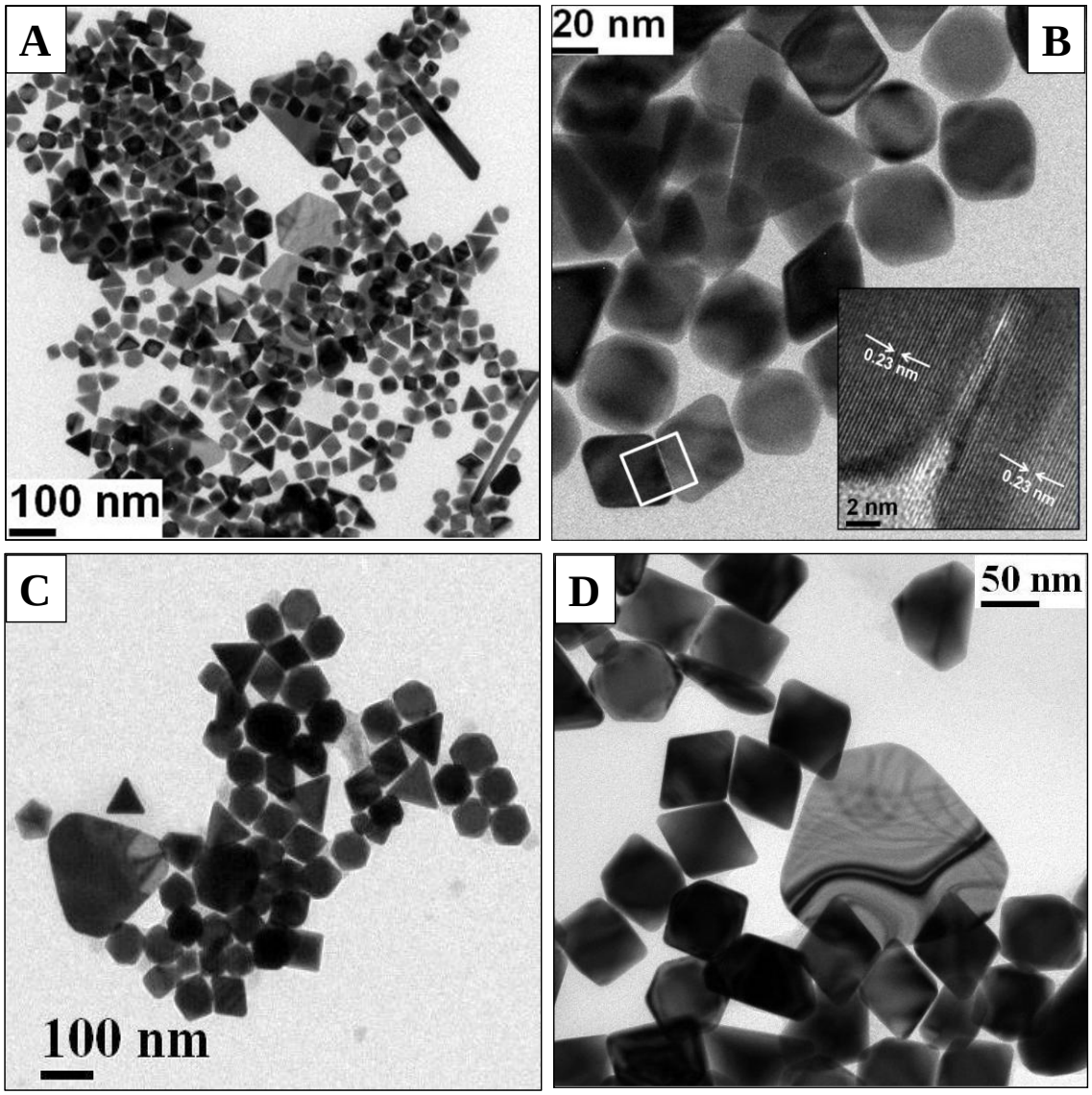

Figure 3A. 13: (A-B) and (C-D) represents the Au nanostructures synthesized at [CTAB]/[$HAuCl_4$]- 12 and 18 respectively. Inset of B represents the magnification of area marked with white box in image B.

,

The yield of the triangular nanoplates is decreased as the ratio increased from 6 to 12 and 18 (figure 3A.13), whereas the number of icosahedral and rhombohedral structures considerably increased. We did not investigate the formation of other anisotropic structures in detail, but in the hydrothermal methods, at high CTAB concentrations are known to give rhombohedral structures when reducing $HAuCl_4$ using citrate.[39]

3A.2.3 Effect of bromide ions:

In the previous section, effect of CTAB on the morphology of Au nanostructures was presented. When the CTAB concentration exceeds certain limit (i.e. [CTAB]/[$HAuCl_4$] is beyond 24), formation of nanostructures was not observed. When CTAB is added to $HAuCl_4$ solution, CTAB releases some bromide ions replacing the chloride ions from $HAuCl_4$ as indicated by a change in the colour of the solution. Hence to understand role of bromide ions in detail, instead of the surfactant CTAB, the synthesis of nanoplates was carried out with HBr at different HBr to $HAuCl_4$ molar ratios (i.e. at 1, 2, 3, 4, 5 and 6) under identical reaction conditions as explained in previous section.

3A.2.3.a UV-Vis-NIR and XRD analysis:

Similar to the case of CTAB, here also the formation of Au nanostructures occurred through colourless Au^{+1} intermediate. As the [HBr]/[$HAuCl_4$] ratio increased to 5, the reaction mixture remained in colourless Au^{+1} state and when the ratio was increased from 5 to 6, even after 1 hour of the reaction, no significant colour change indicative of nanostructure formation was observed. UV-Visible-NIR spectra of the nanostructures synthesized at different [HBr]/[$HAuCl_4$] ratios are shown in figure 3A.14. The regions (I) and (II) that are encircled in image A are magnified in C and D respectively. Corresponding photographs of the samples are given in image B, figure 3A.14. PXRD data of the samples is shown in the figure 3A.14, E.

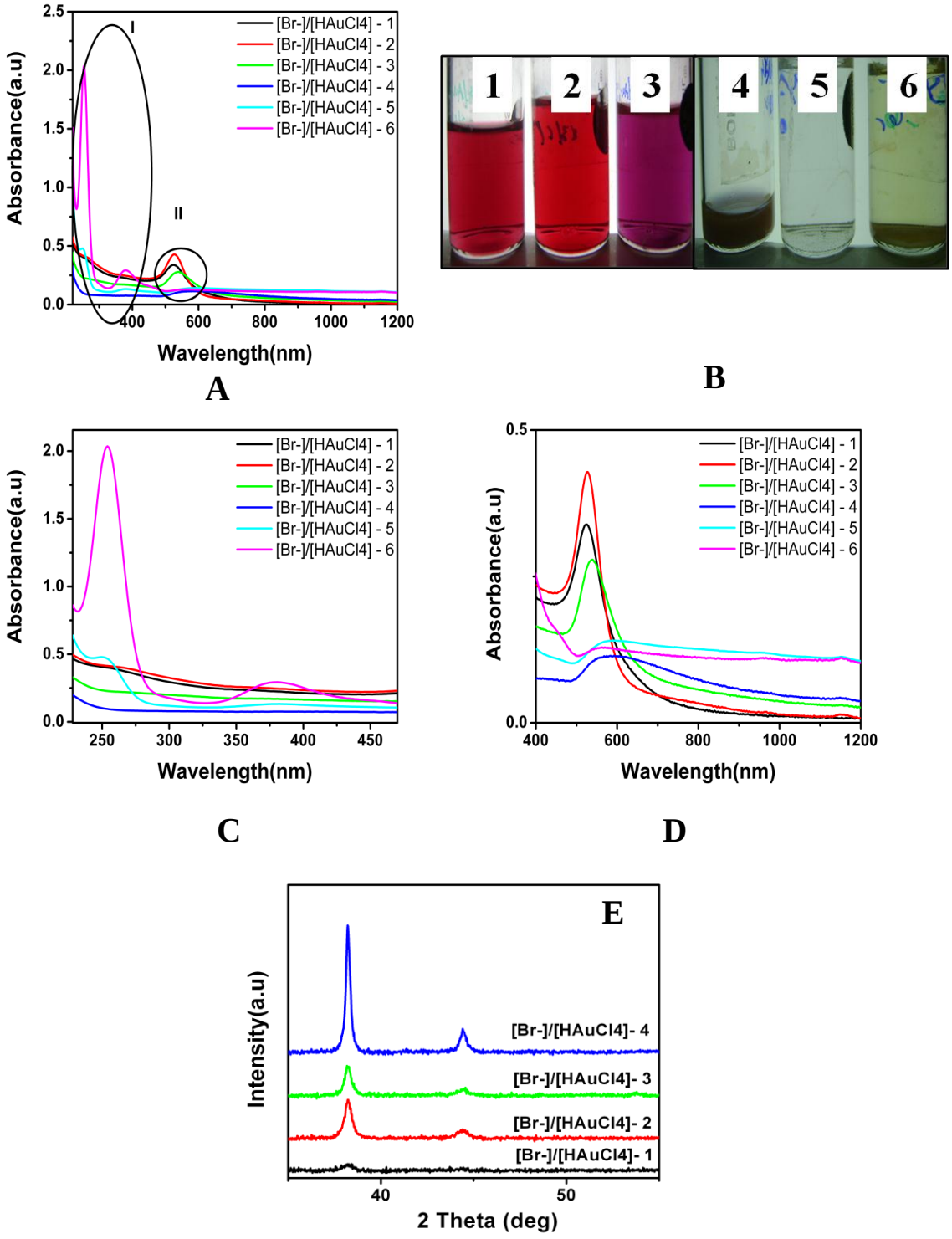

Figure 3A. 14: (A) UV-Vis-NIR spectra of Au nanostructures synthesized at different molar ratios of HBr to $HAuCl_4$ and (B) represents photograph of the corresponding samples. Portions I and II in image A are magnified in images (C & D) respectively and E represents the PXRD of the nanostructures.

3A.2.3.b TEM analysis:

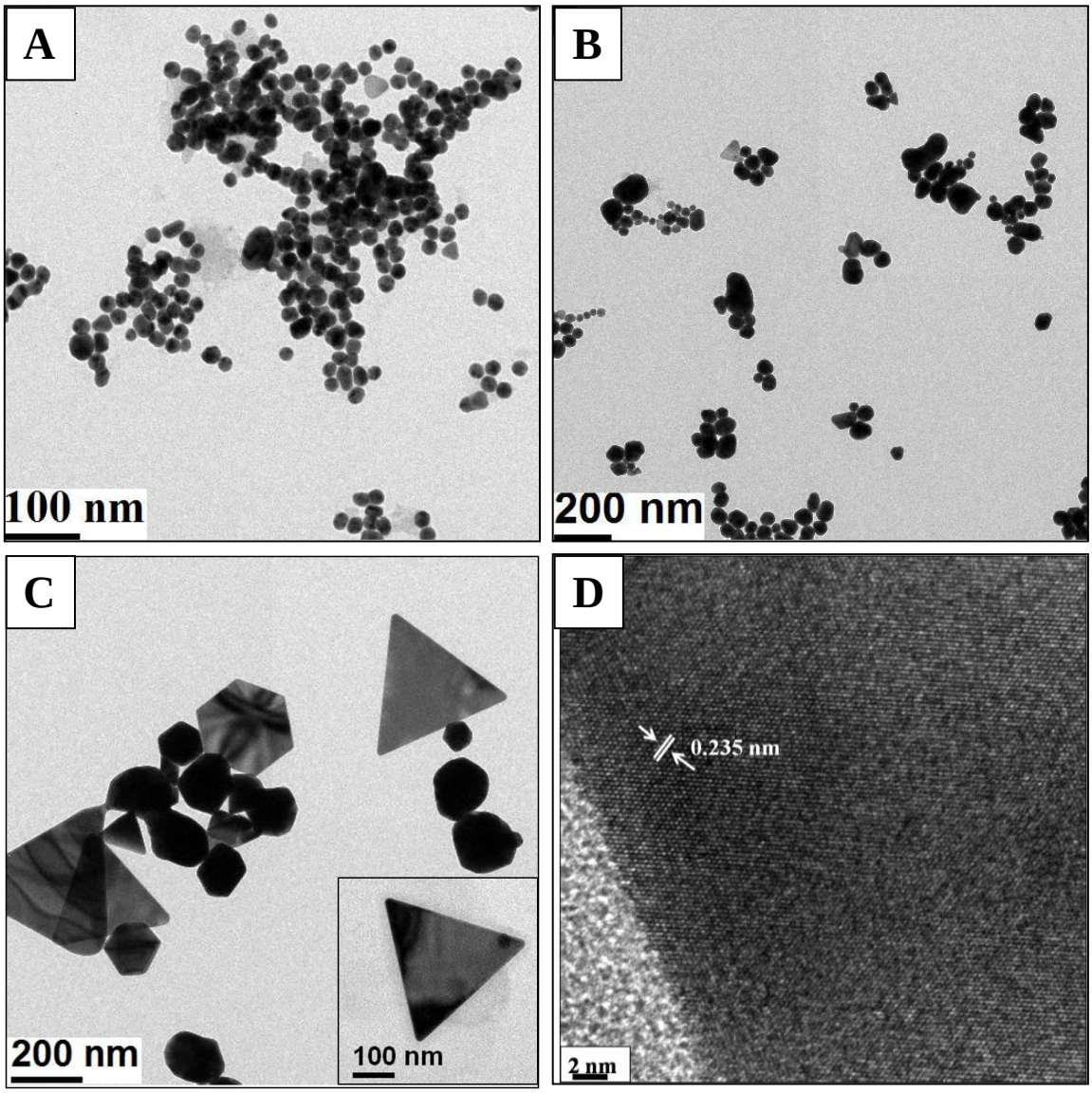

Figure 3A.15: TEM images of nanostructures synthesized using HBr at $[Br^-]/[HAuCl_4]$ - 1(image A), 3(images B) and at 4 (images C). D represents the HRTM image of triangular nanoplate, shown in the inset of C.

TEM images of the nanostructures synthesized at [HBr]/[$HAuCl_4$] ratios 1, 3 and 4 are shown in the figure 3A.15. When the ratio of [HBr]/[$HAuCl_4$] is 1, the morphology of the particles is quasi spherical and as the ratio increased from 1 to 3, aggregates with irregular shapes are observed. Nanoplate morphology is observed when the ratio of [HBr]/[$HAuCl_4$] is 4. In addition to nanoplates high contrast irregular polyhedral particles are also observed. Since there no capping agent/surfactant was used in the synthesis, the nanostructures synthesized in all the cases appeared as aggregates.

3A.2.4 Effect of ODTAB:

In the previous sections, we observed the effect of CTAB and bromide ions on the nanoplate morphology. To probe the suitable counter ion to bromide ions to get maximum yield of triangular nanoplates, we chose another surfactant octadecyl trimethyl ammonium bromide (ODTAB) from the family of quaternary ammonium bromide surfactants. Synthesis of nanostructures was carried out by maintaining ODTAB to $HAuCl_4$ molar ratio 6, at which CTAB gives maximum yield of triangular nanoplates. All the other reaction parameters (i.e citrate concentration, citrate to $HAuCl_4$ molar ratio) were kept same as in case of CTAB (i.e [CTAB]/[$HAuCl_4$] = 6).

3A.2.4.a UV-Visible-NIR and XRD analysis:

Samples synthesized using ODTAB were characterized with UV-Vis-NIR spectra and XRD and the results were compared with the sample synthesized using CTAB.

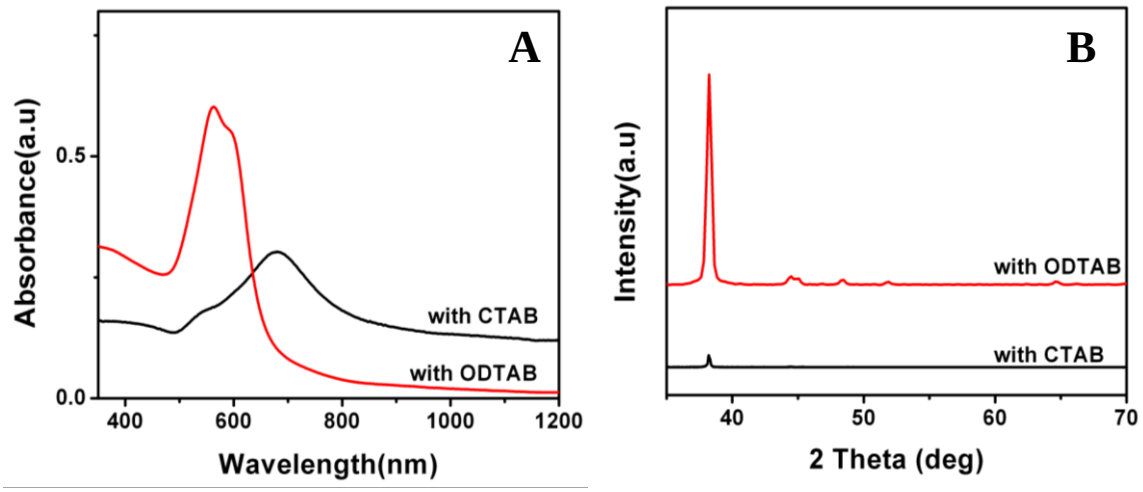

Figure 3A.16: (A) UV-Vis –NIR spectra and (B) PXRD of the Au nanostructures synthesized using ODTAB as shape directing agent instead of CTAB.

UV-Visible-NIR spectra of the samples, synthesized using ODTAB comprised of two peaks and they are positioned at 560 and 600 nm respectively and the sample has zero absorbance in the IR region. In case of sample synthesized using CTAB under similar conditions, peak positions were observed at 550 nm and 700 nm. When CTAB was used, in the PXRD of the sample only (111) peak is observed. On the other hand besides the (111) peak, other peaks corresponding to (200) and (311) planes are also observed when ODTAB was used instead of CTAB (figure 3A.16).

3A.2.4.b TEM analysis:

Micron sized dendritic structures with central core, nanotriangles and spherical particles are observed in the TEM images of sample synthesized using ODTAB (figure 3A.17). At the edges of the dendritic structures triangular and twinned particles are observed. Dendritic structures are known to form as intermediate structures when alkyl ammonium halides used as surfactants.[38, 40] We also observed highly dense dendritic structures in some of the sample aliquots, synthesized using CTAB (see section 3A.2.1).

These dendritic structures may disintegrate to individual particles as the time proceeds and the disintegrated particles may grow completely into triangular shape, depending upon the reaction conditions.

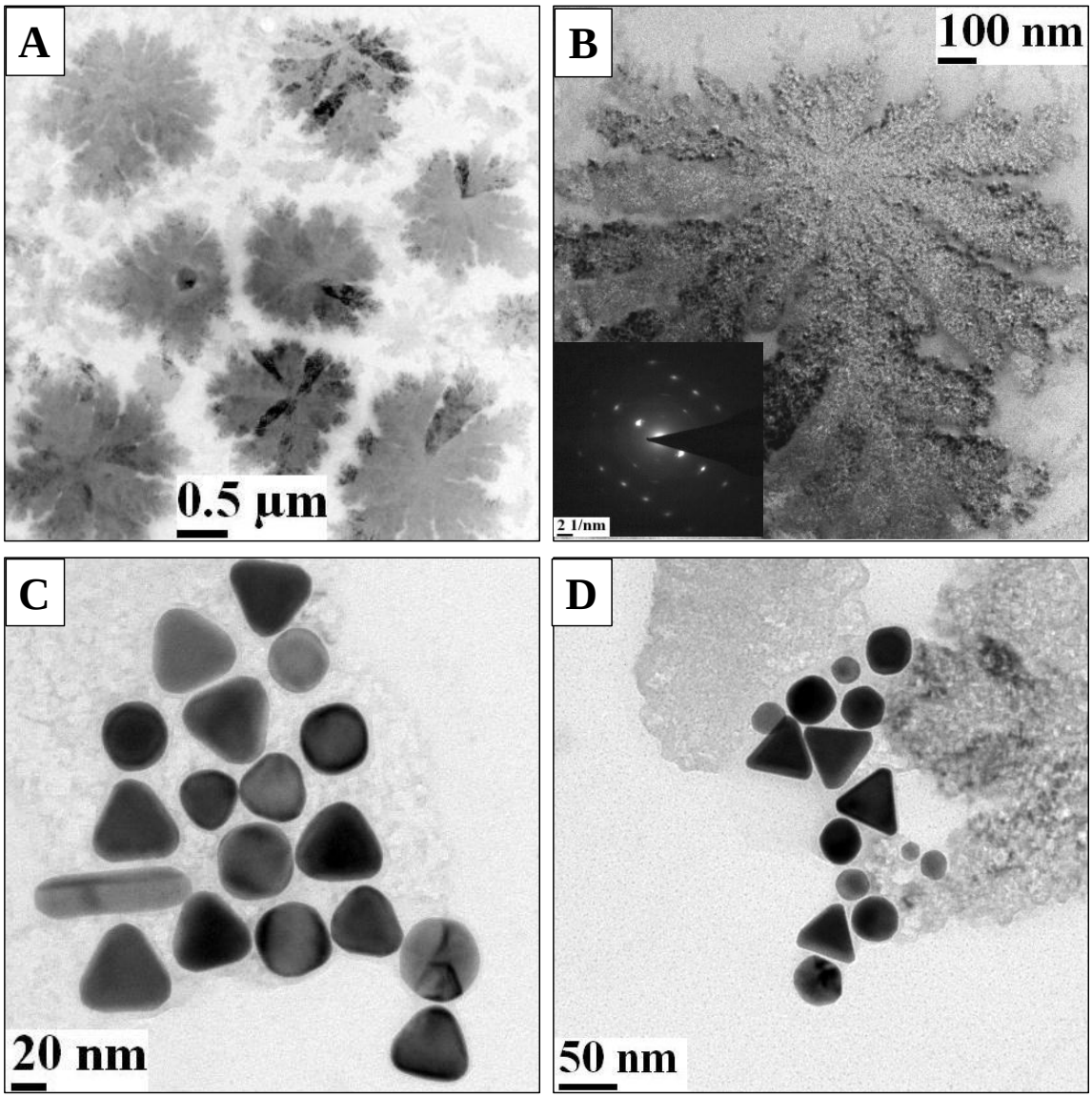

Figure 3A. 17: (A) Dendritic leaf like structures obtained when ODTAB used as shape directing agent. Image (B) show single dendritic structure and corresponding electron diffraction (inset of B). Small triangular nanoplates and twinned particles which are observed at the edges of dendrite are shown in figure (C) and (D).

3A.3 Discussion:

Synthesis of anisotropic nanostructures is sensitive to various parameters which have to be understood and optimized to get control over their shape and yield. To study the effect of temperature on the yield of the triangles, we synthesized nanoplates at different conditions designated as experiments (a), (b), (c) and (d). In experiment (a) only the batch reactor was heated to 90 °C and to this $HAuCl_4$-CTAB and citrate solutions (both the solutions were maintained at room temperature) were added simultaneously. In the remaining experiments (b), (c) and (d), $HAuCl_4$-CTAB solutions maintained at different temperatures i.e. at 27 °C, 50 °C, 70 °C were added to the preheated citrate solutions (90 °C). The design of experiments was done such that in all the experiments nucleation starts at different temperatures, and the time required to reach final reaction temperature also changes. These two variations clearly affected the edge length and yield of the triangular nanoplates. To quantify the effect, exact temperature at point of addition (in other word nucleation temperature) has to be known. Though qualitative arguments on the size and shape dependence of nanoparticles on the rate of reaction and hence on temperature have always been offered, quantitative estimates of such efforts have rarely been discussed. We attempt to do this in the following. When $HAuCl_4$ – CTAB solution of mass m_1, specific heat Cp_1 and at temperature T_1 is mixed to a citrate solution of mass m_2, specific heat Cp_2 and temperature T_2; then the overall temperature of the mixture (T_m) at the point of addition can be calculated from the below equation.

$$T_m = \left[\frac{\{m_1 (T_1 - T_r) + m_2 (T_2 - T_r)\}}{(m_1 + m_2)}\right] + T_r \qquad (1)$$

Taking T_r the reference temperature as 0 °C, the T_m s for experiments (a), (b), (c) and (d) turn out to be 27 °C, 64.8 °C, 74 °C and 82 °C respectively. This clearly indicates that in these different experimental conditions, the nucleation process initializes at four different temperatures and the time (t) required in attaining a final

temperature of 90 °C decreases from experiments (a) to (d). Thus, while the initial temperature of the mixture would control the nucleation rate, the time span required to reach the final temperature (i.e. 90 °C) will govern the growth rate. These two factors thus affect the yield and size of the triangles. The time required to attain final temperature has to be exactly known to quantify its effect on the edge length of the triangles and it can be calculated using the following equation for transient heating in batch mode[41]

$$t = \frac{MC_p}{UA} log \left[\frac{T_b - T_{mi}}{T_b - T_{mf}}\right] \quad (2)$$

Where '*M*' is mass of the solution (kg), *Cp* is specific heat (kJ/kg K), *U* is overall heat transfer coefficient, *A* is area available for heat transfer, T_b is the bath temperature (K), T_{mi} is the initial temperature of the reaction mixture and T_{mf} is the final temperature of the solution which cannot be equal to T_b in reality.

Where U, the overall heat transfer coefficient, is estimated as

$$U = \frac{h_i h_o}{h_i + h_o} \quad (3)$$

h_i - Agitated liquid batch side heat transfer coefficient [41, 42]

$$h_i = 0.36 \left(\frac{\kappa}{D_i}\right) \left(\frac{L^2 N \rho}{\mu}\right)^{0.66} \left(\frac{C_p \mu}{\kappa}\right)^{0.33} \left(\frac{\mu}{\mu_0}\right)^{0.14} \quad (4)$$

κ	Thermal conductivity of the medium (W/m-K)
L	Length of the magnetic stirrer bar (m)
N	Number of revolutions per second
ρ	Density of the medium (kg/m^3)
μ	Viscosity of the medium (kg/m-sec)
C_p	Specific heat (J/kg K)
D_i	Inner diameter of the reactor (m)

h_o Jacket side heat transfer coefficient (Hausen equation[43])

$$h_o = 0.116\left(\frac{\kappa}{D_e}\right)\left({R_e}^{0.66} - 125\right)\left(\frac{C_p\,\mu}{\kappa}\right)^{0.33}\left(\frac{\mu}{\mu_0}\right)^{0.14}\left[1 + \left(\frac{D_h}{L}\right)^{\frac{2}{3}}\right] \qquad (5)$$

κ Thermal conductivity of the circulated liquid through jacket (W/m-K)

D_h Hydraulic diameter which is (D_o-D_i) for annulus[44] (m)

D_e Equivalent diameter in case of annulus[44] (D_o^2- D_i^2)/D_i (m)

R_e Reynolds number ($\rho D_h V$)/μ

ρ Density of the medium (kg/m^3)

μ Viscosity of the medium (kg/m-sec)

C_p Specific heat (J/kg K)

V Velocity (m/sec)

For all the calculations the physical properties of water at 25 °C are taken into account. Another assumption used is that the physical properties of the $HAuCl_4$-CTAB and citrate solution are same as that of water and they do not change with temperature. Values of physicochemical properties were obtained from the literature.[45] Time required to reach the final reaction temperature from the temperature at point of addition is determined to be ~194, 143, 116, 77 seconds for experiments (a), (b), (c), (d) respectively. As stated earlier, the initial temperature at which the nucleation occurred is different in all the experiments and it increases from (a) to (d). When the initial nucleation temperature is around 50 °C - 70 °C [like in experiments (a) and (b)], triangular nanoplate formation is favoured with larger edge length and with high yield. Similar observations from the literature[46] in the synthesis of triangular nanoplates by seed mediated method support our investigations. The low initial reaction temperature under these two conditions gives enough time to the reaction system to maintain the nucleation step at low rate and

this situation favours the formation of triangular nanoplates. In case of metals that crystallize in closely packed *fcc* structures (i.e in case of Au, Ag, Pd etc.) [47,11] it is known that slower reduction rate encourages the stacking faults leading to the formation of plate-like seeds, which finally grow to produce triangular/hexagonal plates. In experiments (c) and (d) as the initial reaction temperatures are high enough the rate of nucleation increases, more nuclei are formed and these finally yield smaller triangles. The results of the experiments (a) to (d) are summarized in table 3B.1.

Table 3B. 1: Summary of the results obtained from different experiments (A) to (D)

Experiment	Initial temperature of reaction mixture (°C) (calculated from eq.1)	Time required to reach final reaction temperature in sec (calculated from eq.2)	Edge length of the triangles (nm)	Number yield of the triangles (%)
Experiment A	27	194.7	150±50	~62
Experiment B	64.8	143.4	75±25	~43
Experiment C	74	116.3	50±10	~40
Experiment D	82	77.5	40±10	~24

The correlation between the nucleation temperature, rate of rise in the temperature, edge length and yield of the triangles were plotted in the figure 3A.18. At low initial nucleation temperature (T_N), estimated using equation (1), although the rate at which temperature reaches the maximum is very high, lager temperature difference favours the growth of the triangular seed which are turn to form at kinetically controlled conditions and gives relatively better yield of the triangles. Triangular plates synthesized at high nucleation temperatures were more uniform in terms of edge length, but in-situ self assembly[48] of the smaller triangular seeds to another anisotropic structures hampered their yield. From these results and the above discussion we can conclude that controlling the rate of nucleation is the key step in getting specific yield of triangular nanoplates while the growth kinetics determine the sizes.

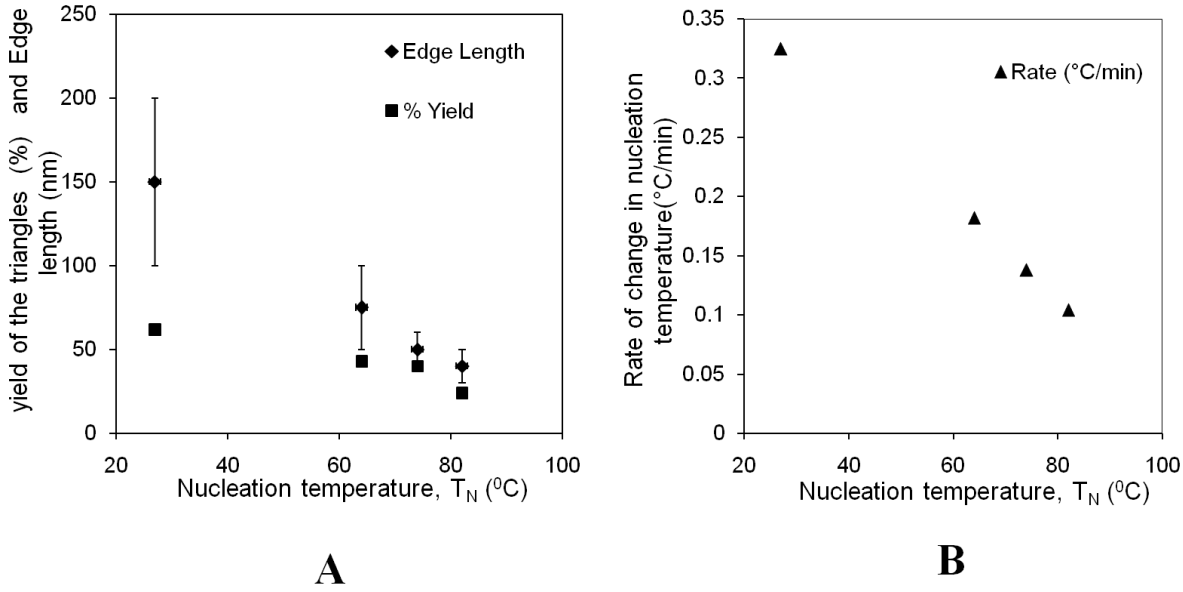

Figure 3A. 18: (A) Edge length/ % yield of the triangles plotted against the nucleation temperature. (B) Rate of change of temperature at different nucleation temperatures was plotted.

CTAB, a widely used surfactant plays an important role in determining the shape of the Au nanostructures. The effect of CTAB on the seed mediated synthesis of Au nanostructures was explored by Murphy and coworkers.[12, 49] Presence of small amounts of other halide ion impurities (especially iodide) can alter the performance of CTAB.[22, 24] But the observations are not unique for all the synthetic methods and when it comes to triangular nanoplates, the effect of halide ions on anisotropic nanostructures is different for different synthetic methods. To understand the effect of CTAB on surfactant assisted thermal processes to synthesize triangular nanoplates, we carried out the synthesis at different molar ratios of CTAB to $HAuCl_4$ by increasing the concentration of CTAB. When CTAB is added to the $HAuCl_4$ solution, depending upon its micellar charge stabilization, bromide ions are released which could replace the chloride ions and change the colour of $HAuCl_4$ from yellow to orange red. Furthermore, the increase in CTAB concentration in the reaction system increases the bromide concentrations, thus affecting the morphology

of the Au nanostructures. In other words studying the effect of CTAB is nothing but the studying effect of bromide ion on synthesis of triangular nanoplates. Recollecting the results from the experiments where the effect of CTAB was studied by varying its concentration ratio with $HAuCl_4$, morphological changes were associated with interesting observations. Except when the [CTAB]/[$HAuCl_4$] = 1, for all other rations of [CTAB]/[$HAuCl_4$], the orange red coloured CTAB – $HAuCl_4$ complex turned to colourless Au (I) intermediate within 1-2 minutes. After this colourless transition, these samples attained different colours that correspond to different morphologies of anisotropic structures. In case of [CTAB]/[$HAuCl_4$] = 1 the reduction of Au^{+3} occurred without any colourless transition and in this the final morphology of nanostructures is predominantly spherical. At the [CTAB]/ [$HAuCl_4$] ratio 6, 12 and 18, CTAB – $HAuCl_4$ complex turned to colourless Au (I) intermediate within 1-2 minutes and the colourless Au (I) is reduced to Au (0) immediately (less than 1-2 min). As the [CTAB]/[$HAuCl_4$] increased from 18 to 24, the reduction of Au (I) to Au(0) becomes very slow and when the ratio increased further from 24 to 36, solution remained in colourless Au(I) state. Increase of bromide in the solution with increase in CTAB quantity replaces the Cl^- ion in $HAuCl_4$. This in turn influences the complex's stability. This could be the reason for the decreased rate of reaction with increase in CTAB concentration. To probe this possibility in detail we carried out another set of experiments where CTAB is replaced by HBr.

Unlike CTAB, HBr dissociates completely into H^+ and Br^- in the reaction mixture, so we carried out the synthesis of Au nanostructures by varying the HBr to $HAuCl_4$ ratio from 1 to 6. Here also we observed that with increase in bromide quantity the rate of reduction of Au(I) to Au(0) decreased and in addition to this, unlike in case of CTAB, decrease in rate of reduction from Au(III) to Au(I) was also observed. For example, when the HBr to $HAuCl_4$ molar ratio was 6, even after 1 hour of the reaction, the reaction mixture remained in an unreduced complex form. As explained previously addition of bromide ions can replace the chloride ions from the $[AuCl_4]^-$ complex and forms a more stable complex of type $[AuCl_{4-x}Br_x]$[50] where x varies from 0 to 4 depending on the added HBr concentration. Formation of such complex is clearly endorsed by the ligand to metal charge transfer (LMCT) spectra.

Figure 3A. 19 show the LMCT spectra of gold-halide complexes with different HBr to $HAuCl_4$ concentration ratios. As the [HBr]/[$HAuCl_4$] is increased from 0 to 4, the peaks at 215 and 285 nm that are found in the spectrum of $[AuCl_4]^-$ complex (inset, figure A) are shifted to 252 and 378 respectively, and this peak positions remain unaltered as the [HBr]/[$HAuCl_4$] ratio changed from 4 to 6 except with a little enhancement in peak intensities. These results suggest that exchange Cl^- by Br^- would be completed when the [HBr]/[$HAuCl_4$] is 4 and at all further HBr to $HAuCl_4$ ratios stable $[AuBr_4]^-$ complex is formed.

Upon the addition of citrate to this stable $[AuBr_4]^-$ complex, Au(III) reduces to Au(I) and forms $[AuBr_2]^-$ complex. $[AuBr_2]^-$ is more stable than the $[AuCl_4]^-$, $[AuCl_2]^-$ complexes as evident from their reduction potentials.[51] Therefore further reduction from Au(I) to Au(0) becomes slower and this condition encourages the formation of kinetically controlled products, viz. hexagonal/triangular plates as in case of [CTAB]/[$HAuCl_4$] = 6 or [HBr]/[$HAuCl_4$] = 4. Further increase in amount of Br^- increases the quantity of stable bromide complex in the system and leaves the system in colourless Au(I) state such as in [CTAB]:[$HAuCl_4$] = 36 or [HBr]/[$HAuCl_4$] = 5. If more bromide is added, the system remained in unreduced Au (III) state even after 60 minutes of reaction as observed in the case of [HBr]/[$HAuCl_4$] = 6.

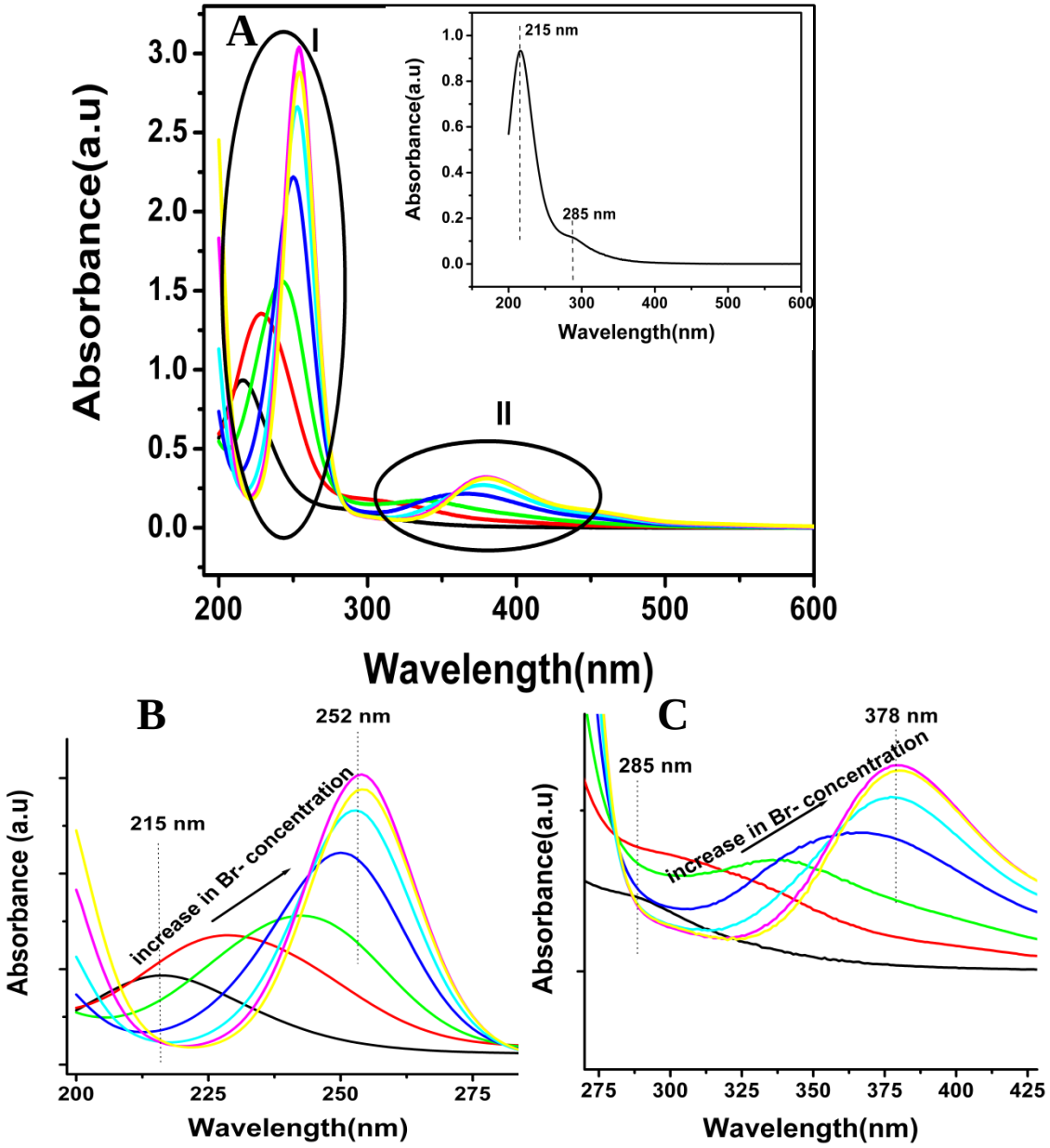

Figure 3A.19: LMCT spectra of aqueous $HAuCl_4$ solution at different molar ratios of HBr to $HAuCl_4$ varying from 1 to 6. Inset of A - LMCT spectrum of pure $HAuCl_4$ solution, without any Br^- . (B & C) indicates the magnified portions of (I) and (II) of image A respectively. LMCT spectra of complexes recorded at identical concentrations used for the synthesis of nanostructures.

In controlling the morphology of noble metal nanoparticles, pH plays an important role[52] and by adjusting the pH of the solution, the morphology of the particles can be changed from simple spherical to plate like structures.[52, 53] Changing the pH of the solution, changes the nature of the initial gold complex and hence the redox potential of the complex varies.[53] In the synthesis of Au nanoplates using HBr, we measured the pH of the reactant solution (mixture of $HAuCl_4$ and HBr at different molar ratios). Figure 3A.20 shows the pH variation of the solution at different [HBr]/[$HAuCl_4$] ratios. As suggested by the morphology diagrams of Ravishankar and coworkers[32, 33], for all the ratios of [Br^-] to [Au^{+3}], the pH is in the range of 2.3 to 2.6 (figure 3A.20) and this pH range should favour the formation of plate like morphology for all the ratios. However our observations show that for given temperature and concentrations, the dependence of the rate of reduction on the nature of the gold complex has more prominent effect than the pH.[54]

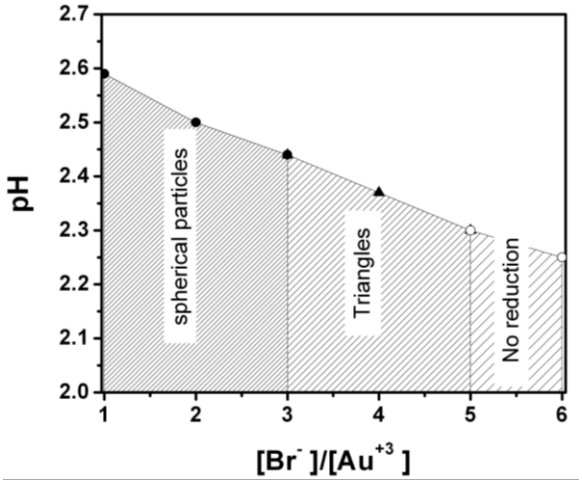

Figure 3A. 20: pH of the gold complex at different HBr to $HAuCl_4$ molar ratios. Morphology of the nanostructures obtained at different [Br^-]/[Au^{+3}] ratios are represented in the figure.

Thus our results with HBr clearly suggest that by changing the reaction parameters and by maintaining favorable conditions, anisotropic Au nanostructures can be easily obtained without using any surfactant. Furthermore, the above experiments clearly prove that simple Br^- source like HBr is enough to bring morphological changes. However CTAB is proved to improve the yield and

homogeneity among the anisotropic particles. Hence to understand the importance of CTA^+ ions to produce maximum number of triangles, we performed another experiment wherein instead of CTAB, octadecyltrimethyl ammonium bromide (ODTAB) is used as surfactant. Here even after continuing the reaction for one hour, micron sized dendritic structures were observed on the TEM grid. To reconcile the results in this case, it is necessary to recollect the results from different CTAB to Au^{+3} concentrations. In case of $[CTAB]/[HAuCl_4] = 1$, the concentration of CTAB is lower than its CMC. Therefore the role of CTAB might be limited as capping agent to spherical nanoparticles (shown in figure 3A.11). When the $[CTAB]/[HAuCl_4] = 6$, concentration of CTAB is 7.5 mM. CTAB forms spherical micelles at this concentration and depending upon fraction of micellar charge stabilization it releases some quantity of Br^- to the solution. As explained previously, the released bromide ions replace the chloride ions and that increases the stability of complex. This is good enough to slow down the reaction kinetics and to produce plate like seeds with stacking faults. These plate like seeds are stabilized by citrate ions which bind to Au (111) planes, which further grow in size with time. Although ODTAB forms micelles (CMC ≈ 0.3 mM) at lower concentration than CTAB (CMC of CTAB ≈ 1 mM), due to the difference in fraction of micellar charge stabilization and its lower solubility in aqueous solutions, sufficient amounts Br^- ions may not get released from ODTAB into water. So it produces less number of triangles under similar conditions where CTAB gives maximum number of triangles. These results summarize that CTA^+ ions are more suitable counterparts to Br^- ions and that CTAB, at a concentration above the CMC, releases the required amounts of bromide ions in solution making it the most successful shape directing agent.

3A.4 Conclusions:

In summary, we have described the effect of temperature and role of Br^- on the edge-length and yield of the triangular nanoplates by surfactant directed thermal approach. Formation of two dimensional plate like structures is a kinetically controlled process, and it can be facilitated at moderate rates of nucleation as higher nucleation results in low yields of triangles and their edge-length also becomes smaller. Addition of Br^- changes the nature of complex and at appropriate

concentrations slows down the reduction of Au(I) to Au(0) impacting the yield and size of triangles again. If Br^- concentration becomes very high, the reduction of Au(III) to Au(I) itself is hindered.

3A.5 References:

1. Pastoriza-Santos, I.; Alvarez-Puebla, R. A.; Liz-Marzan, L. M., *Eur. J. Inorg. Chem.* **2010**, 4288-4297.

2. Xia, Y.; Xiong, Y.; Lim, B.; Skrabalak, S. E., *Angew. Chem., Int. Ed.* **2008,** *48*, 60-103.

3. Zhao, C. X.; He, L.; Qiao, S. Z.; Middelberg, A. P. J., *Chem. Eng. Sci.* **2011,** *66*, 1463-1479.

4. Boleininger, J.; Kurz, A.; Reuss, V.; Sönnichsen, C., *Phys. Chem. Chem. Phys.* **2006,** *8*, 3824-3827.

5. Bullen, C.; Latter, M. J.; D'Alonzo, N. J.; Willis, G. J.; Raston, C. L., *Chem. Commun.* **2011,** *47*, 4123-4125.

6. Sebastian, V.; Lee, S.-K.; Zhou, C.; Kraus, M. F.; Fujimoto, J. G.; Jensen, K. F., *Chem. Commun.* **2012,** *48*, 6654-6656.

7. Knauer, A.; Csáki, A.; Möller, F.; Hühn, C.; Fritzsche, W.; Köhler, J. M., *J. Phys. Chem. C* **2012,** *116*, 9251-9258.

8. Duraiswamy, S.; Khan, S. A., *Small* **2009,** *5*, 2828-2834.

9. Millstone, J. E.; Hurst, S. J.; Metraux, G. S.; Cutler, J. I.; Mirkin, C. A., *Small* **2009,** *5*, 646-664.

10. Tang, T.; Hamley, I. W., *Colloids Surf., A* **2009,** *336*, 1-7.

11. Xiong, Y.; Washio, I.; Chen, J.; Cai, H.; Li, Z. Y.; Xia, Y., *Langmuir* **2006,** *22*, 8563-8570.

12. Sau, T. K.; Murphy, C. J., *J. Am. Chem. Soc.* **2004,** *126*, 8648-8649.

13. Shankar, S. S.; Rai, A.; Ankamwar, B.; Singh, A.; Ahmad, A.; Sastry, M., *Nat. Mater.* **2004,** *3*, 482-488.

14. Chandran, S. P.; Chaudhary, M.; Pasricha, R.; Ahmad, A.; Sastry, M., *Biotechnol. Prog.* **2006,** *22*, 577-583.

15. Gole, A.; Murphy, C. J., *Chem. Mater.* **2004,** *16*, 3633-3640.

16. DuChene, J. S.; Niu, W.; Abendroth, J. M.; Sun, Q.; Zhao, W.; Huo, F.; Wei, W. D., *Chem. Mater.*, Ahead of Print.

17. Ha, T. H.; Koo, H. J.; Chung, B. H., *J. Phys. Chem. C* **2007,** *111*, 1123-1130.

18. Kasture, M.; Sastry, M.; Prasad, B. L. V., *Chem. Phys. Lett.* **2010,** *484*, 271-275.

19. Mirkin, C. A.; Millstone, J. E.; Wei, W.; Jones, M. R.; Yoo, H. Halide ion control of seed mediated crystal growth of anisotropic gold nanoparticles or nanorods. WO2009143222A2, 2009.

20. Rai, A.; Singh, A.; Ahmad, A.; Sastry, M., *Langmuir* **2006,** *22*, 736-741.

21. Garg, N.; Scholl, C.; Mohanty, A.; Jin, R., *Langmuir* **2010,** *26*, 10271-10276.

22. Rayavarapu, R. G.; Ungureanu, C.; Krystek, P.; van Leeuwen, T. G.; Manohar, S., *Langmuir* **2010,** *26*, 5050-5055.

23. Smith, D. K.; Korgel, B. A., *Langmuir* **2008,** *24*, 644-649.

24. Smith, D. K.; Miller, N. R.; Korgel, B. A., *Langmuir* **2009,** *25*, 9518-9524.

25. García, M.; Bouzas, V.; Carmona, N., *Mater. Chem. Phys.* **2011**.

26. Vivek, J.; Burgess, I. J., *Langmuir* **2012,** *28*, 5040-5047.

27. Vivek, J. P.; Burgess, I. J., *Langmuir* **2012,** *28*, 5031-5039.

28. Al-Saidi, W.; Feng, H.; Fichthorn, K. A., *Nano Lett.* **2012,** *12*, 997-1001.

29. Elechiguerra, J. L.; Reyes-Gasga, J.; Yacaman, M. J., *J. Mater. Chem.* **2006,** *16*, 3906-3919.

30. Germain, V.; Li, J.; Ingert, D.; Wang, Z.; Pileni, M., *J. Phys. Chem. B* **2003,** *107*, 8717-8720.

31. Viswanath, B.; Kundu, P.; Ravishankar, N., *J. Colloid Interface Sci.* **2009,** *330*, 211-219.

32. Viswanath, B.; Kundu, P.; Halder, A.; Ravishankar, N., *J. Phys. Chem. C* **2009,** *113*, 16866-16883.

33. Viswanath, B.; Kundu, P.; Mukherjee, B.; Ravishankar, N., *Nanotechnology* **2008,** *19*, 195603.

34. Xiong, Y.; McLellan, J. M.; Chen, J.; Yin, Y.; Li, Z. Y.; Xia, Y., *J. Am. Chem. Soc.* **2005,** *127*, 17118-17127.

35. Washio, I.; Xiong, Y.; Yin, Y.; Xia, Y., *Adv. Mater. (Weinheim, Ger.)* **2006,** *18*, 1745-1749.

36. Shankar, S. S.; Bhargava, S.; Sastry, M., *J. Nanosci. Nanotechnol.* **2005,** *5*, 1721-1727.

37. Chu, H. C.; Kuo, C. H.; Huang, M. H., *Inorg. Chem.* **2006,** *45*, 808-813.

38. Huang, W. L.; Chen, C. H.; Huang, M. H., *J. Phys. Chem. C* **2007,** *111*, 2533-2538.

39. Chang, C. C.; Wu, H. L.; Kuo, C. H.; Huang, M. H., *Chem. Mater.* **2008,** *20*, 7570-7574.

40. Lin, G.; Lu, W.; Cui, W.; Jiang, L., *Cryst. Growth Des.* **2010,** *10*, 1118-1123.

41. Kern, D. Q., *Process heat transfer*. Tata McGraw-Hill: 1997; p 717-719.

42. Chilton, T.; Drew, T.; Jebens, R., *Ind.Eng.Chem.* **1944,** *36*, 510-516.

43. Serth, R. W., *Process heat transfer:principles and applications*. Academic Press: 2007; p 4/128-4/129.

44. Kern, D. Q., *Process heat transfer*. Tata McGraw - Hill: 1997; p 104-105.

45. Green, D. W.; Perry, R. H., *Perry's Chemical Engineers Hand book*. Eighth ed.; Mc-Graw Hill: 2007.

46. Chen, H. M.; Liu, R. S.; Tsai, D. P., *Cryst. Growth Des.* **2009,** *9*, 2079-2087.

47. Lim, B.; Camargo, P. H. C.; Xia, Y., *Langmuir* **2008,** *24*, 10437-10442.

48. Zhang, J.; Liu, H.; Wang, Z.; Ming, N., *Appl. Phys. Lett.* **2007,** *91*, 133112.

49. Murphy, C. J.; Sau, T. K.; Gole, A. M.; Orendorff, C. J.; Gao, J.; Gou, L.; Hunyadi, S. E.; Li, T., *J. Phys. Chem. B* **2005,** *109*, 13857-13870.

50. Elding, L. I.; Groning, A. B., *Acta Chem. Scand A* **1978,** *32*, 867-877.

51. Bard, A. J., *Encyclopedia of electrochemistry of elements*. Marcel Dekker: NewYork, 1975; Vol. 4.

52. Patungwasa, W.; Hodak, J. H., *Mater. Chem. Phys.* **2008,** *108*, 45-54.

53. Ji, X.; Song, X.; Li, J.; Bai, Y.; Yang, W.; Peng, X., *J. Am. Chem. Soc.* **2007,** *129*, 13939-13948.

54. Sau, T. K.; Murphy, C. J., *Philos. Mag.* **2007,** *87*, 2143-2158.

Part B: Flow synthesis of triangular gold nanoplates

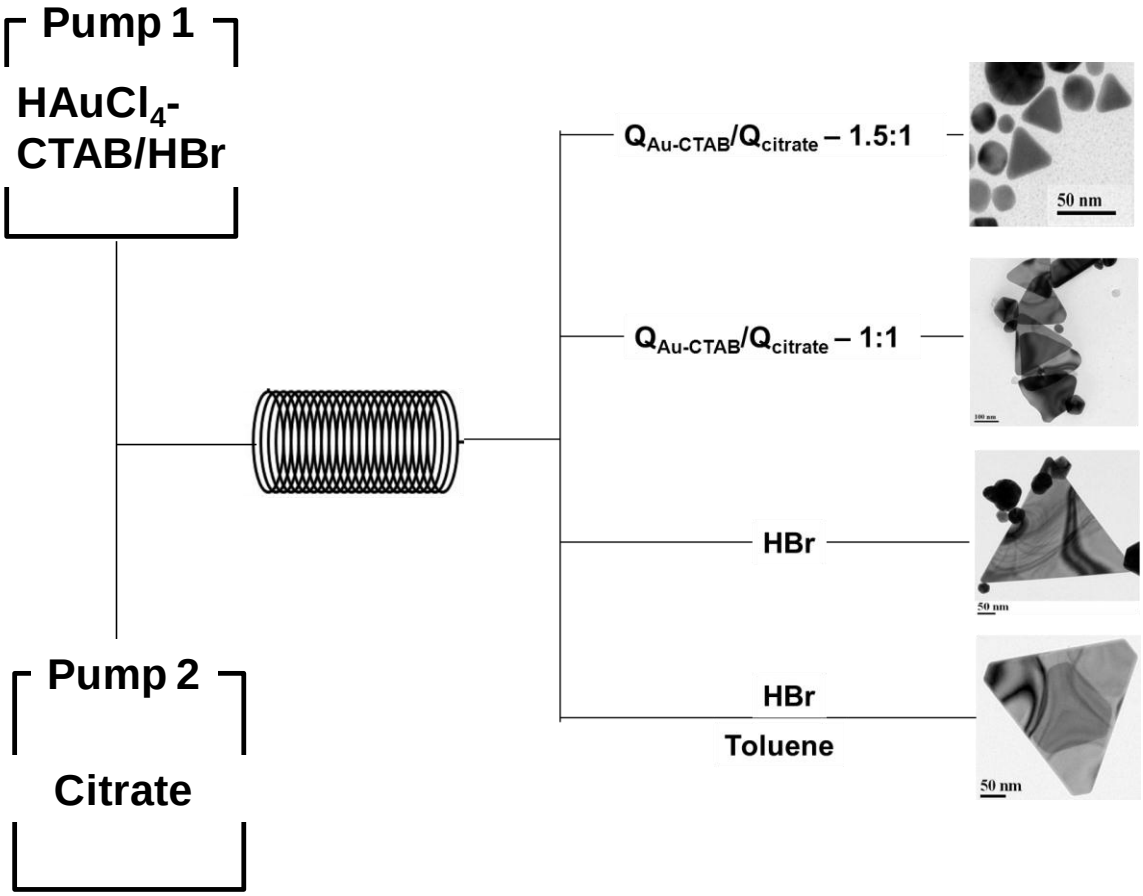

3B.1 Introduction:

It is necessary to understand and optimize the reaction parameters of a batch process for its successful transformation to continuous flow process. To synthesize triangular gold nanoplates by flow methods, in chapter 3 part A, we described the role of reaction parameters to get the maximum yield of the triangular nanoplates and simultaneously we established a surfactant less route to synthesize them using HBr. In this part, these optimized processes to synthesize triangular nanoplates (using surfactant and without surfactant) are taken up further for the continuous flow synthesis, using PTFE helical coil as microreactor. In addition to this, we deal several issues like reactor tube compatibility with growth solution, effect of heat transfer rate on morphology of the nanostructures, particle deposition in micro channel etc.

3B.2 Experimental:

3B.2.1 Microreactor tubing compatibility with $HAuCl_4$-CTAB solution:

In some earlier reports it was suggested that only certain type of tubing materials were compatible with the growth solution for the synthesis of anisotropic nanomaterials. Therefore, before proceeding to the synthesis of triangular gold nanoplates by flow methods, the compatibility of reactor tubing materials with reactant solution ($HAuCl_4$-CTAB) was checked by soaking different tubing materials (pharmed, silicone, PVC, SS316, PTFE) in two different sets of reactant solutions with same concentrations. One set was subjected to heating at 90 °C (which is reaction temperature) for 15-20 minutes and another set was kept on the bench top at room temperature. Controlled experiments were also carried without any tubing materials. Unlike earlier reports,[1] we did not observe any precipitation of growth solution (i.e. $HAuCl_4$-CTAB) at room temperature and precipitation was observed in all the solutions which were heated to 90 °C irrespective of the tubing material. Figure 3B.1 shows the photographs of different tubing material soaked in reactant solution at different temperatures (i.e. at 90 °C and at room temperature 28 °C). Prolonged heating of $HAuCl_4$-CTAB solution at high temperature causes the

surfactant to come out of phase and results in precipitation, clearly establishing that it is the heating that induces precipitation and not the tubing material. However, for the sake of convenience we conducted our experiments with PTFE tubes as microreactor and PEEK (Polyether ether ketone) as micromixer.

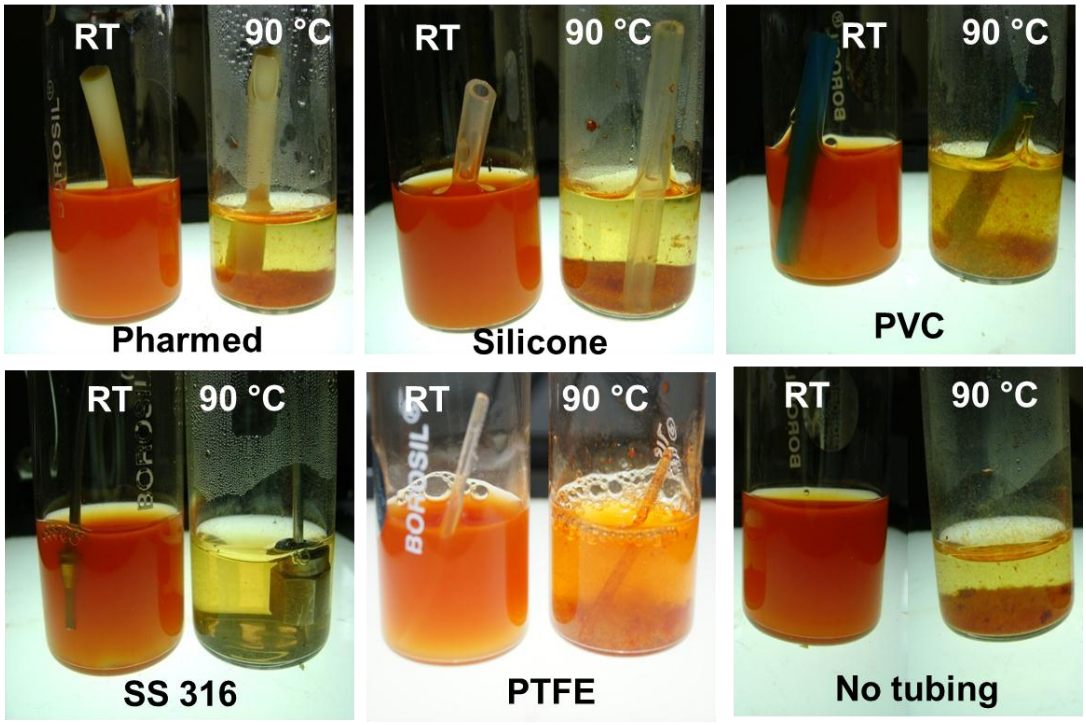

Figure 3B. 1: Photographs of different tubing material with reactant solution at different temperatures.

3B.2.2 Flow synthesis of triangular gold nanoplates using CTAB:

Our first set of experiments were based on surfactant based methods to synthesize triangular nanoplates in flow methods. In a beaker 16 mg of CTAB was added to the 5 mL of 1.25 mM $HAuCl_4$ solution. Upon the addition of CTAB, yellow colour of $HAuCl_4$ turns to red indicating the formation of CTAB-$HAuCl_4$ complex. In another beaker 0.128 mL of 0.1 M tri sodium citrate solution was diluted to 7.5 mL. A Y-shaped PEEK micromixer of i.d 0.5 mm was used as micromixer and this was connected to the PTFE helical tubing of i.d 0.9 mm, which was used as microreactor. Two peristaltic pumps (Longer, China) were used to dispense the solution from

beakers. Synthesis of triangular gold nanoplates was carried out at different temperatures, different volumetric ratios of sodium citrate ($Q_{citrate}$) and $HAuCl_4$ – CTAB solutions ($Q_{HAuCl4\text{-}CTAB}$). Figure 3B.2 shows the experimental setup and table 3B.1 shows the experimental details.

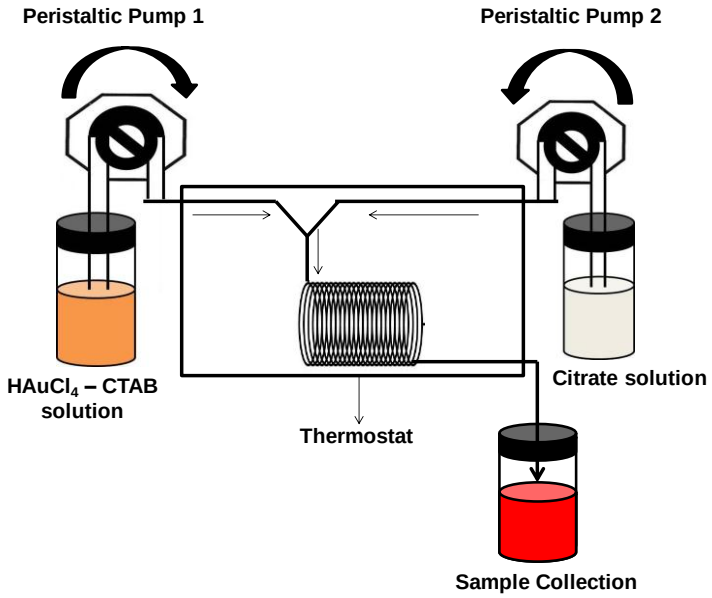

. **Figure 3B. 2: Schematic of the experimental setup used for triangular gold nanoplates using CTAB.**

Table 3B.1: Experimental conditions used for the flow synthesis of Au triangular nanoplates with CTAB

Exp.No	Reaction temperature& residence time	$Q_{citrate}/Q_{HAuCl4\text{-}CTAB}$
1	90 °C, 10 min	1.5:1
2	80 °C, 10 min	1.5:1
3	90 °C, 10 min,	1:1
4	90 °C, 10 min,	0.5:1

3B.2.2.a At different temperatures:

Flow synthesis of triangular gold nanoplates was carried out at two different reaction temperatures (i.e at 90 °C and 80 °C) and the volumetric flow ratio of citrate and $HAuCl_4$ –CTAB($Q_{citrate}/Q_{HAuCl4-CTAB}$) solutions was kept 1.5:1.

3B.2.2.a.1 UV-Vis-NIR and XRD analysis:

Figure 3B.3 shows the UV-Vis-NIR and XRD of Au nanostructures synthesized at different temperatures. Besides 530 nm peak (characteristic for Au nanostructures), broad peak observed at 750 nm indicates the anisotropic nature of the sample synthesized at both the temperatures. Broadening of 530 nm peak observed in the sample synthesized at 80 °C could be due to size distribution of the anisotropic nanostructures. PXRD recorded on samples coated on glass slides showed that the samples are highly oriented along <111> direction.

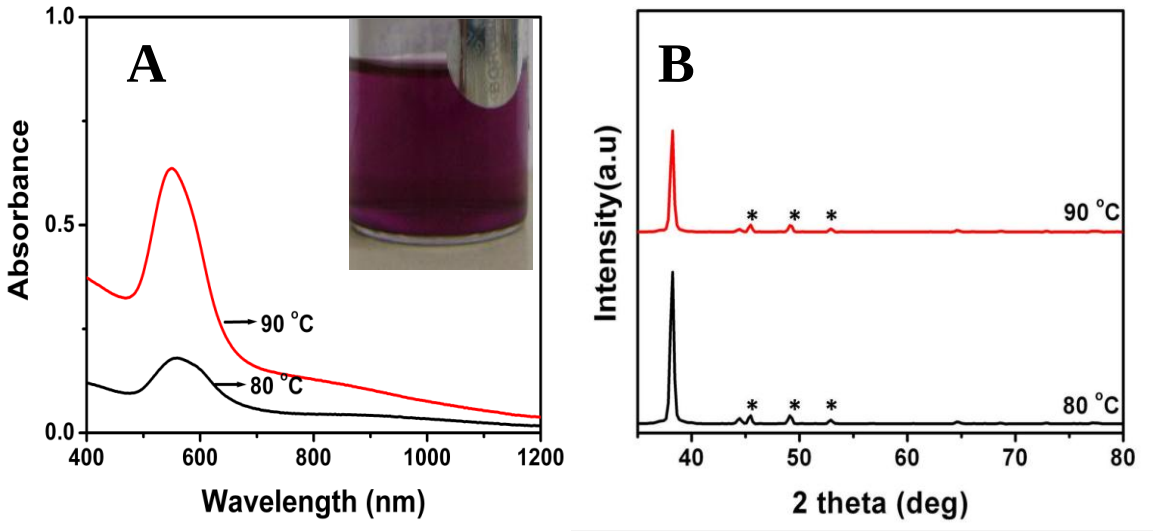

Figure 3B. 3: (A) UV-Visible-NIR spectra and PXRD of Au nanostructures synthesized by flow methods at different temperatures using CTAB, peaks assigned by * are due to CTAB. Inset A shows the photograph of the sample synthesized at 90°C.

3B.2.2.a.2 TEM analysis:

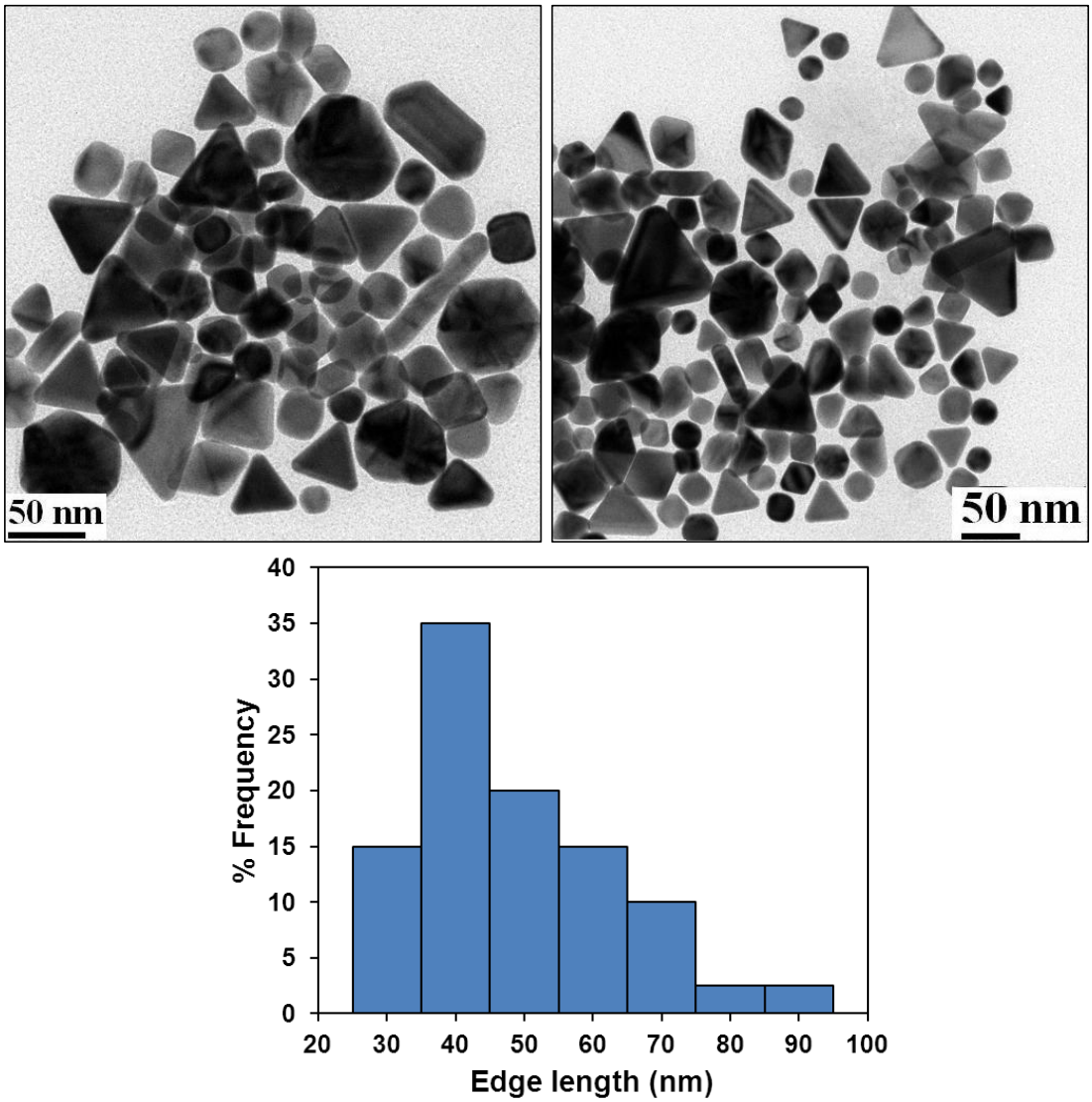

Figure 3B. 4: TEM images and edge length histogram of the triangular gold nanoplates synthesized by flow methods at 90 °C.

TEM images of Au nanostructures synthesized at 90 °C are shown in figure 3B.4. In addition to triangles, twinned particles and decahedrons are also seen in the TEM images. The edge length of triangles varied between 30-90 nm.

.

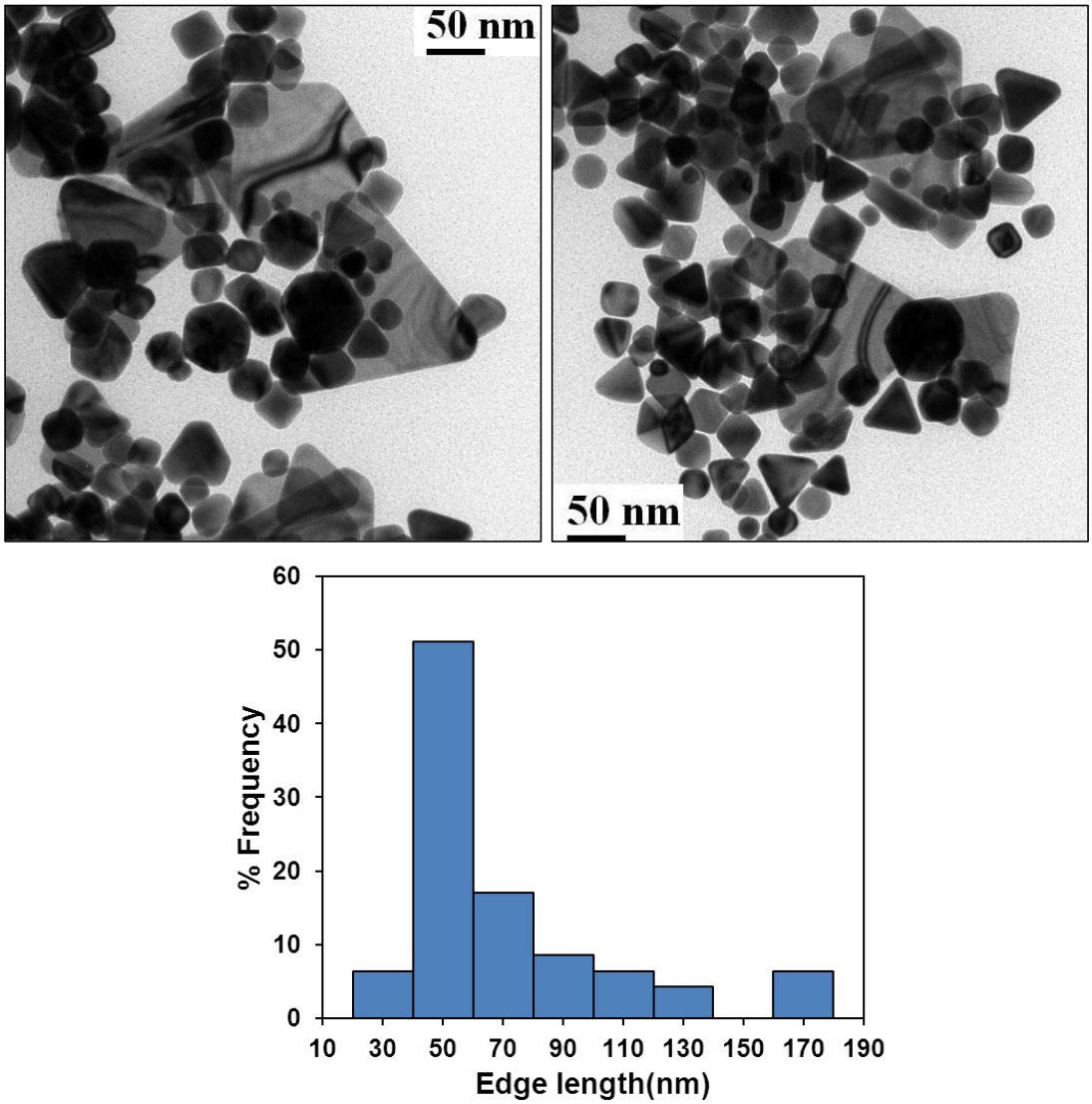

Figure 3B. 5: TEM images and histogram of edge length of triangles synthesized by flow methods at 80 °C

Figure 3B.5 shows the TEM images of the nanostructures synthesized by flow methods at 80 °C. Small (edge length 30-90 nm) and large triangular plates (edge length 110-170nm) can be seen in the sample synthesized at 80 °C and this wide variation in edge length (from 30 nm to 170 nm) is reflected in UV-Visible-NIR spectra of the corresponding sample, as explained in previous section.

3B.2.2.b At different flow ratios of citrate to $HAuCl_4$-CTAB solutions ($Q_{citrate}/Q_{HAuCl4\text{-}CTAB}$):

Flow synthesis of triangular gold nanoplates was carried out at different flow ratios of the citrate to $HAuCl_4$-CTAB solutions ($Q_{citrate}/Q_{HAuCl4\text{-}CTAB}$) for a residence time of 10 min at 90 °C. Flow rates of the solutions were changed by using peristaltic pumps (see table 3B.1).

3B.2.2.b.1 UV-Vis-NIR and XRD analysis:

Figure 3B.6 shows UV-Vis-NIR and XRD of the samples, synthesized at $Q_{citrate}/Q_{HAuCl4\text{-}CTAB}$ 1:1 and 0.5:1. In general UV-Vis-NIR spectra of noble metal nanotriangles show multipolar plasmon peaks[2] which are not observed in the spectra, but the broad UV-Vis-NIR spectra observed in this case are similar to many reported spectra in the literature,[3-7] which arise due to the long edge length. From the PXRD it can be realized that the triangular plates are highly oriented along <111> direction.

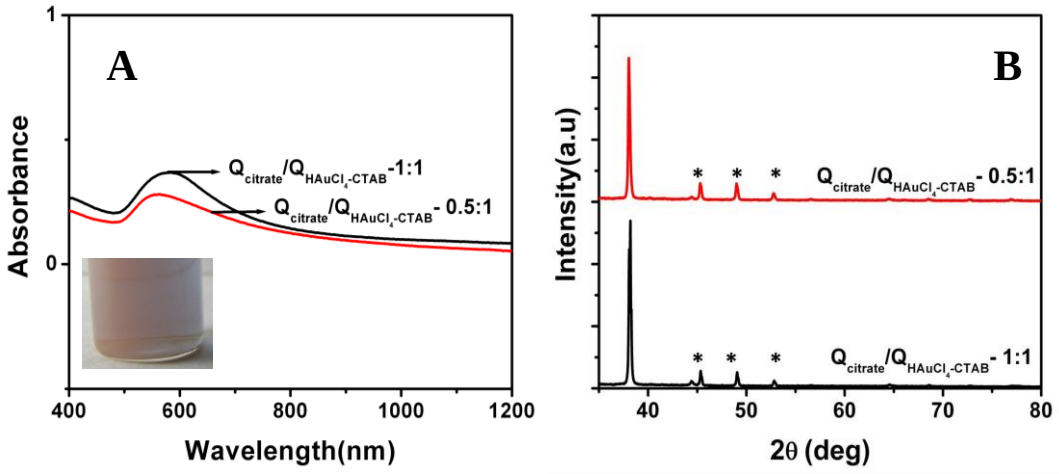

Figure 3B. 6: (A) UV-Visible-NIR spectra (B) XRD of triangular gold nanoplates synthesized at $Q_{citrate}/Q_{HAuCl4\text{-}CTAB}$ ratios 1:1 and 0.5:1 respectively and peaks assigned by * are attributed to excess CTAB present in the samples.

3B.2.2.b.2 TEM & SEM analysis:

As the ratio of $Q_{citrate}/Q_{HAuCl4\text{-}CTAB}$ was changed from 1.5:1 to 1:1 (by decreasing the flow rate of citrate) at 90 °C, the yield of triangles improved. In addition to this, the edge length of triangular plates increased from 30-90 nm (at 1.5:1 ratio) to 90-300 nm (when the ratio was 1:1) (figure 3B.7).

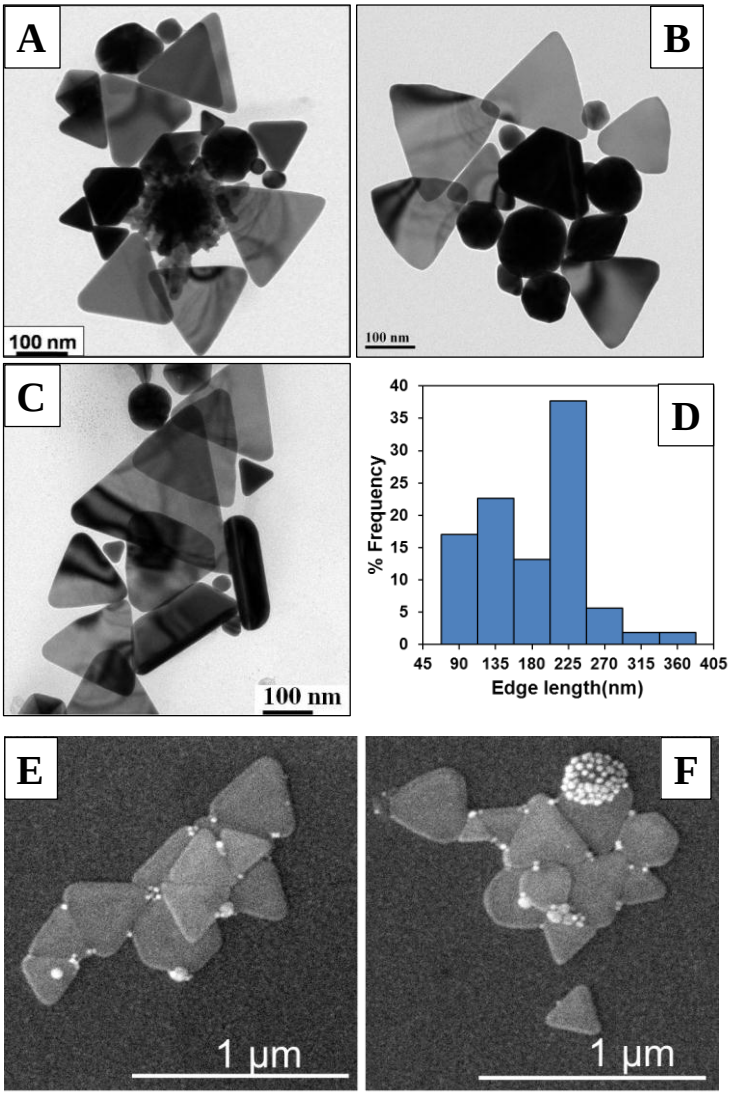

Figure 3B. 7: (A-C) TEM images of the triangular Au nanoplates synthesized at $Q_{citrate}/Q_{HAuCl4\text{-}CTAB}$ ratio 1:1 (D) Histogram of edge length of triangular nanoplates (E-F) SEM images of triangular nanoplates synthesized at same ratio.

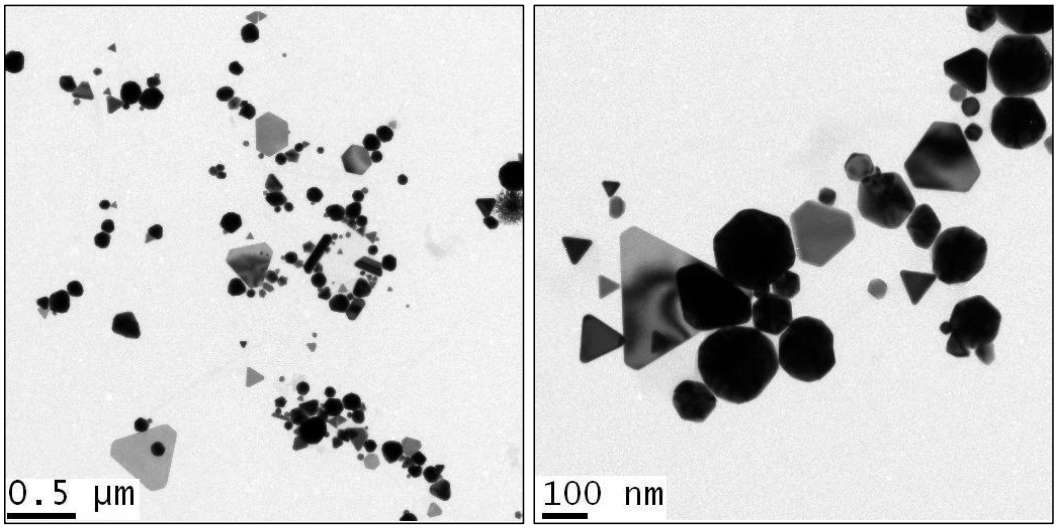

Figure 3B. 8: TEM images of Au nanostructures synthesized at $Q_{citrate}/Q_{HAuCl4\text{-}CTAB}$ at 0.5:1

As $Q_{citrate}/Q_{HAuCl4\ -\ CTAB}$ was further decreased from 1:1 to 0.5:1 the yield of triangular nanoplates gets hampered. This could be attributed to the insufficient amounts of citrate, due to which number of irregular polyhedral particles increased (figure 3B.8).

3B.2.3 Flow synthesis of triangular gold nanoplates using HBr:

Based on the results of batch processes explained in part A of this Chapter, we used HBr instead of CTAB to synthesize triangular nanoplates. As described earlier, to 1.25 mM $HAuCl_4$ solution, 0.1 M HBr was added to maintain HBr to $HAuCl_4$ molar ratio of 4. In addition to this solution, sodium citrate solutions with two different concentrations (2.1 mM and 3.4 mM) were also prepared. $HAuCl_4$-HBr and citrate solutions were taken in two different syringes and solutions were dispensed using syringe pumps. The syringes (Poly Propylene) were connected to the microreactor (PTFE helical coil, 0.9 mm i.d) through a Y-shaped micromixer (PEEK, i.d 0.5 mm). Synthesis of nanoplates was carried out at different volumetric flow ratios of sodium citrate solution ($Q_{citrate}$) and $HAuCl_4$- HBr($Q_{Au\text{-}HBr}$) solutions. Synthesis of nanoplates using HBr was carried out in segmented flow also, using similar experimental set-up (figure 3B.9A). For segment generation toluene was used as inert phase and four connector micromixer (PEEK, 0.5 mm i.d) was used as micromixer instead of Y-

micromixer. Schematic of the experimental setup and the experimental details are given in figure 3B.9 and table 3B.2 respectively.

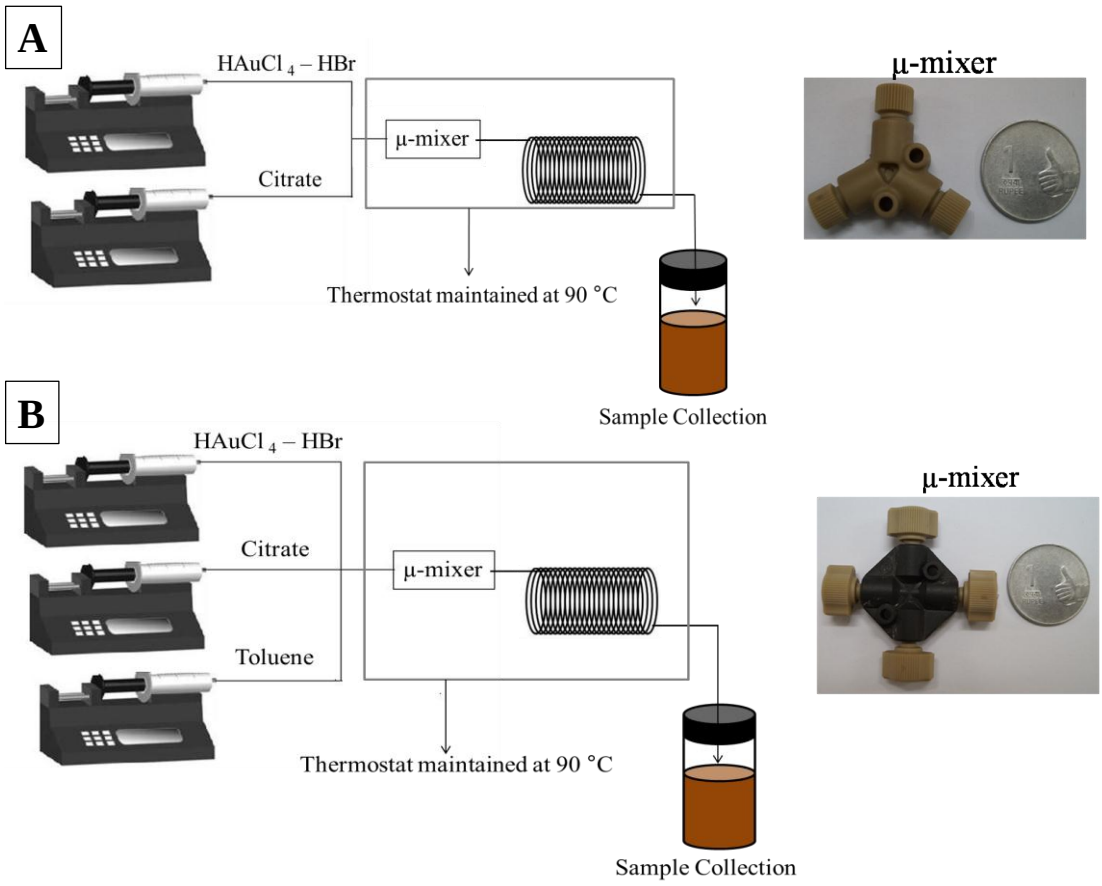

Figure 3B. 9: Schematic of experimental setup used for the flow synthesis of triangular Au nanoplates using HBr (A) without (B) with inert phase toluene.

Table 3B.2: Experimental conditions used for the flow synthesis of triangular plates using HBr

S.No	Experiment	Reaction temperature, residence time & flow conditions	Citrate concentration(mM)	$Q_{citrate}/Q_{Au-HBr}$	$Q_{inert\ phase}/Q_{reactant\ phase}$
1	Exp-A	90 °C, 10 min	2.1	1.5:1	-
2	Exp-B	90 °C, 10 min	3.4	1:1	-
3	Exp-A, segmented flow	90 °C, 10 min, segmented flow	2.1	1.5:1	1
4	Exp-B, Segmented flow	90 °C, 10 min, segmented flow	3.4	1:1	1

3B.2.3.a UV-Vis-NIR analysis:

UV-Visible-NIR spectral features (figure 3B.10) are similar to the previous case where nanoplates were synthesized using CTAB, suggesting the presence of large anisotropic nanostructures. Increase in intensities of absorbance were observed when the flow conditions are changed to segmented flow using toluene indicating that the possibility of particle deposition in the channel was completely eliminated.

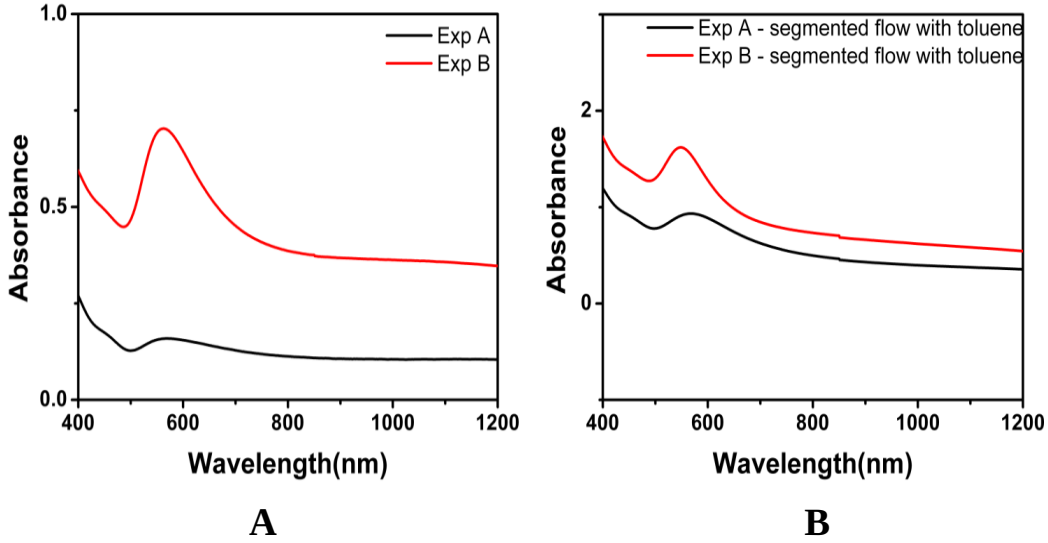

Figure 3B.10: (A) UV-Vis-NIR spectra of triangular Au nanoplates synthesized in experiments A and B (B) UV-Vis-NIR spectra triangular nanoplates synthesized in segmented flow conditions of experiment A and B.

3B.2.3.b TEM analysis:

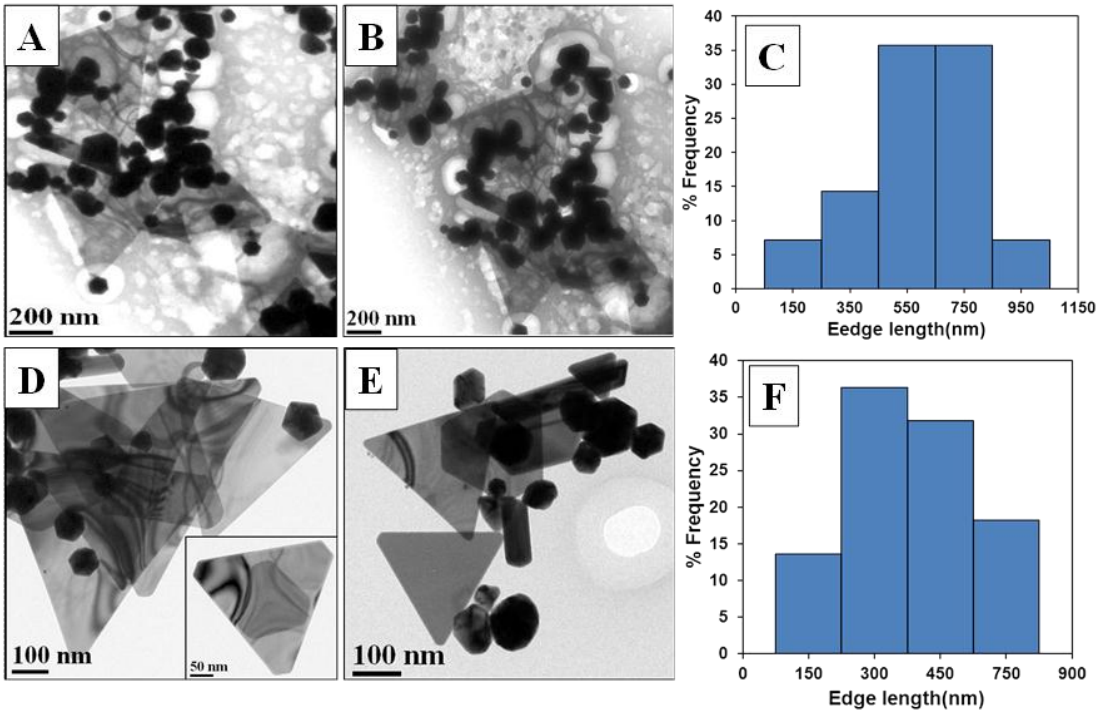

Figure 3B.11: (A-B) TEM images of triangular nanoplates synthesized in exp-A and (C) is corresponding histogram. (D-E) TEM images of nanoplates synthesized in segmented flow conditions of exp-A and corresponding histogram presented in (F).

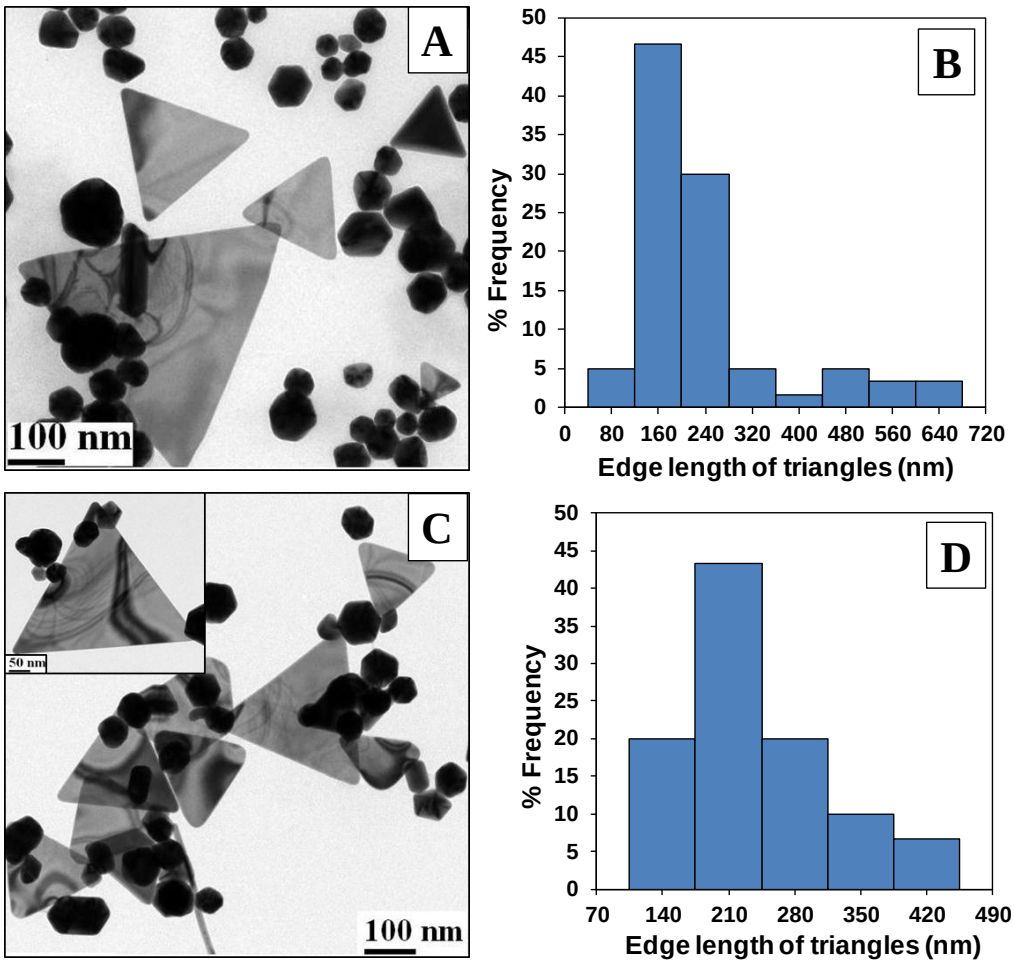

Figure 3B.12: (A) TEM images of triangular Au nanoplates synthesized in experiment B and (B) corresponds histogram of edge length of triangular nanoplates. (C) TEM image of triangular Au nanoplates synthesized in segmented flow conditions of experiment B and (D) is corresponding histogram of edgelength of triangular nanoplates.

Figure 3B.11 A & B show the TEM images of the triangular Au nanoplates, synthesized using HBr by flow method. Here, concentration of citrate was 2.1mM and the citrate to $HAuCl_4$-HBr solution flow rate ratio was maintained at 1.5:1(similar parameters were used for the procedure named as exp – A, see table 3B.2). The edge length of the triangles in the continuous flow methods with HBr was found to vary from 150 nm - 950 nm which is very large and broad as compared to the triangular nanoplates synthesized using CTAB (90 nm-300 nm). This clearly shows the advantage of CTAB as shape directing agent. No formation of large

triangular nanoplates (of edge length >750 nm) were observed when the flow pattern was changed to segmented flow using toluene under identical experimental conditions. Here the edge length was typically 150-750 nm (figure 3B.11 D, E and F). Concentration of citrate was changed from 2.1 mM to 3.4 mM and $Q_{citrate}/Q_{Au\text{-}HBr}$ was decreased from 1.5:1 to 1:1 in Exp B (see table 3B.2). This situation (i.e. increase in no. of moles of citrate) helped to decrease the edge length range of triangular nanoplates (80 nm-640 nm) but broad edge length range was observed as in case of experiment A. Here also, when the flow pattern changed to segmented flow under similar conditions, no large nanoplates (edge length >450 nm) were observed (figure 3B.12).

3B.3 Discussion:

Investigations on synthesis of triangular nanoplates from our group[8] and from other groups[9-14] reveal that their formation is a kinetically controlled process for which nucleation has to be initiated at low temperatures and with sufficiently low rates in order to get the maximum yield.[15] Surfactant assisted methods were identified as the best to synthesize the triangular nanoplates.[16] Initially the synthesis was carried out at different reaction temperatures (i.e. at 80 °C and 90 °C). From the TEM images (figure 3B.4 and 3B.5) we observed that triangular plates were less in number in at both 80 °C and 90 °C. The reduction of Au^{+3} ions to Au (0) using citrate as reducing agent occurs through colourless Au^{+1} intermediate.[17, 18] At the specified reaction conditions and concentrations, the reduction of Au^{+1} to Au (0) does not occur for temperature ≤ 70 °C. Hence the flow synthesis of nanoplates was not employed at these temperatures. Due to high surface to volume ratios, the heat transfer is relatively faster in microreactors than the traditional batch reactors. This can be understood by calculating temperature profiles.

Calculating temperature profiles in PTFE helical coil:

The following dimensional less numbers were calculated to know the temperature T_L at length L of the reactor.[19]

a) Reynolds number $Re = \frac{\rho v D_h}{\mu}$

D_h- Hydraulic diameter = 0.0009 m

ρ – Density of water = 1000 kg/m^3

v – Velocity of the fluid = 0.00865m/sec (for residence time of 10 min)

μ – Dynamic viscosity of water = 0.001 kg/m-sec

(b) Helical Number $He = Re(\frac{d}{2R_c})^{\frac{1}{2}}$

d - Diameter of the channel = 0.0009 m

Rc - Critical radius of the Coil given by $Rc = R\left(1 + \frac{p}{2\prod R}\right)$ where 'p' is pitch (0.0009 m) and 'R' is the helical radius (0.03 m).

(c) Prandtl Number $\Pr = \frac{C_p \mu}{\kappa}$

Cp – Specific heat of water = 4179 J/kg-K

κ – Thermal Conductivity of water = 0.58 W/m-K

(d) Based on Manlapaz- Churchill correlation on helical coils, *Nusselt number (Nu)* can be expressed as[20]

$$Nu = \left[\left(3.657 + \frac{4.343}{\left(1 + \frac{957}{PrHe^2}\right)^2}\right)^3 + 1.158\left(\frac{He}{1 + \frac{0.477}{Pr}}\right)^{\frac{3}{2}}\right]^{\frac{1}{3}}$$

Heat transfer coefficient (h) can be obtained from the following expression

$$h = \frac{\kappa N_u}{D}$$

At tube length 'L' temperature of the fluid in the tube T_L can be obtained from the following equation.

$$\frac{T_L - T_o}{T_w - T_L} = \frac{\prod DhL}{mC_p}$$

T_w – Wall temperature (80 °C & 90 °C)

T_O – Temperature of the fluid at inlet (30 °C)

m – Mass flow rate = 0.0000055 kg/s

D – Density of the fluid in thermostat (water) = 1000 kg/m^3

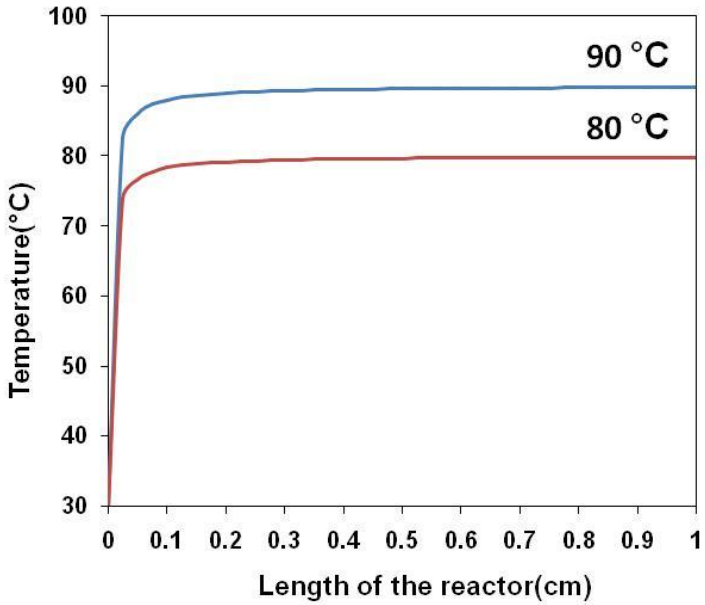

Figure 3B.13: Temperature profiles along the length of the PTFE helical coil at reactions temperatures 80 °C and 90 °C.

Temperature profiles plotted along the length of the reactor shown in the figure 3B.13. This clearly demonstrates the temperature of the fluid in the microchannel rises to final reactor temperature (90 °C) rapidly. Therefore, low nucleation rate could not be maintained at 90 °C and the fast nucleation rate leads to reduction in the yield of the triangles. This situation can be circumvented by (i) integrating temperature controller (heating cartridges) with the microreactor[21] or (ii) by reducing the feed of citrate. Rate of reaction and hence the rate of nucleation of nanoparticles depends upon the concentration of reducing agent and at low concentration of reducing agent, nucleation could be sufficiently slow. In the present case, low citrate concentrations help to maintain the low nucleation rates and the formed plate like seed in nucleation step could grow completely to triangular plates with the use of unreduced growth solution. Hence the synthesis of nanoplates was continued by diminishing the $Q_{citrate}/Q_{HAuCl4\text{-}CTAB}$ from 1.5:1 to 1:1 at 90 °C for 10 minutes. At this condition the number yield of the triangular nanoplates improved (see figure 3B.7). When $Q_{citrate}/Q_{HAuCl4\text{-}CTAB}$ was further decreased from 1:1 to 0.5:1, the yield of triangular plates got hampered, probably due to insufficient amounts of citrate.

Halide ions[22-31] and more specifically bromide ions[32-34] play a major role to determine the shape of nanostructures and our previous investigation describe the preparation of triangular nanoplates in which we replaced CTAB with HBr.[8] The optimized reaction conditions of the batch process were used for the continuous flow synthesis. In experiments A & B (table 3B.2) synthesis of nanoplates was carried under laminar flow conditions (Re=8) and the velocity profiles are parabolic. Formation of large nanostructures without the use of any capping agent, under parabolic velocity profiles causes the deposition of the particles in the channel.[35] To avoid the deposition of particles we synthesized the nanostructures under segmented flow conditions by inducing an inert liquid phase (toluene) using a four connector micromixer. Interfacial tension, density, viscosity differences between the reactant and inert liquid phases cause the breakage of reactant phase into segments. Continuous inert liquid phase helps to avoid the contact between reactant liquid segments with channel wall and eliminates the possibility of deposition of

particles in the channel (which can not be achieved by using gas as inert phase). The UV-Vis-NIR spectra (figure 3B.10) show that the absorbance intensity corresponding to the nanostructures increased when the flow pattern changed to segmented flow. In addition to this the homogeneity of triangular plates also improved. Though few polyhedral particles formed, these can be separated from the triangular plates by recent reported methods[36, 37] and the method of synthesis separation processes can be integrated on a microfluidic platform. Such efforts could be the topic of further studies.

3B.4 Conclusions:

Flow synthesis of gold triangular nanoplates was established using surfactant directed methods. Micro reactor tubing compatibility with the reactant solution was examined with different tubing materials. Understanding the temperature profiles in the microchannel facilitated to tune the operational condition and to improve the number yield of triangular nanoplates. Surfactant less green protocols to synthesis nanoplates were also explored by the flow methods.

3B.5 References:

1. Boleininger, J.; Kurz, A.; Reuss, V.; Sönnichsen, C., *Phys. Chem. Chem. Phys.* **2006,** *8*, 3824-3827.

2. Félidj, N.; Grand, J.; Laurent, G.; Aubard, J.; Lévi, G.; Hohenau, A.; Galler, N.; Aussenegg, F.; Krenn, J., *J. Chem. Phys.* **2008,** *128*, 094702.

3. Tan, Y. N.; Lee, J. Y.; Wang, D. I. C., *J. Phys. Chem. C* **2008,** *112*, 5463-5470.

4. Wang, L.; Chen, X.; Zhan, J.; Chai, Y.; Yang, C.; Xu, L.; Zhuang, W.; Jing, B., *J. Phys. Chem. B* **2005,** *109*, 3189-3194.

5. Shao, Y.; Jin, Y.; Dong, S., *Chem. Commun.* **2004**, 1104-1105.

6. Jiang, P.; Zhou, J. J.; Li, R.; Gao, Y.; Sun, T. L.; Zhao, X. W.; Xiang, Y. J.; Xie, S. S., *J.Nanopart.Res* **2006,** *8*, 927-934.

7. Lim, B.; Camargo, P. H. C.; Xia, Y., *Langmuir* **2008,** *24*, 10437-10442.

8. Kumar, D. V. R.; Kulkarni, A. A.; Prasad, B. L. V., *Colloids Surf., A* **2013**.

9. Xiong, Y.; Washio, I.; Chen, J.; Cai, H.; Li, Z. Y.; Xia, Y., *Langmuir* **2006,** *22*, 8563-8570.

10. Halder, A.; Kundu, P.; Viswanath, B.; Ravishankar, N., *J. Mater. Chem.* **2010,** *20*, 4763-4772.

11. Viswanath, B.; Kundu, P.; Halder, A.; Ravishankar, N., *J. Phys. Chem. C* **2009,** *113*, 16866-16883.

12. Viswanath, B.; Kundu, P.; Mukherjee, B.; Ravishankar, N., *Nanotechnology* **2008,** *19*, 195603.

13. Viswanath, B.; Kundu, P.; Ravishankar, N., *J. Colloid Interface Sci.* **2009,** *330*, 211-219.

14. Langille, M. R.; Personick, M. L.; Zhang, J.; Mirkin, C. A., *J. Am. Chem. Soc.* **2012**.

15. Langille, M. R.; Personick, M. L.; Zhang, J.; Mirkin, C. A., *J. Am. Chem. Soc.* **2012,** *134*, 14542-14554.

16. Huang, W. L.; Chen, C. H.; Huang, M. H., *J. Phys. Chem. C* **2007,** *111*, 2533-2538.

17. Pong, B. K.; Elim, H. I.; Chong, J. X.; Ji, W.; Trout, B. L.; Lee, J. Y., *J. Phys. Chem. C* **2007,** *111*, 6281-6287.

18. Ojea-Jiménez, I.; Romero, F. M.; Bastús, N. G.; Puntes, V., *J. Phys. Chem. C* **2010,** *114*, 1800-1804.

19. Lin, X. Z.; Terepka, A. D.; Yang, H., *Nano Lett.* **2004,** *4*, 2227-2232.

20. Manlapaz, R. L.; Churchill, S. W., *Chem. Eng. Commun.* **1981,** *9*, 185-200.

21. Lee, S. K.; Liu, X.; Sebastian, V.; Jensen, K. F., *Lab Chip* **2012**.

22. Grzelczak, M.; Sanchez-Iglesias, A.; Rodriguez-Gonzalez, B.; Alvarez-Puebla, R.; Perez-Juste, J.; Liz-Marzan, L. M., *Adv. Funct. Mater.* **2008,** *18*, 3780-3786.

23. Ha, T. H.; Koo, H.-J.; Chung, B. H., *J. Phys. Chem. C* **2007,** *111*, 1123-1130.

24. DuChene, J. S.; Niu, W.; Abendroth, J. M.; Sun, Q.; Zhao, W.; Huo, F.; Wei, W. D., *Chem. Mater.*, Ahead of Print.

25. Millstone, J. E.; Wei, W.; Jones, M. R.; Yoo, H.; Mirkin, C. A., *Nano Lett.* **2008,** *8*, 2526-2529.

26. Smith, D. K.; Korgel, B. A., *Langmuir* **2008,** *24*, 644-649.

27. Smith, D. K.; Miller, N. R.; Korgel, B. A., *Langmuir* **2009,** *25*, 9518-9524.

28. Tang, B.; Xu, S.; An, J.; Zhao, B.; Xu, W.; Lombardi, J. R., *Phys. Chem. Chem. Phys.* **2009,** *11*, 10286-10292.

29. Wang, J.; Li, Y. F.; Huang, C. Z., *J. Phys. Chem. C* **2008,** *112*, 11691-11695.

30. Rai, A.; Singh, A.; Ahmad, A.; Sastry, M., *Langmuir* **2006,** *22*, 736-741.

31. Kim, J.; Hong, S.; Jang, H.-J.; Choi, Y.; Park, S., *J. Colloid Interface Sci.* **2013,** *389*, 71-76.

32. Garg, N.; Scholl, C.; Mohanty, A.; Jin, R., *Langmuir* **2010,** *26*, 10271-10276.

33. Si, S.; Leduc, C.; Delville, M.-H.; Lounis, B., *ChemPhysChem* **2012,** *13*, 193-202.

34. Liu, Y.; Liu, L.; Guo, R., *Langmuir* **2010,** *26*, 13479-13485.

35. Yen, B. K. H.; Günther, A.; Schmidt, M. A.; Jensen, K. F.; Bawendi, M. G., *Angew. Chem.* **2005,** *117*, 5583-5587.

36. Guo, Z.; Fan, X.; Xu, L.; Lu, X.; Gu, C.; Bian, Z.; Gu, N.; Zhang, J.; Yang, D., *Chem. Commun.* **2011,** *47*, 4180-4182.

37. Ha, T. H.; Kim, Y. J.; Park, S. H., *Chem. Commun.* **2010,** *46*, 3164-3166.

Chapter 4

Continuous flow synthesis of nanocrystalline MgO (NC-MgO) using microjet micromixer

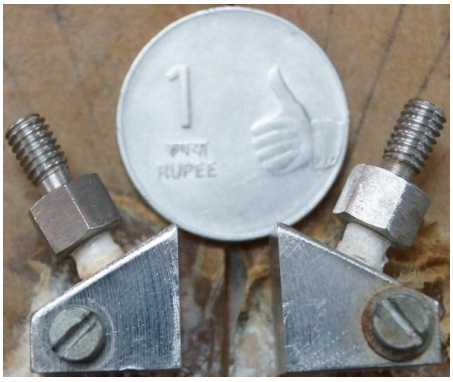

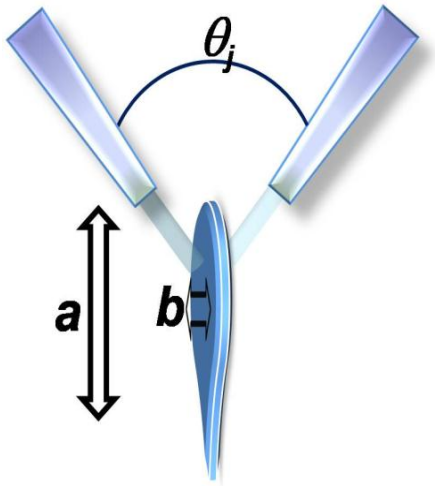

4.1 Introduction:

As a part of this thesis work, we so far concentrated on nanoparticle syntheses which are finally obtained as dispersions in a solvent. While continuous flow synthesis of such materials is itself a difficult task, continuous flow synthesis of materials through sol gel process poses an altogether different level of challenge. The main problems associated with such procedures to be adopted for continuous flow synthesis are (i) clogging of channels because of rigid gel formation and (ii) very fast reaction kinetics. Nevertheless, preparation of such materials by continuous flow methods is necessitated due to the need of large quantities of material without sacrificing the important characteristics like surface area and crystalline nature. As these sol gel processes involve the mixing of two reagents to make the gel one can easily imagine that 'mixining' plays an important role in governing the vital characteristics of the material. In traditional batch processes maintaining uniformity in mixing is not an easy task especially when huge volumes of reagents are involved. Tackling this issue, in this chapter, we provide an alternative method for the continuous flow synthesis of nanocrystalline metal oxide powders using impingement jet micromixer. The metal oxide we chose for this purpose is magnesium oxide.

Nanocrystalline MgO (NC-MgO) is one of the commercially important inorganic oxide.[1-14] Synthesis of high surface area NC-MgO by the sol gel process has been reported earlier.[15-17] The process involves the hydrolysis of magnesium methoxide in methanol-toluene mixtures, which is a rapid process and it forms a rigid gel in 30 sec.[18, 19] In this kind of rapid sol gel processes, mixing plays an important role. Local concentration variations because of the inhomogeneous mixing can alter the rate of hydrolysis and poly condensations, finally affecting the quality of the material. So the mixing has to be faster than the reaction to achieve high quality material. General batch preparative methods could not achieve better mixing, when extended to large scale. In addition to this, because of the rigid gel formation, simple micromixers (where the better and uniform mixing can be expected) also unfit for this process to be scaled up.

Researchers successfully used the confined impingement jet reactors (CIJs) to scale up the production of nanoparticles.[20] Polymer coated nanoparticles,[21] pharmaceutical particles,[22] $CaCO_3$[20] etc. involving rapid precipitation processes were prepared using CIJs. In CIJs, two liquid jets with high flow rates, collide with each other in a confined space[23] and this situation is not suitable for the present process, where the rigid gel formation may block the channel. This limitation can be overcome by allowing the collision of two liquid jets at outside of the micromixer, in a "wall free environment". Figure 4.1 shows one of such micromixer designed by IMM-Mainz, Germany. [24]

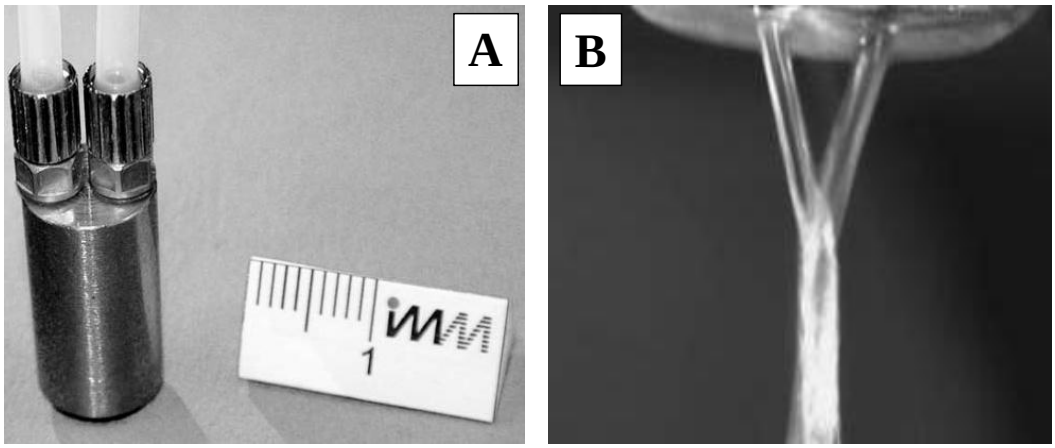

Figure 4.1: (A) Photograph of the micromixer (B) mixing of two liquid jets (taken from reference 24).

Taking the above discussion into consideration, we designed a jet micromixer where the reactant liquid jets collide in wall free environment, and where the angle between the jets can also be changed. This chapter describes the continuous flow process to synthesize nanocrystalline MgO (NC-MgO) by rapid sol gel process using such jet micromixer. We study the effect of angle between the jets, flow rates (Reynolds number, Re) on the thickness and shape of the mixing zone formed and correlate these to the BET surface area of the NC-MgO.

4.2 Fabrication of microjet micromixer:

A microjet device was fabricated and assembled such that it comprises of two micro-machined segments attached on a backbone structure that allows changing the angle between the microchannels in the same plane. The microchannels of 0.3 mm diameter were machined in SS316 segments. The two segments can be adjusted simultaneously to get equal angular distance from the point of jet interaction. Two reactant fluids were pumped in the individual segments using syringe pumps (Longer Precision Pumps Ltd., China). The injected fluids exit the segments at high velocity and intersect to yield a thin sheet of mixing zone followed by a thread. The velocity of the jets was adjusted to get stable mixing zone. The images of the mixing zone at different jet velocities and at different angle between the jets were recorded using high speed camera with a frame rate of 500 frames per second (Red lake, USA). The images were analyzed using Image-Pro Plus (version 5.1) software.

4.3 Synthesis of NC- MgO:

4.3.1 Batch process: NC- MgO was synthesized using sol gel process by earlier reported methods[18, 19] with some modifications. In brief 0.4 M $Mg(OCH_3)_2$ and 0.8 M H_2O solutions were prepared using methanol and toluene solvent mixtures, in such a way that toluene to methanol volume ratio becomes 1.6 upon mixing of equal amounts of both the solutions. A rigid gel formed within 30 sec of mixing of these two solutions. The gel was allowed for aging for 24 hours at room temperature then vacuum died at 90 °C for 6 hours. The dried gel sample was calcinated at 500 °C for one hour.

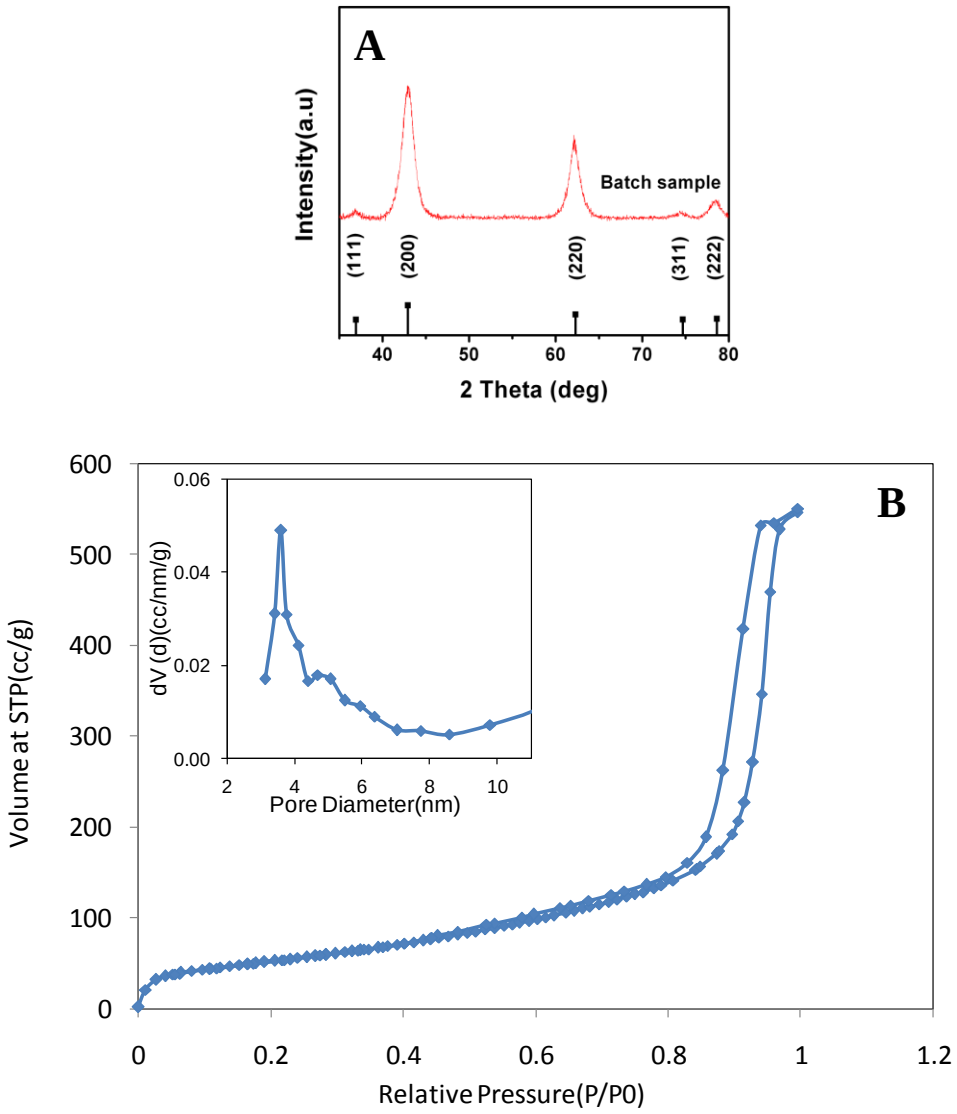

Figure 4.2: (A) PXRD (B) N_2 adsorption- desorption isotherm of the NC-MgO sample synthesized in batch. Inset of B shows pore size distribution of the sample.

Figure 4.2 shows the PXRD and N_2 adsorption – desorption isotherms of NC-MgO synthesized in batch. The isotherm indicates the porous nature of the smaple and the BET surface area turned to be 191 m^2/g with a crystallite size (calculated from Scherrer's formula) of 5.6 nm.

4.3.2 Continuous flow synthesis of NC-MgO:

0.4 M $Mg(OCH_3)_2$ and 0.8 M H_2O solutions were prepared using methanol and toluene mixtures keeping the toluene to methanol volume ratio 1.60. Two different glass syringes were filled with these solutions which were dispensed with syringe pumps (Longer pumps, China). These were connected to microjets using glass to metal connectors.

4.3.2a at different angle between the jets:

The area of mixing zone depends on the angle between the two jets and the synthesis of wet gels was carried out at different angle between the jets by maintaining a total flow rate of 30 mL/min (15 mL/min per syringe). The angle between the jets was varied from 70° to 140°. Angles below and above of these were not considered as a stable mixing zone was not observed. The collected samples were dried as explained in the previous section (see figure 4.3 and 4.4 for details).

4.3.2b at different flow rates:

The Reynolds number (Re) of fluid jet changes with the flow rate and the mixing is expected to change with the Reynolds number. Synthesis of NC- MgO was carried out at a total flow rate of 20 mL/min (10 mL/min per syringe), 30 mL/min (15 mL/min per syringe) and 40 mL/min (20 mL/min per syringe). In each case, the angle between the jets was kept constant at 120°. As equal flow rates were maintained in each syringe, the stoichiometry between these solutions is retained. The collected samples were dried and subjected for characterization. Schematic representation of the experimental setup and mixing zone are represented in the figure 4.3.

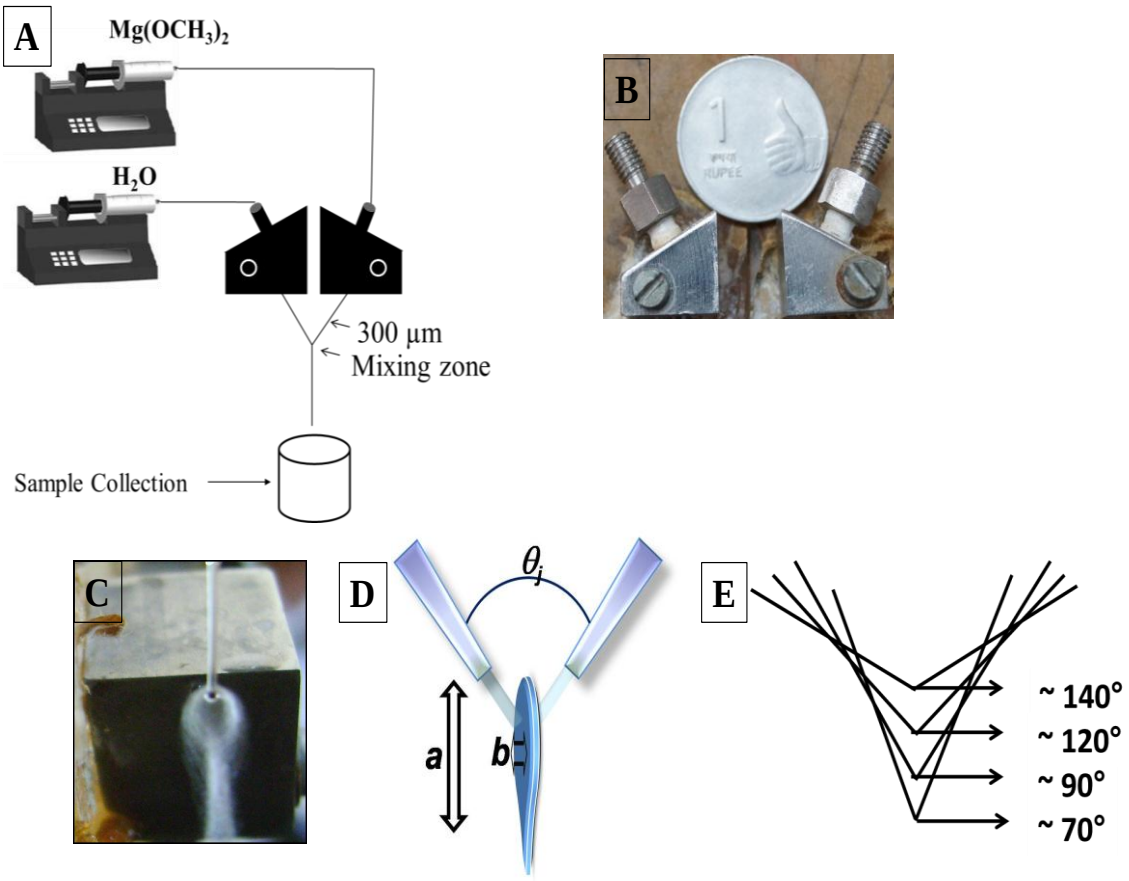

Figure 4.3: (A) Schematic representation of experimental set up (B) Photograph of the micromixer (C) Side view of the mixing zone (D) Schematic of mixing zone in which 'ɵ' is the angle between the jet, 'a' and 'b' are the major and minor lengths of mixing zone and (E) is the schematic of different angle between the jets.

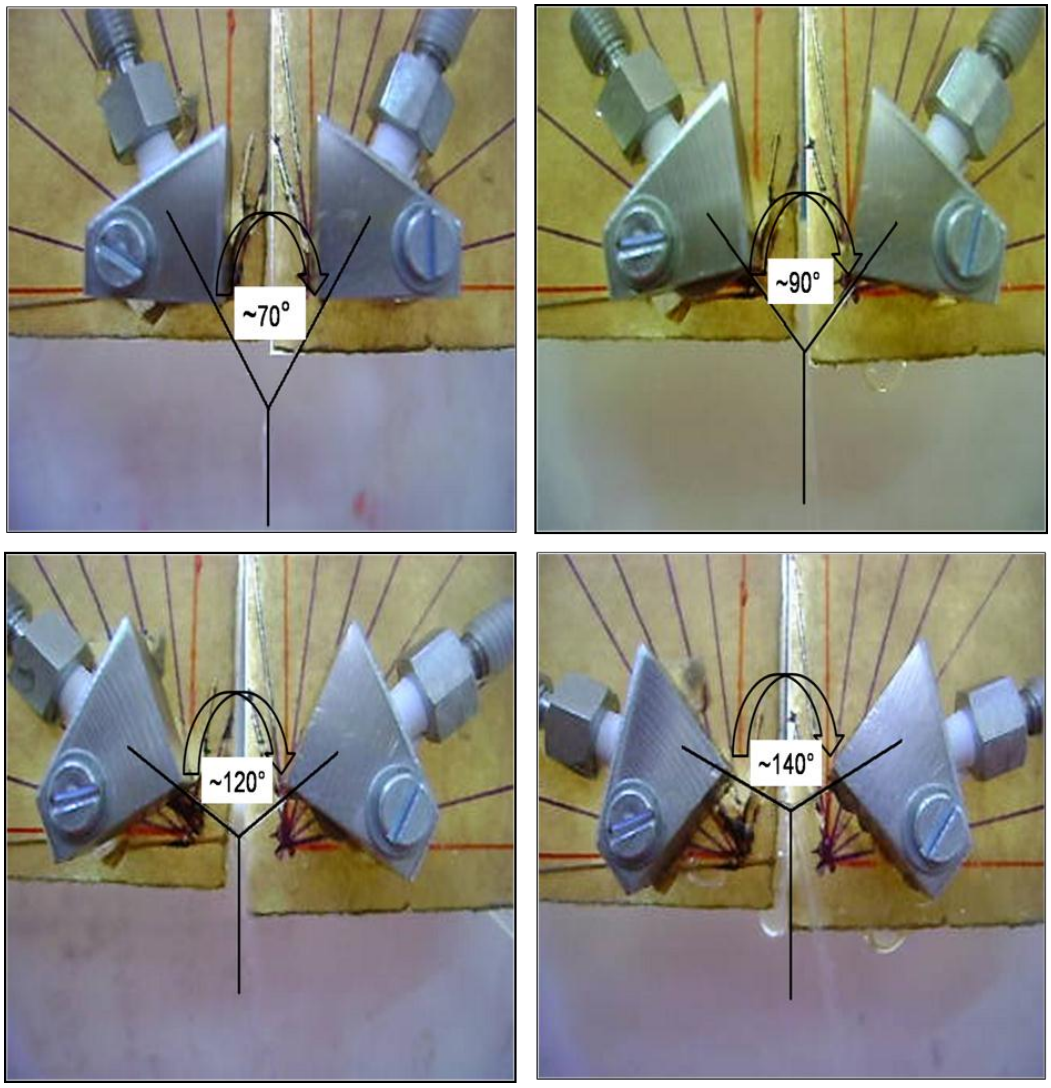

Figure 4. 4: Photographs of the Jet micromixer at different angle between the jets.

4.4 SEM analysis of the wet gels:

Wet gels, synthesized in batch and continuous flow conditions were subjected to SEM analysis by applying small amount of the sample on carbon tape. Figure 4.5 shows the SEM images of the wet gel samples. The images clearly disclose sponge like porous nature of the sample.

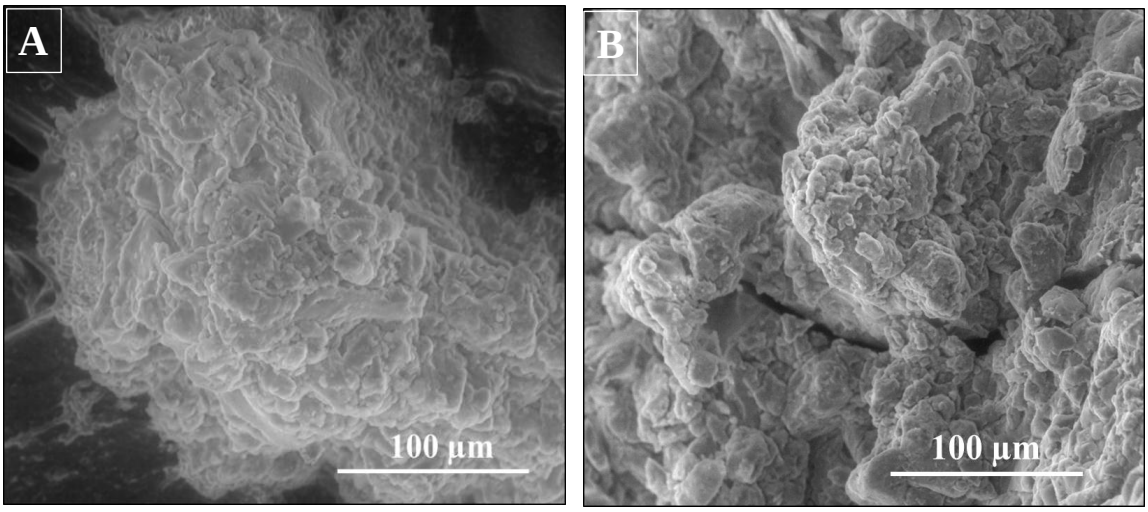

Figure 4. 5: SEM images of the wet gel sample synthesized in (A) batch and (B) continuous flow methods.

4.5 FT-IR analysis:

Figure 4.6 shows the FT-IR spectra of the dried gel (NC-MgO) synthesized in batch and continuous flow conditions. Peak above 3500 cm^{-1} and broad peak in the region of 3300 to 3500 cm^{-1} confirm the presence of O-H and Mg-O-H groups in the sample. Formation Mg-O was confirmed by the appearance of peak at 540 cm^{-1}.

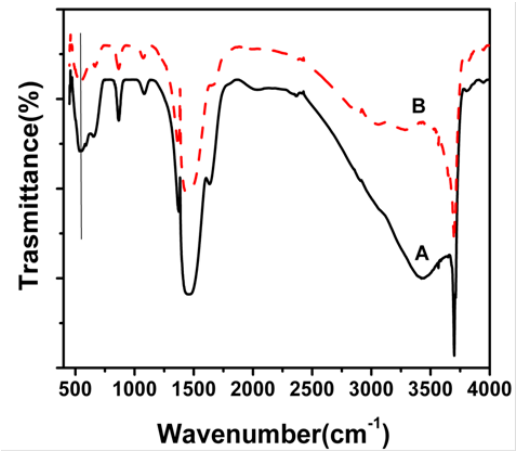

Figure 4.6: FT-IR spectra of NC-MgO samples synthesized in (A) batch and (B) continuous flow methods. Position of Mg-O bond was indicated by straight line.

4.6 TEM analysis:

MgO sample synthesized in continuous flow method was characterized by using TEM. Selective area electron diffraction (SAED) shows the polycrystalline nature of the sample and the corresponding planes were indexed on the diffraction pattern. The lattice plane seen in figure 4.7 B corresponds to (200) plane of MgO.

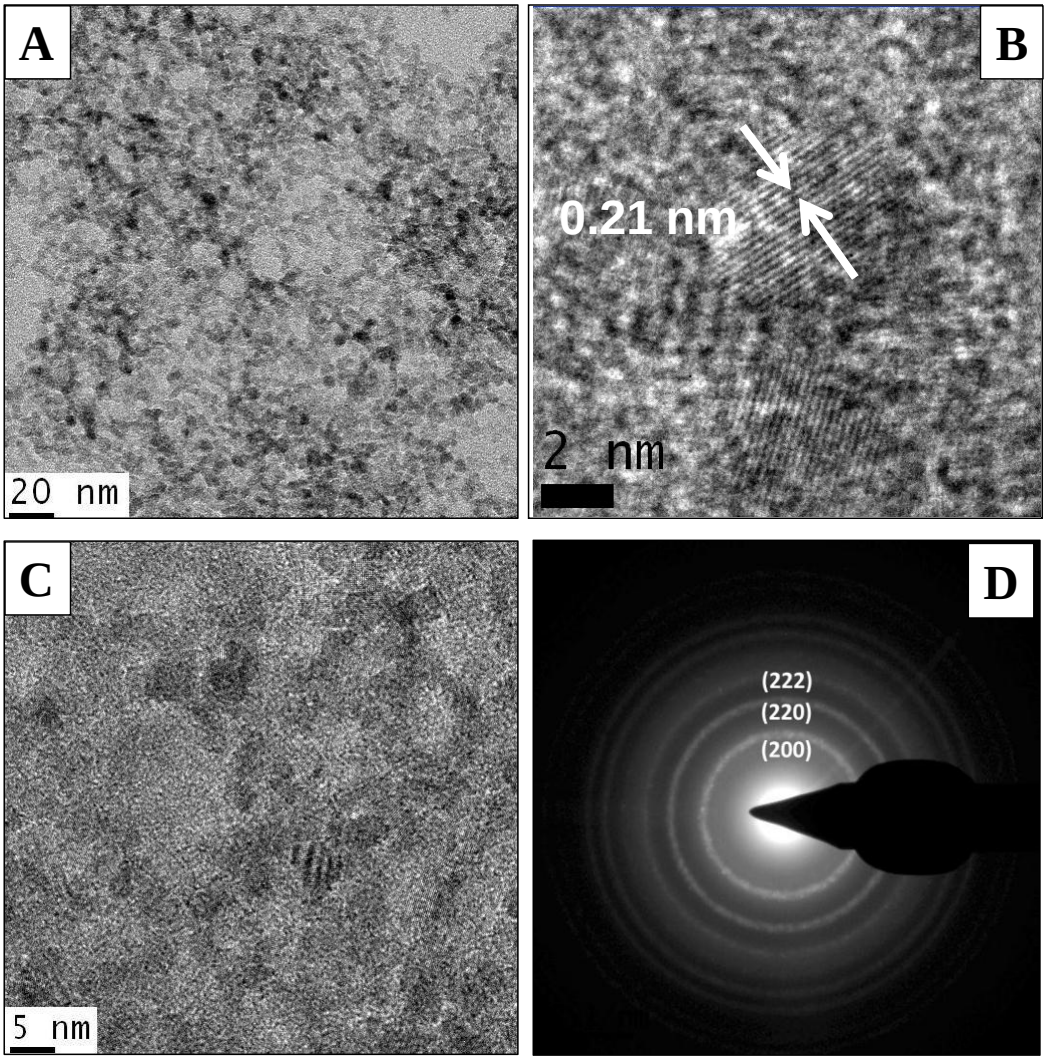

Figure 4.7: TEM image of the MgO sample synthesized in continuous flow manner and corresponding SAED pattern.

4.7 Powder X-ray diffraction and N_2 sorption isotherm analysis:

4.7.1. Samples synthesized at different angles:

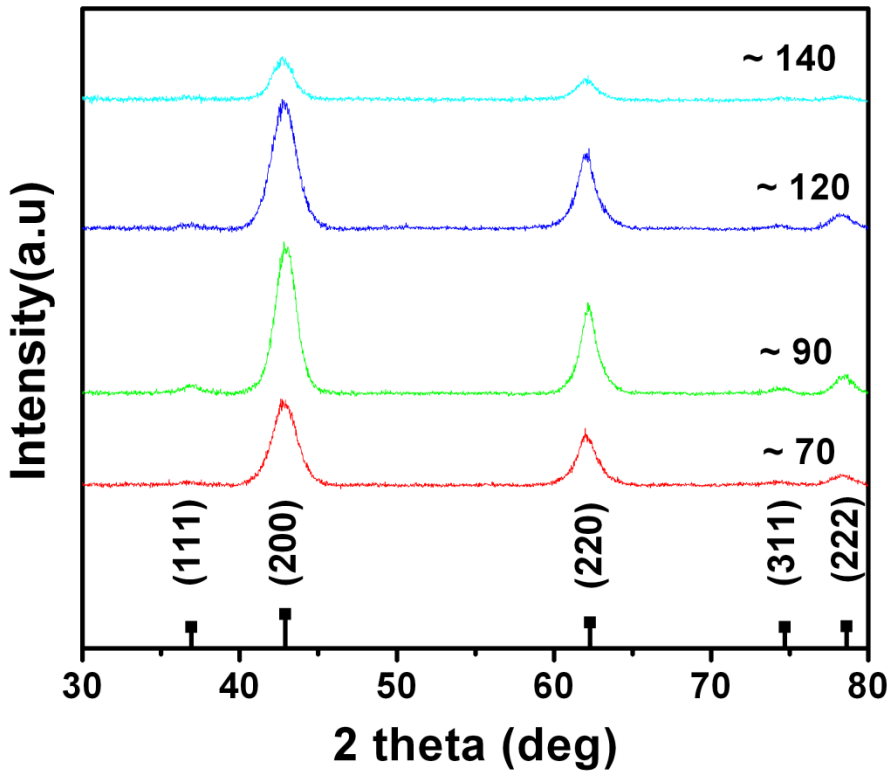

Figure 4.8: PXRD of NC-MgO samples synthesized at different angle between the jets. The total flow rate in all these experiments kept constant at 30 mL/min.

PXRD of the samples synthesized at different angle between the jets was recorded (figure 4.8). Formation of MgO was confirmed by comparing the experimental data with standard JCPDS –PDF file no 45-0946. The crystallite size was calculated for all the samples by using Scherrer's formula and summarized in the table 4.1. All these characterizations confirm the formation of MgO and agree very well with the reported data.[25]

N_2 sorption isotherms:

Adsorption and desorption isotherms using nitrogen were measured on the samples at 77K. The surface areas of the samples were measured by applying BET (Brunauer-Emmet-Teller) method to the adsorption isotherm for relative pressure values (P/P_0) in the range of 0.05 to 0.3. Pore volume was calculated at highest value of relative pressure. Pore size distribution was measured by BJH (Barret-Joyner-Halenda) analysis from the desorption isotherm. Figure 4.9 show N_2 adsorption and desorption isotherms of MgO samples synthesized in continuous flow method at different angle between the jets. All samples exhibit type H1 isotherms, which are typical for porous materials formed by spherical particle aggregates.[26, 27] This is in accordance with the TEM results obtained (figure 4.7). Surface area of the samples, pore volume etc., are summarized in the table 4.1.

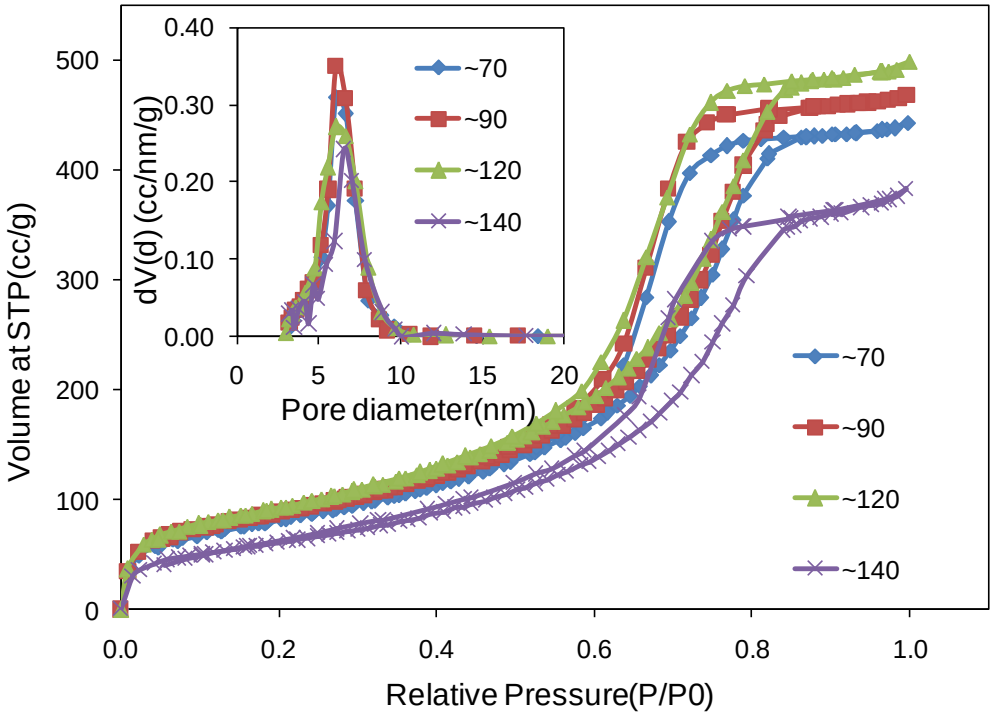

Figure 4.9: N_2 adsorption – desorption isotherms of the MgO samples synthesized at different angles between the jets. (Inset- pore size distribution).

Table 4. 1: Summary of characterization details of the samples synthesized at different angle between the jets

Sample	Angle between the jets	Surface area(m^2 /g)	Pore volume(cc/g)	Crystallite size(nm) from XRD (nm)
1	70°	299	0.69	4.7
2	90°	321	0.72	5.5
3	120°	339	0.77	4.7
4	140°	228	0.59	5.8

4.7.2 Samples synthesized at different flow rates (Re):

MgO samples synthesized at different total flow rates (angle between the jets at all the flow rates is 120°) characterized with PXRD. As explained in the previous section, data was compared with standard JCPDS- PDF 45-0946 to confirm the formation of MgO (figure 4.10). The crystallite size was calculated from Scherrer's formula, summarized in table 4.2.

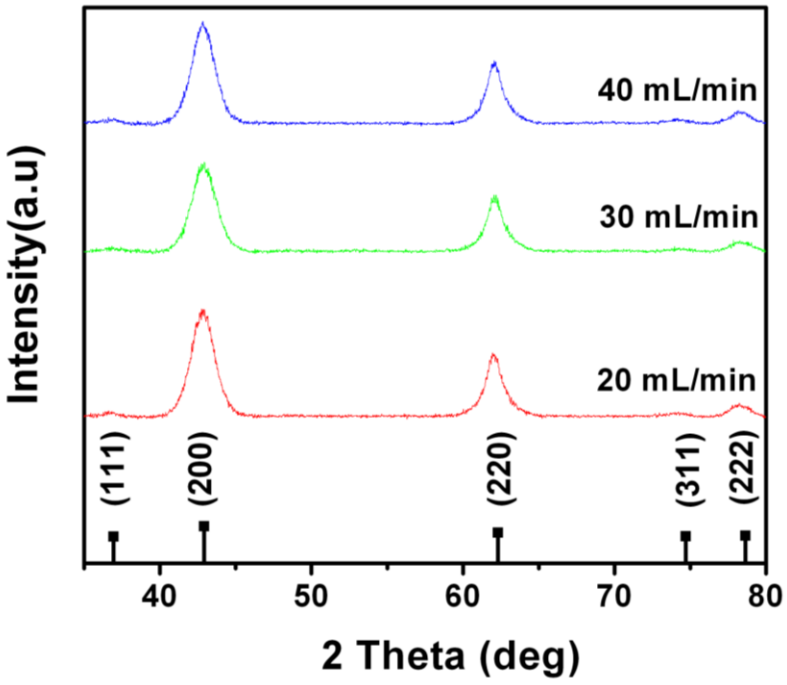

Figure 4. 10: PXRD of the MgO samples synthesized at different flow rates and angles between the jets was kept 120°.

N_2 adsorption – desorption isotherms:

MgO samples were subjected to N_2 adsorption and desorption studies and data was analyzed as explained in the previous section. The results from XRD and N_2 adsorption - desorption isotherms were summarized in table 4.2. Figure 4.11 shows the N_2 adsorption-desorption isotherms of MgO synthesized at different flow rates, all samples show H1 type hysteresis, which indicate the porous nature of the sample, arising due to spherical particle aggregates.[26, 27]

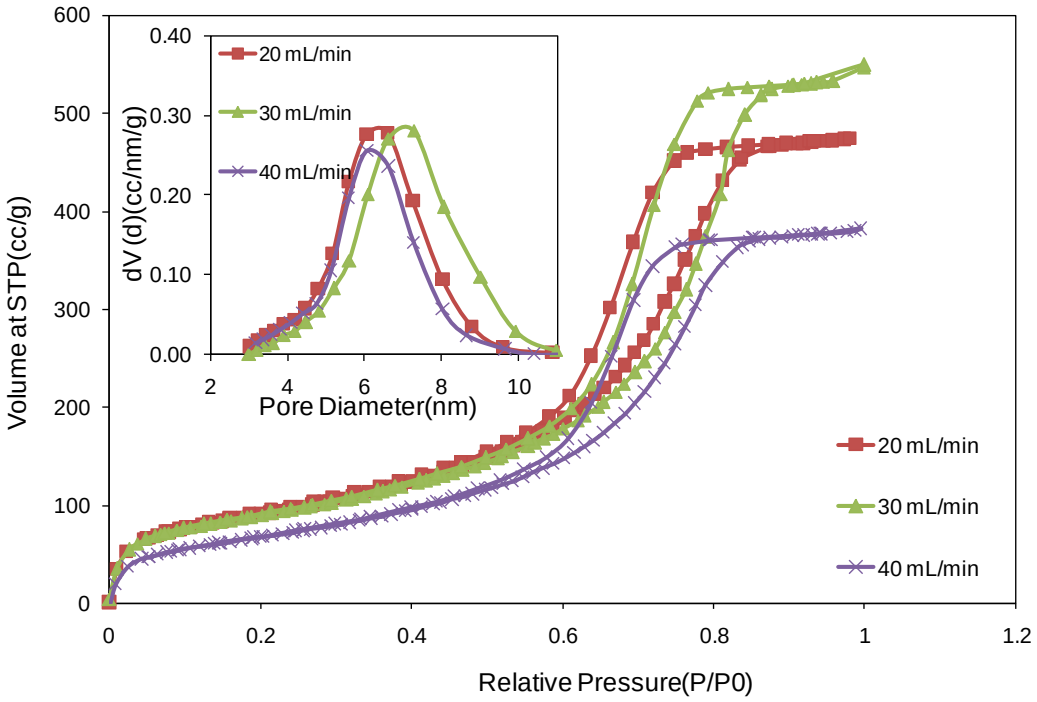

Figure 4. 11: N_2 adsorption – desorption isotherms of the MgO samples synthesized at different flow rates. (Inset shows pore size distribution).

Table 4. 2: Summary of characterization details of the samples synthesized at different flow rates

sample	Total flow rate (mL/min)	Re	Surface area (m^2 /g)	Pore volume(cc/g)	Crystallite size(nm) from XRD
1	20	1040	327	0.73	4.9
2	30	1560	322	0.85	4.6
3	40	2080	250	0.59	4.7

4.8 Discussion:

Mixing is an important phenomenon for very rapid processes and it assumes greater significance when these processes are to be taken to industrial scale. Mixing in industrial scale operations involves high power consumption and hence increases the cost of production.[28] This is one the main reasons why researchers turned to microreactors for scaling up of nanoparticle synthesis. Apart from traditional microreactors/micromixers confined jet micromixer(CIJs) are well studied theoretically and experimentally.[23, 29] These are very useful for the nanoparticle synthesis by rapid precipitation. In this current example where mixing of the two reactants results in the formation of rigid gel, using channeled microreactors and CIJ is also ruled out because the channel may get clogged in confined environment. To overcome this, as described in introduction, we have to allow the mixing to take place in wall free environment and simultaneously mixing has to be fast to initiate homogeneous nucleation. Demyanovich and coworkers studied the rapid mixing by impingement of two thin liquid sheets in free space.[28, 30] Later the nature of mixing zones (i.e mixing sheet formed by the impingement of two liquid jets) was further studied by Li et al.,[31] and atomization pattern produced by the liquid jets was studied by Jung et al.,[32] Mixing in impingement of liquid jets will be affected by thickness of the mixing sheet, pressure drop, and viscosity. The inelastic nature of the collision results in high energy dissipation, making the flow turbulent and ensuing effective mixing. To get relatively efficient mixing Reynolds number (Re) should be more than 1000.[28]

Shape, area and thickness of the mixing zone formed by the impingement of two opposite jets determines the nature of mixing and in the present case we observed considerable change in the area and thickness of the mixing zone by varying the angle between the jets. The volumetric flow rate of the individual jet was maintained as 15 mL/min (total flow rate is 30 mL/min) to obtain strong and stable jet followed by stable mixing zone. From table 4.1 it can be easily noticed that highest surface area was achieved when the angle between the jets was around 120°. Changes in surface areas were minimal when the angle between the jets increased

from 70° to 120°. When the angle increased further from 120° to 140°, Considerable decrease in surface areas were observed (from 339 to 228 m^2/g). This variation in the surface area of the synthesized sample can be understood by analyzing the area of the mixing zone at different angles using high speed camera. Figure 4.12 shows the schematic of the mixing zone and high speed camera images of the mixing zone of the sample jets recorded at different angle between the jets. The high speed camera images were analyzed by Imagepro® software. Aspect ratio of the mixing zone (a/b) and thickness of the mixing zone (t) were measured from the images. Figure 4.13 represents the aspect ratio and thickness of the mixing zone at various angles (i.e angle between the jets is 70°, 90°, 120°).

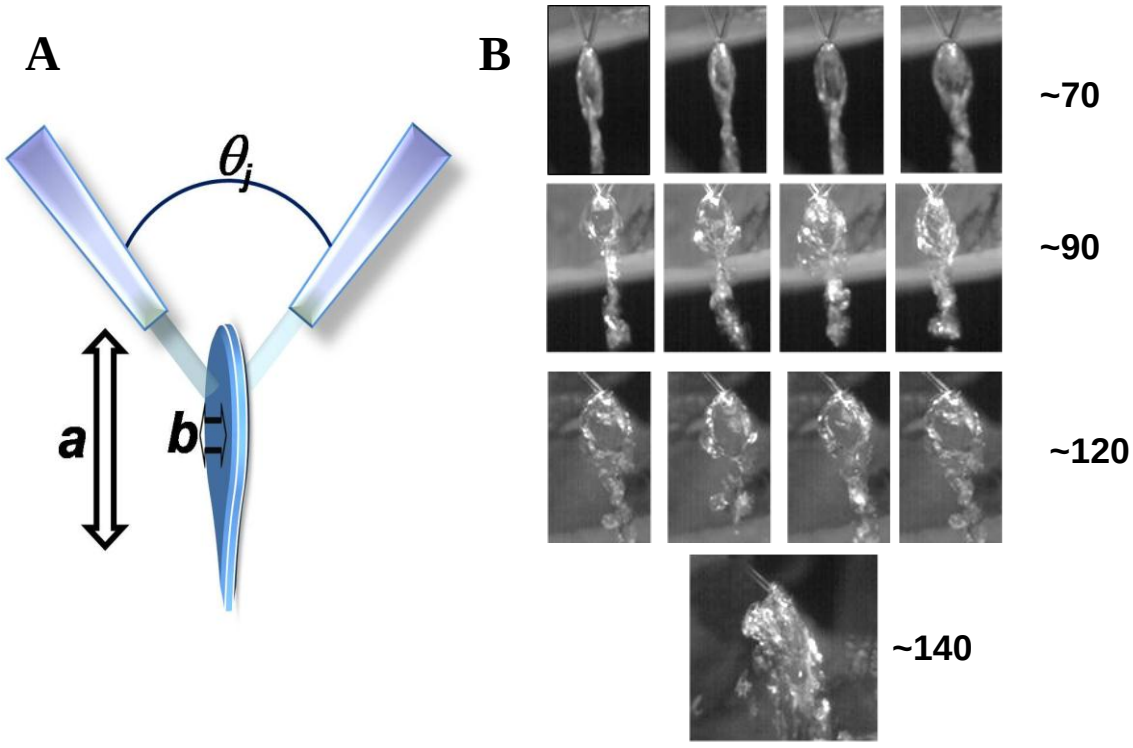

Figure 4. 12: (A) Schematic of the micromixer (B) High speed camera photographs of the mixing zone of the sample jets at different angles between the jets.

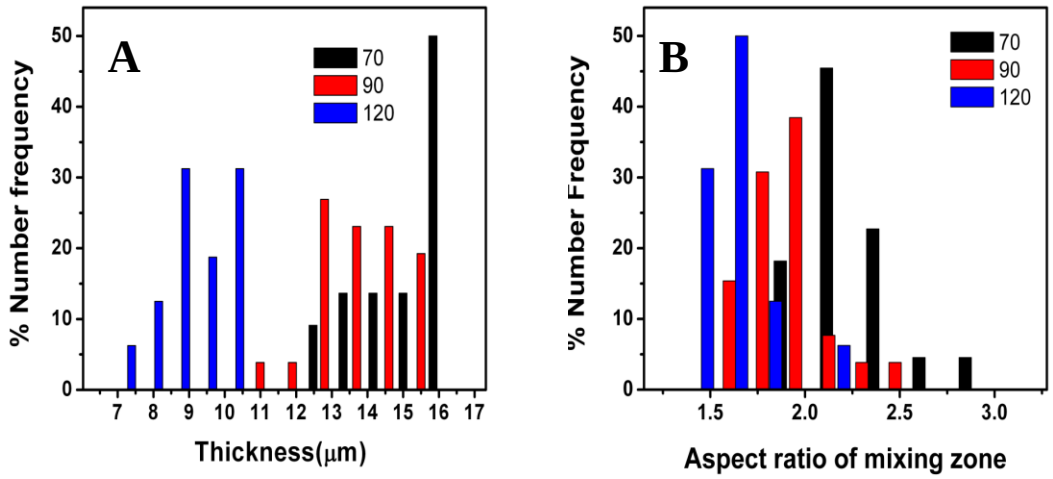

Figure 4. 13: (A) Thickness of the mixing zone (B) Aspect ratio of the mixing zone at different angles between the jets.

As we did not observe stable mixing zone when the angle between the jets is 140°, aspect ratio and thickness of the mixing zone were not taken into account in this case. Table 4.3 correlates the aspect ratio and thickness of the mixing zones with the surface areas of the MgO samples synthesized at different angle between the jets. It can be easily noticed that very thin mixing zone was obtained when the angle between the jets is around 120°. When compared to the remaining angles (70°, 90°), aspect ratio was also minimum at this angle (120°). Since the volume of the reagents pumped was constant and equal flow rates were maintained for the two jets, an enhanced mixing can be expected at 120°, which is purely due to the thin mixing zone with larger area. At this enhanced mixing, the rate of mixing would be more than the rate of reaction allowing a homogeneous nucleation of nanoparticles to take place. This results in the high BET surface area for this sample.

Table 4. 3: Details of the mixing zone and surface area of the sample synthesized at different angle between the jets

Angle between the jets	Average aspect ratio	Average thickness of the mixing zone(μm)	BET surface area (m^2 /g)
~70	2.1	14.3	299
~90	1.8	13.4	320
~120	1.5	8.7	340
~140	-	-	228

After we delineated the effect of angle between the jets on the surface area of the samples, we turned our attention to the effect of flow rates (in another terms Reynolds number, Re), we carried out the synthesis at different total flow rates (at 20 mL/min, 30 mL/min and 40 mL/min) by keeping the angle between the jets constant i.e. 120°. As the volume of the reactants pumped changes at each flow rate, the shape and thickness of the mixing zone also expected to change because of gravity. The surface areas of the samples, synthesized at different flow rates were represented in table 4.2. As flow rate was increased from 20 mL/min to 30 mL/min, the BET surface area of the samples hardly changed (from 327 m^2/g to 322 m^2/g). When the flow rate was increased further to 40 mL/min, BET surface area decreased from 322 m^2/g to 250 m^2/g. To understand these variations in surface areas, we analyzed the high speed camera images of the mixing zone obtained at different flow rates (figure 4.14).

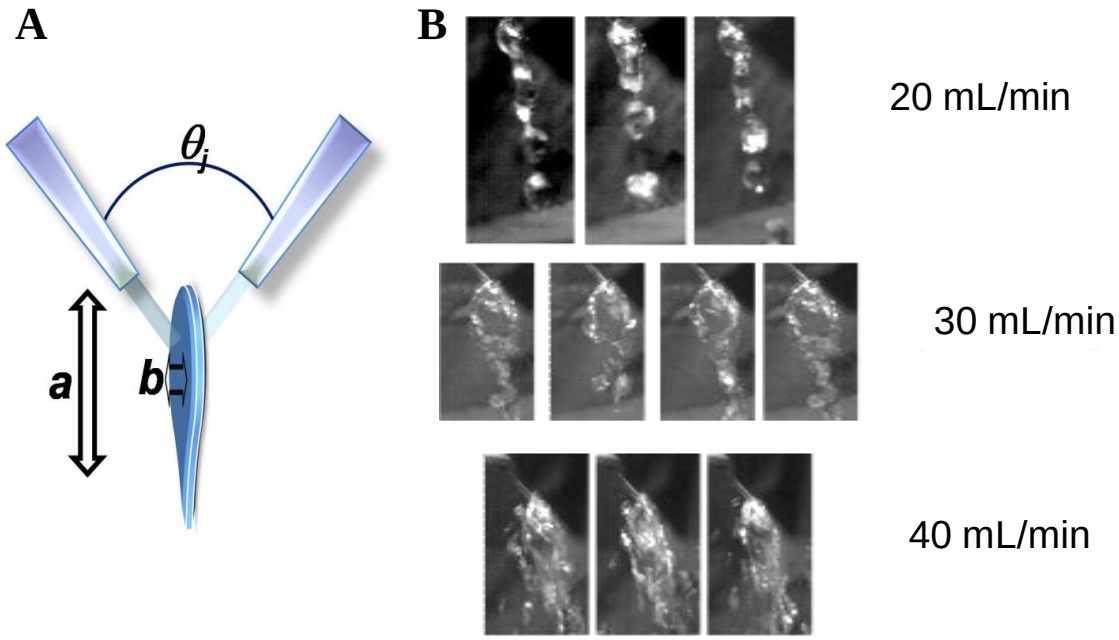

Figure 4. 14: (A) Schematic representation of the mixing zone (B) High speed camera images of the mixing zone at different flow rates.

Figure 4.15 shows the aspect ratio and thickness of the mixing zones at different flow rates and these data are presented and correlated with the surface area of the samples in the table 4.4.

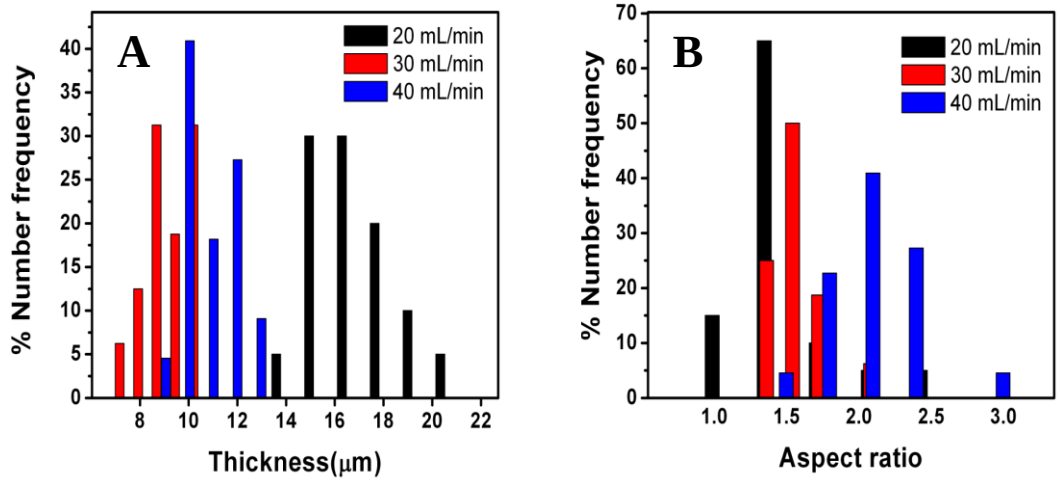

Figure 4. 15: (A) Thickness of the mixing zone (B) aspect ratio of the mixing zone at different flow rates.

Table 4. 4: Details of the mixing zone and surface area of the sample synthesized at different flow rates

Flow rate (mL/min)	Average aspect ratio	Average thickness of the mixing zone(μm)	Surface area (m^2 /g)
20	1.3	16	327
30	1.5	8.7	322
40	1.8	10.02	250

The decrease in surface area at 40 mL/min, is attributed to the instabilities in mixing zone as the flow rate increases (figure 4.14). However, at 20 mL/min though the thickness of the mixing zone is high, we did not observe any decrease in surface area. We conclude that at such low flow rates, both the reactant fluids would be in contact for sufficiently longer times and hence the thickness of the mixing zone did not affect the final surface area of the material greatly.

4.9 Conclusions:

Continuous flow process was developed for the synthesis of nanocrystalline MgO which has a great market potential in the nano products. A rapid sol gel process was successfully transformed to continuous flow process using a jet micromixer. The angle between the jets and flow rates at which the reactor should be operated were optimized to get the maximum surface area of the sample. The surface area of the sample, synthesized through continuous flow methods was comparable to market standards with high reproducibility.

4.10 References:

1. Stoimenov, P. K.; Klinger, R. L.; Marchin, G. L.; Klabunde, K. J., *Langmuir* **2002,** *18*, 6679-6686.
2. Chintareddy, V. R.; Lakshmi Kantam, M., *Catal. Surv. Asia* **2011,** *15*, 89-110.
3. Choudary, B. M.; Chakrapani, L.; Ramani, T.; Kumar, K. V.; Kantam, M. L., *Tetrahedron* **2006,** *62*, 9571-9576.
4. Choudary, B. M.; Jyothi, K.; Kantam, M. L.; Sreedhar, B., *Adv. Synth. Catal.* **2004,** *346*, 45-48.
5. Choudary, B. M.; Jyothi, K.; Roy, M.; Kantam, M. L.; Sreedhar, B., *Adv. Synth. Catal.* **2004,** *346*, 1471-1480.
6. Choudary, B. M.; Kantam, M. L.; Ranganath, K. V. S.; Mahendar, K.; Sreedhar, B., *J. Am. Chem. Soc.* **2004,** *126*, 3396-3397.
7. Choudary, B. M.; Mahendar, K.; Kantam, M. L.; Ranganath, K. V. S.; Athar, T., *Adv. Synth. Catal.* **2006,** *348*, 1977-1985.
8. Choudary, B. M.; Mulukutla, R. S.; Klabunde, K. J., *J. Am. Chem. Soc.* **2003,** *125*, 2020-2021.
9. Choudary, B. M.; Ranganath, K. V. S.; Pal, U.; Kantam, M. L.; Sreedhar, B., *J. Am. Chem. Soc.* **2005,** *127*, 13167-13171.
10. Choudary, B. M.; Ranganath, K. V. S.; Yadav, J.; Kantam, M. L., *Tetrahedron Lett.* **2005,** *46*, 1369-1371.
11. Fierro, J., *Metal Oxides: chemistry and applications*. CRC: 2005; Vol. 108.
12. Kantam, M. L.; Chakrapani, L.; Choudary, B. M., *Synlett* **2008**, 1946-1948.
13. Kantam, M. L.; Roy, S.; Roy, M.; Sreedhar, B.; Choudary, B. M., *Adv. Synth. Catal.* **2005,** *347*, 2002-2008.
14. Mishakov, I. V.; Bedilo, A. F.; Richards, R. M.; Chesnokov, V. V.; Volodin, A. M.; Zaikovskii, V. I.; Buyanov, R. A.; Klabunde, K. J., *J. Catal.* **2002,** *206*, 40-48.
15. Brinker, C.; Sehgal, R.; Hietala, S.; Deshpande, R.; Smith, D.; Loy, D.; Ashley, C., *J. Membr. Sci.* **1994,** *94*, 85-102.
16. Brinker, C. J.; Scherer, G. W., *Sol-gel science: the physics and chemistry of sol-gel processing*. Academic Pr: 1990.
17. Gonzalez, R. D.; Lopez, T.; Gomez, R., *Catal. Today* **1997,** *35*, 293-317.

18. Diao, Y.; Walawender, W. P.; Sorensen, C. M.; Klabunde, K. J.; Ricker, T., *Chem. Mater.* **2002,** *14*, 362-368.

19. Ranjit, K. T.; Klabunde, K. J., *Chem. Mater.* **2005,** *17*, 65-73.

20. Marchisio, D. L.; Rivautella, L.; Barresi, A. A., *AIChE J.* **2006,** *52*, 1877-1887.

21. Zhu, Z.; Anacker, J. L.; Ji, S.; Hoye, T. R.; Macosko, C. W.; Prud'homme, R. K., *Langmuir* **2007,** *23*, 10499-10504.

22. Lince, F.; Marchisio, D.; Barresi, A., *Chem. Eng. Res. Des.* **2009,** *87*, 543.

23. Johnson, B. K.; Prud'homme, R. K., *AIChE J.* **2003,** *49*, 2264-2282.

24. https://www.imm-mainz.de/fileadmin/IMM-upload/Flyer-Katalog_etc/Catalogue09_IJMM.pdf.

25. Trionfetti, C.; Babich, I.; Seshan, K.; Lefferts, L., *Top. Catal.* **2006,** *39*, 191-198.

26. Leofanti, G.; Padovan, M.; Tozzola, G.; Venturelli, B., *Catal. Today* **1998,** *41*, 207-219.

27. Reichenauer, G.; Scherer, G., *J. Non-Cryst. Solids* **2001,** *285*, 167-174.

28. Demyanovich, R. J.; Bourne, J. R., *Ind. Eng. Chem. Res.* **1989,** *28*, 830-839.

29. Gavi, E.; Marchisio, D. L.; Barresi, A. A., *Chem. Eng. Sci.* **2007,** *62*, 2228-2241.

30. Demyanovich, R. J.; Bourne, J. R., *Ind. Eng. Chem. Res.* **1989,** *28*, 825-830.

31. Li, R.; Ashgriz, N., *Phys. Fluids* **2006,** *18*, 087104.

32. Jung, S.; Hoath, S. D.; Martin, G. D.; Hutchings, I. M., *Phys. Fluids* **2010,** *22*, 042101.

Chapter 5

Conclusion

5.1 Summary:

In the first chapter of this thesis, we emphasized the necessity of scale up synthesis of nanomaterials and we showed the potentiality of the continuous flow synthesis using microreactors for this purpose. Hence we adopted the continuous flow techniques and applied them to several systems with different level of complexities, which have huge market value.

Simple, one step protocol to synthesize Ag nanoparticles with stearic acid sophorolipid yields very stable (for months), water dispersible nanoparticles. This method was successfully transformed to continuous flow method, using a novel design spiral micro reactor. We described the importance of geometry of the micro channel to get narrow size distributions, without using segmented flow methods. Our interest is continued and in the next part we studied the combination of fluid flow in spiral microreactor - segmented flow and its effect on particle size distribution.

Staking faults play major role in the formation of two dimensional plate like structures and we described the role various parameters like temperature, surfactant to metal precursor mole ratio, role of bromide ions to induce the staking faults and to produce nanoplates. This understanding helped us to develop the flow synthesis of nanoplates. In detailed manner, we described the flow synthesis of nanoplates with and without surfactant. Role of reactor tubing material, temperature profiles are explained to achieve the maximum yield of the nanoplates.

Other than simple reductions and surfactant assisted methods to synthesize the nanomaterials using flow methods, we explored the possibility of using flow methods for rapid processes like sol to gel formation to synthesize nanocrystalline MgO which involve gel formation. Micro jet micromixer was used for this purpose which allows the reactant to come in contact in wall free environment. Mixing is very important phenomenon in these kinds of reactions and we addressed the role of several fluid dynamic parameters in controlling the shape and thickness of the mixing zone. This eventually affects the properties of the synthesized nanocrystalline MgO. We believe that the work discussed in this thesis would be

helpful to bring significant changes in the area of flow syntheses of nanomaterials in large quantities and it may attract the attention of both academia and industry.

5.2 Future Directions:

Developing alternative energy sources is one of the major challenges of the 21st century. Energy storage devices, photocatalysis, solar cells, fuel cell etc., are playing major role in this area. Silicon is one of the highly efficient material for solar cell applications,[1] because of its less abundance, several research groups developed novel materials which can replace silicon for photovoltaic applications. Table 5.1 shows the comparison of efficiency of several materials for photovoltaic applications.

Table 5. 1: Efficiency of different solar cell materials(Ref 1)

Table 1 Performance of photovoltaic and photoelectrochemical solar cells

Type of cell	Efficiency (%)* Cell	Module	Research and technology needs
Crystalline silicon	24	10–15	Higher production yields, lowering of cost and energy content
Multicrystalline silicon	18	9–12	Lower manufacturing cost and complexity
Amorphous silicon	13	7	Lower production costs, increase production volume and stability
$CuInSe_2$	19	12	Replace indium (too expensive and limited supply), replace CdS window layer, scale up production
Dye-sensitized nanostructured materials	10–11	7	Improve efficiency and high-temperature stability, scale up production
Bipolar AlGaAs/Si photoelectrochemical cells	19–20	—	Reduce materials cost, scale up
Organic solar cells	2–3	—	Improve stability and efficiency

*Efficiency defined as conversion efficiency from solar to electrical power.

From the above table it can be easily recognized that in solar cell technologies materials like $CuInSe_2$ electro chemical bipolar materials like AlGaAs/Si show high efficiency (almost equal to single crystalline silicon). The major problem associated with these materials is scale up. Jin et al.,[2] and Shavel et al.,[3] showed the possibility

of continuous flow synthesis of $CuInS_2$ and Cu_2ZnSnS_4, as a proof of concept, but the scale up synthesis of these materials is really unexplored. Moreover, microfluidc platforms offer the possibility of combinatorial synthesis and this gives opportunity to synthesize different compositions of copper based quaternary chalcogenides from the single microfluidic chip.

Furthermore, it is not difficult to imagine the applications of photoluminescent carbon dots[4] in biological imaging and detection, as they are more biocompatible than semiconductor quantum dots. Solution based synthesis of carbon quantum dots are sparse and the existing solvothermal,[5] electrochemical methods[5-7] can not provide large quantities needed for such applications. In these circumstances one can easily imagine the challenge associated with the conversion of solvothermal based methods to flow based procedures and the opportunities offered by large scale synthesis of carbon nanodots.

5.3 References:

1. Gratzel, M., *Nature* **2001,** *414*, 338-344.
2. Jin, H. D.; Chang, C.-H., *J.Nanopart.Res* **2012,** *14*, 1-9.
3. Shavel, A.; Cadavid, D.; Ibáñez, M.; Carrete, A.; Cabot, A., *J. Am. Chem. Soc.* **2012,** *134*, 1438-1441.
4. Cao, L.; Meziani, M. J.; Sahu, S.; Sun, Y. P., *Acc. Chem. Res.* **2013,** *46*, 171-180.
5. Mitra, S.; Chandra, S.; Pathan, S. H.; Sikdar, N.; Pramanik, P.; Goswami, A., *RSC Adv.* **2013,** *3*, 3189-3193.
6. Shinde, D. B.; Pillai, V. K., *Chem.--Eur. J.* **2012,** *18*, 12522-12528.
7. Shinde, D. B.; Pillai, V. K., *Angew. Chem., Int. Ed.* **2013,** *52*, 2482-2485.

Appendix – I

Instruments Used

UV-Vis-NIR spectrophotometer: UV-Visible-NIR spectral measurements were carried out using JASCO V-570 model UV-Visible spectrophotometer with a resolution of 1 nm.

FTIR spectrophotometer: FTIR spectra were recorded on a Perkin Elmer Spectrum One FTIR spectrophotometer in diffuse reflectance mode, operating at a resolution of 4 cm-1.

Dynamic Light Scattering: DLS measurements were carried out on Brookhaven Instrument model 90 Plus Particle Size Analyzer.

X-ray Diffraction: The diffractograms were recorded on a PAN alytical Xpert promachine using a CuKα (λ=1.54Å) source and operating conditions of 40 mA and 30 kV at different scan rates depending upon the sample.

Transmission Electron Microscopy: Samples were characterized with Technai T-20 transmission electron microscope operated at 200kV. For high resolution images Technai T-30 instrument operated at 300 kV was used. TEM samples were prepared by coating drop casting the samples on TEM grid and allowed to dry under ambient conditions.

Scanning Electron Microscopy: SEM images of the samples were recorded using FEI Quanta environmental SEM operated at 20kV.

Surface area and Pore size/Volume analysis: BET Surface area of the samples measured using Quantachrome autosorb instrument.

Appendix – II

List of abbreviations

SERS	Surface Enhanced Raman Scattering
SL	Sophorolipid
OASL	Oleic acid sophorolipid
SASL	Stearic acid sophorolipid
PMMA	Poly (methyl methaacrylate)
PEEK	Polyether ether ketone
CNC	Computer Numerical Control
UV-Vis-NIR	Ultraviolet - Visible - Near Infrared
DLS	Dynamic Light Scattering
TEM	Transmission Electron Microscopy
XRD	X-Ray Diffaraction
De	Dean Number
Re	Reynolds Number
We	Weber Number
Ca	Capillary Number
Dh	Hydraulic Diameter
P	Density
μ	Viscosity

V	Velocity of the fluid
Rc	Radius of the curvature of curved channel
ɣ	Interfacial/Surface Tension
CTAB	Cetyl(hexadecyl) Trimethyl Ammonium Bromide
PVP	Poly Vinyl Pyrrolidine
ODTAB	Octadecyl Trimethyl Ammonium Bromide
SPR	Surface Plasmon Resonance
Cp	Specific Heat
U	Heat transfer Coefficient
κ	Thermal Conductivity
Pr	Prandtl Number
Nu	Nusselt Number
CIJ	Confined Impingement Jet
BET analysis	Brunauer - Emmett-Teller-analysis
BJH analysis	Barrett - Joyner - Halenda analysis

Appendix – III

List of Publications

1. **Kumar, D.V.R**., Kasture, M.B.,Prabhune, A.A., Ramana, C.V., Prasad, B.L.V., Kulkarni,A.A., Continuous flow synthesis of functionalized silver nanoparticles using bifunctional biosuarfactants, ***Green Chem***., **2010**,*12*,609-615.

2. **Kumar, D.V.R**., Prasad, B.L.V., Kulkarni, A.A., Segmented flow synthesis of Ag nanoparticles in spiral microreactor: Role of continuous and dispersed phase. ***Chem.Eng.J.***, **2012**,*192*,357-368 (**Cover page Article).**

3. **Kumar, D.V.R**., Kulkarni, A. A., Prasad, B.L.V., Surfactant directed synthesis of triangular gold nanoplates: Understanding and optimization of reaction parameters, ***Colloids. Surf A.,*** **2013**,*422*, 181-190.

4. **Kumar, D.V.R**., Prasad, B.L.V., Kulkarni, A. A., Microfluidic platform to synthesize triangular gold nanoplates (Communicated).

5. **Kumar, D.V.R**., Kulkarni, A. A., Prasad, B.L.V., Rapid Sol-Gel Process for the synthesis of Nanocrystalline MgO using Impingement Jet Micromixer (Communicated).